beta-bcc and amorphous Ti-based biocompatible alloys for human body implants

Yaofeng Guo

To cite this version:

Yaofeng Guo. beta-bcc and amorphous Ti-based biocompatible alloys for human body implants. Materials. Université de Grenoble, 2014. English. NNT : 2014GRENI017 . tel-01290049

HAL Id: tel-01290049
https://theses.hal.science/tel-01290049

Submitted on 17 Mar 2016

UNIVERSITÉ DE GRENOBLE

THÈSE

Pour obtenir le grade de

DOCTEUR DE L'UNIVERSITÉ DE GRENOBLE

Spécialité : **Ingénierie Matériaux mécanique énergétique environnement procédés production (Grenoble)**

Arrêté ministériel : 7 août 2006

Présentée par

« Yaofeng GUO »

Thèse dirigée par **« Alain Reza Yavari»** et
codirigée par **« Konstantinos Georgarakis»**

préparée au sein du **Laboratoire Science et Ingénierie des Matériaux et Procédés - SIMaP**
dans **l'École Doctorale IMEP2/MATERIAUX, MECA, GENIE CIVL, ELECTRPCHIMIE**

Beta-BCC et Alliages Amorphes Biocompatibles à Base de Titane pour les Implants

Thèse soutenue publiquement le **« 7 Avril 2014»**,
devant le jury composé de :

M. A. Lindsay Greer
Professeur - Université de Cambridge (Président, Membre)
M. Gérard Le Caër
Professeur - Université de Rennes I (Rapporteur, Membre)
M. Walter Jose Botta
Professeur - Université Fédérale de Sao Carlos (Rapporteur, Membre)
M. Alain Reza Yavari
DR1 CNRS - CNRS/Grenoble INP (Directeur de thèse, Membre)
M. Konstantinos Georgarakis
Grenoble INP (Co-encadrant de thèse, Membre)

This work was funded by EC ITN Network "BioTiNet" (grant No. 264635)

Acknowledgements

This Ph.D. research was performed under ITN project (grant No. 264635) entitled “Innovative Biocompatible Titanium-based Structures for Orthopaedics”, at SIMaP laboratory CNRS UMR - No. 5266 at Institut Polytechnique de Grenoble.

I would like to thank Prof. Michel Pons, director of research CNRS and director of SIMaP, for having hosted me in his laboratory during this work.

I would like to greatly thank Prof. A. Lindsay Greer of University of Cambridge for accepting to preside over the jury of the thesis, and sincerely thank Prof. Gérard Le Caër and Prof. Walter J. Botta for the expert evaluation work as “rapporteur” in the jury.

Thanks are also due to Dr. Konstantinos Georgarakis, who co-supervised this thesis work.

I wish to gratefully thank Prof. Alain Reza Yavari (director of CNRS “classe exceptionnelle” / SIMaP) for accepting me in his team and supervising my work over more than past three years.

I would also like to thank Prof. Tao Zhang for giving me the opportunity to go to France and opening me the possibility of my European thesis in France.

Thanks are also due to Dr. Xiangjin Zhao for teaching me the techniques of rapid solidification in BeiJing, M. Alain Le Moulec who always provided technical support in SIMaP, as well as to J.J. Francoise, L. Artaud, S. Coindeau, T. Encinas, F. Charlot of the CMTC and Mrs. F. Fonseca, H. Collas, Mrs. S. Champavier, Dr. M. Zhang. I am also very thankful of useful conversions and experimental collaboration with team members, Prof. A. Moreira Jorge Jr. and Dr. I. Bataev.

Many thanks are also due to Prof. M. Kotani, director of AIMR (Advanced Institute for Materials Research) of Tohoku University and in particular to Prof. D.V. Louzguine and Y. Yokoyama for providing experimental facilities during two months visit at the AIMR.

Finally, I would like to express my appreciations to my fellows of ITN network and to the co-ordination team of Prof. Jürgen Eckert (M. Calin. D. Beitelschmidt and their colleagues).

I wish to dedicate this work to my family. You make me a better man.

Contents

General Introduction

In the near future, skeletal injuries and disorders due to the ageing will affect 25% of the aging populations in the western world, but only limited technological and clinical breakthroughs have been achieved in the past decades in materials development for permanent implants in oral implantology and orthopaedics. Metals such as titanium alloys are current favored for orthopaedic or dental implants because their surface properties provide a biocompatible interface. However, their long term clinical performance may be compromised by the different mechanical properties exhibited by titanium when compared to those of bone, creating strong stress shielding effects at the bone – implant interface.

There are three major requirements for optimum medical bone implants: a) minimum stress - shielding effect due to the mismatch of the Young Moduli between the implant and the bone; b) biocompatibility and absence of toxic components such as Ni and Cu; c) adjusted bio-activity and corrosion rates as there is usually a contradiction between anticorrosive properties and acceptable bioactivity of implanted materials. It is thus a major scientific challenge to develop implant materials free of toxic components which can provide simultaneously minimal stress-shielding effect, good biocompatibility, (Ni, Cu etc.) and adjusted corrosion resistance and bio-activity.

The research of present thesis will be based on two approaches.

1) Study of the stabilization of the β-Ti structure which has lower elastic constants than α-Ti by developing new Ti based alloys using rapid solidification techniques (copper mould casting).

2) Development of Ti based metallic glasses with reduced stiffness compared to their crystalline counterparts and free of toxic element additions.

This thesis contains four chapters and the content of each chapter is briefly described below:

Chapter 1 presents the literature study of applications of human body implant alloys and the current remaining issues during usage. The equilibrium and non-equilibrium crystalline phases in Ti-based crystalline alloys and the associated phase transformation between them during cooling and isothermal annealing are summarized. The reason of shape memory effect and the superelasticity in Ti-based crystalline materials is also described. For Ti-based amorphous alloys, the definition of glassy state and formation of glass is first discussed. The designing rules of alloys of good glass forming ability and good Ti-based glass former are then summarized. The unique properties of metallic glasses, which is attracting for body implant alloys, are finally described.

Chapter 2 lists the experimental techniques employed in current thesis. These techniques include the synthesis of alloys through rapid solidification and, characterization of microstructure, thermal properties and mechanical properties.

The synthesis and properties characterization of Ti-Nb(-Sn) based crystalline alloys is discussed in

Chapter 3. First the Ti-Nb(-Sn) based crystalline alloys are fabricated through rapid solidification techniques. The alloys are then subjected to heat treatments followed by either furnace cooling or water quenching. The microstructure and its formation in the above heat treated as well as as-cast alloys are then analyzed. The compositional dependence of stability of β phase in alloys of different states is studied. The mechanical properties of the Ti-Nb(-Sn) based crystalline alloys in different states are also investigated. The alloys exhibit different behaviors upon cyclic loading - unloading process. Shape memory effect and superelasticity are found. The Young's modulus of β phase based alloys is measured and is lower than that of the currently used Ti-based alloys.

The formation of Ti-Fe-Si based glassy alloys and their properties are discussed in Chapter 4. The Ti-Fe-Si based glassy alloys are designed according to the "deep eutectic" rule and synthesized by rapid solidification techniques. The microstructure and thermal properties of the glassy alloys are studied. The structural evolution of selected glassy alloys during annealing is investigated. The corrosion properties in simulated body fluid (Hanks solution) is characterized by potentiodynamic polarization. The corrosion resistance of current Ti-Fe-Si based glassy alloys are compared to those of other Ti-based glassy alloys and commercial purity Ti, which is used as body implant alloys. At last, *in situ* observation of amorphization of one Ti-based good glass former in synchrotron beam was conducted. The alloy was successfully vitrified in an aerodynamic levitation apparatus and the associated structural evolution during cooling is analyzed.

Finally, the main results are summarized in the general conclusion part.

The experimental work in current thesis was conducted in the laboratory SIMaP of Institut Polytechnique de Grenoble" and is under the supervision of Professor Alain Reza Yavari, director of CNRS research "classe exceptionnelle" / SIMaP and co-supervision of Dr. Konstantinos Georgarakis.

Chapter 1 Literature Study

Introduction

1.1.1 History of biomaterials for human body implants

In late 19th century, the awareness and concept of aseptic surgery was established, which greatly decreased the possibility of infection for human body implantation. Perhaps the first modern implant surgery was conducted by Harold Ridley when he implanted polymethylmethacrylate (PMMA) as intraocular lenses for British pilots in 1949. At the same time, numerous surgeons began to develop various implants, such as hip implants, vascular graft and so on [1]. Since then, owing to the great development of refining and processing techniques of materials, the first generation of implant alloys was commercialized in 1960s and 1970s [2]. They were developed as medical devices, e.g. artificial joints, dental implants, ocular lenses or vascular stents. Thanks to these implants, the quality of life of millions of patients was greatly improved. At that stage, scientists concentrated on minimizing the immune response of implanted alloys through tuning physical and chemical properties of implants. Due to this, these implant alloys have, nowadays, been categorized as “inert” biomaterial or biocompatible implants. In the field of metallic implant materials, stainless steel, Co-Cr alloys and Ti-6Al-4V were developed. Regarding non-metallics, PMMA and polytetrafluorethylene (PTFE) were synthesized and used as implant materials [2].

In 1980s, some scientists shifted their focus from biocompatible to bioactive materials. The second generation of implant alloys was fabricated in 1990s. These materials were designed to evoke biological reaction or response at the interface between host tissue and implant alloys [3]. Ti-based implant alloys and ceramic based materials, as well as porous structure materials were produced. These materials are used for example in orthopaedics, dentistry and cardiology.

In the 21st century, progress in molecular biology leads to the emergence of third generation implant materials, the “biodegradable materials” [4]. These materials can dissolve completely to surrounding tissues in host body after implantation. They are, therefore, also referred to as “bioresorbable” implants.

Although the idea of biologically inspired designing was proposed as early as the 1950s, recent development in this respect resulted in the emergence of fourth generation biomaterials. They are based on the idea that biomimetic matrices can be developed to mimic natural structure assemblage of genera and species [2]. Extracellular matrices are recreated to capture the complex molecular architecture of natural tissue, then from cell to tissue and finally to organ could be recreated.

The continuous and rapid development of biomaterials has generated a vast industry with market value expected to be 58.1 billion US dollars by 2014, with a compounded annual growth rate of 15% from 2009 to 2014 [5]. In addition, orthopaedic implants compose the majority of the implanted devices, with value around 10 billion US dollars for a variety (1.5 million) of cases per year worldwide. Table 1.1 lists the medical uses of current biomaterials. Classical biocompatible metallic implant alloys are greatly used as orthopaedic implants. They are designed to replace the damaged tissue and provide structural replacement or support. Next, several widely used surgical implant alloys are introduced separately.

Table 1.1 Medical uses of biomaterials [1]

Artery graft	Mechanical heart valve
Breast implant	Nerve guidance tube
Cochlear implant	Ophthalmic drug delivery device
Dental implant	Pacemaker
Ear drainage tube	Renal dialyzer
Feeding tube	Stent
Glaucoma drainage tube	Tissue adhesive
Hydrocephalous shunt	Urinary catheter
Intraocular lens	Valve, heart
Joints (hip, knee, shoulder)	Wound dressing
Keratoprosthesis	X-ray guide
Left ventricular assist device (LVAD)	Zirconium knee joint

1.1.2 Specific body implant alloys

Stainless steel alloys

The two types of stainless steel listed in Table 1.2 are of the type 316L, which are based on the 18-8 steel (18 weight % Cr and 8 wt.% Ni) [6]. The addition of molybdenum and small amount of carbon increase the corrosion resistance particularly to pitting and intergranular corrosion [2]. The stainless steel alloys are the cheapest and easiest to fabricate among the currently used implant metallic alloys and are widely used as fracture fixation devices. During the fabrication of stainless steel alloys, special care must be taken in controlling the impurity content, such as carbon. Alloy surface must also be carefully prepared to develop a suitable passivation layer and minimize the surface impurity to improve the corrosion resistance.

Co-Cr alloys

As indicated by their name, these alloys are made mainly of cobalt and chromium with either molybdenum or nickel as the third main constituent element [7]. Co-Cr-Mo exhibits high abrasion resistance and therefore is often used in bearing applications. However, its higher rate of work hardening limits its application in implant devices with fixed configuration, for example, total hip replacement. Co-Cr-Ni on the contrary, possesses lower rate of work hardening and much higher maximum strain (60% prior to fracture, see Table 1.3), which makes it more suitable for various purposes of implantation. Nevertheless, this Ni bearing Co-Cr alloy shows lower corrosion resistance, particularly to crevice corrosion. Although the Co-Cr based alloys, in general, show better corrosion resistance and improved yield strength, the relatively higher price limits their market.

Polymethylmethacrylate (PMMA)

Although metallic implant alloys are often used as structural replacements due to their superior strength and ductility, polymethylmethacrylate (PMMA) as a polymer material is also widely used to provide structural support [2]. As stated previously, PMMA was used for artificial lenses in the first modern implantation surgery as early as 1949 in Britain. Nowadays, intraocular lenses are implanted in 10 million human eyes every year [7]. In addition to applications in ophthalmology, PMMA is used as “cement” materials during total hip insertion. Because of its thermoplastic property in amorphous state, PMMA can be filled between bones and fixation plates during the time of hip replacement surgery [7]. The side effect of PMMA is hypotension and hypoxemia once it dissolves in the surrounding tissues. In addition, the exothermic polymerization can also invoke damage to the surrounding tissues and low resistance to abrasion greatly limits its application in bearing application [8].

Table 1.2 Compositions of widely used surgical implant alloys [6]

surgical implant alloys	Composition (weight %)
stainless steel ASTM F55 or F56 (wrought)	Fe: 59-70, Cr: 17-20, Ni: 10-14, Mo: 2-4, C: 0.03*, Mn: 2.00*, P : 0.03*, S : 0.03*, Si : 0.75*
stainless steel ASTM A296 (cast)	Fe: 62-72, Cr: 16-18, Ni: 10-14, Mo: 2-3, C: 0.06*, Mn: 2.00*, P : 0.045*, S : 0.03*, Si : 1.0*
Co-Cr ASTM F75 (cast)	Co: 57.4-65, Cr: 27-30, Ni: 2.5*, Mo: 5-7, Fe: 0.75*, C: 0.35*, Mn: 1.0*, Si: 1.00*
Co-Cr ASTM F90 (wrought)	Co: 46-53, Cr: 19-21, Ni: 9-11, W: 14-16, Fe: 3.0*, C: 0.05-0.15, Mn: 2.0*, Si: 1.00*
Ti (pure) ASTM F67 Grade 4 (cast/wrought)	Ti: 99, Fe: 0.5*, C: 0.10*, O: 0.45*, N: 0.07*, H: 0.015*
Ti-6Al-4V ASTM F136 (cast/wrought)	Ti: 88.5-92, Al: 5.5-6.5, V: 3.5-4.5, Fe: 0.25*, C: 0.08*, O: 0.13*, N: 0.05*, H: 0.015*

* maximum quantity

Ceramic materials

Ceramic materials undergo intense investigations owing to their high resistance to wear, high compressive strength and excellent biocompatibility [2, 9, 10]. Al_2O_3 and ZrO_2 have been used in dental implants, artificial femoral heads and vertebral ceramic prostheses. However, low ductility greatly limits their use as fixation plate in orthopaedics.

Ti-based alloys

When compared to other metallic implant alloys, titanium and its alloys possess the Young’s moduli closest to that of bone (as shown in Table 1.3). This leads to reduction of so called stress shielding effect and can in turn improve bone regeneration [11]. Moreover, there is a stable passive TiO_2 layer on the surface of Ti-based alloys, which enhances their corrosion resistance and biocompatibility. Finally, the high specific strength (tensile strength to density ratio) of Ti makes it and its alloys very attractive to body implant since weight savings are very important for implant materials. The disadvantages of Ti based implant alloys are low shear strength, poor abrasion properties and high price compared to stainless steel.

Table 1.3 Mechanical properties of several surgical implant alloys (compiled based on data in[6]*)*

alloys	UTS (MPa)	0.2% YS (MPa)	MS (%)	E (GPa)
stainless steel ASTM F55 or F56 (wrought)	> 480 860*	170 690*	> 40	200
stainless steel ASTM A296 (cast)	> 480	200	> 30	190
Co-Cr ASTM F75 (cast)	> 650	450	> 8	250
Co-Cr ASTM F90 (wrought)	> 900 1720*	380 1310*	> 50	240
Ti (pure) ASTM F67 Grade 4 (cast/wrought)	> 550	480	> 18	100
Ti-6Al-4V ASTM F136 (cast/wrought)	860 - 900	790 - 830	> 10	110
UTS: ultimate tension strength. YS: yield strength. MS: maximum strain. E: Young's modulus. *: after cold work				

Pure Ti and Ti-6Al-4V (additions in weight%) were initially designed as structural materials for aerospace in the middle of the last century. Later they were adopted in the medical use as implant materials. The properties of both alloys are largely dependent on impurity concentration, especially Oxygen. The higher the impurity content in the alloy, the higher the strength and the lower the ductility. Addition of 6 wt.% Al and 4 wt.% V to pure Ti leads to much improved strength, comparable to cold worked stainless steel. However, it was found that V possesses toxicity [12]. Since then, V-free Ti based implant alloys were developed, such as Ti-6Al-7Nb [13] and Ti-5Al-2.5Fe [14], as well as Ti-15Zr and Ti-15Sn-based alloys [15]. All the above Ti based alloys are α+β type alloys (α and β phase of titanium). Although the Young's moduli of these α+β type alloys are much lower than those of stainless steels and Co-Cr alloys, they are still much higher than that of cortical bones, and this consequently leads to bone resorption. It was later established that β-Ti possesses much lower Young's modulus than α-Ti and scientists shifted focus to β type Ti alloys. A series of β type alloys were then developed, such as Ti-13Nb-13Zr [16], Ti-15Mo [17], Ti-15Zr-4Nb-4Ta [18], Ti-35Nb-7Zr-5Ta [19] (all additions in weight percent) and others. These β type alloys are designed to exhibit Young's moduli as low as possible. Besides α+β and β or near β type Ti-based implant alloys, researchers are also attempting to develop alloys exhibiting shape memory effect and superelasticity, such as Ti-Ni [20, 21], Ti-Nb-Ta [22] and Ti-Nb-Sn [23]. Table 1.4 lists the medical applications of Ti based implant alloys.

1.1.3 Some current problems of orthopaedic implant alloys

Orthopaedic implant alloys constitute the majority of implant materials. There exist several major issues concerning the current orthopaedic implant alloys.

A. The Young's moduli of currently used implant alloys are still much higher compared to those of human bones.

B. Toxic or hypersensitive reactions occur due to ions released by constituent elements of implant alloys.

C. Relatively low wear or abrasive resistance of implant alloys makes them difficult to meet the needs of joint replacement.

Table 1.4 Ti-based alloys for medical applications [7]

alloy	type
pure Ti (ASTM F67-89) Grade 1-4	α
Ti-6Al-4V	α+β
Ti-6Al-7Nb	α+β
Ti-5Al-2.5Fe	α+β
Ti-5Al-3Mo-4Zr	α+β
Ti-15Sn-4Nb-2Ta-0.2Pd	α+β
Ti-15Zr-4Nb-2Ta-0.2Pd	α+β
Ti-13Nb-13Zr	near β
Ti-12Mo-6Zr-2Fe	β
Ti-15Mo	β
Ti-16Nb-10Hf	β
Ti-15Mo-5Zr-3Al	β
Ti-15Mo-2.8Nb-0.2Si-0.26O	β
Ti-35Nb-7Zr-5Ta	β
Ti-29Nb-13Ta-4.6Zr	β
Ti-40Ta, Ti-50Ta	β

1.1.4 Bone structure and the stress fielding effect

For human bones, there exist two main bone tissues: cortical bone and cancellous or trabecular bone (as shown in Fig. 1.1). The cortical bone supports the whole body, protects organs, provides levers for movement and stores and releases chemical elements. The cancellous bone possesses porous structure and therefore is less dense. The greater surface of cancellous bone makes itself a more suitable place for metabolic activities, such as exchange of calcium ions. From the point of view of materials science, bone tissue is composed of 60 wt.% ceramic crystalline-type mineral, most often referred to as hydroxyapatite, 30 wt.% collagen and 10 wt.% water [24]. The elastic properties of human femoral cortical bone were investigated by Reilly. The femoral cortical bone shows great elastic anisotropy (as shown in Table 1.5).

Table 1.5 Anisotropic elastic properties of human femoral cortical bone [25]

Longitudinal modulus (GPa)		17.9 (3.9) *
Transverse modulus (GPa)		10.1 (2.4)
Shear modulus (GPa)		3.3 (0.4)
Longitudinal Poisson's ratio		0.40 (0.16)
Transverse Poisson's ratio		0.62 (0.26)
Longitudinal	ultimate tensile strength (MPa)	135 (15.6)
	ultimate compression strength (MPa)	205 (17.3)
Transverse	ultimate tensile strength (MPa)	53 (10.7)
	ultimate compression strength (MPa)	131 (20.7)
Shear strength (MPa)		65 (4.0)
* Standard deviations are given in parentheses.		

In a healthy individual, enough loads are required to generate new bone tissues and keep the normal metabolic activities. However, if there exists a stiffer element (e.g. orthopaedic implant) next to the bones, it will bear more loads and leave the adjacent bone tissues underload. In other words, this stiffer element acts as a "shield", shielding surrounding bones from the stress. Consequently, the bone tissue is reabsorbed by the body. The remaining bone then becomes overly porous. The phenomenon is called "stress shielding" or osteopenia and can lead to osteoporosis. This effect was first observed in hip implant surgeries and nowadays attracts intensive concerns [11, 26, 27]. The mechanical reason for the stress shielding effect is the large discrepancy of Young's moduli between implant alloys (100-200 GPa) and those of human bones (10-20 GPa). Reducing or inhibiting stress shielding requires fabrication of new implant alloys with Young's modulus as close to that of bones as possible.

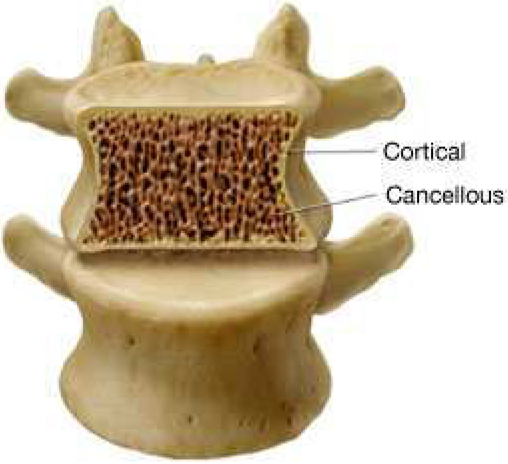

Fig. 1.1 Two osseous tissues which form human bones, cortical and cancellous bone.

1.1.5 Toxicity of elements used in current implant alloys

It has been shown that Co, Cr and Ni ions released by implants can lead to toxic or hypersensitivity reactions and induce carcinogenesis [28, 29]. These elements are mainly contained in the stainless steel and Co-Cr implant alloys. For Ti-based implant materials, V has been classified in the toxic group and the biocompatibility of Al is also not good due to tissue response of its capsule [12, 17, 30]. This leads to increasing concerns regarding utilization of Ti-6Al-4V implant alloys. Other elements like Mn, Cu, Mo, Zn, Ag are classified as low biocompatible or toxic [29, 31-34].

1.2 Introduction of Titanium based crystalline alloys

1.2.1 α and β phase of Titanium

Pure Ti forms hexagonal close packed (hcp) α phase at room temperature and transforms to body centered cubic (bcc) β phase on heating up to 882°C [35]. α phase has $P6_3/mmc$ space group with 2 atoms per unit cell, located at (0,0,0) and (1/3, 2/3, 1/2) positions. The lattice parameters of α phase are a=0.296 nm, c=0.468 nm and c/a=1.583, smaller than the perfect ratio in hcp structure, c/a $=\sqrt{8/3} \approx 1.633$ [36]. β phase has $\mathrm{Im\bar{3}m}$ space group also with 2 atoms per unit cell, at (0,0,0) and (1/2, 1/2, 1/2) positions [36]. The lattice parameter is a= 0.332nm [37]. The orientation relationship for transition between α and β phase follows Burgers relation, as shown in Fig. 1.2, $(0001)\ \alpha // \{011\}\ \beta,\ <11\bar{2}0>\alpha // <1\bar{1}1>\beta,\ \{1\bar{1}00\}\ \alpha // \{121\}\ \beta$ [38].

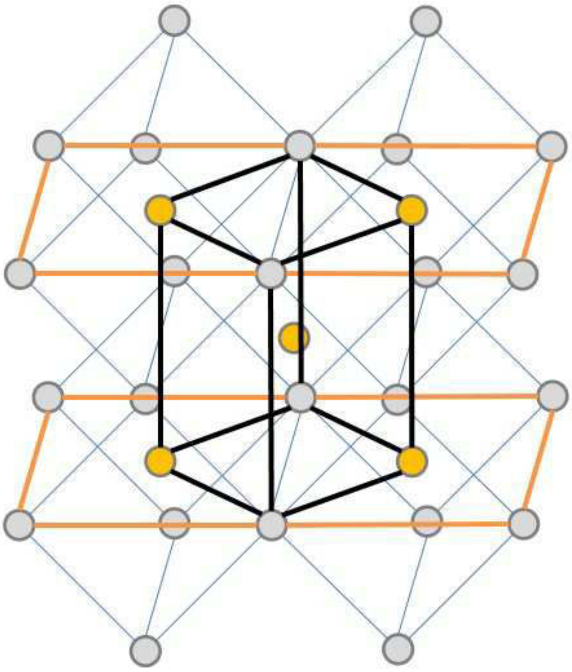

Fig. 1.2 Burgers relationship between α and β phase [38]

Depending on the thermodynamics of Ti based binary alloy phase diagram, the elements can be divided into two main categories: α stabilizer and β stabilizer [35, 39]. In the β stabilizer group, there exist another two subgroups: β isomorphous and β eutectoid. Fig. 1.3 shows different kinds of Ti based binary phase diagrams. Alloying elements like Hf, Ga, B, Sc, La, Ce, Ge, Al, Zr, Sn, O, N and C belong to α stabilizers group. In the β stabilizer group, the β isomorphous (Mo, V, Ta, Nb) means that the element is completely miscible with Ti in both liquid and solid states and all the β isomorphous elements are of bcc structure. The β eutectoid stabilizers are Fe, Cr, Mn, Co, Ni, Cu, W, Au, Ag, Pt and Pd. The effect of addition of α stabilizer and β stabilizer can be quantified in terms of Al and Mo equivalency (in weight percent), respectively [35], as shown below.

$$\mathrm{Al_{eq}} = \mathrm{Al} + 0.17\mathrm{Zr} + 0.33\mathrm{Sn} + 10\mathrm{O}$$

$$\mathrm{Mo_{eq}} = \mathrm{Mo} + 0.2\mathrm{Ta} + 0.28\mathrm{Nb} + 0.4\mathrm{W} + 0.67\mathrm{V} + 1.25\mathrm{Cr} + 1.25\mathrm{Ni} + 1.7\mathrm{Mn} + 1.7\mathrm{Co} + 2.5\mathrm{Fe}$$

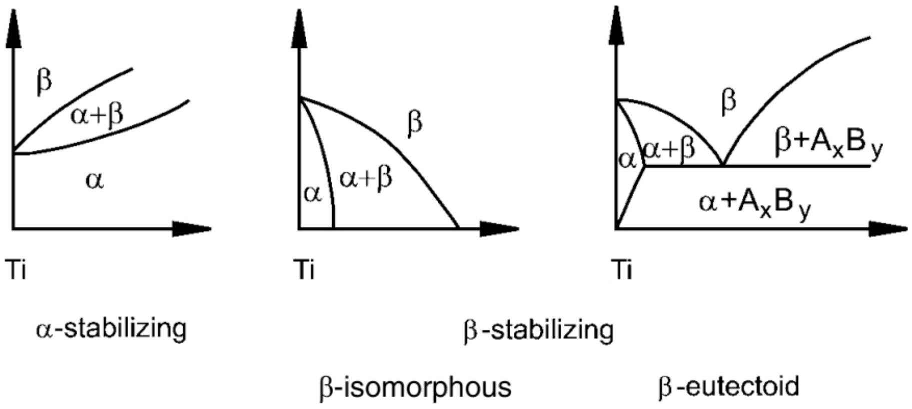

Fig. 1.3 Different types of Ti based binary phase diagrams [39]

1.2.2 Other metastable phases of Titanium at room temperature

ω phase

Ti also exhibits a metastable ω phase either on alloying or when exposed at high pressure. Moffat plotted the pressure-temperature phase diagram of pure Ti based on the data from Bundy and Jayaraman [40], as shown in Fig. 1.4. It can be seen that ω phase exists at low temperature or high pressure in pure Ti. ω phase was first found by Silcock [41] in Ti-V, Ti-Mo and Ti-Cr systems. It was found that there existed lines of intensities of {111} planes in the selected area diffraction (CBED) pattern. She concluded that this new phase possesses hexagonal structure with c/a=0.613 and orientation relationship with β phase is: (0001) ω // (111) β, $[2\bar{1}\bar{1}0]$ ω // $[1\bar{1}0]$ β. Further investigations [42-48] confirmed this structure and found out that three atoms exist in each unit cell of ω phase, one at (0,0,0) and two at ±(1/3, 2/3, u) positions, with u=0.48 for quenched form and 0.5 for aging form [48]. Since there are four <111> β directions, there are four variants of ω phase. Sass and De Fontaine [42, 49-51] proposed that bcc structure becomes metastable relative to longitudinal phonon waves propagating along <111> β direction, which initiates the β to ω transition. It has been suggested that the morphology of ω phase is related to atom misfit between Ti and alloying elements [48]. For small misfit, as in Ti-Nb and Ti-Mo, ω phase is of elliptic shape to minimize the surface energy, whereas in large misfit systems like Ti-V, Ti-Mn, Ti-Fe, Ti-Cr, ω phase is of cubic shape to minimize the elastic strain energy at the ω/matrix interface.

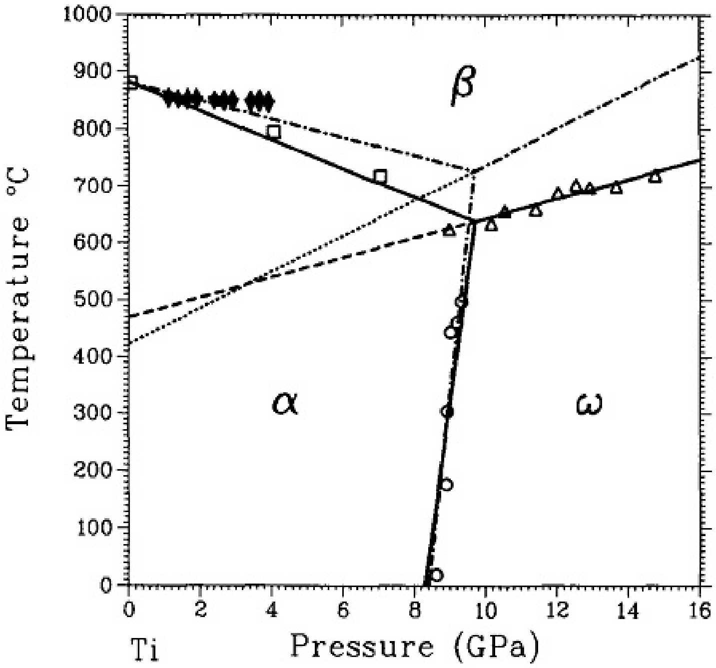

Fig. 1.4 The pressure-temperature phase diagram of pure Ti. The open points are from Bundy, the filled ones, Jayaraman. [40]

Martensitic phase (α’ and α’’)

When cooling from above β transus temperature (882°C), if the cooling rate is high enough, martensitic phases like α’ and α’’ can form. In Ti based alloys with low concentrations of β stabilizer, the martensitic phase possesses a distorted hcp structure, similar to that of α, and is referred to as α'. When alloying concentration increases, martensitic phase is of orthorhombic structure, named as α'' [35, 52, 53]. The orientation relationship between β and α'' is as follows: [100] β // [100] α'', [010] β // 1/2 $[01\bar{1}]$ α'', [001] β // 1/2 [011] α'', as can be seen in Fig. 1.5. α'' can be viewed as transition phase between α and β [52].

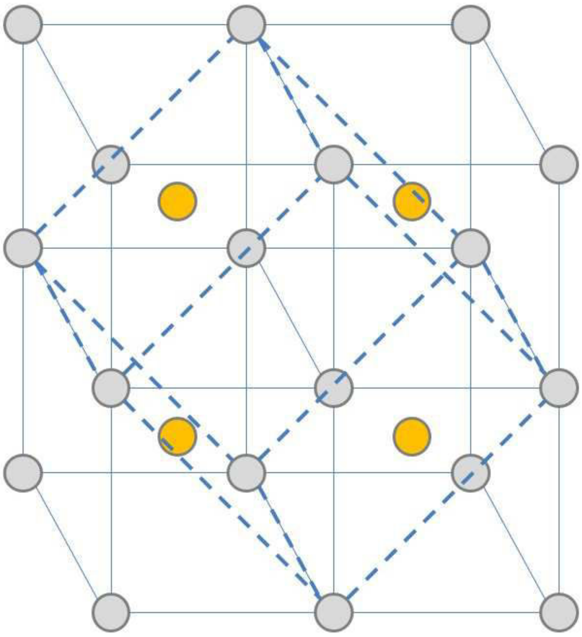

Fig. 1.5 Illustration of lattice correspondence between β phase (solid line) and α'' phase (dashed line).

Moffat [40, 45, 46] systematically investigated the phase transformation in quenched and aged states in a series of Ti-Nb alloys. Special attention was paid to interstitial and impurity content, because they can both change the constitution phases greatly. It was found that ω and α'' phases compete to form when cooling from above β transus temperature during quenching. The β to ω and β to α'' transformation are locally mutually exclusive. On quenching, slow cooling rate favors ω phase, whereas high cooling rate favors α'' phase. On isothermal aging, ω and α phases compete to precipitate from β matrix. ω phase precipitates on aging at low temperature (≤400^{o}C). Based on these results, Moffat plotted the metastable phase diagrams in Ti-Nb binary system.

1.2.3 Young's modulus of Titanium and its alloys

As stated previously in this chapter, a high Young's modulus of an implant alloy leads to the stress shielding effect, which is detrimental to human bone structure. It is shown in Fig. 1.6 that for commercial purity Ti, Young's modulus decreases monotonically with increasing temperature and its value at room temperature is within the range of 100 - 110 GPa. It will be shown in next subsection that Ti based alloys exhibit various tendencies depending on alloying elements due to the fact that equilibrium α phase and metastable phases possess different Young's moduli. The Young's modulus of ω phase is highest among the four non equilibrium phases at room temperature (ω, α', α'' and β), but the determination of values for single phase α', α'' and β has not come to firm conclusion, as different researchers have contradictory results [35, 54, 55]. This is because of elastic anisotropy of corresponding crystalline structures. From the point of view of lowering Young's modulus, ω phase should first be avoided and its formation can be retarded by addition of Al, Sn, O [56]. Besides alloying, plastic deformation and heat treatment can also change Young's modulus of Ti based alloys. For example, cold rolling with deformation ratio of 89% can decrease Young's modulus of Ti-35wt.%Nb-4wt.%Sn alloy from 55GPa to 42GPa in the rolling direction [54]. The essence of varying Young's modulus is through changing atomic bonding forces by increasing of lattice parameter or alteration of crystal structures.

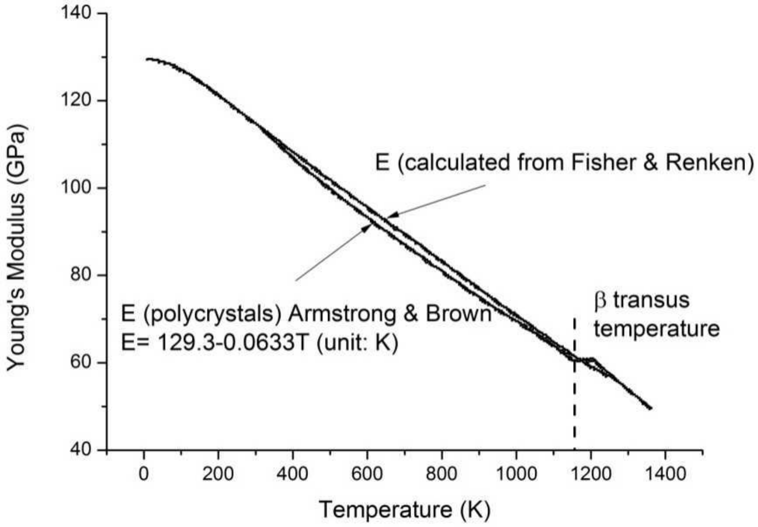

Fig. 1.6 Temperature dependence of Young's modulus of commercial purity Ti (<99.8 wt.%) (replotted from [35])

1.2.4 Young's moduli of selected Ti based binary alloys

α stabilizer

Ti-Hf binary alloys [57] were synthesized by water quenching. For all the compositions investigated (0-40 wt.% Hf), there exists only one phase in the as-prepared samples, hexagonal α' martensite. The microstructure of α' varies from lamellar to needle-like shape with increasing Hf content. The addition of Hf increases the lattice parameter, consequently decreases the Young's modulus, but only gently (from 115 to 110 GPa).

It has been proven that Sn can suppress the precipitation of ω phase [56]. The addition of Sn is thus expected to lower the Young's modulus of Ti alloys. As can be seen in Table 1.6, apart from the pure intermetallic phase, the Ti-Sn binary alloys can possess very low Young's modulus.

Table 1.6 Young's moduli of binary Ti-Sn alloys.

composition	E/GPa	Microstructure	Ref.
Ti_3Sn	207	Intermetallic	[58]
$Ti_{87}Sn_{13}$	120	Intermetallic + HCP α-Ti + martensite	
$Ti_{80}Sn_{20}$	77		
$Ti_{78}Sn_{22}$	55		

β stabilizer

The microstructures and Ta content dependence of Young’s moduli of Ti-Ta binary alloys are shown in Table 1.7 and Fig. 1.7 [55]. It can be seen in Table 1.7 that addition of Ta suppresses precipitation of ω phase. In addition, there exist two minima of Young’s modulus as shown in Fig. 1.7.

Table 1.7 Microstructures of Ti-Ta binary alloys

Ta content	microstructure	Morphology
< 20 wt.% *	Hexagonal α’ martensite	Lamellar α’
30 - 50 wt.%	Orthorhombic α’’ martensite	Needle-like α’’
60 wt.%	β+α’’	Equiaxed β + needle-like α’’
> 60 wt.%	β	Equiaxed β
* boundary between α’ and α’’ differs from various reference sources [55, 59, 60]		

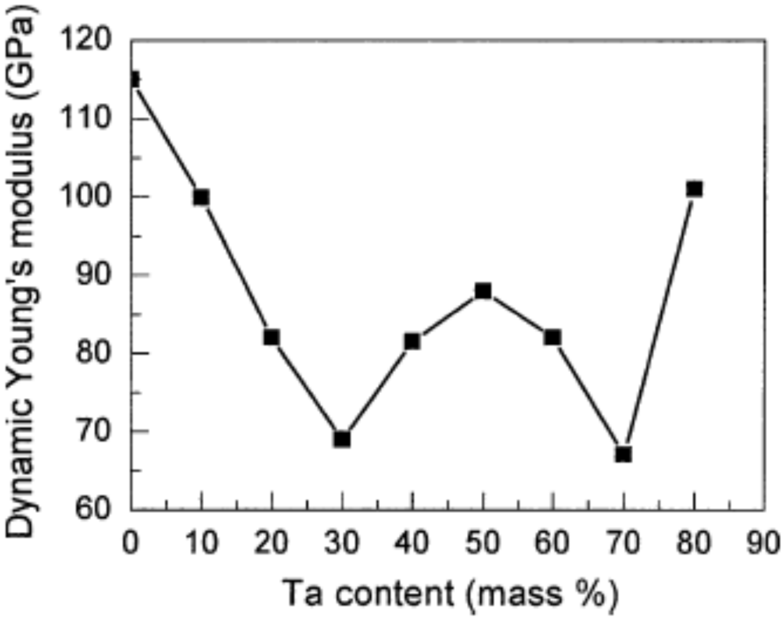

Fig. 1.7 Dynamic Young's modulus of Ti-Ta binary alloys. [55]

Similar to the Ti-Ta binary system [61], there also exist two minima of Young’s modulus for Ti-Nb binary alloys corresponding to the compositions where ω phase is suppressed. Due to its low Young’s modulus, Ti-Nb has attracted intensive investigations. The combining effect of Zr and Sn addition on Young’s modulus of Ti-Nb alloys was investigated by Hao [62]. Single β phase alloy of Ti-24Nb-4Zr-7.5Sn was produced, which exhibits Young’s modulus as low as 52 GPa. With varying the content of Zr and Sn, microstructures of the alloys can be α’’ + β or single β or finally to ω + β.

The composition dependence of Young’s modulus of Ti-V binary alloys [61] exhibits a similar trend as that of Ti-Nb and Ti-Ta alloys. It is shown in Fig. 1.8 that the minimum value is around 65 GPa, corresponding to the disappearance of ω phase. In addition, V is a more effective β stabilizer since only 16 wt.% V yields an alloy with single β phase.

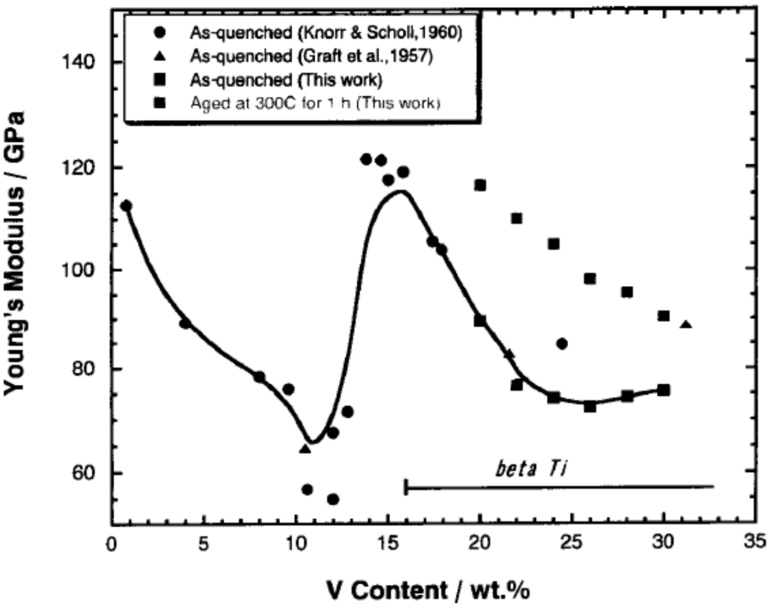

Fig. 1.8 Young's modulus of Ti-V binary alloys. [61]

1.2.5 Chill zone alloys

When alloys are cast into moulds, the part adjacent to the cold mould forms a chill zone due to high cooling rate while the inner volume forms columnar zone of elongated grains and equiaxed zone due to slow cooling rate. As the dimension of cast alloys decreases, the proportion of chill zone increases. The concept of "chill zone alloy" was considered by Yavari et al [63-65]. It can be seen in Fig. 1.9 that moving inwards from near surface, the X-ray diffraction patterns change from continuous rings to discontinuous streaks and finally to discrete spots. This indicates that the structures change from nanostructure to larger grain or dendritic structure. This type of composite structure (hard outer shell and soft inner volume) leads to a combination of high yield strength and large fracture strain.

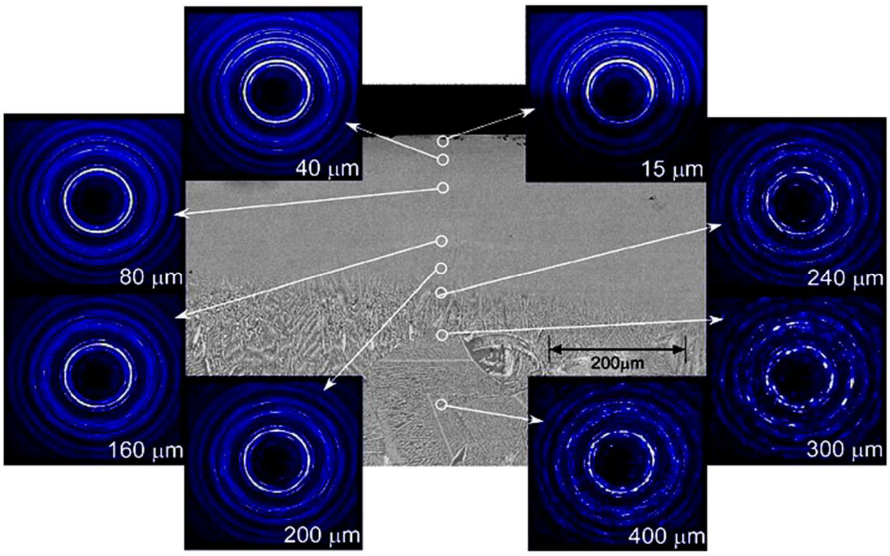

Fig. 1.9 The cross-section of $Cu_{90}Zr_5Hf_5$ alloy was scanned by a synchrotron micro-beam in transmission mode. The X-ray diffraction patterns show that the continuous rings gradually break up into streaks and finally to discrete spots, as moving inwards from the sample surface.

1.2.6 Martensitic transformation

When an alloy is cooled from high temperatures, any supersaturation of solute can be relieved by precipitation or transformation to new phase(s). Besides the reactions requiring long range diffusion of atoms, there exist reactions without need of diffusion. The new phase(s) is of exactly the same composition as the parent high temperature phase but with a different crystal structure. This diffusionless reaction, first observed in steel, is referred to as martensitic transformation [66, 67]. Martensitic transformation is stress-assisted in nature and no thermally activated atomic diffusion required during interface migration [68]. This is the key difference between martensitic transformation and massive transformation, since in the latter case the new phase(s) is also of the same composition as the parent high temperature phase.

The transformation occurs by shearing of atoms uniformly (as shown in Fig. 1.10), and each atom moves a distance less than one interatomic distance. There exists a fixed orientation relationship between parent phase and martensitic phase, and the interface between them is called habit plane or invariant plane. The interface between martensite and parent phase is glissile, probably consisting of an array of dislocations, which ensure the interface can migrate at very high rates, close to the speed of sound waves.

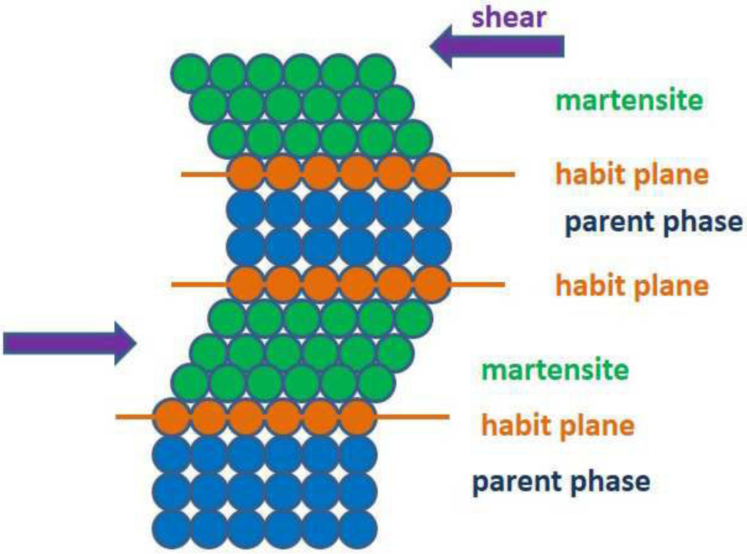

Fig. 1.10 Illustration of martensitic transformation.

The temperature at which the martensitic transformation occurs upon cooling from high temperature is called martensitic start temperature, M_s. Other characteristic temperatures are shown in Fig. 1.11. Below the temperature M_f (martensitic finish temperature), all parent phase is transformed to martensite and the transformation finishes. On heating, the martensite then starts to transforms back to high temperature parent phase at temperature A_s (austenitic start temperature), and finishes at A_f (austenitic finish temperature).

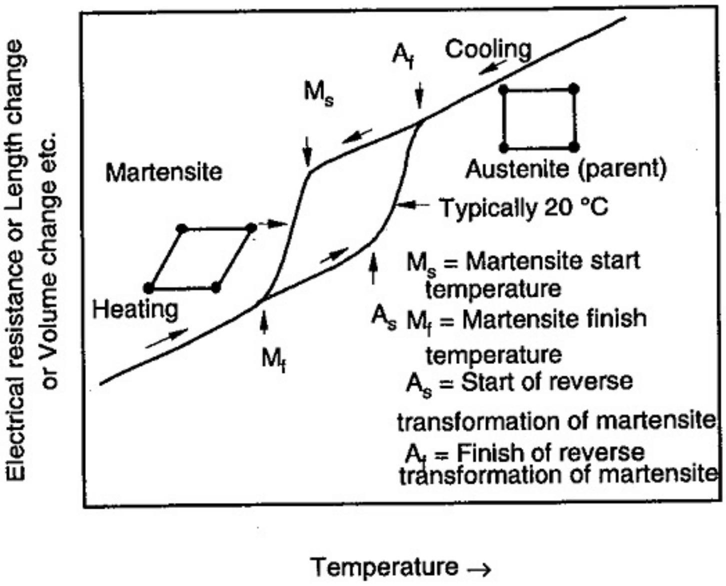

Fig. 1.11 Schematic illustration of physical properties' varying tendency during martensitic transformation in binary Ti-Ni alloy. [35, 69]

External stress can assist martensitic transformation at temperatures close to or above A_f as martensitic phase can form with the aid of external stress [66, 70]. This stress aiding martensitic transformation is possible up to a temperature M_d (the upper temperature limit at which the stress-induced martensites can form) and this is the essence of superelasticity (SE).

Martensitic transformation is a first order transformation and proceeds by nucleation and growth [66, 71]. This in turn requires the undercooling (T_0-M_s) or superheating (A_s-T_0) for the spontaneous transformation initiation (as shown in Fig. 1.12). Similarly, T_0-M_d is the undercooling required for martensitic transformation to occur with the aid of external stress.

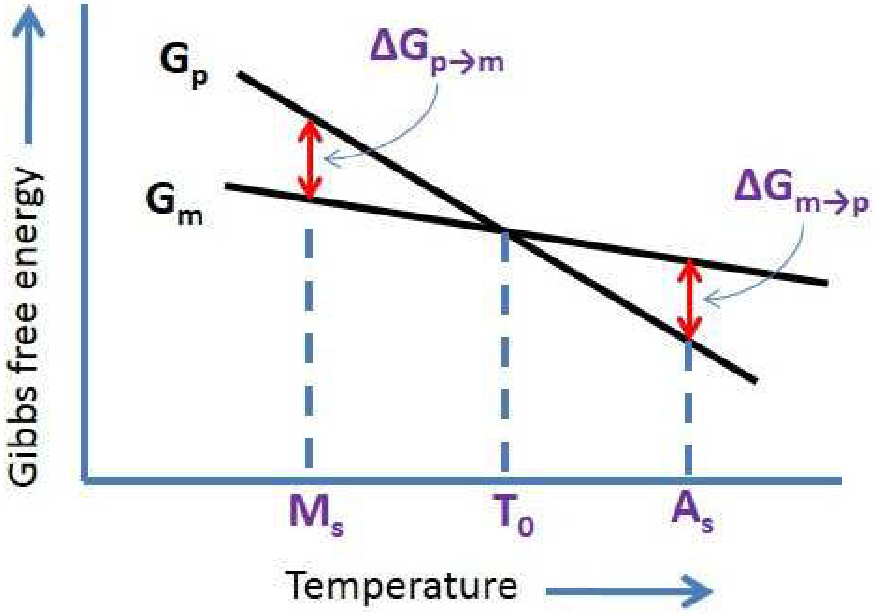

Fig. 1.12 Schematic illustration of free energy curves for martensite and parent phase. T_0 is temperature where Gibbs free energy of martensite is same as that of parent phase.

1.2.7 Shape memory effect (SME) and superelasticity (SE)

For a metastable alloy whose A_f is below but close to temperature T_1, if it is subjected to loading at temperature T_1, it's corresponding stress-strain curve behaves as that shown in Fig. 1.13 [70]. On loading, AB segment is the elastic deformation of parent phase. When stress reaches $\sigma^{P\text{-}M}{}_{T1}$ (point B), stress-induced martensitic transformation occurs and does not finish until point C. At point C, the transformation finishes. Then CC′ segment represents the elastic deformation of martensite. Finally, the yield strength of martensite ($\sigma^{P}{}_{y}$) is achieved at D and then the sample deforms plastically until fracture. If the stress stops at point C′, upon unloading, the sample behaves first elastically, corresponding to the elastic deformation of martensite. Then at point F ($\sigma^{M\text{-}P}{}_{T1}$), the stress induced reverse martensitic transformation occurs. At point G, the reserve transformation from martesite to parent phase finishes. Finally GH segment is the elastic unloading of parent phase. The total strain may or may not totally recover and segment AH shown in Fig. 1.13 is the residual strain. This phenomenon is called superelasticity (SE).

If the metastable alloy deforms at temperature below A_f, then upon unloading, the deformation strain would largely remain and can only recover when heating to a temperature above A_f. This phenomenon is referred as shaper memory effect (SME).

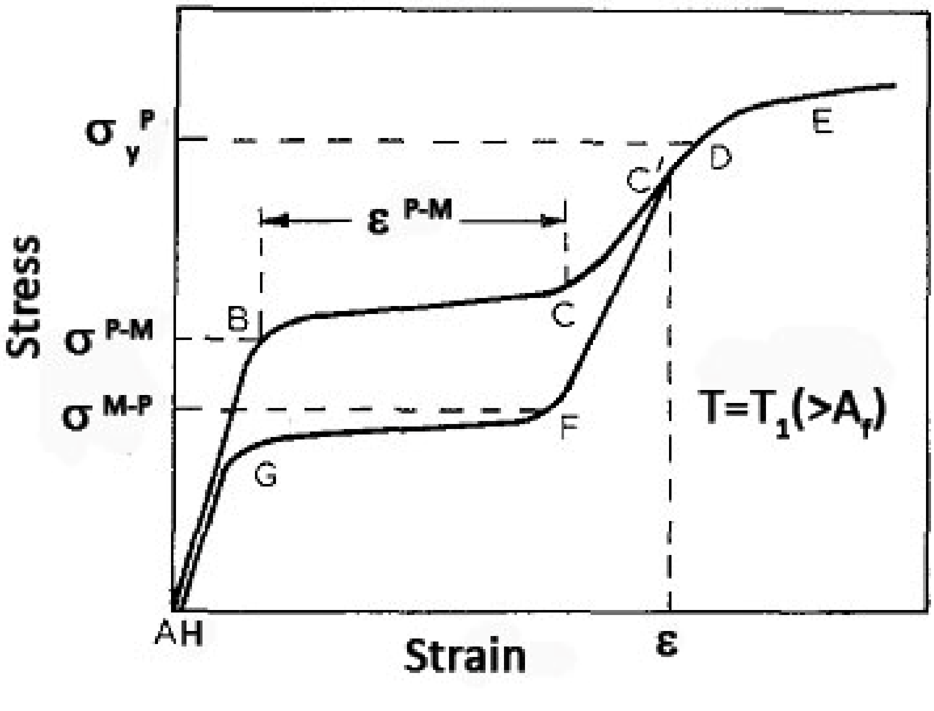

Fig. 1.13 Schematic illustration of a stress-strain curve showing superelasticity. [70]

Fig. 1.14 presents a series of tension stress-strain curves as a function of temperature for Cu-Zn-Sn single crystal. For samples which deform at temperatures below A_f, the residual strain is recovered upon heating above A_f as indicated by dash line. Whereas for samples deform at temperatures above A_f, the strain recovers just upon unloading. The former corresponds to shape memory effect and the latter, superelasticity. These two phenomena have been found in many Ti based crystalline alloys, such as Ti-Ni [35, 66, 69], Ti-Mo[72-74], Ti-Nb [52, 53, 75, 76],Ti-Nb-Sn, [54, 77, 78], Ti-Nb-Sn-Zr [62, 79].

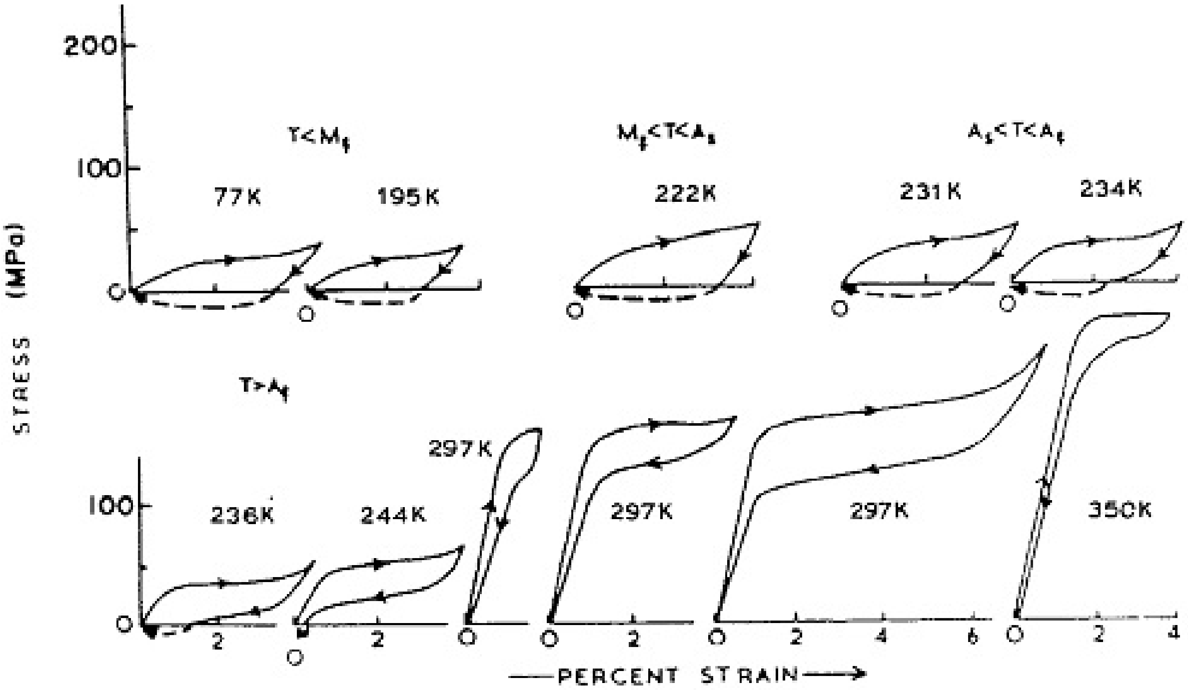

Fig. 1.14 Tensile stress-strain curves as a function of temperature for Cu-34.7wt.%Zn-3wt.%Sn alloy single crystal, for which M_s=221 K, M_f=208 K, A_s=223 K and A_f=235 K. [66]

1.3 Introduction to Ti based metallic glasses

1.3.1 Formation of metallic glasses

When metallic liquid is cooling below its liquidus temperature, there is a driving force of for solidification ($\Delta G_V = G_L - G_S$, where G_L and G_S is Gibbs free energy of liquid and solid, respectively). When liquid solidifies, it experiences a first order transformation of crystallization. The energy barrier to overcome for homogeneous nucleation (ΔG_{hom}) can be expressed in the following equation:

$$\Delta G_{\mathrm{hom}} = -\frac{4}{3}\pi r^3 \Delta G_V + 4\pi r^2 \sigma$$

where ΔG_V is the Gibbs free energy difference between liquid and solid, r is the radius of nucleus and σ is the interface energy between liquid and solid [80]. The homogeneous nucleation rate (N_{hom}) can then be expressed in the following formula:

$$N_{\mathrm{hom}} = \omega C_0 \exp\left(-\frac{\Delta G_m}{kT}\right) \exp(-\frac{\Delta G^*}{kT})$$

where ω is a factor including atomic vibration frequency and area of the critical nucleus, C_0 is number of atoms per unit volume, ΔG_m is activation energy of atom migration and ΔG^* is the critical energy barrier of homogeneous nucleation [68]. Since the temperature dependence of ΔG^* and ΔG_m is just contrary, the homogeneous nucleation rate is large only at intermediate undercooling. After the nucleus forms, it grows with a velocity (v). The fraction of crystals (f) after a time interval (t) is given by the following equation:

$$f = \frac{\pi}{3} N_{\mathrm{hom}} v^3 t^4$$

The situation for heterogeneous nucleation is quite similar to homogeneous nucleation except that it exhibits a lower critical energy barrier of nucleation. With the above equation for crystal fraction over time, one can establish the time - temperature - transformation (TTT) curves for the onset of crystallization transformation. The crystal fraction (f) is usually taken as f << 0.01. The TTT curve, as shown in Fig. 1.15, usually exhibits a C shape, indicating that the time required for crystallization is the shortest at intermediate temperature.

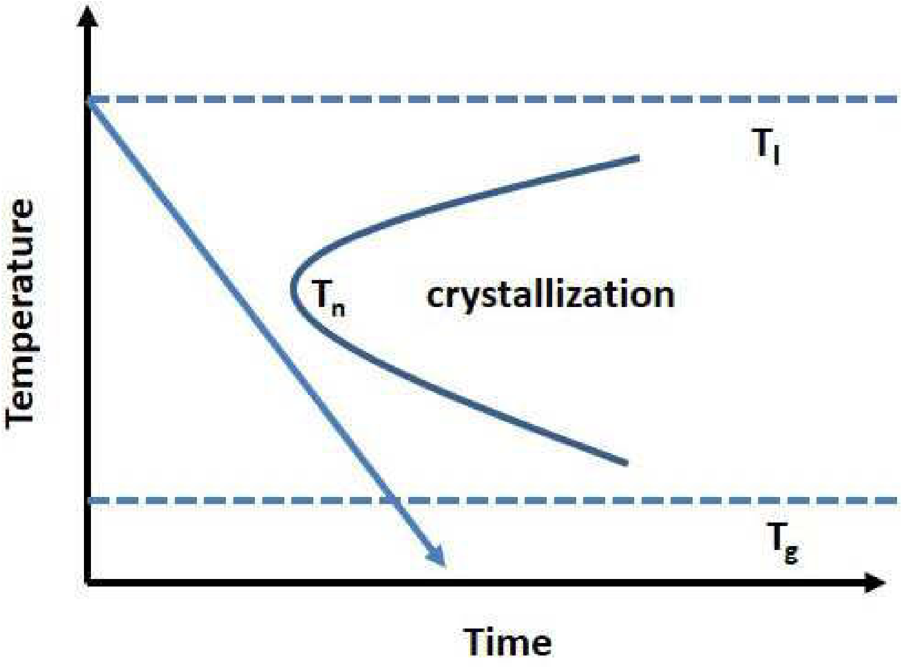

Fig. 1.15 Schematic presentation of time - temperature -transformation curve, T_m and T_g is melting temperature and glass transition temperature, respectively.

If the temperature at nose of C shape TTT curve is referred to as T_n, then the critical cooling rate (R_c) required to bypass the crystallization can be calculated by the following formula:

$$R_c = \frac{T_l - T_n}{t}$$

where T_l is the liquidus temperature and t is time. If this cooling rate is reached, then the liquid solidifies to its glassy state.

The glass may be referred to as a frozen liquid without long range order. It is shown in Fig. 1.16 that when liquid is cooled from above liquidus temperature T_l, for crystalline materials, the specific volume experiences a sudden change at some temperature below T_l in order not to reach the characteristic value of an isomorphic crystal. For glass former, on the other hand, the specific volume decreases monotonically on cooling, until at some temperature T_g (glass transition temperature) the liquid loses its ability of flow and glass forms [81, 82]. The common quoted value of viscosity with which T_g is defined is 10^{13} Pa•S. However, there is no strict definition of this value.

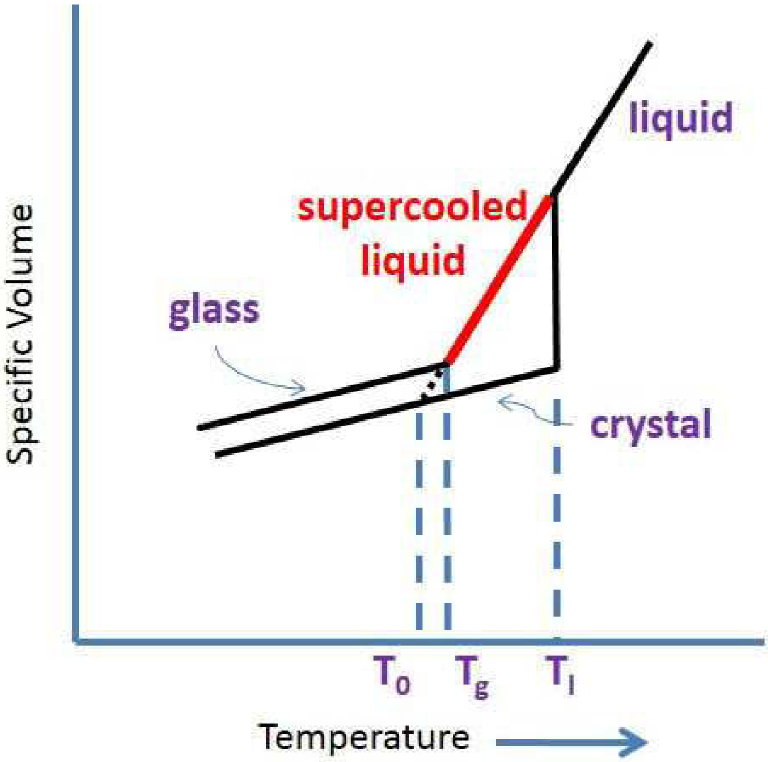

Fig. 1.16 Temperature variance of specific volume during solidification of liquid.

Fig. 1.17 shows the typical X-ray diffraction pattern of amorphous alloys. It can be found that the pattern only consists of diffuse amorphous diffraction peak which is different from the sharp Bragg peaks in crystalline materials.

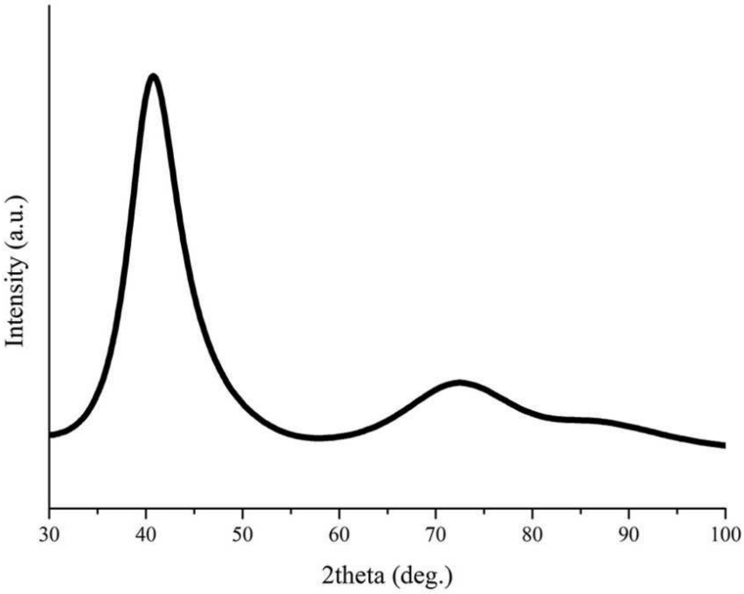

Fig. 1.17 Typical X-ray diffraction pattern of amorphous alloys.

The temperature dependence of heat capacity of glass, its crystalline counterpart and supercooled liquid is shown in Fig. 1.18. For a glass former, when its liquid is cooled below liquidus temperature, the heat capacity of supercooled liquid gradually increases with decreasing temperature, until at the glass transition temperature, it experiences a dramatic drop. The sudden decrease of heat capacity indicates a sudden loss of freedom. Moreover, the heat capacity of the glass is very close to that of its crystalline counterpart.

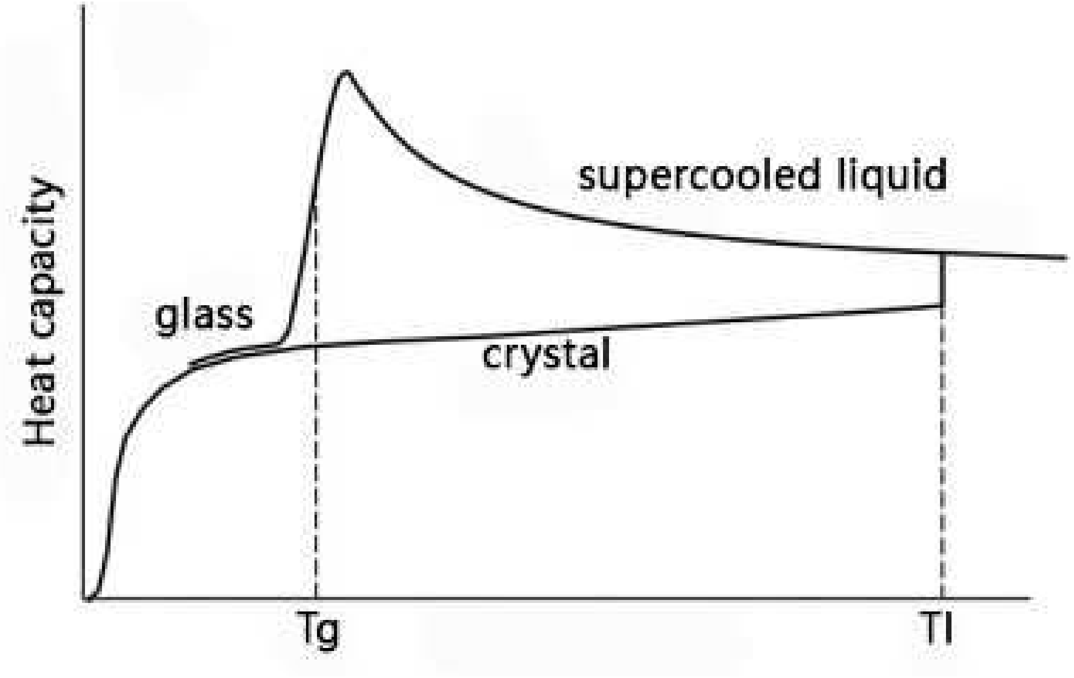

Fig. 1.18 The temperature dependence of heat capacity of glass, crystal and supercooled liquid. T_g *is glass transition temperature and* T_l *is liquidus temperature [83].*

The existence of glass and glass transition are ubiquitous in nature. For example, glass transition plays an importance role in preservation of food and keeps the insects in the desert alive from drought [84]. However, the ease of formation of glass depends on the bonding nature between atoms in the materials and extent of complexity of structure. For strong bonding like covalent bonding as existed in oxide glasses and complex structure as existed in polymer, the glass transition is easy. The difficulty of crystallization arises from long time required for relaxation in term of laboratory time scale and high viscosity of liquid [85, 86]. The formation of crystalline nuclei is much easier in the metallic based alloys due to the low viscosity of metallic melts and small critical size of crystalline nuclei. These intrinsic difficulties greatly postpone the time when glass was successfully synthesized in metallic systems.

Metallic glass (MG), as the newest member of glass, with the composition is mostly composed of metals, were first synthesized by Duwez in 1960s [87]. Although, theoretically speaking, anything can be vitrified as long as the cooling rate is high enough. Practically, however, precise compositions are required to form metallic glasses due to the limit of cooling rate obtained by current technology, for instance 10^6 K/s by melt spinning.

After metallic glass was first fabricated in Au-Si system by Duwez, thousands of metallic glasses were synthesized. Chen first synthesized millimeter-scale MG in ternary Pd-Cu-Si system in 1969 [88] and this started the new era of bulk metallic glasses (BMGs). In late 1980s, Inoue synthesized

BMGs in La-Al-Cu, La-Al-Ni and Zr-Al-Ni systems [82, 89-91]. In 1990s, Johnson found BMG compositions in Zr-Ti-Cu-Ni-Be system [92]. So far, the BMG with largest critical diameter is $Pd_{40}Cu_{30}Ni_{10}P_{20}$ with 72 mm in diameter [93] and critical cooling rate reaches as low as 0.1K/s.

After more than a half century development of metallic glasses, researchers have concluded many criteria for designing the metallic glasses of good glass forming ability. The earliest one perhaps is the deep eutectic criterion, since the first metallic glasses was synthesized in Au-Si eutectic system [87]. Since then, many other criteria were proposed, such as high reduced glass transition temperature ($T_{rg}=T_g/T_l$) [94], large supercooled liquid region ($\Delta T_x=T_x-T_g$) [95], high γ value ($\gamma=T_x/(T_g+T_l)$) [96] and so on. Inoue also proposed the three empirical rules based on large amount of experiments [97], the composition of alloy must be constituted by at least three elements, the difference of atomic size of main constituent element must be larger than 12% and the heat of mixing of main constituent elements must be negative.

The unique properties of MG make it a very promising candidate material for implant alloys. MGs possess lower Young's moduli comparing to their crystalline counterparts and this makes them a good candidate material as orthopaedic implants since it can reduce the stress shielding effect [98, 99]. MGs also possess very high corrosion resistance due to lack of grain boundaries and other conventional defects as existed in metal crystalline alloys [31, 81]. This in turn reduces the possibility of releasing metallic ions into surrounding tissues once implanted. MGs exhibit very high hardness which leads to high wear resistance [82, 97]. Consequently, this makes them potential materials for joint replacement. MGs' high strength makes them suitable as orthopaedic structural implants [82, 97]. In addition, the net-shape casting of MGs can greatly reduce the time and financing cost during processing and can fulfill the requirement of complex shape of some implants [100, 101].

1.3.2 Ti based metallic glasses

Ti-Ni-Cu-based system is so far one of the two Ti-based alloys with high glass forming ability (GFA). Glassy $Ti_{50}Ni_{25}Cu_{25}$ alloy of the form of ribbon was firstly synthesized by Inoue [102] in 1994. Since then, based on this ternary system, numerous studies have been performed on the effect of elemental additions on GFA of Ti-Ni-Cu based alloys.

Ni-free Ti based alloys can also be vitrified. Due to its potential application as superconductive materials, Ti-Nb-Si ternary system was extensively studied in early 1980s [103, 104]. GFA of other alloys, such as Ti-M-Si (M=Fe, Co, V, Nb) [105], $Ti_{85-x}M_xSi_{15}$ (M=V, Cr, Mn, Fe, Co, Ni, Cu, Zr, Nb, Ta) [105], $Ti_{90-x}M_xB_{10}$ (M=Cr, Mn, Fe, Co, Ni) [105] were also studied. Table 1.8 lists the glass forming ability of Ti based metallic glasses.

Table 1.8 Glass forming ability of Ti based bulk metallic glasses (BMGs).

Ti-Ni-Cu based BMGs						Other Ti based BMGs free of Ni content		
Composition	critical size (mm)	reference	Composition	critical size (mm)	reference	Composition	critical size (mm)	reference
Ti50Cu25Ni25	ribbon	[102, 106]	Ti60Cu14Ni12Sn4Ta10	ribbon	[107-109]	Ti80Si20	ribbon	[110]
Ti50Cu25Ni20Co5	ribbon	[106, 111]	(Ti0.5Zr0.05Cu0.25Ni0.15Sn0.05)100-xMox (x=2.5, 5)	ribbon		Ti-Ni-Si system		
Ti50Cu25Ni20Sn5	6	[112]	Ti47.5Cu21.85Ni19Sn6.65Mo5	ribbon	[113]	Ti72Fe12Si16		
Ti50Cu32Ni15Sn3	1	[114]	Ti50Cu20Ni24Si4B2	1	[115]	Ti85Si15		[116]
Ti50Cu25Ni15Sn3Be7	2	[114, 117]	Ti50Cu23Ni20Sn7	ribbon	[113]	Ti85-xVxSi15 (x= 10, 25, 30, 40at.%)		
Ti45Zr5Cu25Ni15Sn3Be7	5	[114]	(Ti0.5Cu0.23Ni0.2Sn0.07)95Mo5	ribbon	[113]	Ti85-xNbxSi15 (x= 5, 10, 30at.%)		
Ti40Zr25Ni8Cu9Be18	8	[114]	Ti53.5Cu25Ni15Si3B0.5Zr3Alx (x=0-5 at.%)	1-2.5	[118]	Ti85-xTaxSi15 (x= 10, 20, 30, 40at.%)		
Ti40Zr21Cu10Ni9Be20	10	[119]	Ti53Cu27Ni12Zr3Al7Si3B1	2	[120]	Ti78Fe15Si7		[121]
Ti45Zr16Cu10Ni9Be20	10		Ti41.5Zr2.5Hf5Cu42.5Ni7.5Si1	2	[122]	(TixZryTaz)85Si15		[123]
Ti50Zr15Cu9Ni8Be18	6		Ti57Ni35Si8	ribbon	[124]	Ti45Zr10Pd10Cu35-xSnx (x=1-8 at.%)	1-4	[125]
Ti55Zr10Cu9Ni8Be18	6		Ti33Cu47Zr9Ni6Sn2Si1Nb2	3	[126]	Ti44.1Zr9.8Pd9.8Cu30.38Sn3.92Nb2	5	[127]
Ti60Zr5Cu9Ni8Be18	2		Ti45.8Zr6.2Cu39.9Ni5.1Sn2Si1	4	[128]	Ti40Zr10Cu36Pd14	6	[129]
Ti40Zr29Cu9Ni8Be14	2		(Ti43.89Cu43.60Zr6.75Ni5.76)Six x=0.5, 1 at.%	2-3	[130]	Ti40Zr10Cu34Pd14Sn2 Ti40Zr10Cu32Pd14Sn4	10	[131]
Ti45Zr28Cu7Ni6Be14	2		Ti44Cu38.9Co4Zr6Sn2Be5.1	4	[132]	Ti70Zr6Fe7Si17 Ti64Zr5Fe6Si17Mo6Nb2	ribbon	[133]
Ti55Zr18Cu7Ni6Be14	2		(Ti44Cu38.9Co4Zr6Sn2Be5.1)Agx x=1-2 at.%	6		Ti45Zr50-xPdxSi5 (x = 35, 40, 45)	ribbon	[134]
Ti53Cu27Ni12Zr3Al7Si3B1	2	[120, 135-137]	(Ti44Cu38.9Co4Zr6Sn2Be5.1)Six x=1-2 at.%	6		(Ti40Zr10Cu36Pd14)(100-x) Nb-x (x=1, 3, 5 at.%)	2	[138]
Ti53Cu15Ni18.5Al7M3Si3B0.5 (M=Sc, Hf, Ta, Nb)	1.5-2		Ti45.8Zr6.2Cu45-xNixSn2Si1 (x = 0, 2, 4, 5, 7, 9, 11, 13 and 15 at.%)	4	[139]	Ti47.4Cu42Zr5.3TM5.3 (TM = Co, Fe)	ribbon	[140]
Ti56Cu16.8Ni14.4Sn4.8Ta8	ribbon	[107-109]	Ti52-yZryCu40.9Ni5.1Sn2 (y = 4, 6, 8, 10, 12, 14 and 16 at.%)	4		Ti75Zr10Si15 Ti60Nb15Zr10Si15	ribbon	[31]

Chapter2 Experimental Techniques

2.1 Introduction

Ti based alloys were synthesized through different techniques and then their microstructure, chemical compositions and thermal as well as mechanical properties were characterized using various methods.

2.2 Sample Preparation

The sample preparation was conducted at the lab SIMAP, France and WPI-AIMR Tohoku University, Japan. The master ingots of Ti based alloys were produced from metal of purity by arc melting. Before melting, the arc-melter chamber was pumped to primary vacuum by oil-sealed rotary vane pump. The melting of ingots was conducted under Ar atmosphere together with pure Ti priorly used as oxygen getter. All the ingots were melted repeatedly more than five times to ensure chemical homogeneity.

The ingots were then cast to different shapes according to respective requirements. For Ti-Nb based crystalline alloys, due to their high melting temperature, the suction casting and tilt casting methods were employed to produce bulk cylindrical samples of different diameters, 4mm from the former and 8mm from the latter. For suction casting, the mother ingot was melted above the copper mould by arc. It then suctioned into the copper mould due to pressure difference above and below the mould, as shown in Fig. 2.1. For tilting casting, the ingot was first melted in a copper crucible and then poured into the copper mould to obtain sample of large diameter.

For Ti-Fe-Si based alloys, melt spinning was used to produce ribbon shaped samples. As shown in Fig. 2.2. The chamber of melt spinning was first pumped to 10^{-3} Pa by a diffusion pump and then filled with high-purity Ar gas. The ingot, contained in a quartz tube, was then melted by induction heating. Molten alloys were subsequently pushed out through a nozzle hole located at the bottom of quartz tube. The diameter of this hole is less than 1 mm. When the projected liquid alloy meets the rotating copper wheel (diameter is around 280 mm), it is rapidly cooled and solidifies into ribbon shape and is ejected into a tube-shaped chamber where the flying ribbon is collected. With this method, the cooling rate during quenching can reach as high as 10^6 K/s [94], therefore, for suitable compositions glassy states can be frozen down to room temperature.

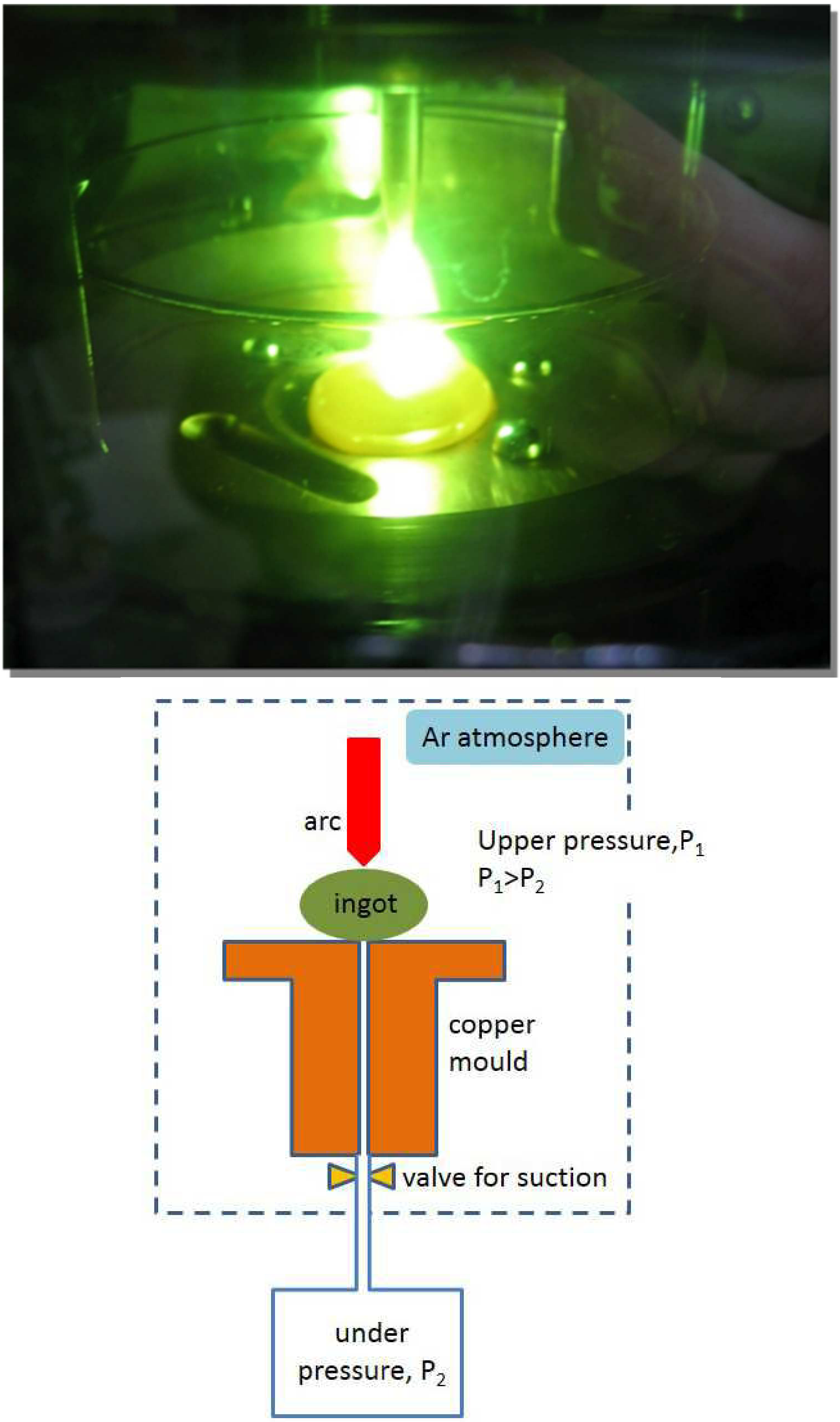

Fig. 2.1 Arc melter (top) and schematic presentation of suction casting (down).

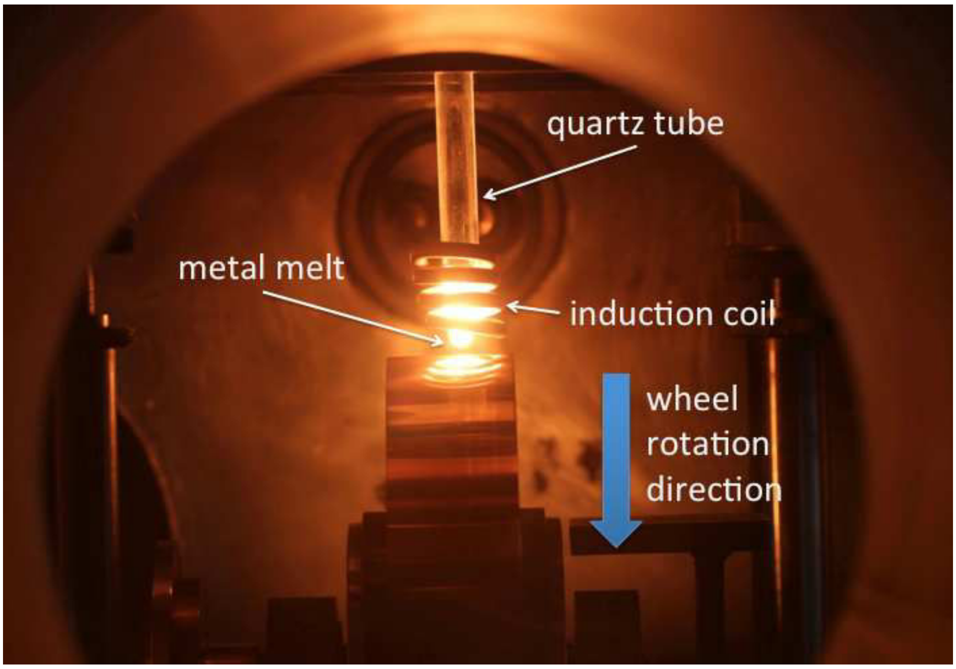

Fig. 2.2 The chamber of melt spinning during experiment.

2.3 Material Characterization

2.3.1 Thermal analysis

Thermal properties of studied materials were investigated through differential scanning calorimetry (DSC). As shown in Fig. 2.3, sample and the reference material with well defined heat capacity in the investigated temperature range (usually Al_2O_3 powder) are kept in separate crucibles. The temperature of either crucible is obtained by measuring the voltage difference of thermocouple A and B. For “true” DSC, i.e. power compensation DSC, two separate heaters are used to provide heat to maintain identical the temperature of these two crucibles and the difference of energy is recorded as differential signal for further investigations [141]. However, the DSCs used in this thesis are of another type, the heat flux DSC, which is similar to differential thermal analysis (DTA). For this type of DSC, the differential signal is the temperature difference between sample and well defined reference and only one heater is employed as heating source. The difference between DTA and heat flux DSC is that, for the latter, there is one metal strip connecting the two crucibles. This metal strip exhibits high thermal conductivity, which minimizes the temperature difference between the two crucibles and, in turn, leads to higher accuracy of measurements. Although neither DTA nor heat flux DSC can reach the accuracy of power compensation DSC, they are more suitable to operate at high temperature >1000^{o}C.

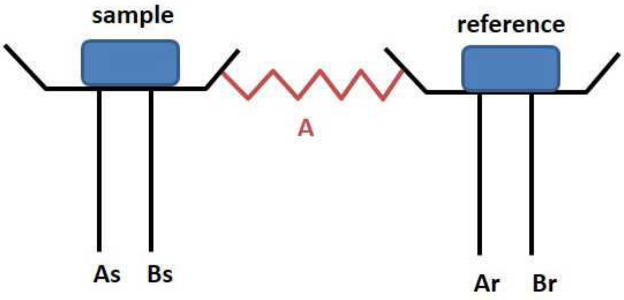

Fig. 2.3 Schematic of heat flux DSC

The heat flux DSCs utilized in this thesis are SDT-Q600 and EXSTAR DSC6300 at WPI-AIMR Tohoku University. Their working temperature ranges from room temperature to 1500^{o}C. The maximum heating rates are 100^{o}C/min and 40^{o}C/min, respectively. The characteristic temperatures of phase transformations are measured through DSC. The typical phase transformations of a metallic glass are illustrated in Fig. 2.4, with glass transition temperature (T_g), crystallization temperature (T_x), solidus temperature (T_s) and liquidus temperature (T_l) illustrated in the sequence of heating direction.

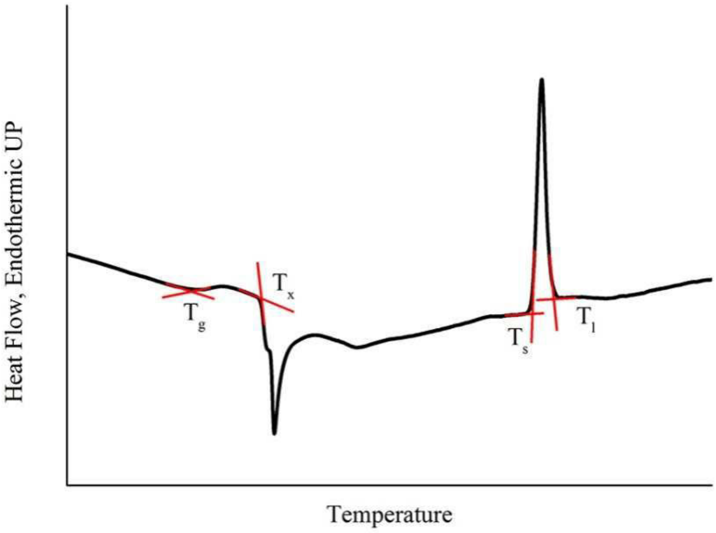

Fig. 2.4 Typical phase transformations of metallic glasses during heating.

2.3.2 Mechanical properties

2.3.2.1 Density Measurement

The densities of synthesized alloys were measured by the Archimedes method. By measuring the weight difference of the sample in the air and in a liquid with well-defined density, one can obtain the densities of tested samples. In the present thesis, the liquid used is n-Tridecane, with molar mass of 184.36 g/mol. The density of test sample can be calculated through Equation 2.1:

$$\rho_s = \rho_r \frac{\Delta m_r}{\Delta m_s} \frac{m_s}{m_r}$$

Equation 2.1

where ρ_s, ρ_r are density of samples and reference (Si in present work), Δm_r and Δm_s are mass difference of samples and reference in air and liquid.

2.3.2.2 Ultrasonic Measurement

The present thesis is devoted to searching for biocompatible implant alloys of low Young's modulus, such that obtaining accurate Young's modulus of synthesized alloys is of great importance. In this work, Young's modulus (E) as well as shear modulus and Poisson's ratio are determined by ultrasonic measurements. The ultrasonic measurement and density measurement were conducted at WPI-AIMR Tohoku University.

The experimental system consists of two main parts: echo-pulse providing unit and sensor unit. The echo-pulse unit includes one echometer and an oscilloscope, which determines the time delay between transmitted and received waves. The sensor unit is actually one transducer for longitudinal wave (frequency 10 MHz) and another one for shear wave (frequency 5 MHz). The sample surfaces were ground to P2400 to ensure they are parallel to each other. The sample surfaces were also kept larger than the area of transducers to avoid edge effects. Moreover, ultrasonic couplants were used between the transducer and the tested sample to facilitate the transmission of sound energy, because any air existing between transducer and sample can greatly impede the transmission of sound waves.

The velocities of longitudinal (V_L) or shear (V_T) waves were determined by Equation 2.2, then Young's modulus (E) as well as shear modulus (G) and Poisson's ratio (ν) of the tested sample can be calculated through Equation 2.5-2.7 [142].

$$V_L(\text{or } V_T) = \frac{\text{sample thickness}}{\text{time of flight}/2}$$

Equation 2.2

$$\nu = \frac{1 - 2(V_T/V_L)^2}{2 - 2(V_T/V_L)^2}$$

Equation 2.3

$$E = \frac{V_L^2 \rho (1+\nu)(1-2\nu)}{1-\nu} = \frac{\rho V_T^2 (3V_L^2 - 4V_T^2)}{V_L^2 - V_T^2}$$

Equation 2.4

$$G = V_T^2 \times \rho$$

Equation 2.5

2.3.2.3 Mechanical Test

The room temperature compression test was conducted on a universal mechanical test machine of the type Shimadzu Autograph AG-X (50 kN) at WPI-AIMR Tohoku University. Cylindrical samples with height/diameter ratio 2:1 were used and strains were measured by extensometer attached to the sample surface. The strain rate was 2.08×10^{-4} /s.

2.3.3 Microstructure and chemical composition analysis

2.3.3.1 Scanning electron microscope

The samples' surface morphologies and chemical compositions were analyzed through conventional scanning electron microscope (SEM) of the type LEO Stereoscan 440 at the lab "Consortium des Moyens Technologiques Communs (CMTC)". This SEM is also coupled with back scattering electron (BSE) detector and energy dispersive spectrometer (EDS) detector. The EDS is Si(Li) detector cooled by liquid nitrogen with energy resolution 130 eV. Fig. 2.5 presents the scheme of conventional SEM. The tungsten filament is heated to generate electrons. The energy of electrons beam used in this thesis ranges from 1.5 kV to 30 kV and spatial resolution can reach 6 nm with 30 kV. [143].

Once the beam arrives at the sample surface, the electrons interact with the sample and excite many different signals. Various detectors are employed to capture these signals, analyze them and finally display on the user screen. The interaction volume of electrons with sample is shown in Fig. 2.6. In this "Bulb" shape interaction zone, secondary electrons are better to reveal the sample surface morphology [143]. Their low energy (typically less than 50 eV) is such that only the near surface secondary electrons can escape the sample without being absorbed. The back scattering electrons resulting from the elastic interaction between incident electrons and those of sample atoms. Samples with higher atomic number emit more BSE and therefore appear brighter in the back scattering mode.

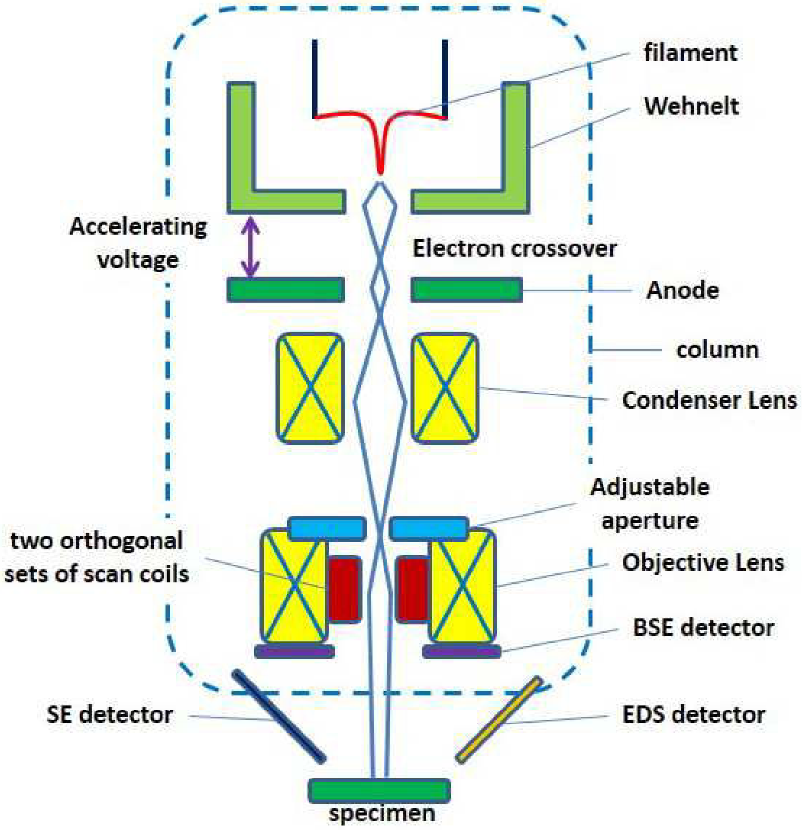

Fig. 2.5 Scheme of conventional scanning electron microscope

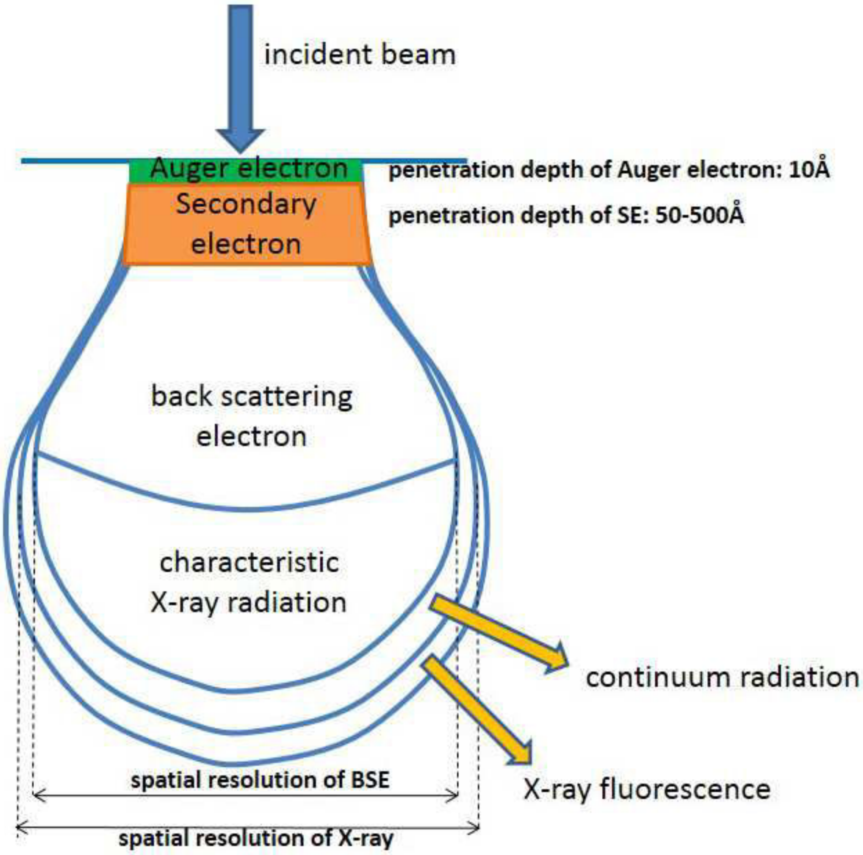

Fig. 2.6 Interaction volume of incident electron beam on samples [143]

The EDS is employed to capture the characteristic X-rays and then provide the chemical composition of test sample. The bulb size determines the spatial resolutions of various detectors. This bulb shaped zone will become gradually hemispherical with sample of high atomic number and/or low energy of incident electron beam.

2.3.3.2 Transmission electron microscope

Transmission electron microscope (TEM) used in current thesis was FEI - Tecnai G2 20 Twin. The experiment was conducted under the collaboration with Dr. I. Bataev from Novosibirsk State Technical University, Russia. The point resolution is 0.27 nm and the line resolution is around 0.15 nm. It possesses an accelerating voltage of 200 kV. It is equipped with CCD detector for bright field (BF) and dark field (DF) imaging. The filament of the TEM is thermal emission tungsten filament. Due to the small size of the crystallites, convergent beam electron diffraction (CBED) was used to obtain the diffraction patterns. Specimens for TEM were thinned by double jet electropolishing. A solution of 5% $HClO_4$ and 95% ethanol was used at -30^{o}C.

2.3.3.3 X-ray diffraction

The microstructures of synthesized alloys were also analyzed by X-ray diffraction (XRD) of the type PANalytical X’Pert Pro MRD at the lab CMTC. As shown in Fig. 2.7, the X-ray source and detector apply to a θ/θ goniometric geometry. X-ray of the wavelength of Cu kα=1.5406 Å is provided by a Cu tube working at 45 kV/40 mA. Graphite analyzer positioned just before the detector is used to provide monochromatic X-ray. The detector of the type X’Celerator is actually composed of 127 point detectors with angle spacing 0.0167^{o}. With this silicon-based position-sensitive detector, the time for measurement is 20 times shorter than conventional point detector. The texture of thermomechanically treated sample was characterized by drawing the pole figure in the range 0-89^{o}. The measurement was conducted using Rigaku smartlab with 2θ goniometric geometry at the lab CMTC. The Cu tube works at 45 kV/200 mA. The Ni Kβ filter was used to provide only Kα radiation.

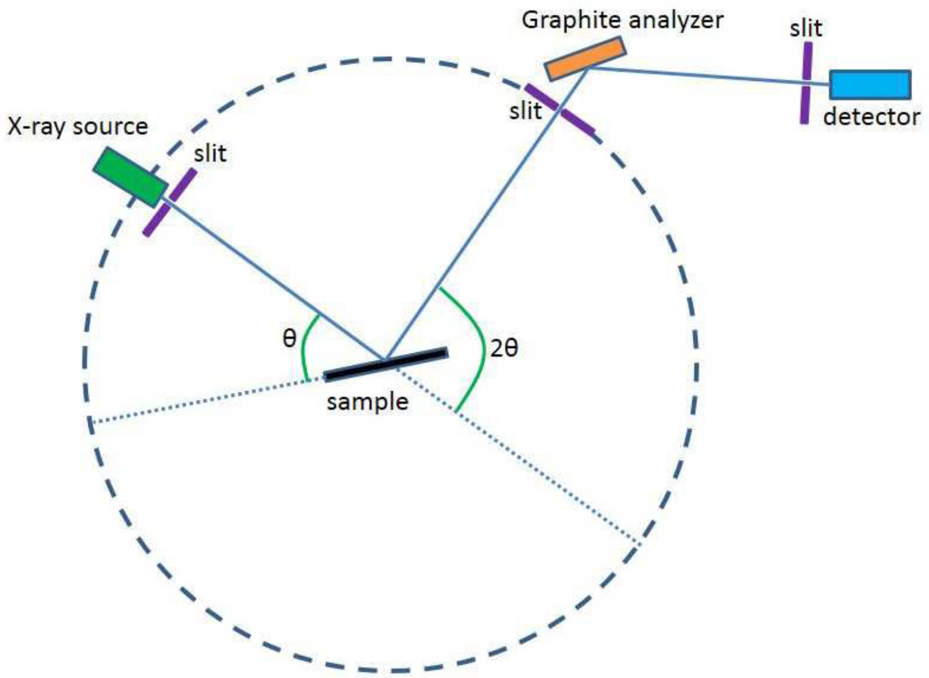

Fig. 2.7 Schematic presentation of X-ray diffraction with graphite analyzer

2.3.3.4 Synchrotron Radiation

The synchrotron experiments reported in this thesis were conducted at the beamline ID11 and ID15 in European Synchrotron Radiation Facility (ESRF) in Grenoble, France. The ESRF is a third generation synchrotron beam source with energy ranging from 10 keV to 130 keV. Due to its high energy, the synchrotron beam at ESRF can penetrate materials that conventional X-rays with longer wave-lengths cannot.

At the ESRF synchrotron, electrons are generated in linear accelerator to an energy of 200 MeV, and then they are injected into the booster synchrotron (Fig. 2.8, A), where they will be further accelerated to an energy of 6 GeV and finally injected to storage ring. The storage ring possesses an extremely high vacuum of the order of 10^{-7} Pa. When the electron trajectories turn due to undulator unit (Fig. 2.8, C), they emit synchrotron light of high brilliance. Next the radiation beam is tuned to the required energy range and aligned in the optical cabin. Finally the beam shoots into the studied specimen located in the experimental cabin (Fig. 2.8, D).

The incident beam will generate a set of Debye-Scherrer diffraction cones behind the sample, as shown in Fig. 2.8, following Bragg's law. The diffracted photons meet the detector located behind the sample. The detector then converts the photon signals either to visible light signals (scintillation detector) or to electrical signals (semiconductor detector). The image obtained by the detector camera is shown in Fig. 2.8 ii. It can be seen that the pattern consists of a set of concentric rings at the intersection of Debye-Scherrer diffraction cones and the detector, which is aligned perpendicular to the axis of diffraction cones. The big dark spot in the middle of Fig. 2.8 is the projection of beam stop used to avoid damage to the detector by the strong beam. Another shallow dark spot in the left bottom of Fig. 2.8 (red circle) results from the defect or contamination of the detector. The image (EDF file) recorded by detector is then integrated radially to obtain the Intensity (I) versus wave vector (Q) curve (Fig. 2.8 iii). Sometimes, the I-Q curves are converted to I-2θ curve to facilitate further identification of diffraction peaks, since most of the standard reference patterns are given in Cu kα 2θ scale. The conversion is done by using Equation 2.6.

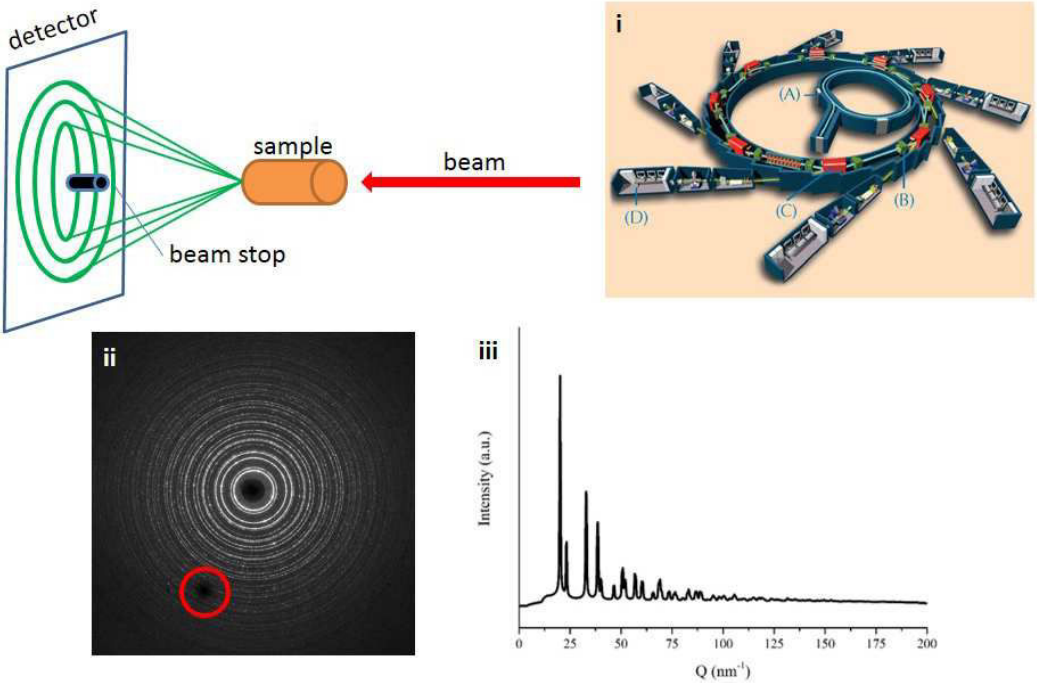

Fig. 2.8 Schematic presentation of synchrotron radiation

$$\sin(\theta_{\mathrm{Cuk}\alpha}) = \frac{\sin(\theta_{\mathrm{synch}}) \times \lambda_{\mathrm{Cuk}\alpha}}{\lambda_{\mathrm{synch}}}$$

Equation 2.6

The data must be calibrated before further analysis. First the geometry of Debye-Scherrer rings and instrumental setup must be calibrated. This is usually done by measuring the diffraction pattern of an external standard (in this work, CeO_2 powder) using the same experimental setup. The following two corrections are not exhaustive of all possible scenarios which could happen to the data, they are merely the two main scenarios that often happened during the analysis of data in the present thesis work. As shown in Fig. 2.9 (A), some overexposed spots exist on the diffraction rings, which result from, in this case, too long acquisition time. The intensity of these spots then correspond to the maximum capacity value of the detector rather than their actual values and it also causes blooming, i.e. brilliant pixels expand over their neighbors. Therefore, these overexposed spots must be excluded during the radial integrations. It can be seen in Fig. 2.9 (B) that there exist double diffraction as highlighted by the red circle. This results from large sample thickness as what happens during transmission electron microscopy experiments. Fig. 2.9 (C) shows the comparison of integrated Intensity – Wave vector (Q) curve before and after the above corrections. As can be seen in the figure, the overexposed spots and double diffraction lead to the shift of the diffraction peaks, causing failure of identification of diffraction pattern with standard reference pattern.

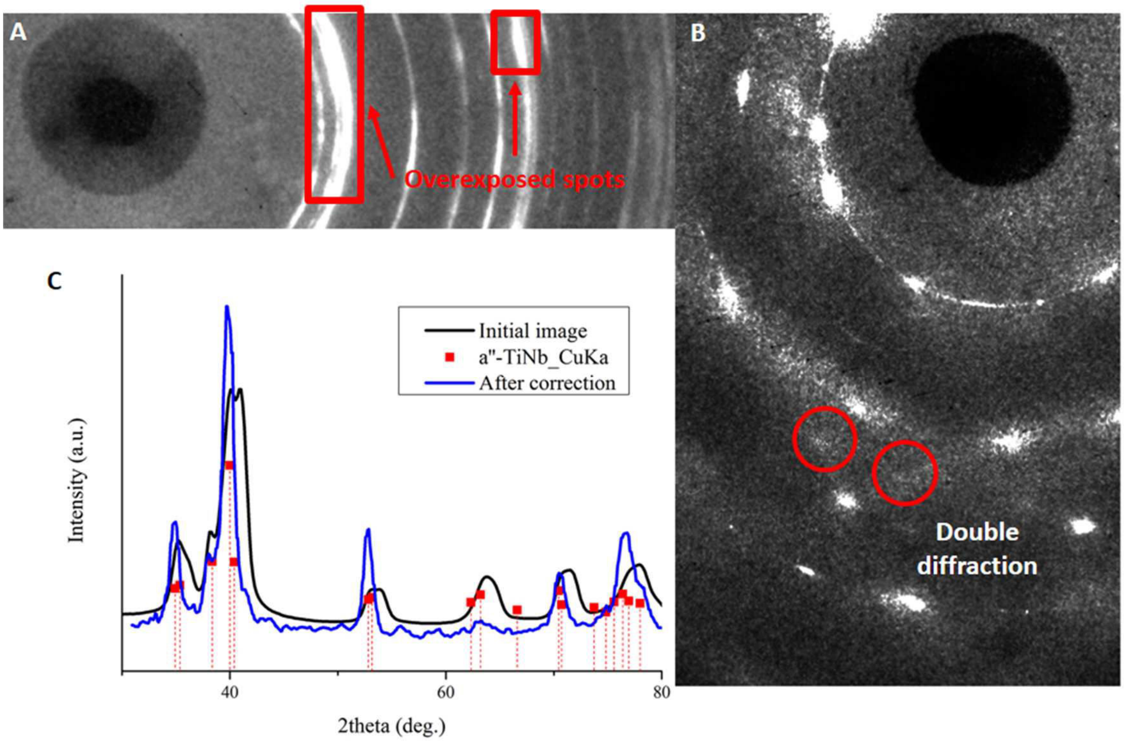

Fig. 2.9 Calibration of data obtained through synchrotron radiation. (A), example diffraction pattern showing overexposed spots. (B), example of pattern showing traces of double diffraction. (C), the comparison of integrated Intensity (I)- wave vector (Q) curves in conventional Cu Kα 2theta angle scale.

In situ tension at the ESRF

The *in situ* tension experiment of TiNb based alloys was conducted on beamline ID11 second hutch of the ESRF. The beam energy E is 98.5 keV with wavelength λ of 0.125857 Å (E=hc/ λ, where h is the Planck constant and c is speed of light). The detector is a 14bit FReLoN (Fast Readout Low Noise) 2D CCD camera. It contains 2048×2048 pixels and each pixel is of 50×50 μm. The sample dimension used is shown in Fig. 2.10. The thickness of tension sample is 0.5 mm. The loading device is ADMET 5 kN stress rig with MTESTQuattro software package for controlling loading and recording stress-strain data. During tension loading, the synchrotron beam was aimed at gauge length of tension sample to conduct *in situ* observation of evolution of microstructure.

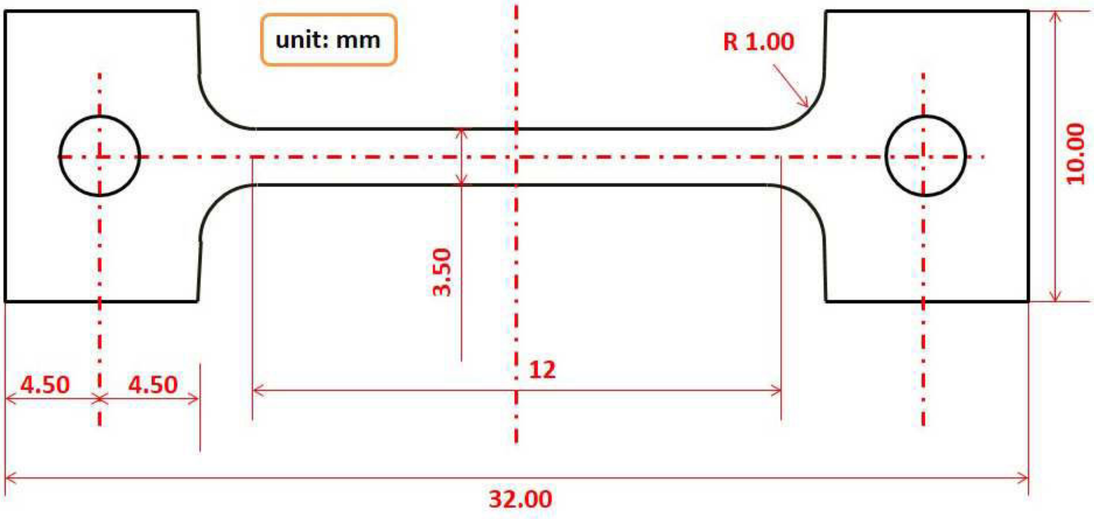

Fig. 2.10 Geometric dimensions of tension sample used in ESRF

Levitation melting at the ESRF

The levitation melting experiment was conducted on beamline ID15 in ESRF using an aerodynamic device. The synchrotron beam energy is of 99.6 keV with the wavelength of 0.12454 Å. The scheme of experimental system is shown in Fig. 2.11. Sphere sample of diameter of 2.4 mm is positioned at nozzle of sample holder. The sample is maintained at equilibrium position by high purity Ar flow. A pyrometer and an external video camera are used to record the sample temperature and monitor the melting process. The melting of sample is performed by three water cooled CO_2 laser beams [144]. The contactless melting diminishes the possibility of heterogeneous nucleation from the contact with any container crucible as used in conventional melting. This levitation melting system coupled with high energy synchrotron beam enables the direct observation of microstructural evolution of studied material during cooling and heating. In this thesis, a Ti-based quinary metallic glass was chosen to study its microstructure evolution during cooling from above liquidus temperature [145].

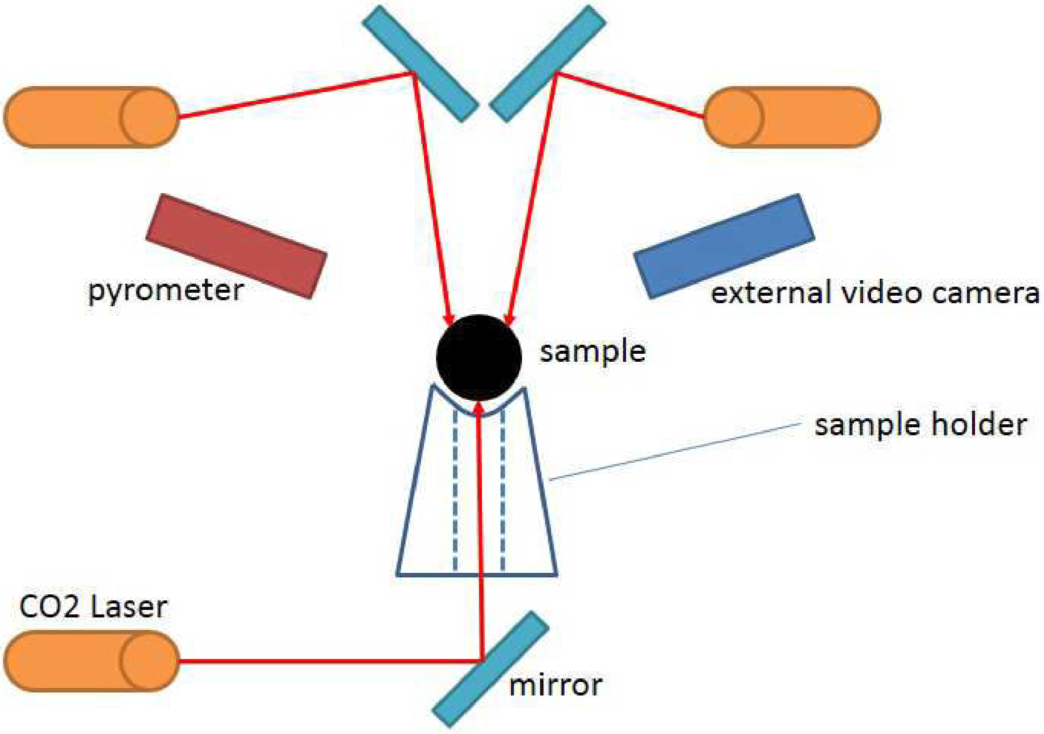

Fig. 2.11 Representation of levitation melting experiment in ESRF

Chapter 3 Phase transformations and mechanical properties of TiNb based crystalline alloys

3.1 Introduction

Titanium based alloys have been widely used as biomaterials for body implants [146] such as hip joints, dental implants and medical devices due to their excellent corrosion resistance, high yield strength and good ductility. However, most commercially used Ti-based implant alloys exhibit considerably higher Young’s modulus (E) compared to human bones (around 30 GPa) and the resulting stress shielding effect results in bone resorption [26]. So it is of great importance to develop Ti- based alloys with lower Young’s modulus.

There exist four non-equilibrium phases in Ti alloys at room or body temperature. These are body-centered β phase which has a Young’s modulus well below that of the equilibrium hexagonal α phase, and hexagonal ω phase. In addition, the martensitic α’ and α’’ phase can be obtained through quenching from above the equilibrium α/β transition temperature depending on the composition and quenching rate, while ω phase can be formed either by quenching, referred to as athermal ω, or by aging, referred to as isothermal ω [147]. Young’s modulus (E) of ω phase is the highest among the above four non equilibrium phases, but the value of E for single phase α’’ and β has not been determined with certainty and different researchers have presented contradictory results [54, 55, 148]. Therefore, in order to achieve low Young’s modulus, ω phase should be avoided; it can be retarded by the addition of Al, Sn, O [56]. Moreover, metastable β phase can be retained with increasing content of β stabilizing elements such as Mo, V, Ta and Nb. With the addition of such elements, many β and near β alloys have been synthesized, such as Ti-Nb-Ta-Zr [149], Ti-Nb-Si [150], Ti-V-Sn [151].

As far as biocompatibility is concerned, most of the widely used Ti-based implant alloys contain toxic elements. For example, V has been classified in the toxic group, the biocompatibility of Al is disputed due to tissue response of its capsule [152], while toxic Ni can be released as metal ions and result in hypersensitivity [153]. Thus, implant alloys free of toxic elements are needed and for this reason, TiNb has drawn great interest due to its good biocompatibility and excellent corrosion resistance. Fig. 3.1 shows Ti-Nb binary phase diagram. β phase exists at high temperature and α phase exists at low temperature. Moreover, the β phase region becomes larger with increasing amount of Nb content, indicating that Nb is β phase stabilizer element.

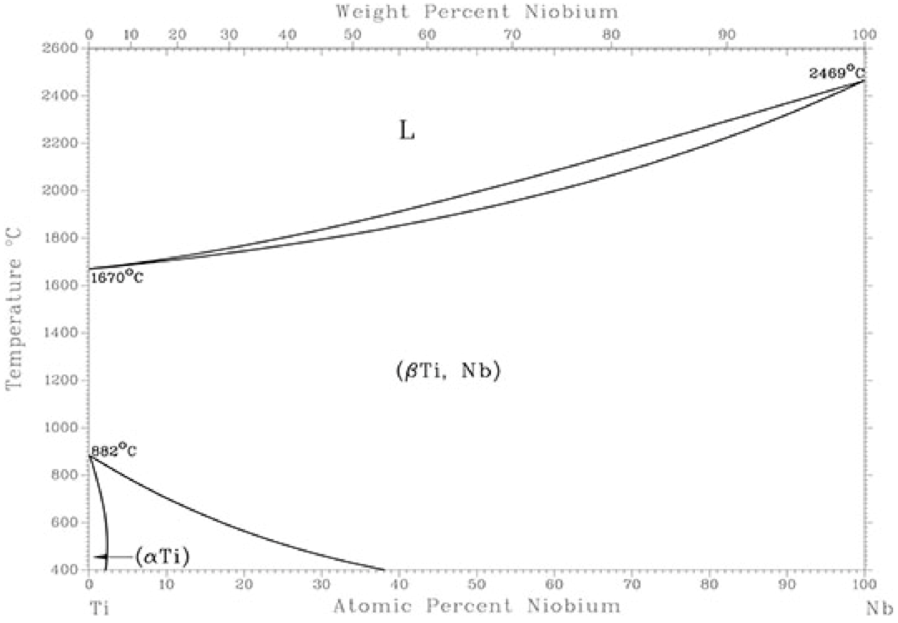

Fig. 3.1 Ti-Nb binary phase diagram [147].

In this chapter, two TiNb binary alloys were selected and fabricated through copper mould suction casting. The microstructures are characterized by XRD, synchrotron radiation, SEM and optical microscope. Thermal properties and mechanical properties were investigated using DSC and universal mechanical testing machine, respectively.

The main criterion for the selection of the TiNb based alloy compositions studied in the present thesis is their low Young modulus.

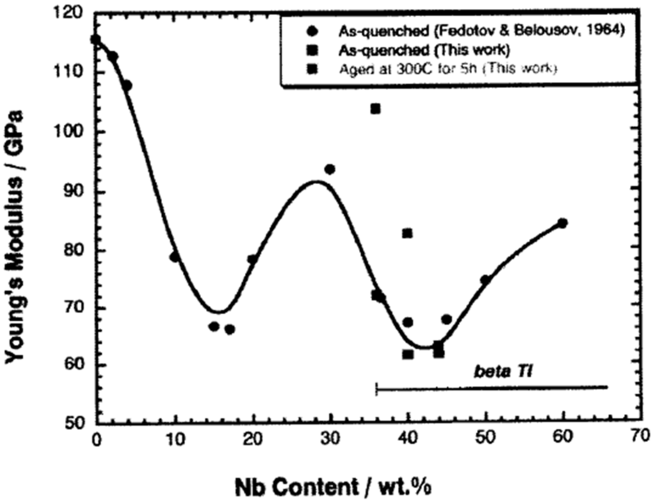

Fig. 3.2 Compositional dependence of Young's modulus of water quenched TiNb binary alloys [61].

Fig. 3.2 shows the Young's modulus as a function of Nb content in the Ti-Nb binary system. Two minima exist around 15wt.% Nb and 40 wt.% Nb and therefore, the corresponding alloys $Ti_{92}Nb_8$ and $Ti_{74}Nb_{26}$ (at.%), were selected for further studies. A new alloy with composition $Ti_{73}Nb_{25}Sn_2$(at.%) was also synthesized in order to study the effect of Sn addition in Ti-Nb alloys since Sn has the ability to suppress the formation of ω phase [56].

3.2 Ti-Nb based alloys

3.2.1 Experimental procedure

Pure elements of Ti (99.9%), Nb (99.9%) and Sn (99.8%), were melted under Ar atmosphere in an arc melter. The arc-melted ingots were then injected into copper moulds using the suction casting technique. The as-cast samples were subsequently wrapped in Ti foils and encapsulated in sealed quartz tubes in an Ar inert atmosphere. Then the samples were annealed at 1000^{o}C for 5 hours followed by either slow furnace cooling (FC) to room temperature or fast quenching in ice water (WQ). The furnace cooling was realized by turning off the oven and leaving samples to cool in the quartz tube under Ar atmosphere, while water quenching was achieved by breaking the quartz tube in a container filled with ice water.

3.2.2 Microstructural characterization

X-ray Diffraction (XRD) patterns of the arc-melt ingots and suction cast samples with different diameters (4 mm and 8 mm) for all three compositions are presented in Fig. 3.3 and Fig. 3.4. It is shown in Fig. 3.3(a) that the ingot of Ti$_{92}$Nb$_{8}$ exhibit α phase reflections, while the spectra for the two cast samples show only Bragg peaks which correspond to the a” martensitic phase. Thus it becomes clear that suction casting with higher cooling rate favors formation of martensitic α’’ phase, while slow cooling facilitates formation of α phase. The conventional XRD patterns of ingot and as-cast samples of Ti$_{92}$Nb$_{8}$ are further zoomed in between 30^{o} and 45^{o} in Fig. 3.3(b). It can be more clearly seen that the two as-cast samples possess similar Bragg peaks, indicated as martensitic α’’ phase, which are different from those of ingot sample.

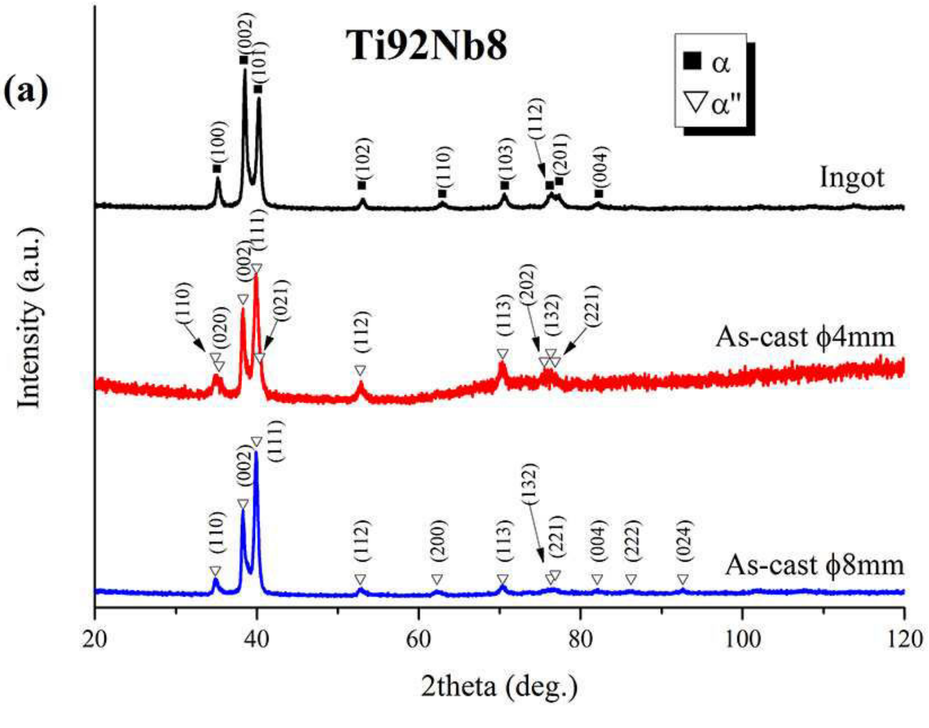

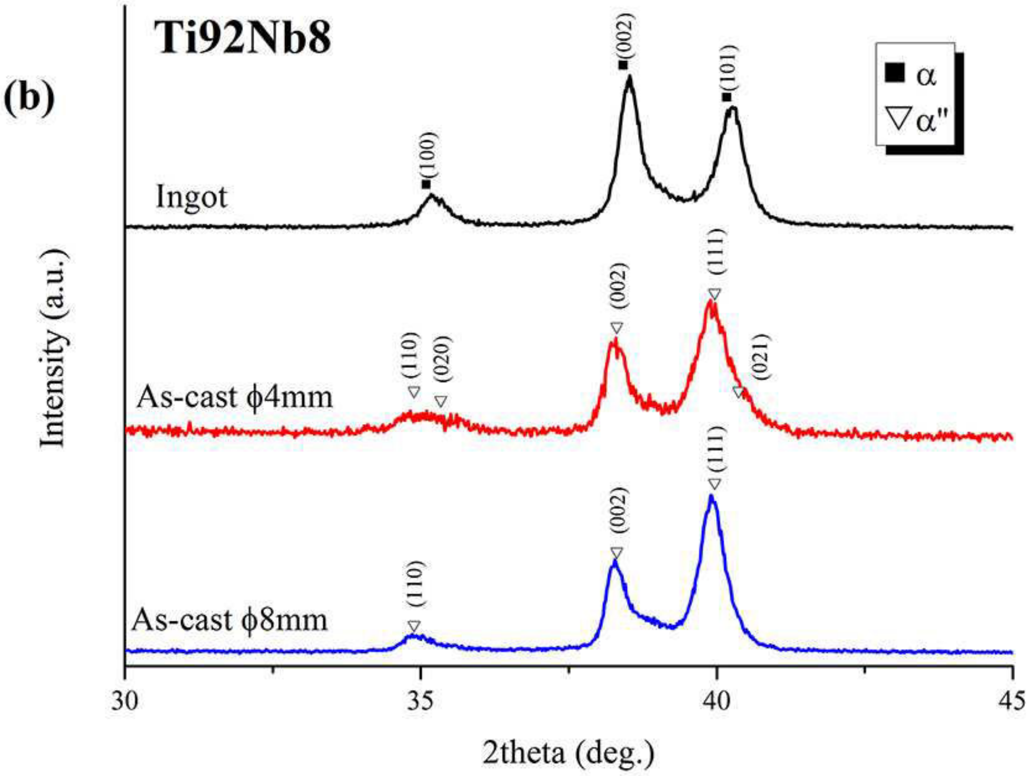

Fig. 3.3 Conventional X-ray diffraction patterns of as-melted ingot and casting samples in different diameters of $Ti_{92}Nb_8$ alloys (a) and zoom in range between 30^o and 45^o (b).

As shown in Fig. 3.4 (a) and (b), the compositions with higher Nb content, $Ti_{74}Nb_{26}$ and $Ti_{73}Nb_{25}Sn_2$, mainly consist of β phase regardless of the preparation method (as-melted ingots and castings in both 4 mm and 8 mm diameter). This is because of the higher content of Nb which stabilizes the β phase.

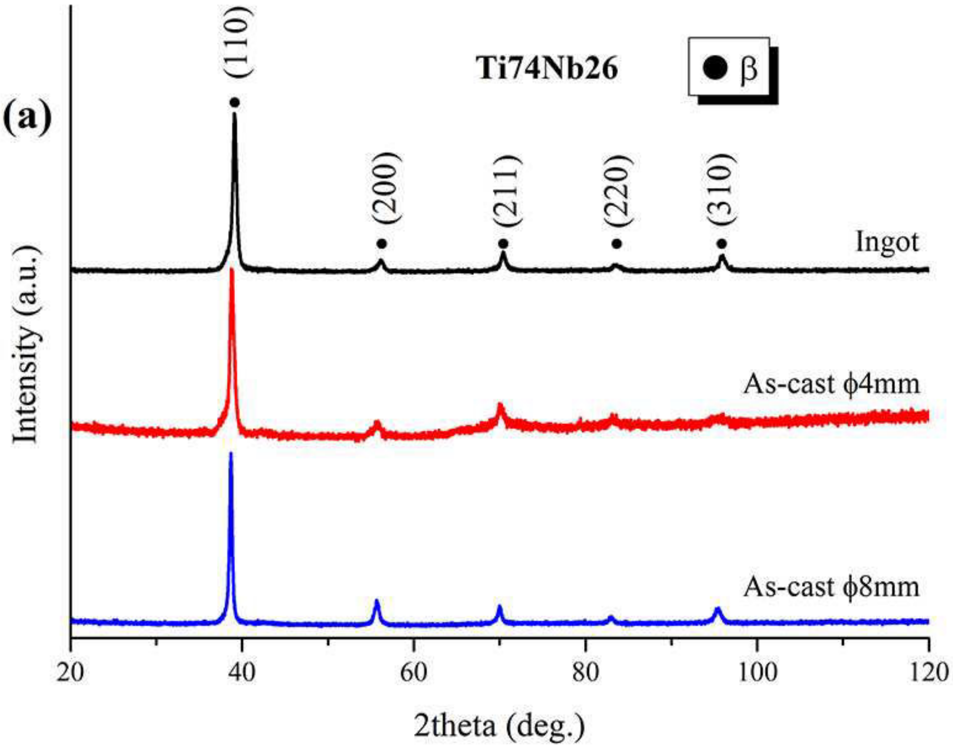

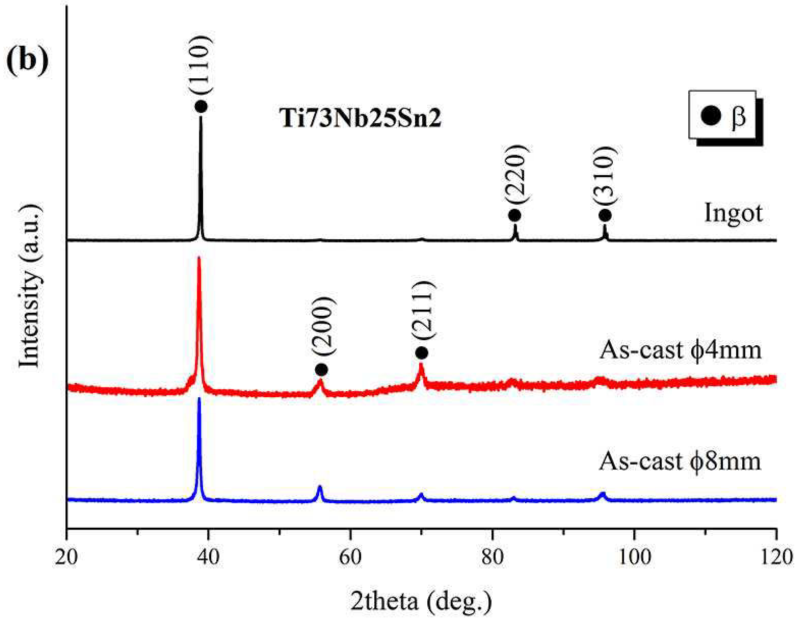

Fig. 3.4 Conventional X-ray diffraction patterns of as-melted ingot and casting samples in different diameters of $Ti_{74}Nb_{26}$ (a) and $Ti_{73}Nb_{25}Sn_2$ (b) alloys.

The crystal structure of TiNb based alloys in as-cast, water quenched and furnace cooled state are shown in Fig. 3.5. For the lower Nb content alloy, $Ti_{92}Nb_8$, high cooling rate (copper mould casting and water quenching) favors the martensitic phase α'' and low cooling rate leads to formation of HCP α phase as shown by the equilibrium phase diagram, Fig. 3.1. The α'' martensitic phase is a transition phase between high temperature stable phase, β phase and low temperature stable α phase. Due to the addition of β stabilizer, Nb, the β phase region extends to low temperature. However, 8 at.% Nb is still not enough to retain the high temperature phase at room temperature. During cooling, β phase starts to transform to low temperature α phase. If the cooling rate is high, such as in the case of copper mould casting or water quenching, transition phase, α'' martensite, can be retained at room temperature. If cooling rate is low, like in furnace cooling, β phase is able to transform to α phase.

Different from the scenario shown in Fig. 3.5 (a) for $Ti_{92}Nb_8$, the alloys with high Nb content ($Ti_{74}Nb_{26}$ and $Ti_{73}Nb_{25}Sn_2$) exhibit β phase as the main phase at room temperature in all three states (as-cast, furnace cooled and water quenched), as shown in Fig. 3.5 (b) and (c). In addition, for the water quenched state, both high Nb content alloys possess α'' martensitic phase. This is interesting since water quenching exhibit an intermediate cooling rate compared to copper mould casting and slow furnace cooling. The reason might be twofold. The pattern shown here is obtained by conventional XRD with working voltage of 40 kV. The penetration depth of XRD to current TiNb based alloys is around 7 μm. So the XRD pattern basically reveals the microstructure near the surface, not all the bulk sample. In addition, according to the phase diagram established by Moffat [40], the martensitic starting temperature, M_s, for $Ti_{74}Nb_{26}$ alloy is around room temperature. So for this specific composition, according to the lever rule of phase diagram, the structure at room temperature should mainly consist of high temperature β phase together with very small quantity of α'' martensite. The presence of α'' martensite can be observed in the diffraction pattern obtained by synchrotron beam in transmission mode shown in Fig. 3.24. From this point of view, it can be expected that small quantity of α'' martensite is not observed in XRD pattern which only reveals the microstructure near the surface, as shown in the as-cast and furnace cooling state. It has been shown that the oxygen content can change the M_s temperature [154-157]. In the case of water quenched $Ti_{74}Nb_{26}$ alloys, the oxygen dissolved in the water can increase the M_s to above room temperature. This may lead to some β phase transforming to α'' martensite. The reason why oxygen content can increase M_s in current $Ti_{74}Nb_{26}$ alloy might be due to formation of Nb-rich oxide near surface. This leads to enrichment of Ti in the matrix, which consequently results in an increase of M_s temperature. However, further experiments need to be conducted to confirm this speculation. The situation of as-cast and furnace cooled alloys is different from the water quenched state, since they are conducted under Ar atmosphere without presence of oxygen.

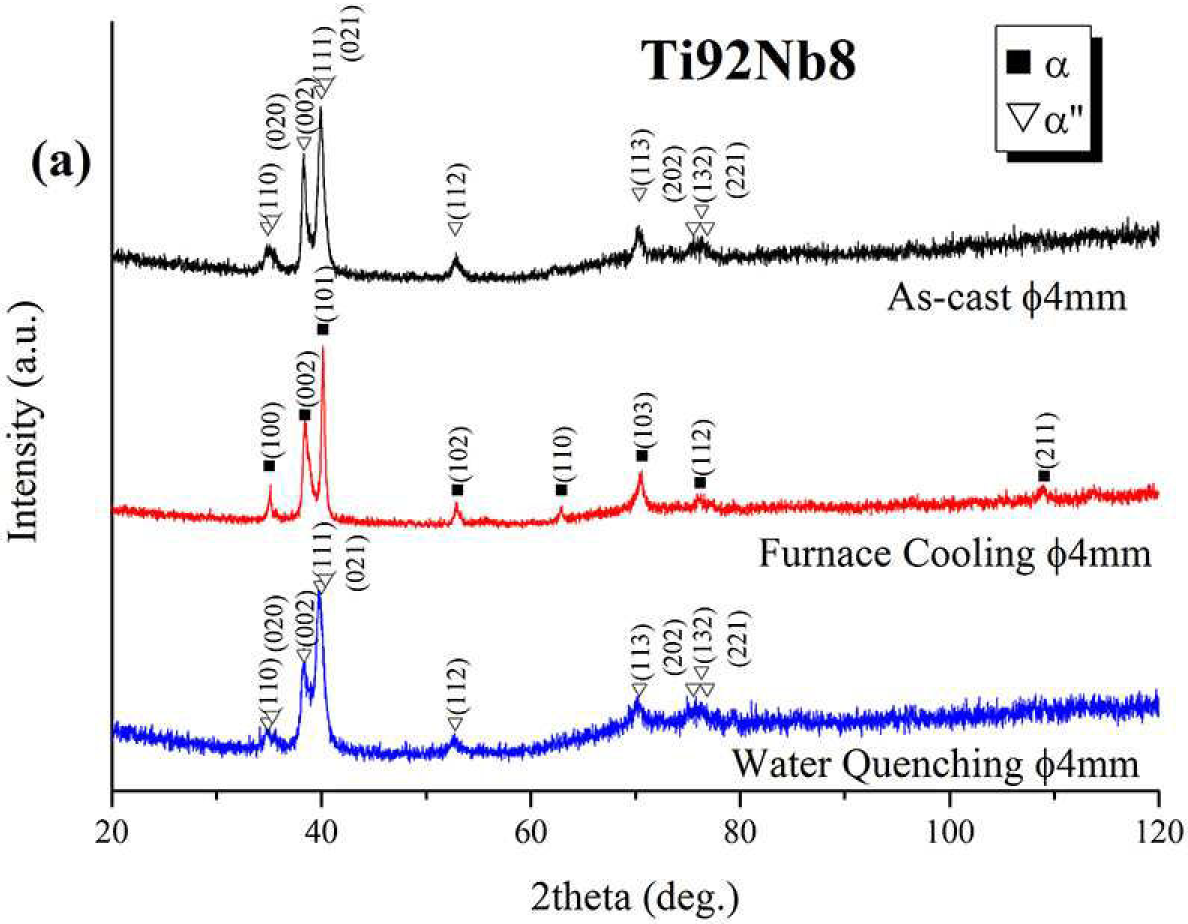

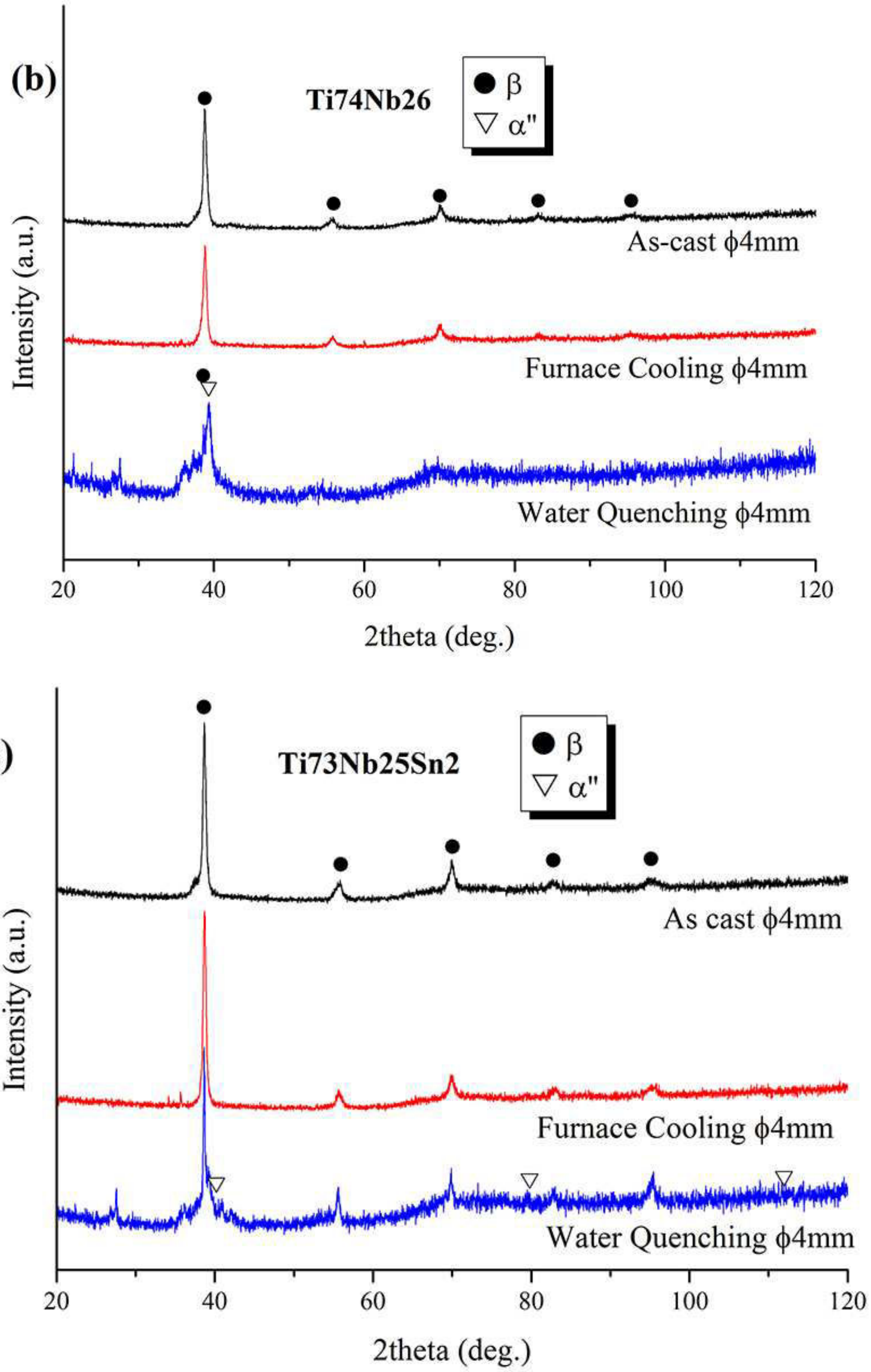

Fig. 3.5 XRD patterns of TiNb based alloys in as-cast, water quenched and furnace cooled state.

The surface of a cast cylinder was observed using a conventional SEM. The images shown in Fig. 3.6 come from non-etched surfaces of a $Ti_{92}Nb_8$ cast rod. Equiaxed chill zone grains of different sizes at various locations of the cast cylinder can be seen in Fig. 3.6. At the top, where the cooling rate is lower, the grains size is around 200 µm, whereas grains at the bottom are around 100 µm or smaller. Moreover, martensite platelets exist in the equiaxed grains. This is due to the M_s temperature of $Ti_{92}Nb_8$ alloy which is above room temperature, leading to the transformation of the high temperature β phase to α'' martensite.

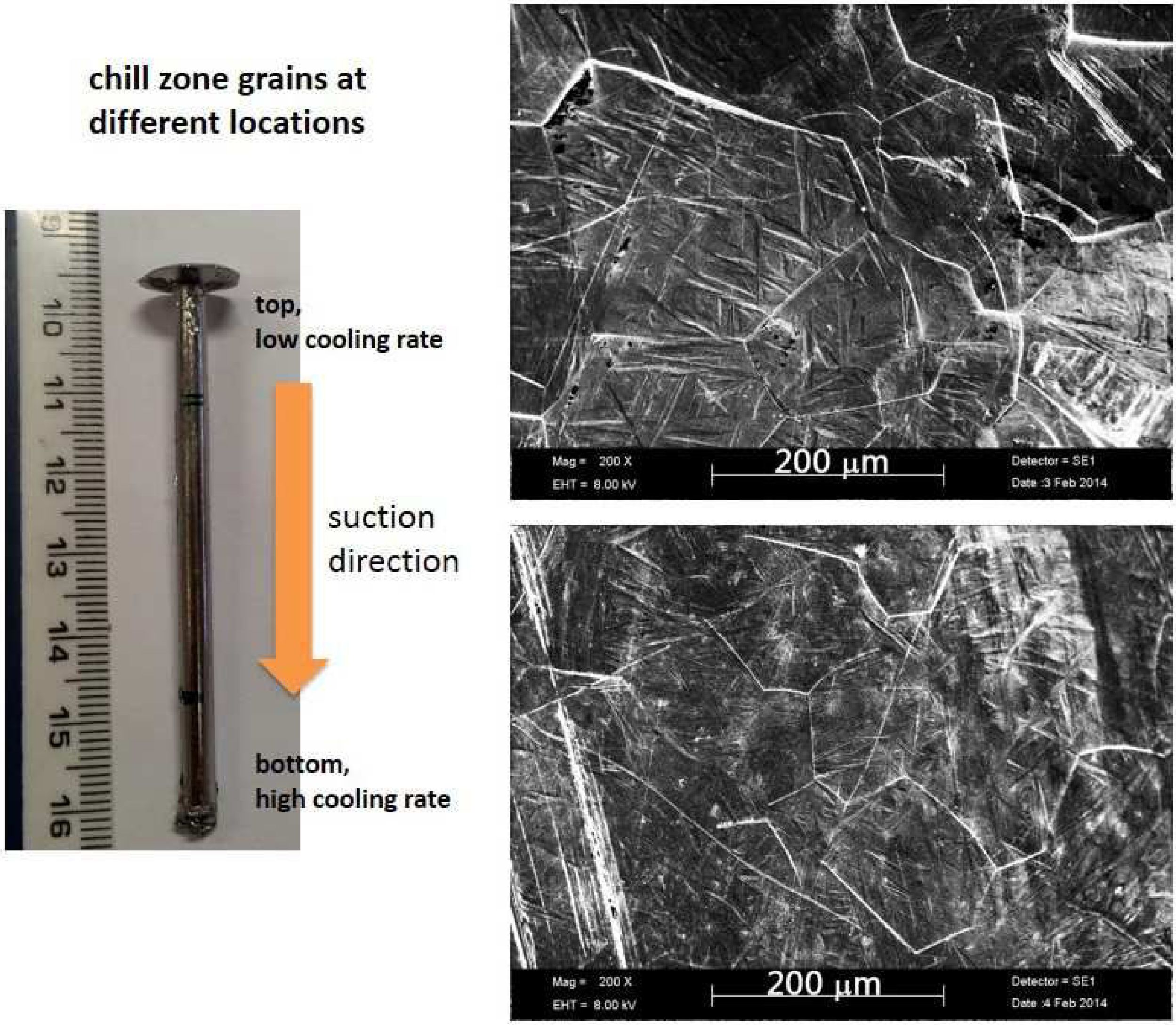

Fig. 3.6 Secondary electron images of the surface (side view) of a $Ti_{92}Nb_8$ as-cast rod from different locations.

In order to reveal better the microstructure of TiNb based alloys, a solution of 8% hydrofluoric acid, 15% nitric acid and 77% water (volumetric concentration) was used to chemically etch the surface. Fig. 3.7 shows an optical micrograph of the cross section of a $Ti_{92}Nb_8$ as-cast rod. It can be seen that there exist many martensite platelets near the surface. In addition, the solidification mode changes from cellular near surface to columnar dendritic at the center. A secondary electron image (Fig. 3.8) from the marked region in Fig. 3.7, confirms this feature. It can be seen that the cellular solidification mode at top right corner and columnar dendritic mode at down left corner.

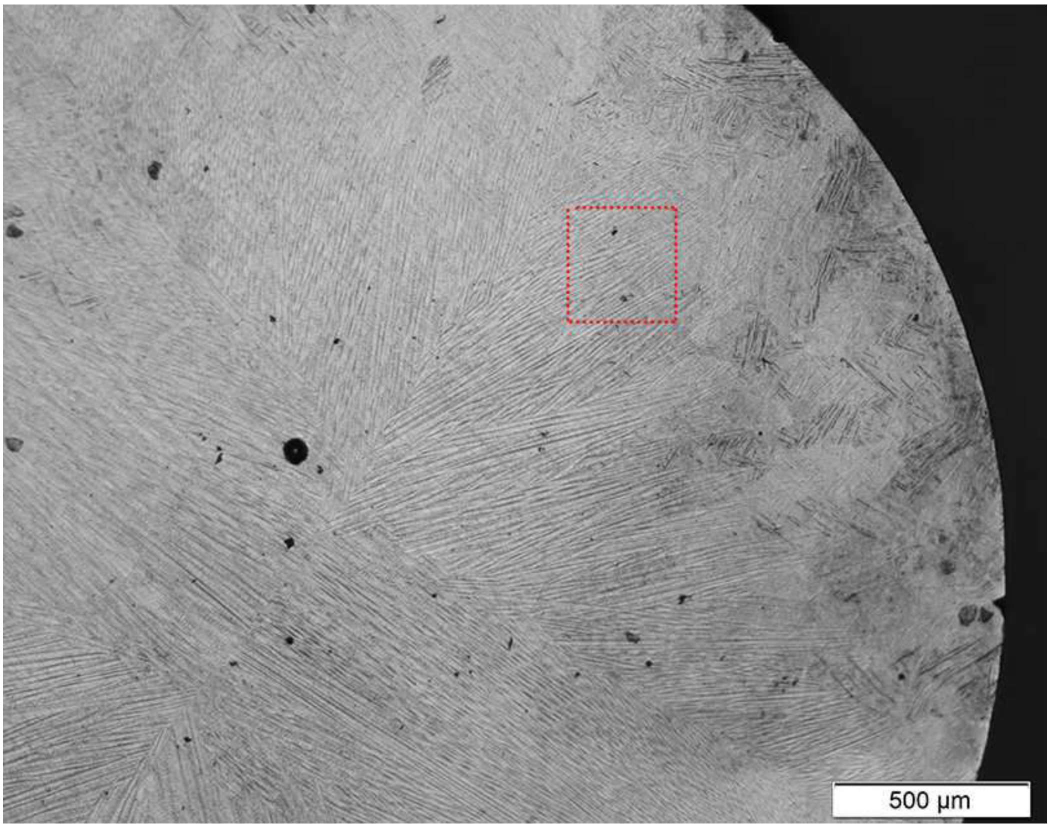

Fig. 3.7 Optical micrograph of the cross section of a$Ti_{92}Nb_8$ *rod in as-cast state. The dot rectangle indicates the region where FEG SEM observation is conducted.*

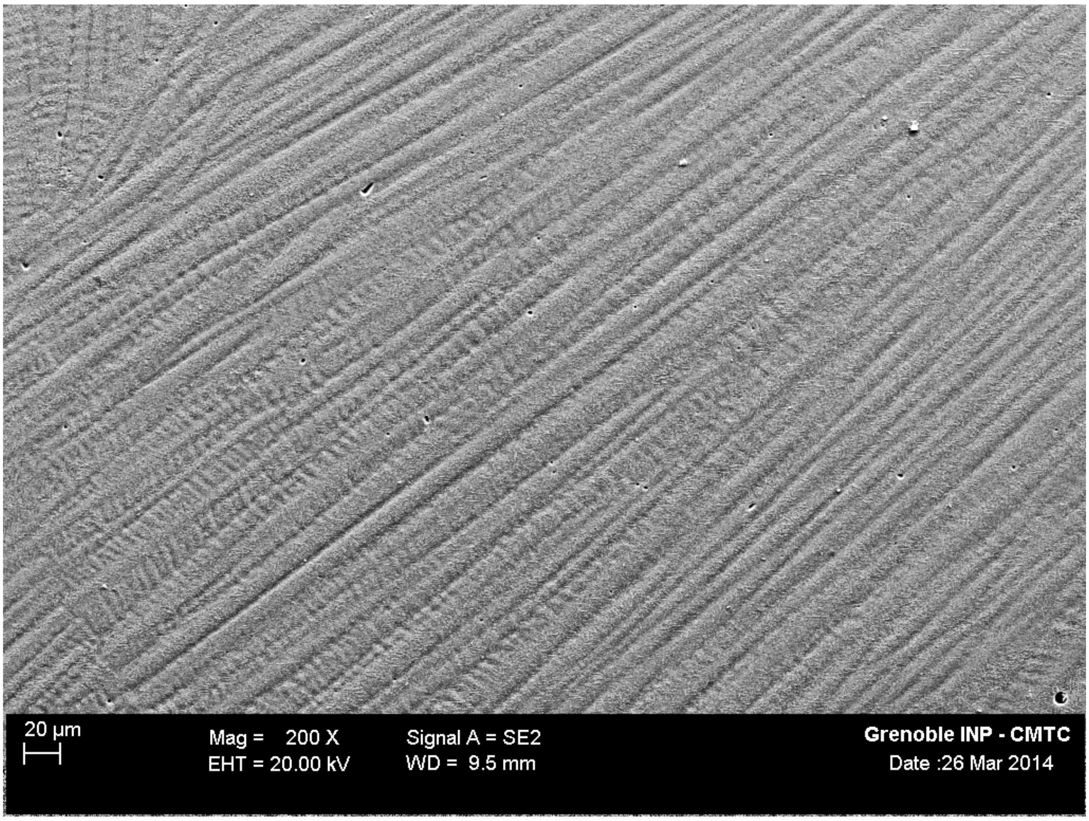

Fig. 3.8 Secondary electron image shows changes of solidification mode

A higher magnification image taken at the same place (Fig. 3.9) shows that martensite platelets are the overwhelming feature. This is in accordance with XRD patterns shown in Fig. 3.3 and Fig. 3.5.

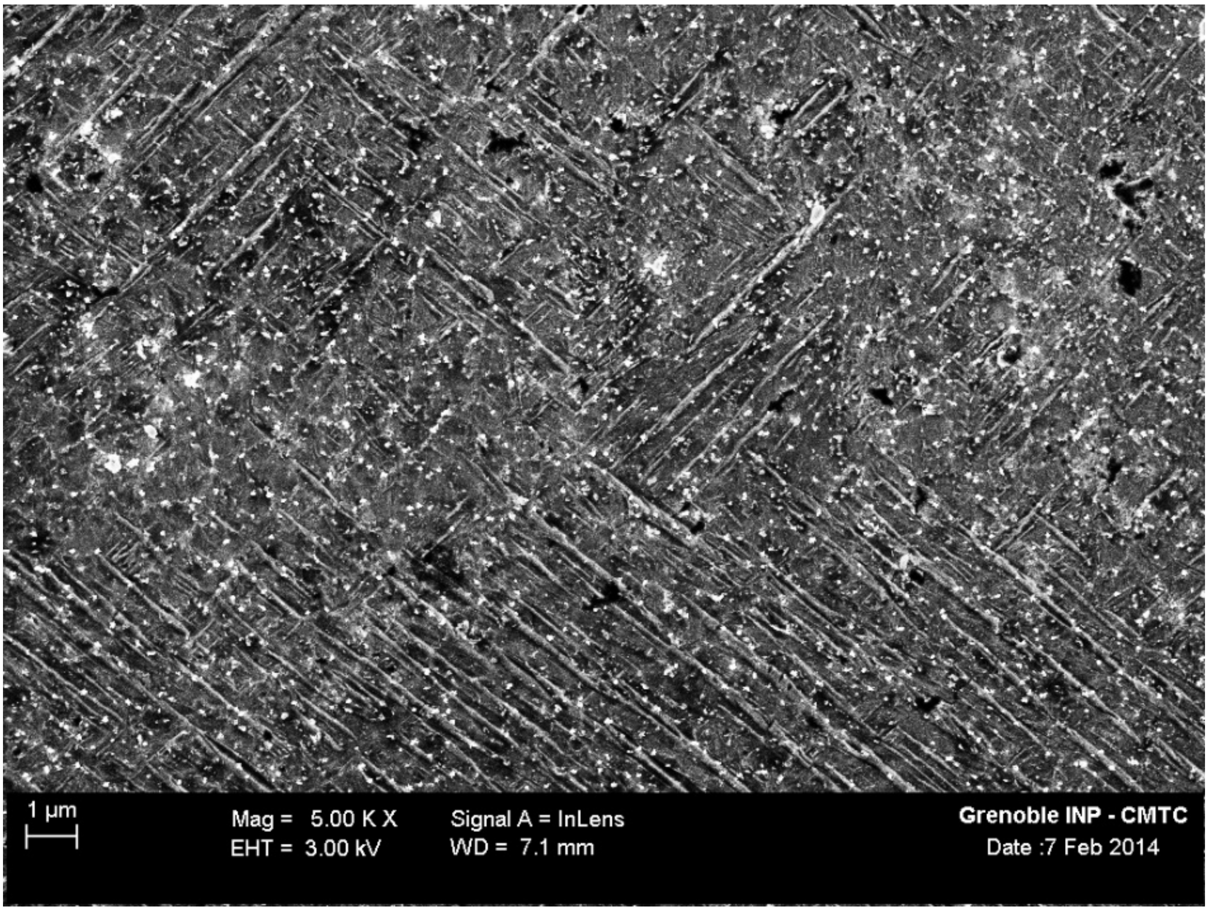

Fig. 3.9 Secondary electron image of transverse cross section of $Ti_{92}Nb_8$ *as-cast alloy showing numerous martensite platelets.*

The martensite platelets shown in Fig. 3.9 (b) are around 0.2 µm wide and several microns long. They are at right angle to each other, indicating that they are martensite variants. As shown previously in Fig. 3.3, the martensite in $Ti_{92}Nb_8$ as-cast alloy is of orthorhombic structure, which has 4 types of symmetric operations. While high temperature β phase is of cubic structure, which has as many as 24 symmetric operations. Therefore, there can exist 6 (6=24/4) martensite variants in the case of cubic-to-orthorhombic transformation. Each martensitic variant corresponds to one energy well in which the material can reside. In addition, the energy density for all BCC high temperature phase transforming to one single martensite variant is larger than transforming to a mixture of different variants [158]. Therefore, the structure of martensite shown in Fig. 3.9 (b) is the consequence of minimizing energy during transformation. Moreover, the habit plane of α''/β phase is {001}α // {110}β plane, as reported in [76, 159]. The interplanar angle between {110} planes can be 0^o, 60^o and 90^o, respectively. Thus the martensite variants based on different {110}β planes can be perpendicular to each other, as shown in Fig. 3.9 (b) or 60^o to each other, shown in Fig. 3.10.

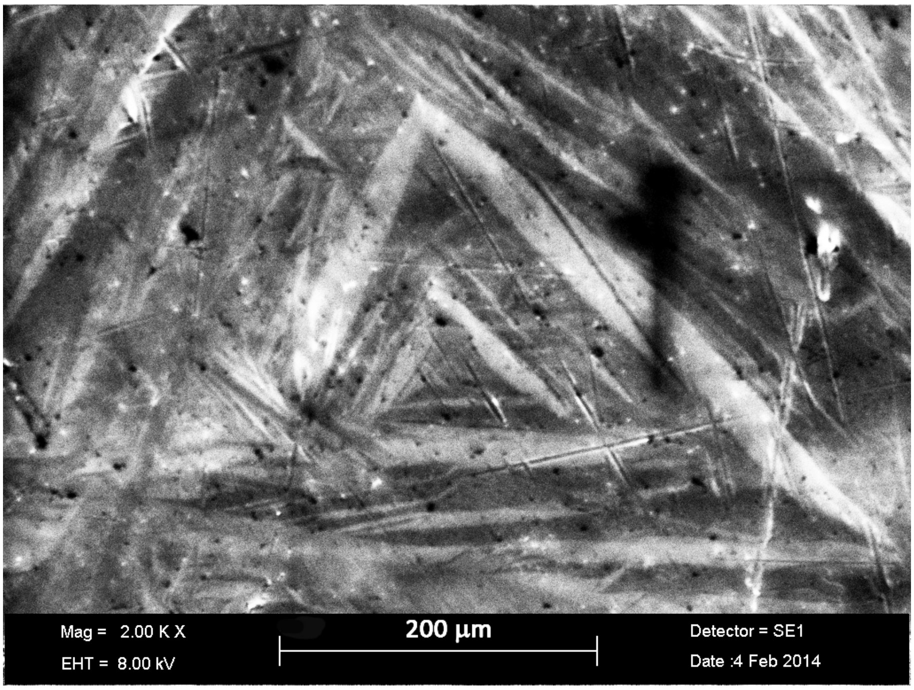

Fig. 3.10 Secondary electron image shows martensite platelets on the unetched surface of casting cylinder of $Ti_{92}Nb_8$ alloy.

The cross section microstructure of heat treated $Ti_{92}Nb_8$ alloys is shown in Fig. 3.11. For the furnace cooled specimen, Fig. 3.11(a), a basket weave like pattern is observed. This pattern is also called Widmanstätten pattern, named after the discoverer. The white long lath (B) in Fig. 3.11 (a) is α phase and dark region (C) between laths is residual high temperature β phase. When $Ti_{92}Nb_8$ alloy is annealed in the equilibrium β phase region, equiaxed β phase grains form. When the $Ti_{92}Nb_8$ alloy is slowly cooled below α/β transition temperature, α phase nucleates on the grain boundary of equiaxed β grain, following Burgers relationship, i.e. {110}β//{0001}α, $[111]$β//$[11\bar{2}0]$α [38]. On further cooling, α phase grows at the expense of β phase until different α grains meet each other. In this case, $Ti_{92}Nb_8$ alloys were slowly cooled in the furnace to room temperature. This leads to most of the β phase transforming to α phase.

As shown above, the 6 different {110} planes in BCC structure are the habit planes between parent β phase and new α phase. So there are 6 possible orientations for α phase nucleating within any given β grain. The high symmetry of cubic β phase then leads to the formation of a basket weave like morphology, similar to the β/α'' martensitic transformation.

Nuclei are usually bound by a combination of rough incoherent interfaces and smooth coherent or semicoherent facets. The shape of the new phase then depends on the competition of migration rates of different interfaces[68]. In the case of α/β transition, due to the difference of their crystallographic structure, the migration of coherent or semicoherent interfaces can only rely on the ledge mechanism. If there is difficulty of providing new ledges, the migration rate of coherent or semicoherent interfaces will be very slow. On the contrary, in presence of roughness, atoms will be very easily accommodated during interface migration. This leads to high mobility of incoherent interfaces. The difference of migration rate between coherent and incoherent interfaces then results in the long lath shape α phase. The illustration of formation of Widmanstätten pattern is shown in Fig. 3.12. Due to low cooling rate, α phase colonies, marked A in Fig. 3.11 (a), are also observed.

For water quenched samples, as shown in Fig. 3.11 (b), needle-like martensite, marked D in Fig. 3.11 (b), nucleated at the grain boundary of high temperature β phase. High cooling rate of water quenching leads to the formation of α'' martensite.

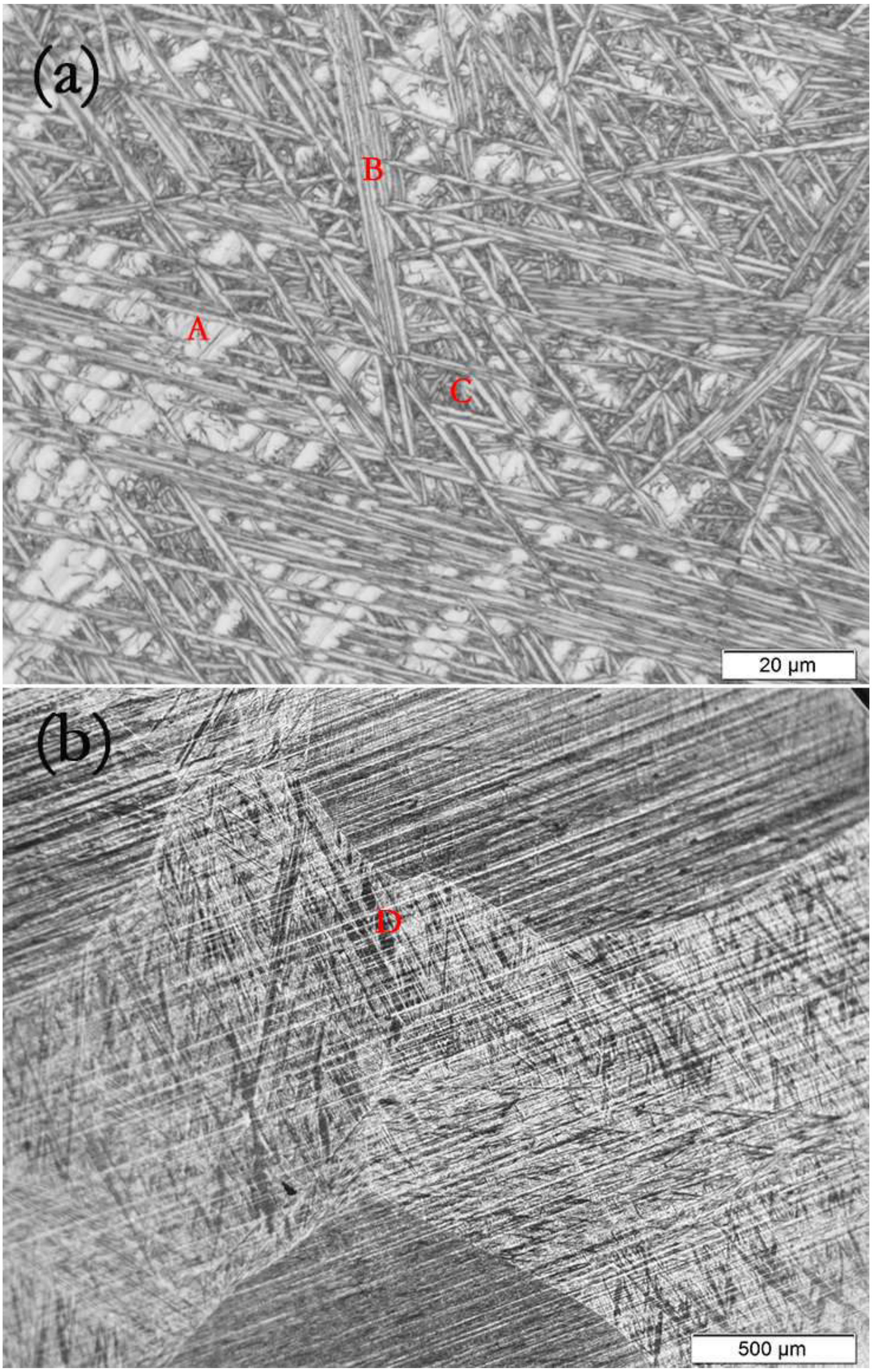

Fig. 3.11 Optical micrographs of heat-treated $Ti_{92}Nb_8$ alloys, furnace cooling in (a) and water

quenching in (b).

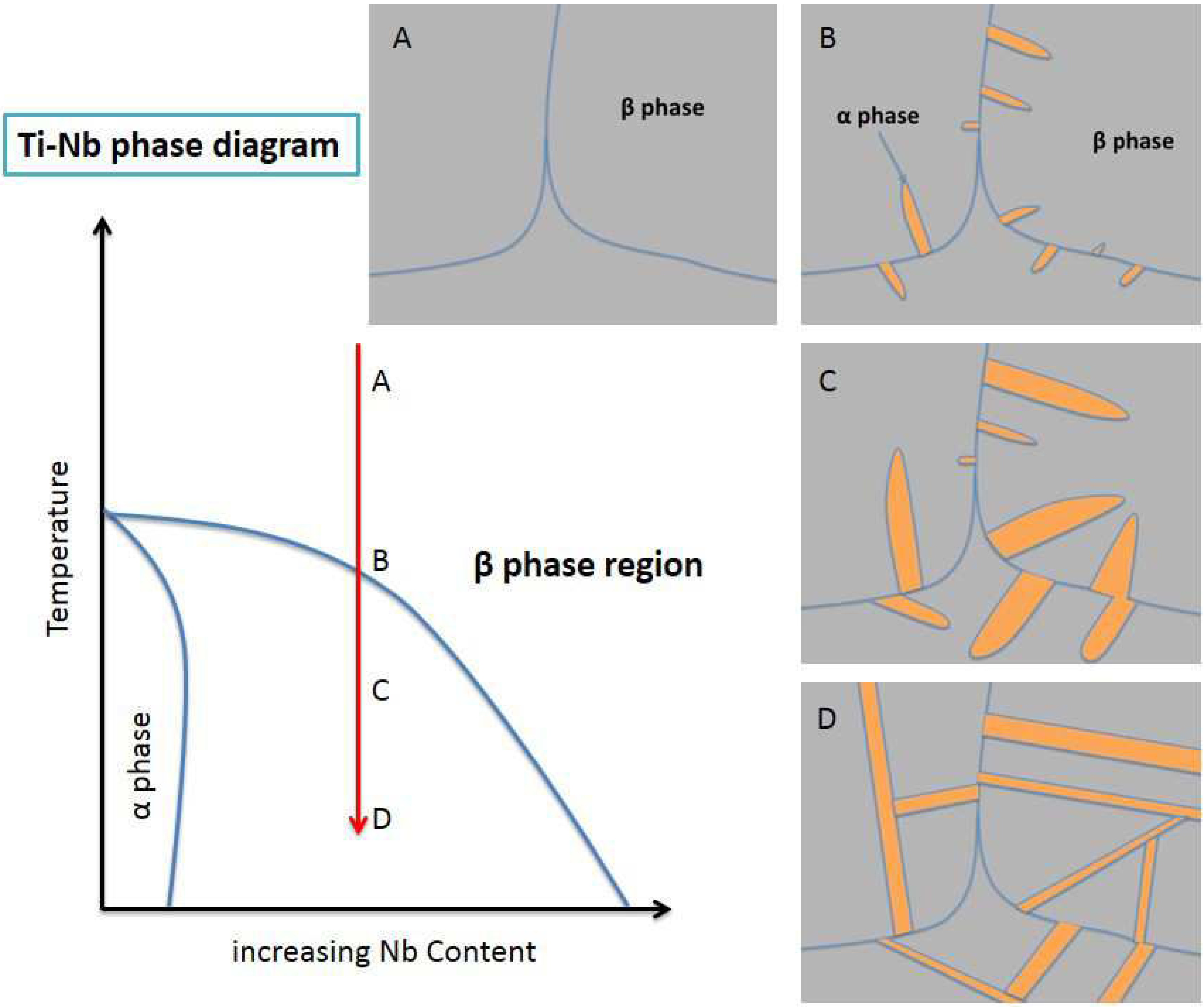

Fig. 3.12 Schematic representation of formation of Widmanstätten pattern in furnace cooled $Ti_{92}Nb_8$ alloy. Microstructures at various temperatures during slow cooling from β phase region, α phase highlighted in orange and β phase in grey. [68]

Optical micrographs of $Ti_{74}Nb_{26}$ alloys in as-cast state are shown in Fig. 3.13. With increasing Nb content, the as-cast microstructures of TiNb based alloys change from cellular and columnar dendrites to equiaxed dendrites. The equiaxed dendrites are of β phase according to the conventional XRD patterns shown previously.

As can be seen in Fig. 3.13 (a), β phase dendrites of random orientations distribute all over the cross section of as-cast sample. There is no obvious columnar zone, different from the case of $Ti_{92}Nb_8$ shown in Fig. 3.7 and $Ti_{73}Nb_{25}Sn_2$ alloy which will be shown later in Fig. 3.19 (a). In addition, there exists a region (marked A in Fig. 3.13 a) near the surface where equiaxed grains with martensite can be observed. The martensite can be better seen at higher magnification, Fig. 3.13 (b). The martensite nucleates at the grain boundaries of β phase grains and grows inwards. The presence of α'' martensite is confirmed by XRD patterns obtained via synchrotron beam, Fig. 3.24 (c).

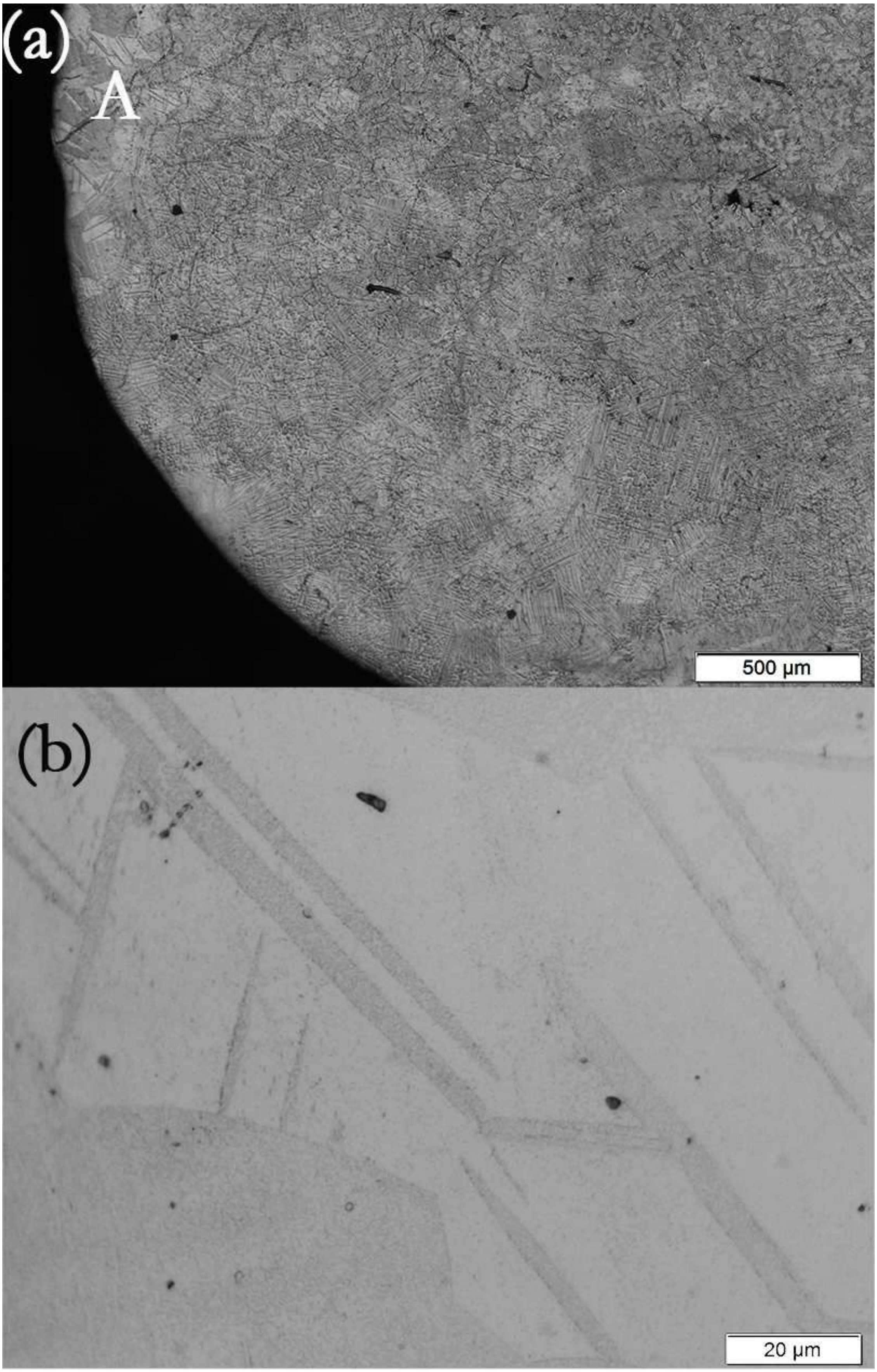

Fig. 3.13 Optical micrographs of cross section of as-cast Ti$_{74}$Nb$_{26}$ *alloy (a), equiaxed β grains with martensite platelets are observed near the surface (b).*

Solidification of alloys is often discussed on the basis of constitutional supercooling, which results from composition change during solidification. On cooling below liquidus temperature (Tl), the newly formed solid is richer in solute atoms (Nb, in this case) than the liquid. Consequently, the liquid just in front of solid/liquid (S/L) interface would be solute-poor. The solute concentration level gradually increases in the surrounding liquid diffusion layer. This leads to the corresponding profile of equilibrium liquidus temperature at various solute concentration levels, as shown in Fig. 3.14. If the actual temperature gradient of the liquid just in front of S/L interface (the red line shown in Fig. 3.14) is below the critical gradient, then there exists the constitutional supercooling. The solid will then grow into liquid.

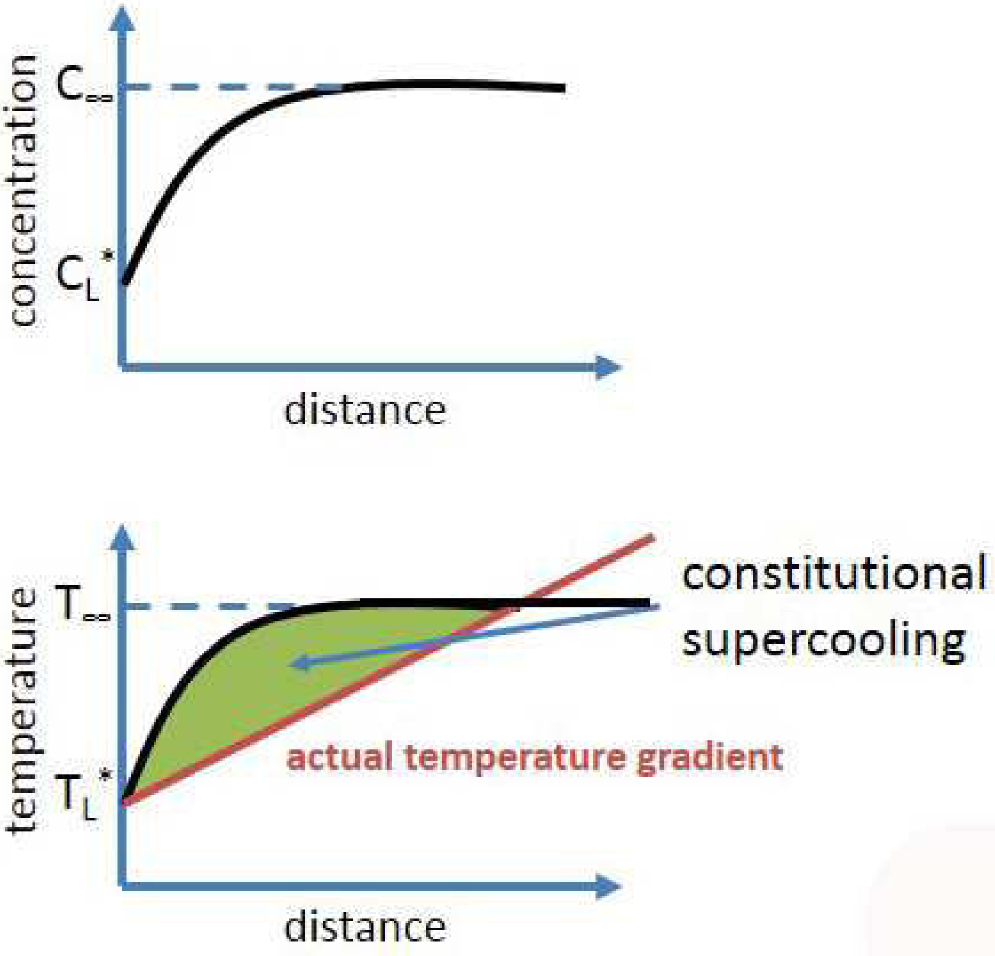

Fig. 3.14 Schematic presentation of constitutional supercooling in TiNb binary alloys. Solute concentration at S/L interface, C_L** and in the liquid far away from the interface,* C_∞*. The corresponding equilibrium liquidus temperature at S/L interface,* T_L** and far away from interface,* T_∞*. [68]*

Depending on the actual liquid temperature gradient (G) and growth velocity (R), the solidification modes can change from planar to cellular, then from columnar dendritic to equiaxed dendritic. Fig. 3.15 shows that the variation of solidification modes on increasing constitutional supercooling.

When cellular S/L interface is advancing, the surfaces of cells can also be unstable, depending on the level of local constitutional supercooling. Then secondary or even tertiary arms may form, leading to cellular to columnar dendritic transition.

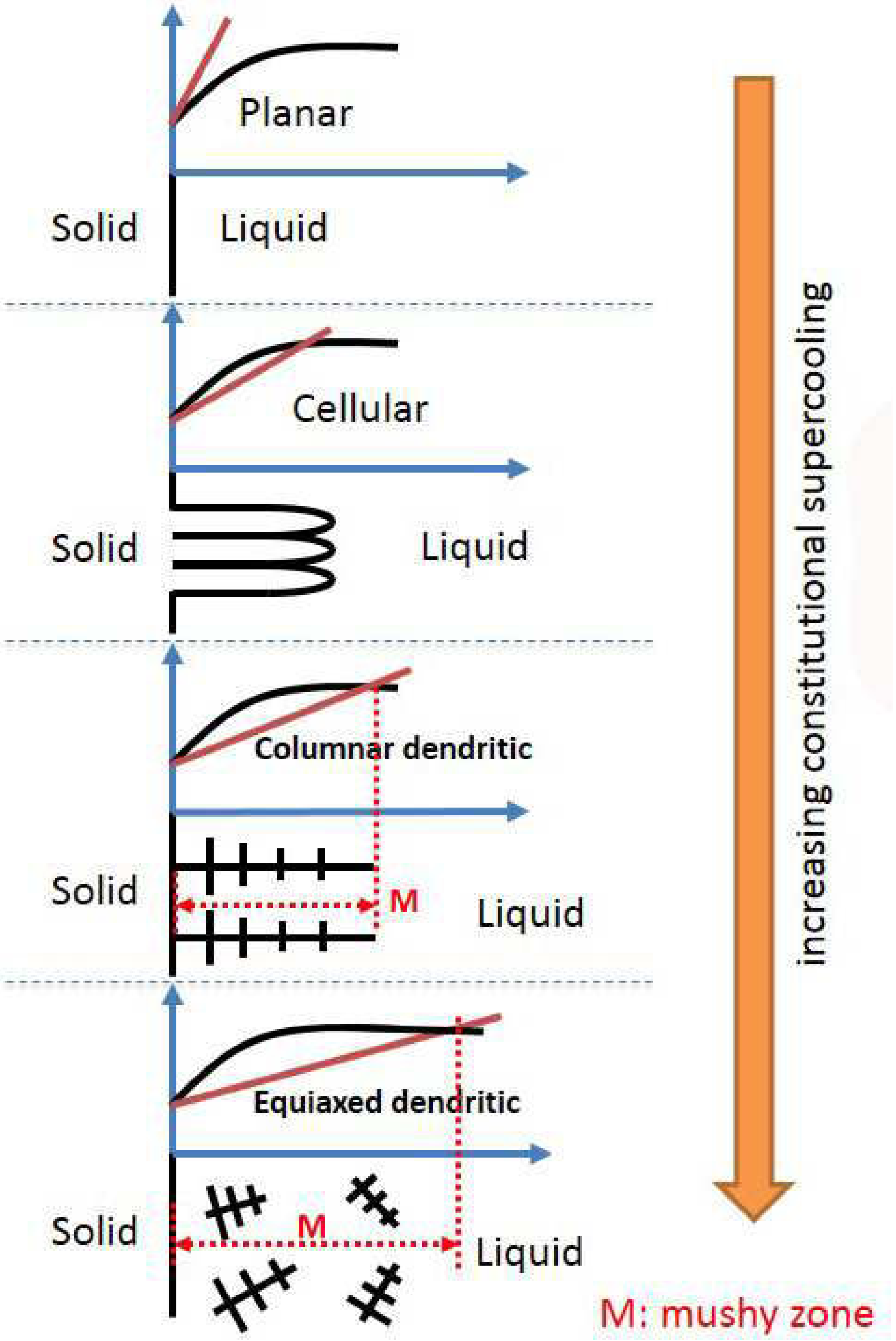

Fig. 3.15 With increasing constitutional supercooling, the solidification mode changes from planar to cellular, then from columnar dendritic to equiaxed dendritic.

In dendritic solidification mode, the region between the tip of growing dendrites and the last drop of solidifying liquid is called mushy zone. The length of this zone is directly correlated with equilibrium freezing range, (T_L-T_S) at given composition [68]. If this mushy zone is very long, it is then difficult for columnar dendrites to stretch all the way through mushy zone. This could lead to a transition from columnar to equiaxed dendritic solidification. In addition, in the case of TiNb binary system, when dendritic arms grow, more solute (Nb) to the tip, leaving less solute at the root of dendritic arms. According to the above TiNb binary phase diagram, less solute indicates lower melting temperature. Consequently, the root will turn to be more easily melted, as shown in Fig. 3.16. This melting leads to the detachment of dendritic arms from their main trunk. And if the detached arms can survive, they will act as nucleation spots and can grow larger on further solidification. The above scenario can happen when the difference between melting temperature and casting temperature are close.

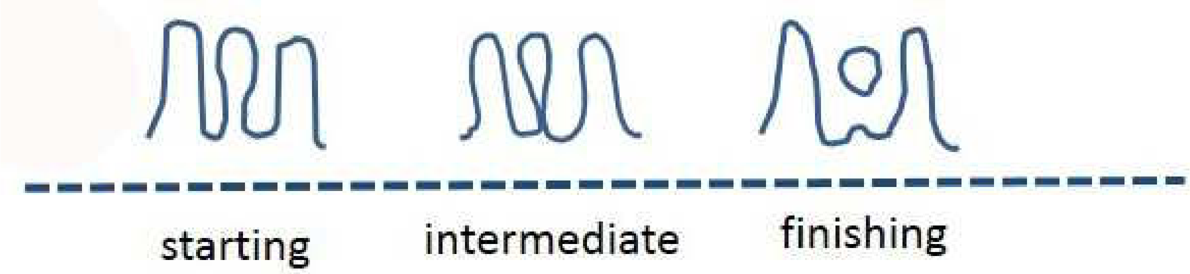

Fig. 3.16 Detachment of dendritic arm

The condition for stable planar Solid/Liquid interface is:

$$\frac{G}{R} > \frac{T_{\text{Liquidus}} - T_{\text{Solidus}}}{D_L}$$

Equation 3.1 [68]

Where G is the temperature gradient in the liquid and R is growth velocity, T_L and T_S is equilibrium liquidus and solidus temperature, respectively. T_L-T_S at a given composition is the freezing temperature range and D_L is the diffusion coefficient of solute in the liquid.

Assuming a temperature gradient in the liquid as well as growth velocity and diffusion coefficient do not change dramatically, and only considering the difference between T_L-T_S between $Ti_{92}Nb_8$ and $Ti_{74}Nb_{26}$ alloys, the resulting constitutional supercooling in the above binary alloys could be that shown in Fig. 3.17. Then it could be concluded that the constitutional supercooling of $Ti_{92}Nb_8$ is smaller than that of $Ti_{74}Nb_{26}$. According to the solidification modes shown in Fig. 3.15, it is appropriate to expect that $Ti_{92}Nb_8$ alloy exhibits cellular and/or columnar dendritic growth, whereas $Ti_{74}Nb_{26}$ alloy possesses equiaxed dendritic growth.

In addition, since $Ti_{92}Nb_8$ alloy exhibits smaller freezing range, compared to $Ti_{74}Nb_{26}$ alloy, the mushy zone of $Ti_{92}Nb_8$ is also narrow. This indicates that on continuous cooling, the liquid region will gradually narrow until the last drop of liquid solidifies. Then there will be a central cavity left due to shrinkage of liquid on solidification, as shown in Fig. 3.7. On the other hand, for $Ti_{74}Nb_{26}$ alloy, whose freezing range is large, the mushy zone is also large. Liquid can flow to compensate the solidification shrinkage. However, if the flowing channel of liquid between dendrites is closed on solidification, the liquid will be locked there and leave a small cavity on complete solidification. Therefore, it can be seen at the top right region of Fig. 3.13 (a) that many small cavities are left on complete solidification.

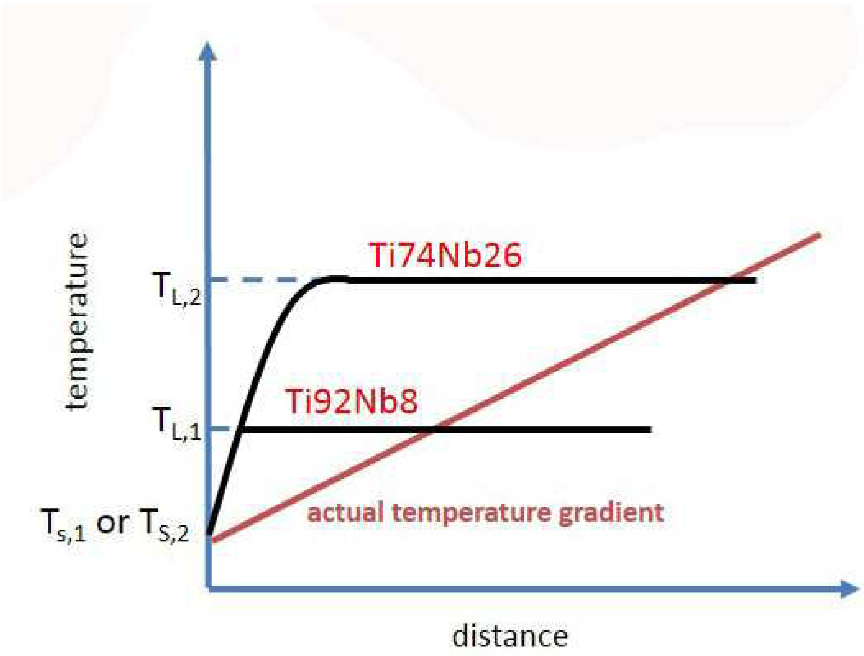

Fig. 3.17 A possible scenario of constitutional supercooling in $Ti_{92}Nb_8$ and $Ti_{74}Nb_{26}$ alloys.

On annealing at β phase region for long time, the dendritic arms have enough time to grow and merge to combine as equiaxed grains, as shown in Fig. 3.18. On water quenching, the oxygen content in water increases M_s temperature above room temperature, which in turn leads to many α'' martensite nucleating at the grain boundaries of β phase.

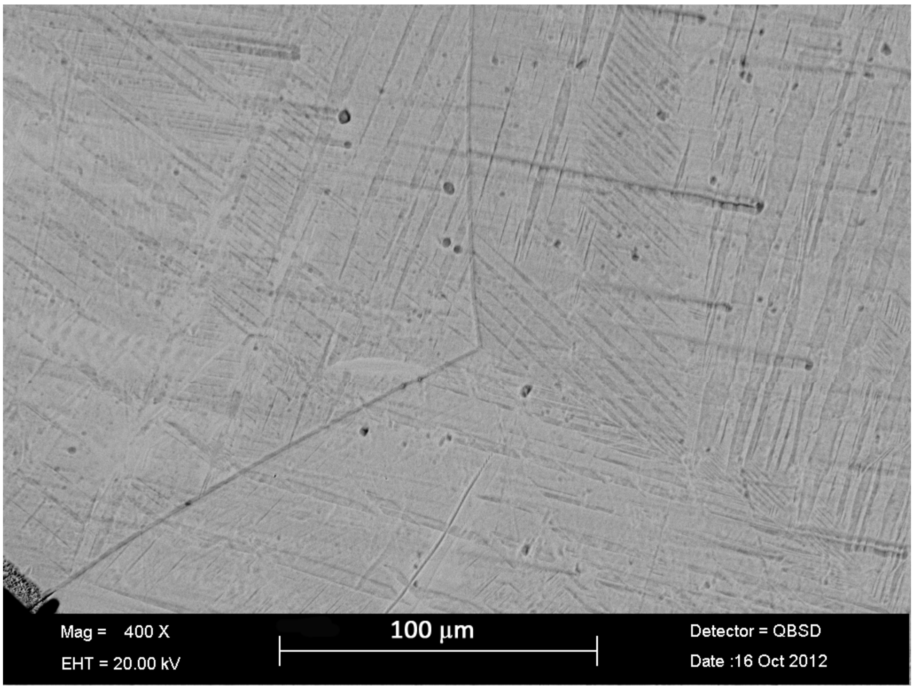

Fig. 3.18 Back scattered electron image of cross section of water quenched $Ti_{74}Nb_{26}$ alloy. Equiaxed dendrites have transformed to large grains. On water quenching, oxygen content stored in the water increases the M_s temperature, leading to many martensites nucleating at the grain boundaries of β phase.

26 at.% Nb content is enough to retain most of the β phase at room temperature in both copper mould casting and water quenching. However, some β phase still transforms to α'' martensite on cooling. In terms of modifying alloy compositions, two methods can be employed to further

stabilize the β phase. One is to increase Nb content. However, as shown in Fig. 1.8, more Nb content beyond 26 at.% will increase the Young's modulus, which is contradictory to the current research goal. The other method is to introduce the third element to further stabilizes β phase. As shown in Ti-Sn binary phase diagram [147, 160], small amount of Sn (up to 6 at.%) can stabilize β phase. Moreover, as stated in chapter 1, Sn addition can suppress the formation of ω phase whose Young's modulus is highest among the four metastable phases of Ti [56]. Finally, the Young's modulus of Sn is only 50 GPa, much lower than that of Ti, 116 GPa. Based on the above thoughts, 2 at.% Sn was introduced to the $Ti_{74}Nb_{26}$ master alloy, giving a new composition of $Ti_{73}Nb_{25}Sn_2$.

The microstructure of the cross section of as-cast $Ti_{73}Nb_{25}Sn_2$ rod is shown in Fig. 3.19. It can be seen that there is chill zone layer near the surface of thickness around 200 µm. This corresponds to the planar solidification mode. With increasing constitutional supercooling from surface to the sample center, the solidification mode changes accordingly from cellular to columnar dendritic and finally to equiaxed dendritic mode at the center.

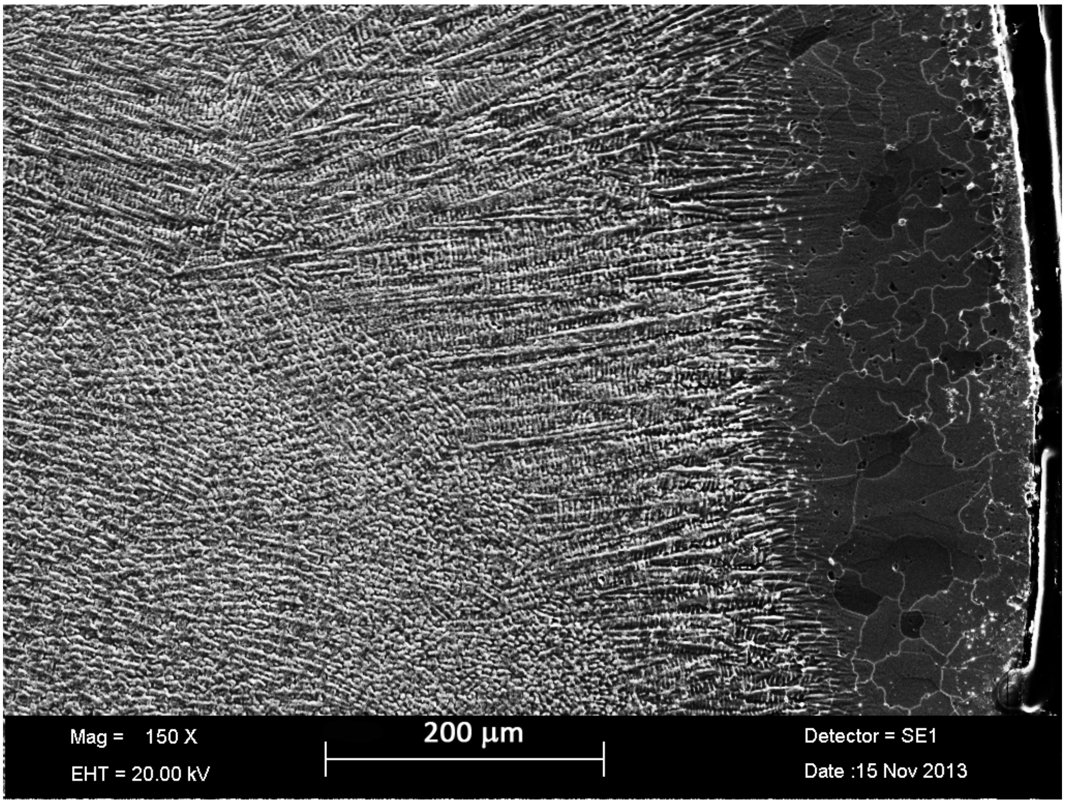

Fig. 3.19 Secondary electron image of transverse cross section micrograph of as-cast $Ti_{73}Nb_{25}Sn_2$ alloys.

On quenching into copper mould, the liquid in contact with the cold mould is rapidly cooled below liquidus temperature, leading to many nuclei forming on the mould wall. According to the binary TiNb phase diagram, as shown in Fig. 3.1, these nuclei would be high temperature β phase due to the high cooling rate of copper mould casting. In addition, at this stage, the S/L interface is planar.

On further cooling, the planar S/L interface becomes unstable and breaks into many cells. The solidification mode then changes to cellular mode. Then with increasing constitutional supercooling, the cellular mode changes to columnar dendritic mode. Finally, the already formed columnar dendrites grow into the melt and the liquid ahead of S/L interface is continuously supercooled. When supercooling is enough to overcome the nucleation barrier of remaining melt, nucleation will then occur in the remaining melt. When the growing columnar dendrites meet the newly formed nuclei, they will be blocked and can only coarsen on following cooling. This process is called columnar to equiaxed transition [161-166]. The solidification mode then changes from columnar dendrites to equiaxed dendrites.

In the surface layer of $Ti_{92}Nb_8$ and $Ti_{74}Nb_{26}$ alloys, the equiaxed grains partially transform to α'' martensites, due to low stability of high temperature β phase. In the case of $Ti_{73}Nb_{25}Sn_2$ alloy, due to addition of Sn, the β phase is more stable and is retained to room temperature without any transformation to α'' martensite.

Synchrotron X-ray diffraction patterns of all three TiNb based alloys in as-cast state are shown in Fig. 3.20. The sample for this synchrotron experiment is cylinder with 4 mm in diameter and 4 mm in height. The size of synchrotron beam was chosen at $5 \times 10\ \mu m^2$ in cross section. For the chosen monochromatized bean energy (100 keV), the penetration depth for TiNb based alloy is of the order of centimeter, as shown in Table 3.1. So the synchrotron beam can penetrate the entire thickness of the sample. The information in the diffraction patterns comes from all the irradiated volume of the material.

For $Ti_{92}Nb_8$ alloy, continuous ring patterns were observed near the sample surface. As shown previously (Fig. 3.7 and Fig. 3.9), there exist many parallel cells and/or columnar dendrites in this region. The average width of cells and dendritic arms is around 3 μm. So within the $5 \times 10\ \mu m^2$ beam, in the thickness of 4 mm sample, there are roughly around 4000 cells and dendrites. Although this is a rough estimation, the amount of dendrites is large enough to produce ring diffraction pattern, as shown in Fig. 3.20 (a). In the center of $Ti_{92}Nb_8$ alloy, the dendrites coarsen due to low cooling rate. But they has not merged to form large equiaxed grains, as shown in Fig. 3.7. Therefore, the structure produces discontinuous rings with numerous spots, Fig. 3.20 (b).

For $Ti_{74}Nb_{26}$ alloy, large near equiaxed dendrites are distributed all over the sample. This leads to no obvious difference between the synchrotron diffraction patterns obtained from near surface and at the center, Fig. 3.20 (c) and (d). Oversaturated spots in diffraction patterns indicate very large dendrites comparing to the beam size.

For $Ti_{73}Nb_{25}Sn_2$, similar to $Ti_{92}Nb_8$ alloy, long narrow cells and columnar dendrites near surface produce continuous ring patterns, Fig. 3.20 (e), while at the center, the large equiaxed dendrites result in discontinuous spotty pattern with many oversaturated spots, Fig. 3.20 (f).

In addition, according to Fig. 3.20, it can be found that the alloys investigated possess different textures. The analysis of textures for these three alloys will be conducted later via the intensity (I) - 2θ diffraction patterns obtained by integration of these images.

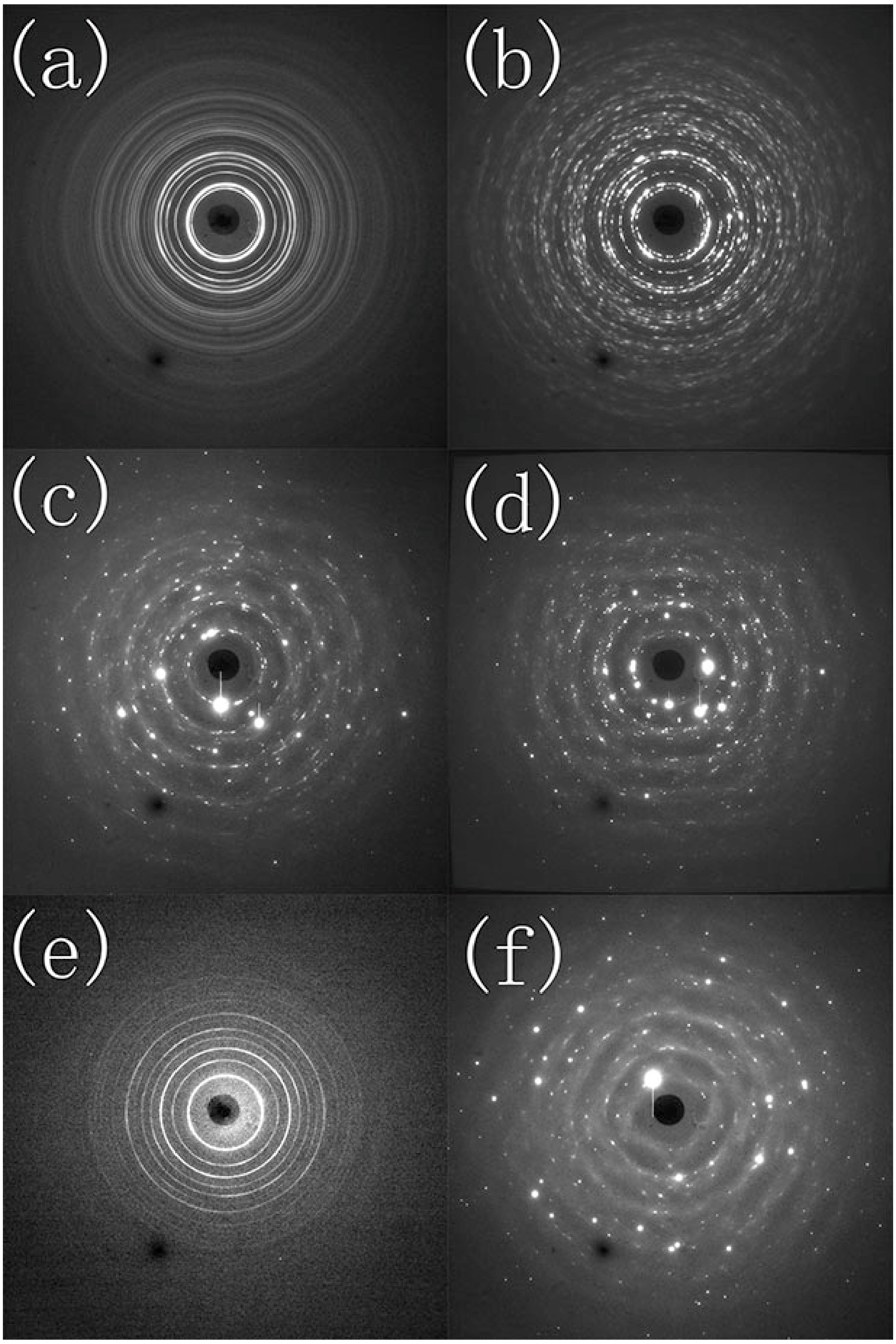

Fig. 3.20 The diffraction patterns obtained by synchrotron beam of TiNb based alloys in as-cast state. $Ti_{92}Nb_8$ alloy, near sample surface (a) and in the center (b). $Ti_{74}Nb_{26}$ alloy, near sample surface (c) and in the center (d). $Ti_{73}Nb_{25}Sn_2$ alloy, near sample surface (e) and in the center (f).

Table 3.1 penetration depth of X-ray in TiNb based alloys.

alloy composition	penetration depth (I/I_0=0.5) conventional X-ray (Cu kα, 40 kV)	penetration depth (I/I_0=0.5) synchrotron radiation (100 keV)
$Ti_{92}Nb_8$	7.2 µm	2.11 cm
$Ti_{74}Nb_{26}$	6.6 µm	1.07 cm
$Ti_{73}Nb_{25}Sn_2$	6.5 µm	0.98 cm

The microstructures of furnace cooled and water quenched $Ti_{73}Nb_{25}Sn_2$ alloys are shown in Fig. 3.21 (a) and (b). Only equiaxed β grains are observed in both cases. In the case of furnace cooled sample, only large grains of over 200 µm are observed, Fig. 3.21(a). The Sn addition stabilizes β phase even though the cooling rate in this case is very low. For the water quenched sample, although XRD patterns indicate some β phase transforming to α'' martensite, no martensite traces were observed by optical microscopy.

Different from the cases of $Ti_{92}Nb_8$ and $Ti_{74}Nb_{26}$, the surface layer of the as-cast $Ti_{73}Nb_{25}Sn_2$ alloy does not show any evidence of β-to-α'' transformation. For heat treated samples, β phase was also retained at room temperature without transformation to another phase in both furnace cooling and water quenching. From this point of view, it can be concluded that β phase is stabilized by the addition of Sn in TiNb alloys.

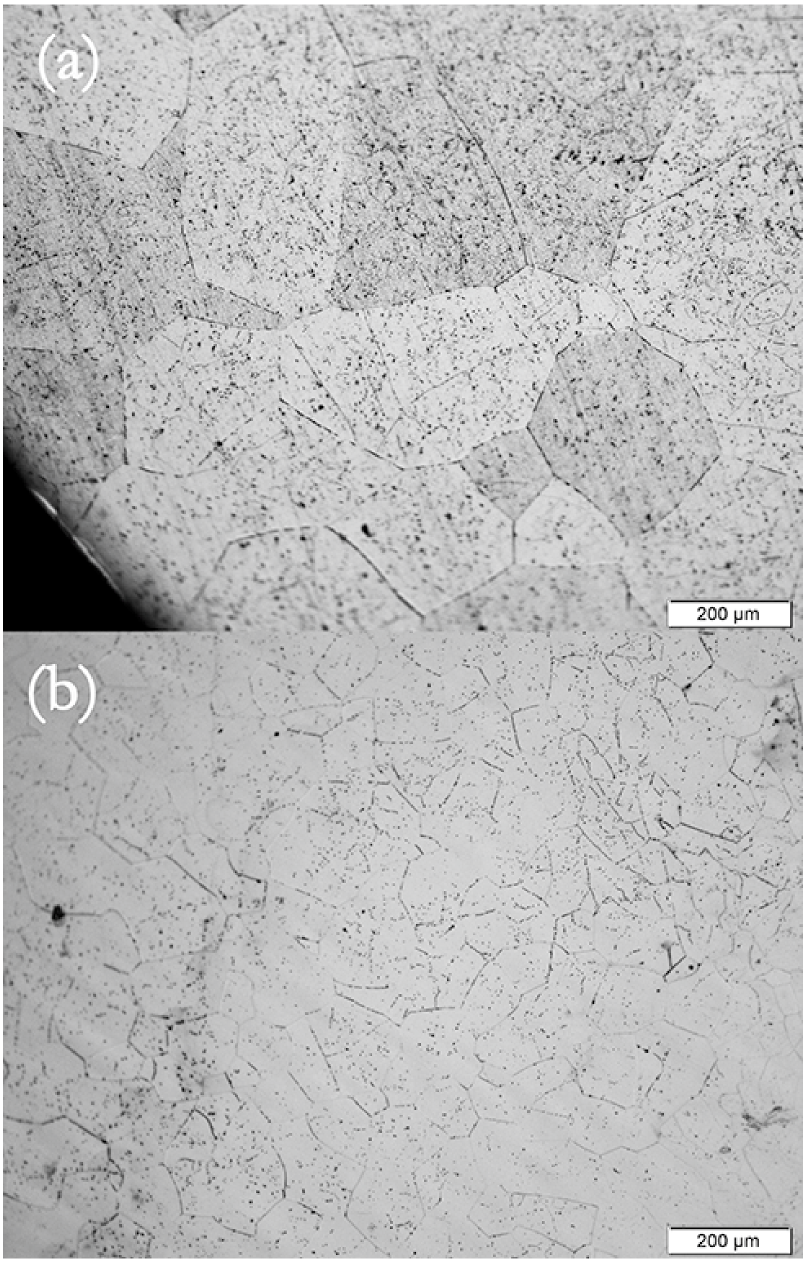

Fig. 3.21 Optical micrographs of furnace cooled (a) and water quenched (b) $Ti_{73}Nb_{25}Sn_2$ alloys.

3.2.3 Thermal properties

A DSC curve of the as-cast sample of $Ti_{92}Nb_8$ alloy is shown in Fig. 3.22 (a). There exist transformations during heating and following cooling. This transformation corresponds to α''/β transition and the characteristic temperatures are as follows: martensite start temperature (M_s) 710°C, martensite finish temperature (M_f) 570°C, austenite start temperature (A_s) 645°C and austenite finish temperature (A_f) 830°C. The M_s is slightly higher than that estimated according to Moffat's Ti-Nb metastable phase diagram [40]. There also exists a peak after α''/β transition during heating, and it disappears during the subsequent reheating. The reason for this phenomenon is still under investigation. Enthalpy of the transformation during heating and cooling is 2.36 kJ/mol and 1.23 kJ/mol, respectively. These values are between those of transformation in pure Ti (4.20 kJ/mol, [167]) and in $Ti_{74}Nb_{26}$ binary alloy (0.34 kJ/mol, [53]). This is in agreement with widening of β region with increasing Nb content in Ti-Nb binary phase diagram [147]. Since M_s of $Ti_{74}Nb_{26}$ is around 0°C [53], the main phase in the as-cast sample is single β phase. Therefore, no signal of transformation upon heating and cooling of single β phase is observed in DSC curves as shown in Fig. 3.22 (b).

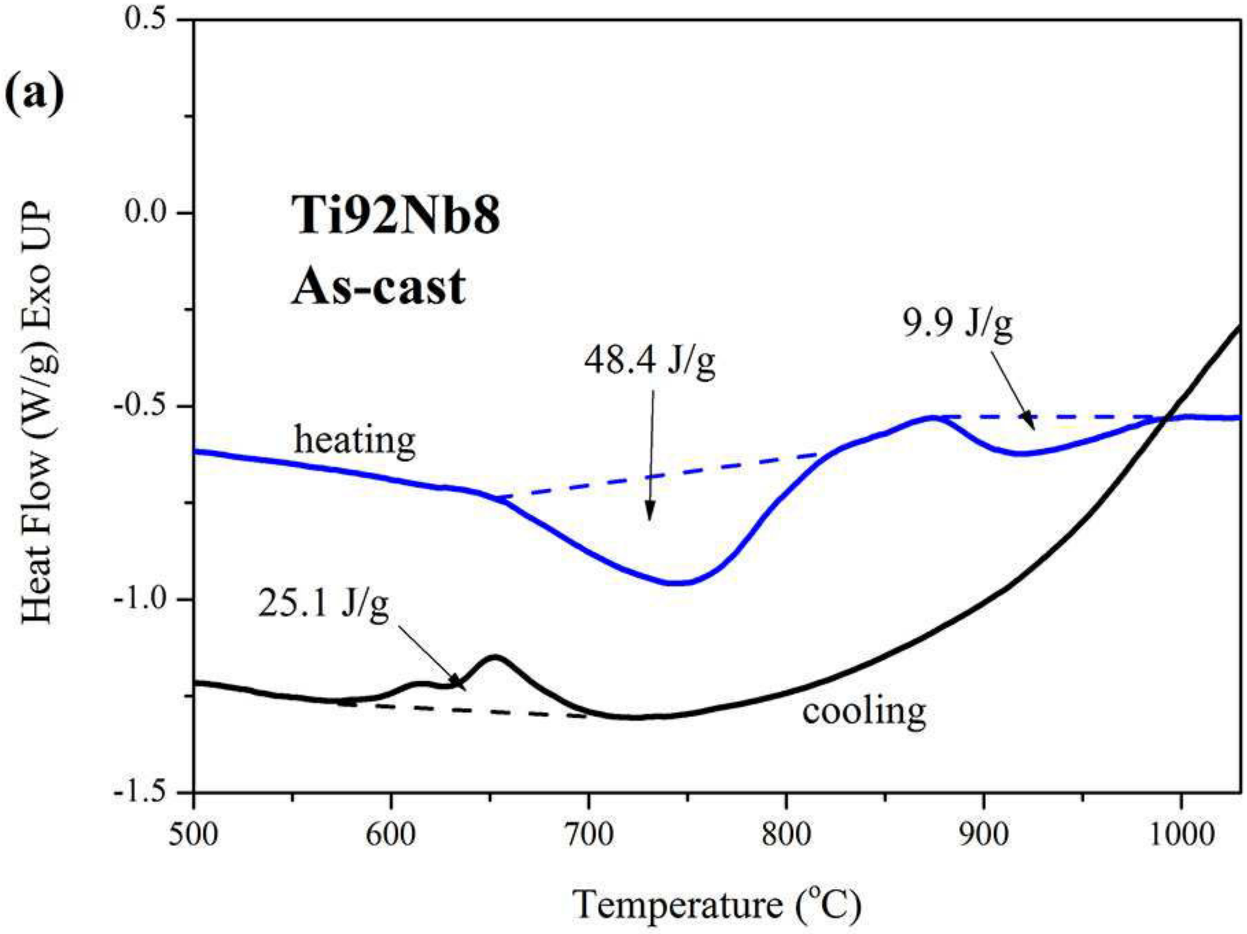

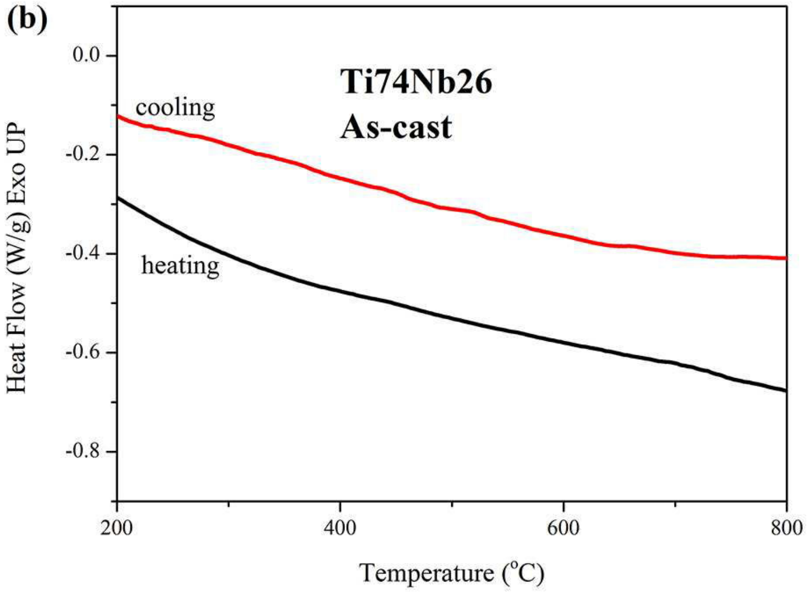

Fig. 3.22 DSC curves of as-cast $Ti_{92}Nb_8$ (a) and $Ti_{74}Nb_{26}$ (b) alloys

3.2.4 Mechanical Properties

The compressive behavior of all the samples in three different states (as-cast, heat treated followed either by furnace cooling or water quenching) were investigated.

It is shown in Fig. 3.23(a) that the $Ti_{92}Nb_8$ samples in all three states exhibit non-linear behavior during loading-unloading cycles. Moreover, the residual strain was recovered to some extent when the sample was heated above the M_s temperature. The shape memory effect was observed for $Ti_{92}Nb_8$ samples and it results from the reorientation of existing martensites. However, due to the slower cooling rate, the non-linear elastic behavior is much less obvious in furnace cooled samples than in samples which were subjected to higher cooling rate. This results from the precipitation of equilibrium α phase rather than transformation of martensitic α'' in the furnace cooled sample, and precipitation of equilibrium α leads to the decrease of the shape memory effect. This is confirmed by results of synchrotron experiment, Fig. 3.23 (b). The microstructure of the furnace cooled sample contains mainly of equilibrium α with small quantities of β and α'' phases. It can also be seen that, for the as-cast and water quenched samples, there is little difference in the stress-strain curves, indicating that the martensites obtained by suction casting and ice water quenching are similar. Comparing the XRD patterns of as-cast samples obtained in reflection mode and transmission mode, more Bragg peaks are observed in transmission mode, especially at high angles. This results from the fact that the high energy beam can penetrate the specimen. It can also be seen that XRD patterns in both reflection and transmission mode of ingot and as-cast samples show textures of strong preferential orientations, (002)α and (101)α in ingot, while (002)α'' and (111)α'' in as-cast samples. However, for heat treated samples, Fig. 3.23 (b), textures with other orientations grew to larger extent, indicated by the increase of intensities of Bragg peaks. Therefore, it can be concluded that due to the high cooling rate and short time of nucleation and growth in arc-melted ingots and as-cast alloys, only textures of orientations that can grow rapidly in along the thermal gradient dominate, whereas in heat treated alloys, textures of other orientations also have opportunity to grow larger. Furthermore, it can be seen in Fig. 3.23(b) that very small quantities of β phase were retained in heat treated samples. When alloys were annealed in the β temperature region for long time, β phase was stabilized and grew into larger grain size. Moreover, Nb is a strong β stabilizing element and 8.34 at.% of Nb is quantitively enough to suppress the decomposition of β phase to some extent during cooling.

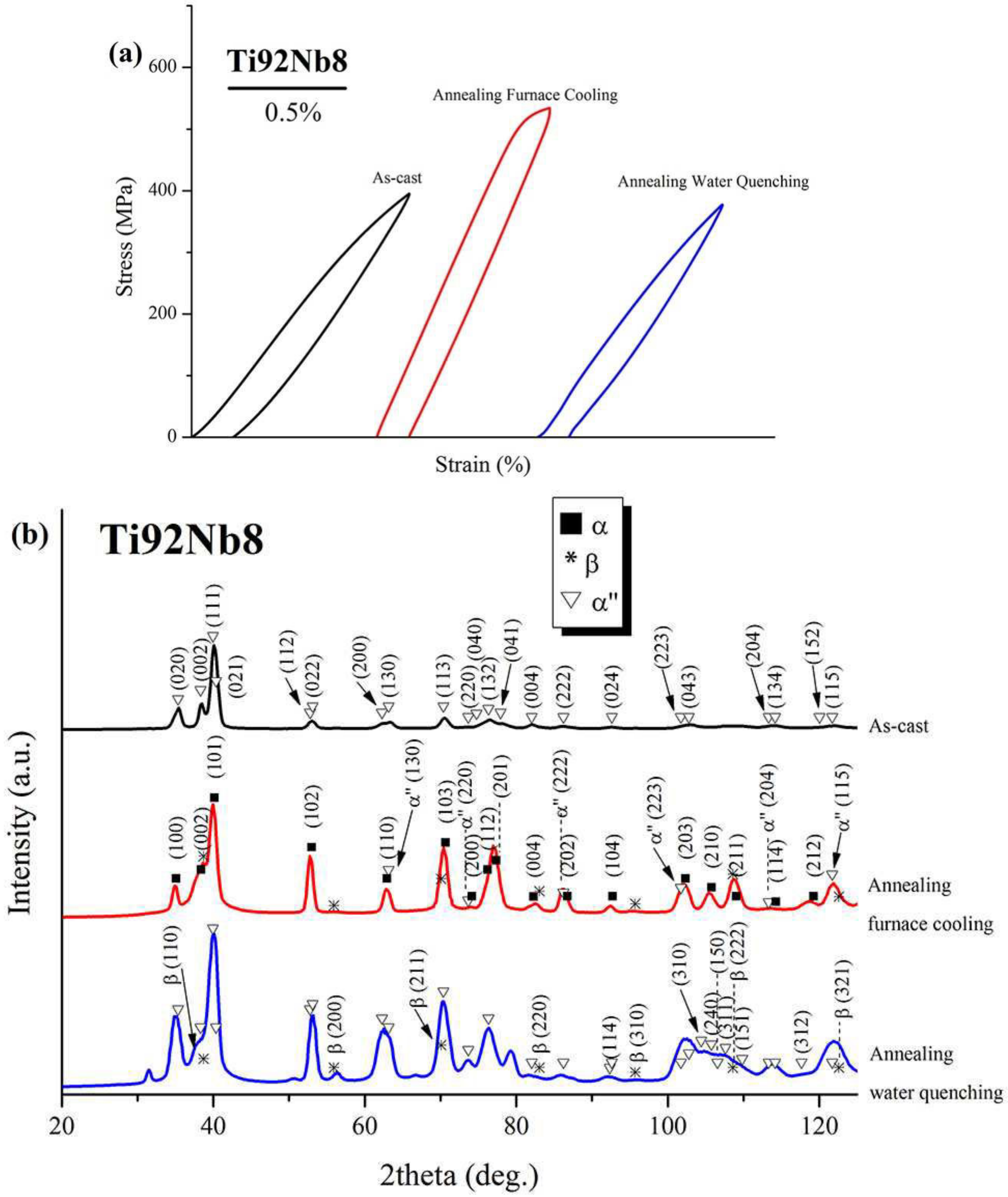

Fig. 3.23 Compressive stress-strain curves of $Ti_{92}Nb_8$ alloys in three different states, i.e. as-cast, heat treatment followed either by furnace cooling or water quenching (a). Transmission X-ray diffraction patterns obtained by synchrotron radiation of these samples after compression. The direction of transmission beam is perpendicular to the axis of cylindrical compression sample. (b). The patterns have been converted from wave vector Q (nm^{-1}) scale to conventional Cu Kα diffraction angle scale 2ϑ (^{o}) using $\sin(\vartheta_{CuK\alpha})$ =

$Q_{synch}\times\lambda_{CuK\alpha}/4\pi$.

Fig. 3.24(a) shows that the non-linear elastic behavior is much stronger for the $Ti_{74}Nb_{26}$ alloy compared to the $Ti_{92}Nb_8$ alloy. This superelasticity originates from the stress-induced martensitic transformation. The M_s of $Ti_{74}Nb_{26}$ is around 0°C [53], and previous XRD patterns show that β phase is the only phase in the samples at ambient temperature. However, with the aid of stress during loading, this high temperature β phase can transform into martensitic α'' phase; while during unloading, the martensitic α'' phase becomes unstable and mostly transforms back to the β phase. The structure of the samples after compression was revealed by diffraction in transmission. The occurrence of retained martensitic α'' phase is visible in Fig. 3.24(c).

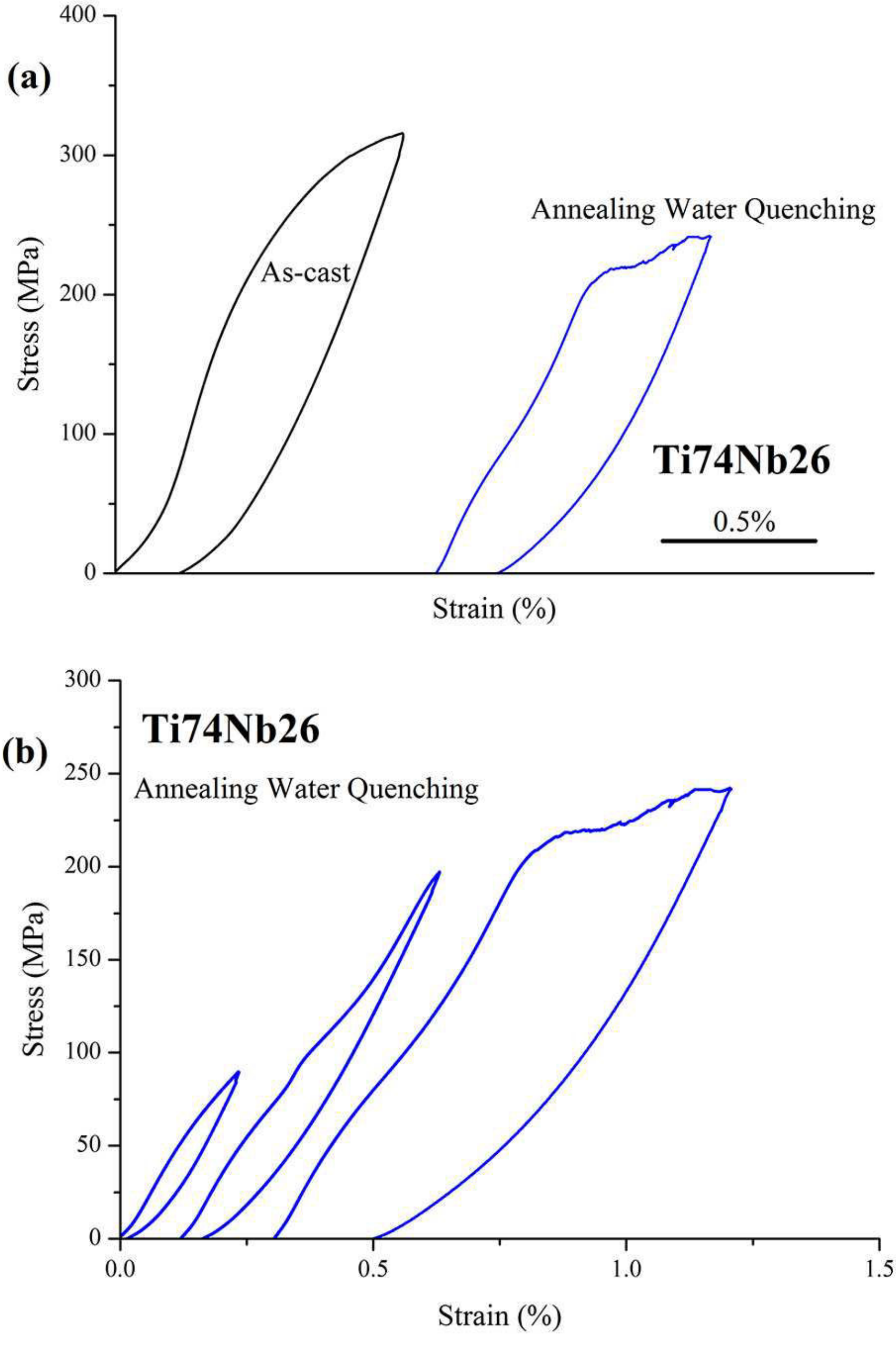

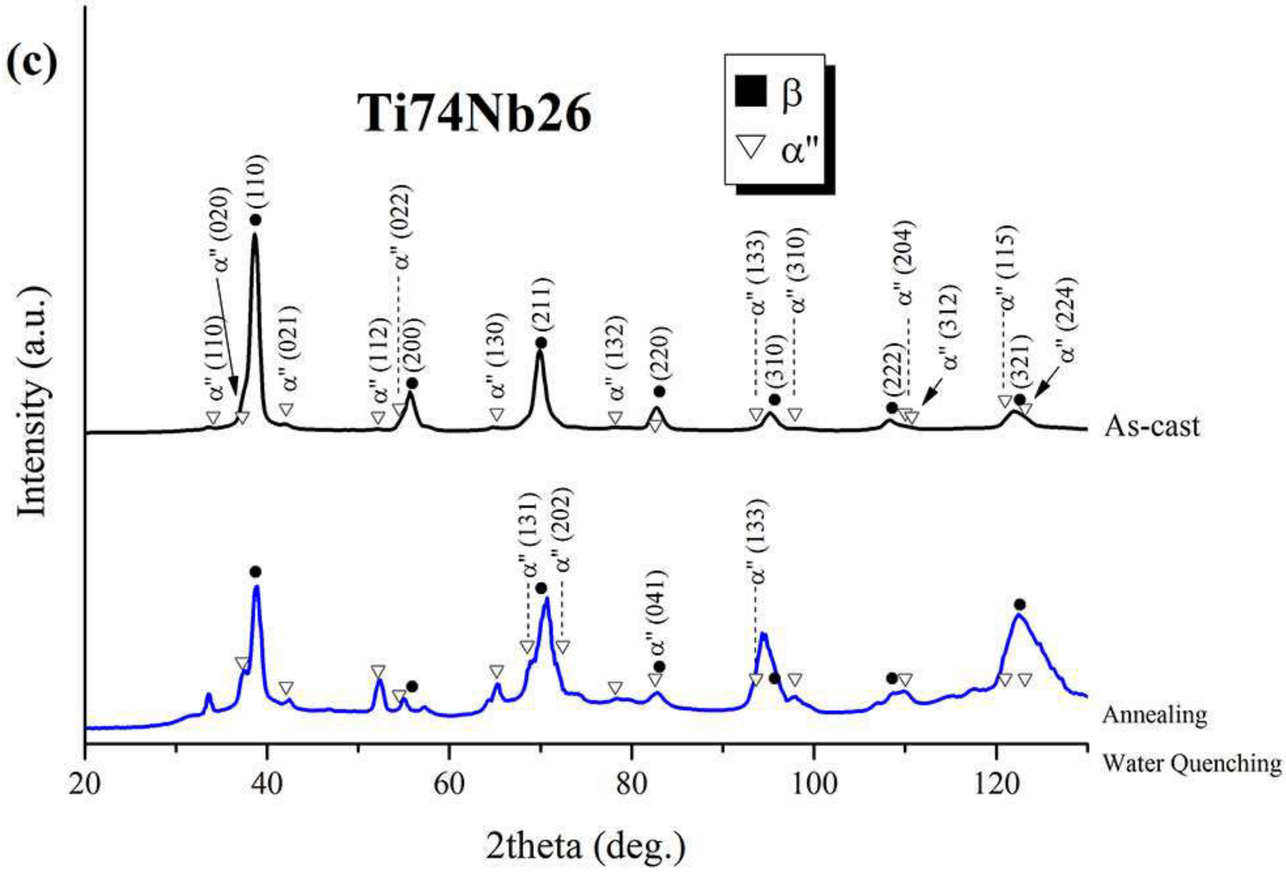

Fig. 3.24 Compressive stress-strain curves of $Ti_{74}Nb_{26}$ alloys in as-cast and water quenched states (a). Compressive stress-strain curves obtained by cyclic loading-unloading for the water quenched sample (curves are shifted to have better view) (b). Transmission X-ray diffraction patterns obtained by synchrotron radiation of as-cast and water quenched samples after compression. The direction of transmission beam is perpendicular to the axis of cylindrical compression sample. (c). The patterns have been converted from wave vector Q (nm^{-1}) scale to conventional Cu Kα diffraction angle scale 2ϑ (^{o}) using $\sin(\vartheta_{CuK\alpha}) = Q_{synch} \times \lambda_{CuK\alpha}/4\pi$.

Fig. 3.24(b) shows the cyclic loading-unloading stress-strain curve of water quenched sample. It indicates that with increasing strain, the superelastic behavior becomes incomplete. This is due to the onset of permanent plastic deformation of TiNb alloy. In the $Ti_{74}Nb_{26}$ alloy, there exist two competitive deformation mechanisms, stress-induced martensitic transformation and permanent plastic deformation. The deformation with lower critical stress commences first and diminishes the extent of the other deformation. However, the low critical stress of plastic deformation of TiNb alloys impedes the occurrence of superelasticity. Therefore any methods that increases the critical stress for permanent plastic deformation will enhance the stability of superelasticity. It has been established that introduction of high densities of dislocations by cold rolling or high densities of dispersed particles by heat treatment can indeed improve the stability of superelasticity [53, 78, 168].

As can be seen in both Fig. 3.4(b) and Fig. 3.24(c), similar to those of $Ti_{92}Nb_8$, the as-melted and as-cast samples of $Ti_{74}Nb_{26}$ also show strong preferential orientations. Texture of (110)β is favoured in the conditions of high cooling rate and short growth time. XRD patterns obtained in transmission mode show that (211)β also grows preferentially. While for heat treated sample, textures of other orientations of β phase, such as (310)β and (321)β also grew to large extent. It can also be found in Fig. 3.24(c) that the intensities of Bragg peaks of α'' phase in as-cast sample are lower than those in water quenched sample, indicating varying fractions of martensitic α'' phase. Due to the high cooling rate of copper mould casting, β phase is retained at room temperature with little of it transforming to martensitic α'' phase. Nevertheless, the lower cooling rate in the case of water quenching leads to transformation of β phase to α'' martensite, despite the fact that more of the equilibrium β phase is obtained by long time annealing.

Different from the non-linear behavior of stress-strain curve of the two binary alloys, the $Ti_{73}Nb_{25}Sn_2$ ternary alloys exhibit rather “normal” behavior. There is no hysteresis in the loading and unloading curves or superelasticity, as better seen in the inset of Fig. 3.25(a). It can also be seen in the Fig. 3.25(a) that there is little difference among these three curves of as-cast and annealed samples, except that the yield stress of as-cast sample is slightly higher than those of the other two samples. Fig. 3.25(b) shows transmission X-ray diffraction patterns of the compressed samples. It is seen that the β phase is the main phase although very small quantity of α'' phase is also observed. However, the intensities of α'' phase of $Ti_{73}Nb_{25}Sn_2$ alloys in as-cast and water quenched states are much lower than those of binary $Ti_{74}Nb_{26}$ alloys. From this point of view, it can be concluded that addition of Sn stabilizes the retained β phase, which indicates that M_s temperature of $Ti_{73}Nb_{25}Sn_2$ alloys is further decreased, lower than that of $Ti_{74}Nb_{26}$. Similar to the situation in $Ti_{74}Nb_{26}$ alloys, preferred texture of (110)β is observed for $Ti_{73}Nb_{25}Sn_2$ ternary alloys in as-melted and as-cast, as well as water quenched states. (211)β texture also grew preferentially inside the sample. However, there are differences between textures of $Ti_{74}Nb_{26}$ and this $Ti_{73}Nb_{25}Sn_2$ ternary alloy in their as-cast states. In $Ti_{73}Nb_{25}Sn_2$ as-cast alloy, the preferred texture highlights the (310)β and (321)β reflections although (110)β and (211)β textures are also strong. However, the annealed then furnace-cooled sample highlights mostly the (211)β reflection. This might again be explained by difference in cooling rates. The cooling rate inside the sample is lower than near surface. This higher cooling rate leads to preferential (110)β texture near surface, as clearly observed in XRD patterns obtained in conventional reflection mode. By contrast, slower cooling rate inside the sample favors the (211)β reflection of β phase as in the XRD patterns acquired in transmission. Finally, the slow cooling rate in furnace cooling generates more pronounced (211)β Bragg intensity as seen in Fig. 3.25(b).

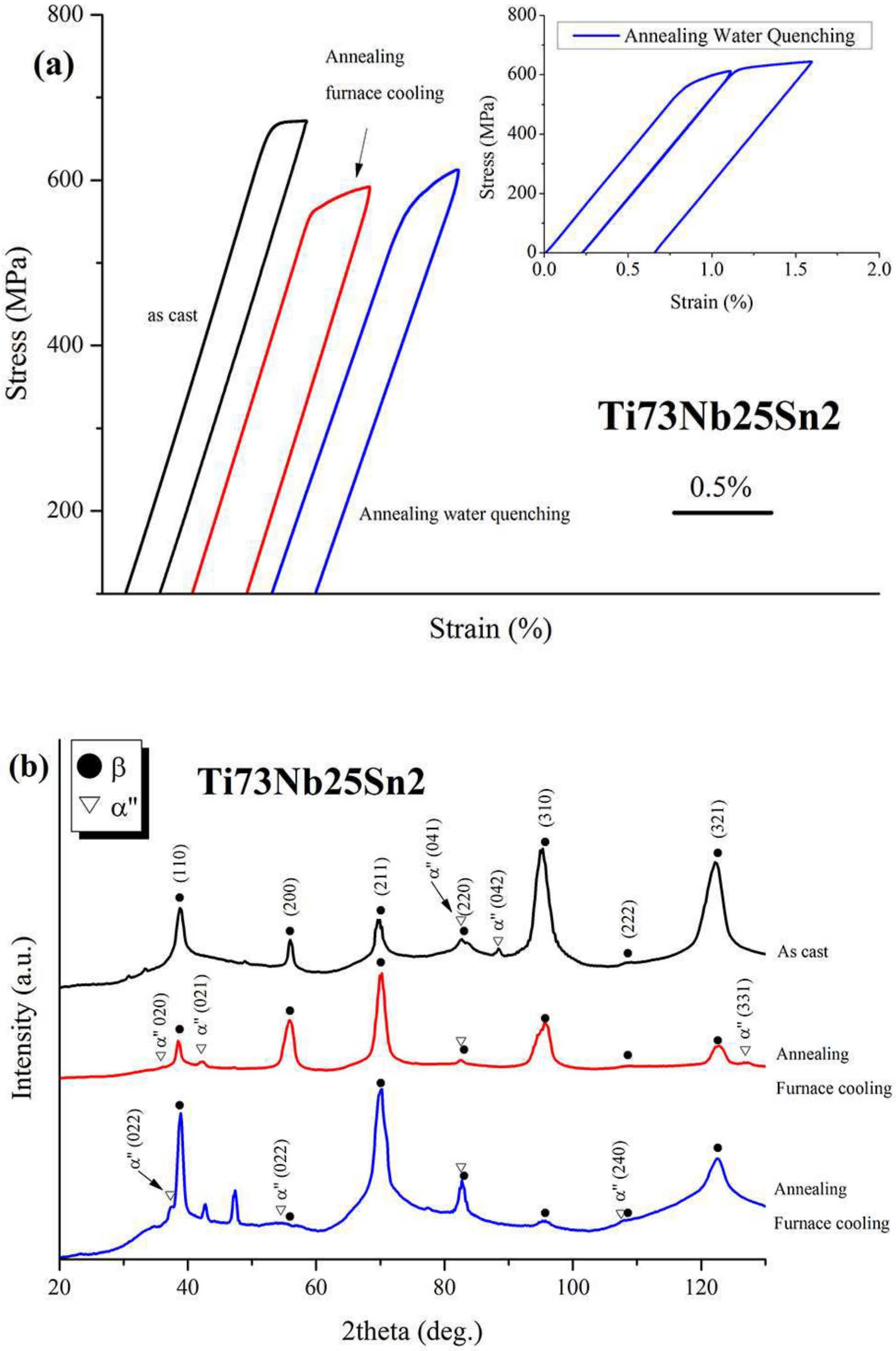

Fig. 3.25 Compressive stress-strain curves of $Ti_{73}Nb_{25}Sn_2$ alloys in three different states (a). Compressive stress-strain curves obtained by cyclic loading-unloading for the water quenched sample ((a) inset). Transmission X-ray diffraction patterns obtained by synchrotron radiation of these samples after compression (b). The patterns have been converted from wave vector Q (nm^{-1}) scale to conventional Cu Kα diffraction angle scale 2ϑ (°) using $\sin(\vartheta_{CuK\alpha}) = Q_{synch} \times \lambda_{CuK\alpha}/4\pi$.

Due to the existence of superelasticity, it is of little physical meaning to calculate the Young's modulus (E) from the stress-strain curves. Ultrasonic measurements were therefore conducted to measure E as reported in Table 3.2. Since there is no superelasticity in the $Ti_{73}Nb_{25}Sn_2$ ternary alloys, their values calculated through stress-strain curves are also listed in Table 3.2 for comparison. It can be seen that the furnace cooled $Ti_{92}Nb_8$ possesses the highest E, resulting from the precipitation of equilibrium α phase. Moreover, the close values of Young's moduli of as-cast and water quenched $Ti_{92}Nb_8$ alloys confirm the similar nature of these two martensites. Comparing the Young's moduli of the ternary alloys and those of the binaries, it is found that addition of Sn has little influence on Young's modulus. For alloys with higher Nb content, the samples subjected to water quenching exhibit the lowest E. Finally, the Young's moduli derived from stress-strain curves and measured by ultrasonic wave show similar values.

*Table 3.2 Young's moduli (E) obtained by ultrasonic measurements for $Ti_{92}Nb_8$, $Ti_{74}Nb_{26}$ and $Ti_{73}Nb_{25}Sn_2$ alloys in three different states (as-cast, heat treatment followed either by furnace cooling or water quenching). Some Young's moduli calculated from stress-strain curves are also listed as comparison (indicated by *).*

E (GPa)	$Ti_{92}Nb_8$	$Ti_{74}Nb_{26}$	$Ti_{73}Nb_{25}Sn_2$	
as-cast	71	81	77*	77
furnace cooling	93	77	76*	81
water quenching	72	60	69*	64

3.3 $Ti_{74}Nb_{26}$ alloys with improved superelasticity

In the previous section, it was shown that $Ti_{74}Nb_{26}$ alloy possesses superelasticity, as shown in Fig. 3.24 (a) and (b). However, the superelasticity in both as-cast and water quenched state of $Ti_{74}Nb_{26}$ is not stable, i.e. the cycle of loading - unloading curve is incomplete and there is residual strain after unloading. As stated in Chapter 1, shape memory alloy, like TiNi (Nitinol), can be used as body implant alloys in the field of carotid artery stent, tissue spreader, kidney calculus extractor, deformable spatulas for neurosurgery and so on. So it is of great important to explore shape memory alloys. In the following section, a new thermomechanical treatment was explored to improve the superelasticity of $Ti_{74}Nb_{26}$ alloy.

3.3.1 Experimental procedure

Two competitive deformation mechanisms exist in $Ti_{74}Nb_{26}$ alloy, stress-induced martensitic transformation and permanent plastic deformation. The mechanism with lower critical stress starts first, which in turn decrease the extent of the other deformation mechanism. In both as-cast and water quenched $Ti_{74}Nb_{26}$ alloys, the large equiaxed dendrites and equiaxed grains lead to very low critical stress of plastic deformation. Therefore, the plastic deformation is more favored than stress-induced martensitic transformation and the method to improve the stability of superelasticity is to enhance the critical stress for permanent plastic deformation. It can be enhanced by work hardening, solid solution strengthening, precipitation or particles strengthening and grain boundary strengthening via Hall-Petch effect [169]. In the present work, a processing strategy of work hardening at first followed by precipitate strengthening was designed to increase the yield strength of $Ti_{74}Nb_{26}$ alloy. Work hardening was realized by introduction of high density of dislocations through cold rolling. Precipitation strengthening was achieved by annealing at intermediate temperature.

The alloys were subjected to 94% reduction ratio of cold rolling, as shown in Fig. 3.26. The cold rolled samples were then wrapped by Ti foil and sealed in the quartz tube together with several Ti oxygen getters under 20 kPa Ar atmosphere. The samples were first annealed at 600°C for 10 minutes and then aged at 300°C for 1 hour. Finally the samples were subjected to water quenching by breaking the quartz tube in the water.

Fig. 3.26 $Ti_{74}Nb_{26}$ as-melted ingot and subjected to 94% reduction ratio of cold rolling.

3.3.2 Microstructural characterization

The XRD patterns obtained via conventional Cu kα radiation are shown in Fig. 3.27. It can be seen that BCC β phase is the only phase in the thermomechanically treated $Ti_{74}Nb_{26}$ alloy. Different from that in as-cast state, there exists preferred orientation of (200)β in new $Ti_{74}Nb_{26}$ alloy.

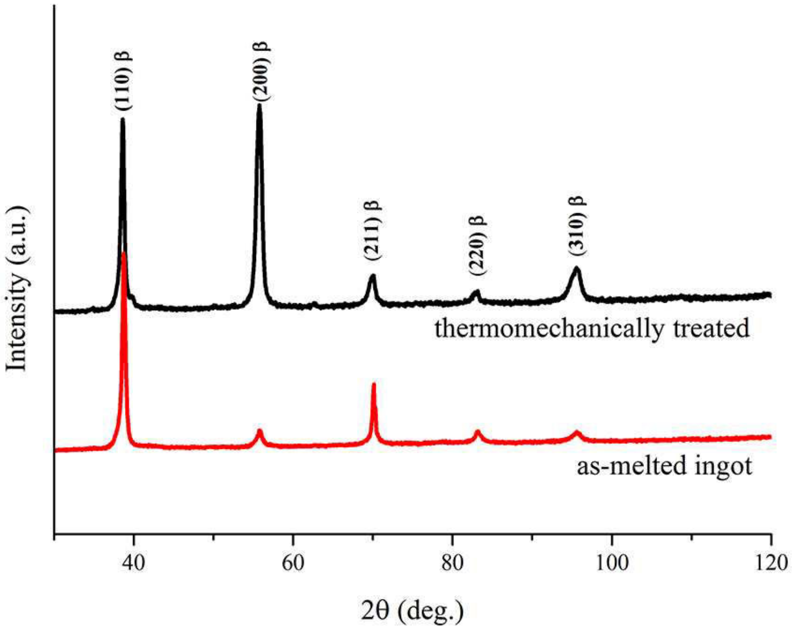

Fig. 3.27 XRD patterns of thermomechanically treated $Ti_{74}Nb_{26}$ alloy

When samples are subjected to cold rolling, depending on the reduction ratio, grains in the specimen tend to align along one or more specific crystallographic orientation(s). This non-random orientation distribution corresponds to texture. The high reduction ratio cold rolling employed for the current $Ti_{74}Nb_{26}$ alloys is supposed to introduce texture. For randomly orientated β-Ti alloys, (110) plane possesses the highest Bragg intensity in XRD pattern. However, it can be seen in Fig. 3.27 that the diffracted intensity of (200) plane is also very high. This indicates that there exists some texture in the thermomechanically treated $Ti_{74}Nb_{26}$ alloys. Pole figure was then used to investigate the alloy texture.

The texture of cold rolling structure is usually defined by the plane (hkl) that lies parallel to the plane of rolled sheet and the direction [uvw] in which the rolling direction lies. It can be seen in the pole figure (Fig. 3.28), that the cold rolled $Ti_{74}Nb_{26}$ alloy surface is (001)β plane and the rolling direction lies in [110]β direction. In (211)β pole, the angle between high intensity {211}β plane (red) and (100)β plane is 35.26^o, and the angle between less intense {211}β plane and (100)β plane is 65.90^o. So the thermomechanically treated $Ti_{74}Nb_{26}$ alloy possesses {001}β<110>β rolling texture, which is the typical rolling texture formed in BCC β-Ti alloys [23, 54, 170]. Fig. 3.28(d) gives the stereographic projection of {001}β<110>β texture.

During deformation, grains deform in such a manner that all deformation is accommodated within the grains without creating voids between them. The deformation is accommodated through dislocation slip and lattice rotation. Quite often, operation of one slip system is cancelled by others. Following Von Mises, five independent slip systems are needed to accommodate plastic deformation [171]. In addition, the principle of least work governs which slip system operates [171]. So the five slip systems requiring lowest work during deformation are favored. The combination of these slip systems finally leads to the preferred texture after cold rolling.

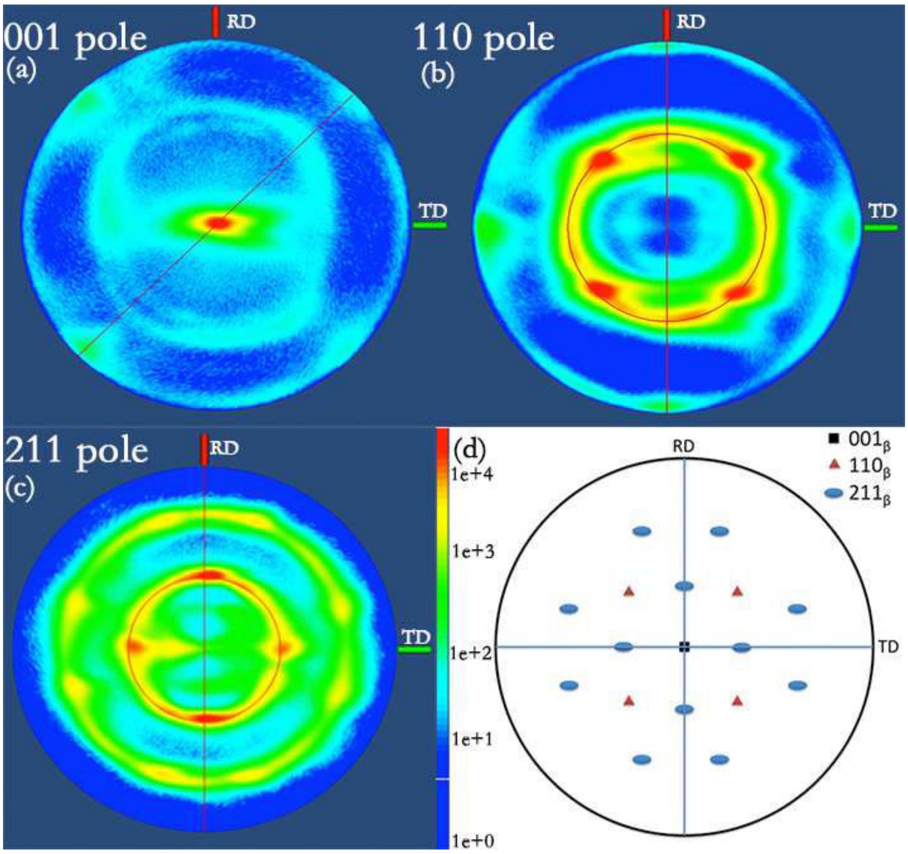

Fig. 3.28 Pole figure of thermomechanically treated Ti$_{74}$Nb$_{26}$ alloy using 001$_\beta$, (a), 110$_\beta$, (b) and 211$_\beta$, (c) poles and stereoprojection of the {001}$_\beta$<110>$_\beta$ type texture, (d).

The microstructure of the thermomechanically treated Ti$_{74}$Nb$_{26}$ alloy is observed through optical microscope and SEM. It can be seen in Fig. 3.29 (b) that initial grains as seen in (a) were elongated along the rolling direction. The regions with high density dislocations and/or grain boundaries are preferentially etched. After heat treatment, grains in Ti$_{74}$Nb$_{26}$ ingot are of different sizes, as shown in Fig. 3.29 (a).

During cold rolling, small grains are subjected to more severe plastic deformation, generating more dislocations. It has been reported that screw dislocations in Ti$_{75}$Nb$_{25}$ alloy tend to split into partial dislocations [172]. It can then be expected that the Ti$_{74}$Nb$_{26}$ alloy should also behave similarly. Therefore, the dislocations generated during severe plastic deformation will propagate in random orientations, until impeded by the initial grain boundaries. Then more and more dislocations accumulate near the grain boundaries. Dislocations of different signs will annihilate each other, while those of same sign will align to form an ordered array to lower the system energy. These ordered arrays of dislocations form the low angle grain boundaries (LAGB) and the part of grain within these LAGBs forms subgrain. On further plastic deformation, more and more dislocations arrive at these LAGBs, leading to overlapping of dislocation cores. Finally, it is impossible to distinguish individual dislocation core. Now the LAGBs change to high angle grain boundaries (HAGBs) and the subgrains change to grains. As can be seen in Fig. 3.29 (c), some initially large grains were only elongated along rolling direction after high reduction ratio cold rolling, and some other grains have broken into very small grains.

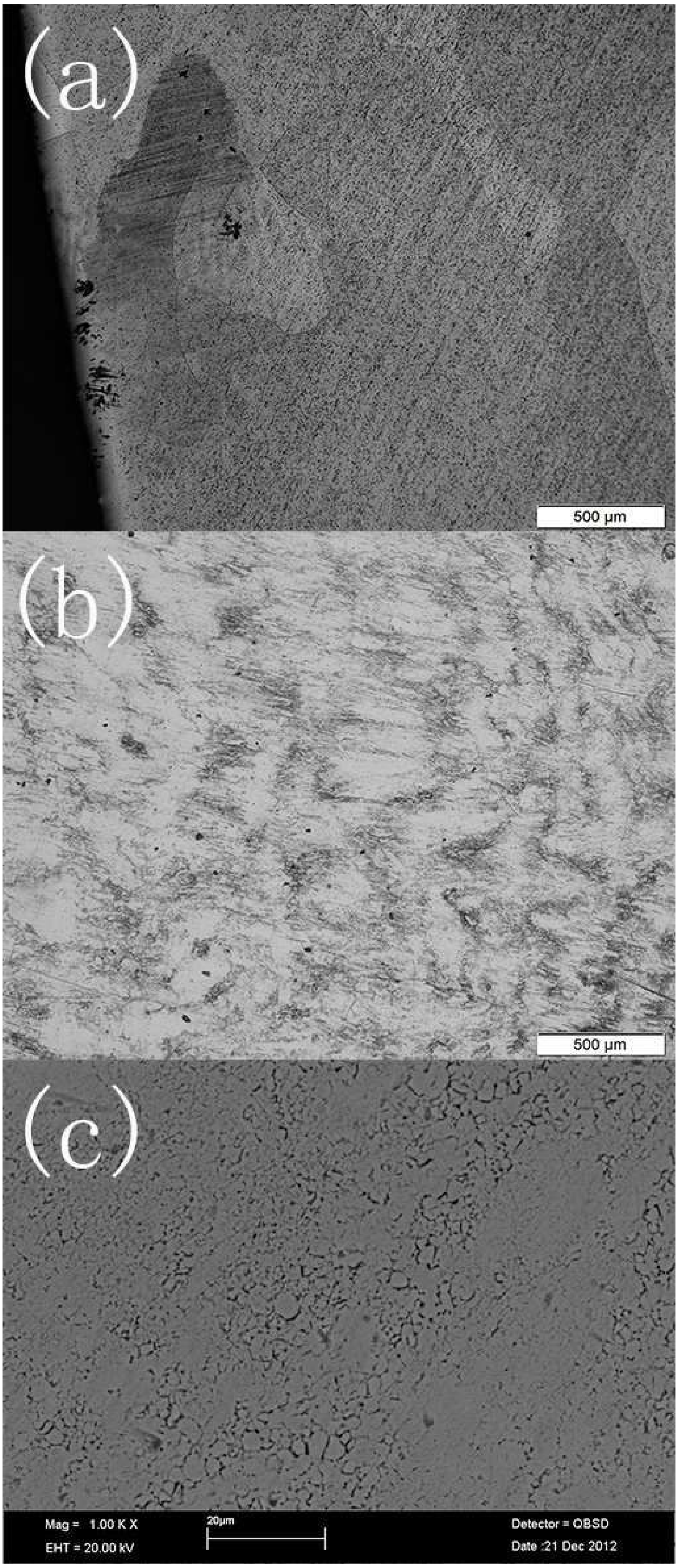

Fig. 3.29 Optical micrograph of $Ti_{74}Nb_{26}$ *ingot after heat treatment (a). Optical micrograph (b) and back scattered electron image (c) of thermomechanically treated* $Ti_{74}Nb_{26}$ *alloy.*

3.3.3 Mechanical properties

Cyclic tensile test was conducted to investigate the mechanical properties of thermomechanically treated $Ti_{74}Nb_{26}$ alloys. Two series of experiments were conducted to investigate superelasticity at different stress levels. As can be seen in Fig. 3.30, during cyclic tension, the superelasticity hysteresis loop is kept intact. No residual strain is left upon unloading even after stresses up to 400 MPa are applied. Comparing to the incomplete loop of water quenched $Ti_{74}Nb_{26}$ alloy, shown in Fig. 3.24 (b), the stability of superelasticity is greatly improved in the thermomechanically treated $Ti_{74}Nb_{26}$ alloys. As stated previously, this results from the enhanced critical stress of permanent plastic deformation. It can be concluded that on introducing high density dislocations and suitable heat treatment, the stability of superelasticity is greatly improved in $Ti_{74}Nb_{26}$ alloys.

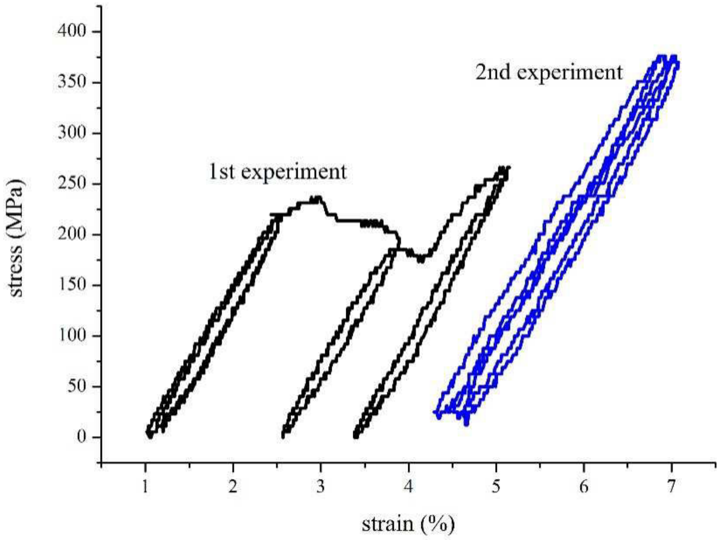

Fig. 3.30 The tensile stress-strain curve of thermomechanically treated $Ti_{74}Nb_{26}$ alloys. The curves are shifted horizontally for better clarity.

In situ tension test in synchrotron beam was then performed to understand the microstructure evolution during stress induced martensitic transformation. As can be seen in Fig. 3.31, before deformation, the ring diffraction pattern contains many elongated arcs where intensity of rings is stronger. Phase identification shows presence of single β phase. The ring pattern results from the small grain size as shown in Fig. 3.29 (c). The elongated arcs are in accordance with the textures developed during material processing. During deformation, the β phase transforms to α'' martensite with the aid of stress. The occurrence of martensites is marked by red arrows in Fig. 3.31. They come from the diffraction intensity of (002) plane of orthorhombic α'' martensite. In addition, the ring of (110)β plane (first ring from inside) also intensifies during deformation. This results from the occurrence of (110)α'' and (020)α'' planes. The ring of (220)β plane (fourth ring from inside) also becomes thicker. This results from the contribution of (220)α'' plane. On unloading, these above intensities of α'' phase disappear, leaving only the initial β phase.

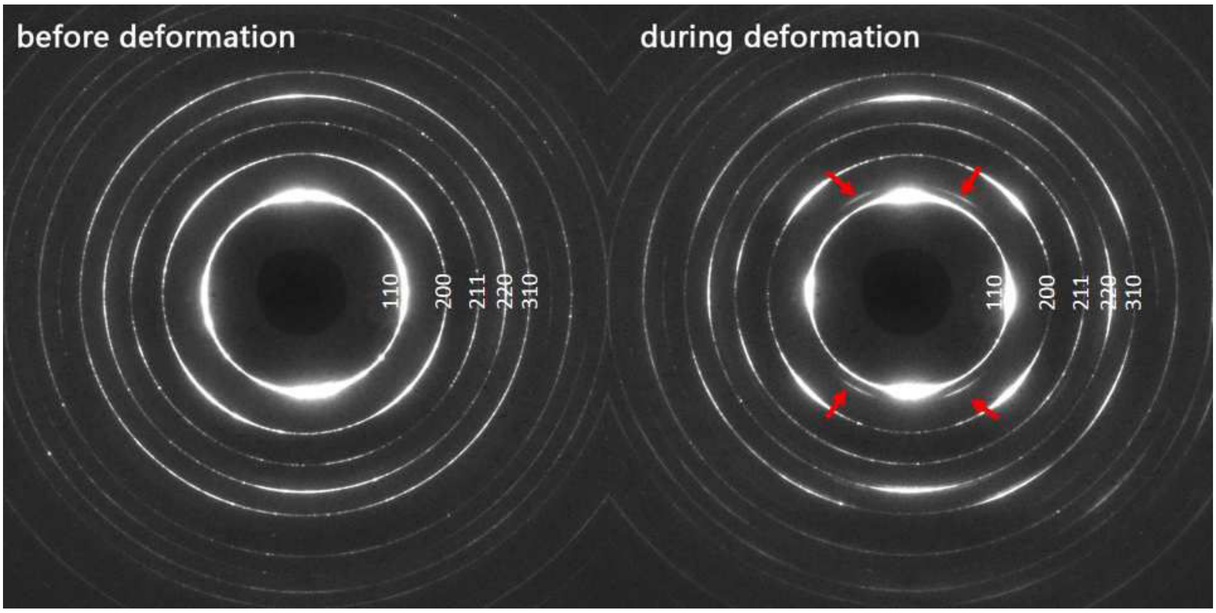

Fig. 3.31 Diffraction patterns of thermomechanically treated $Ti_{74}Nb_{26}$ alloy during in situ tension test in synchrotron beam. The red arrows indicate the occurrence of α'' martensites during tension.

3.4 Conclusions

The microstructure, thermal stability and mechanical properties of three TiNb(Sn) alloys were investigated. It was found that $Ti_{92}Nb_8$ alloys possess martensitic α'' phase in the as-cast and water quenched states and equilibrium α phase in the furnace cooled state. DSC results show an α''/β transition during heating of the as-cast sample and the characteristic temperatures of the martensitic transformation were evaluated. $Ti_{74}Nb_{26}$ and $Ti_{73}Nb_{25}Sn_2$ alloys, however, possess single β phase due to the higher content of β stabilizer element.

The mechanical properties of $Ti_{92}Nb_8$, $Ti_{74}Nb_{26}$ and $Ti_{73}Nb_{25}Sn_2$ alloys in different cooling state (as-cast, heat treatment followed by either furnace cooling or water quenching) were studied by cyclic loading-unloading compression tests. It was shown that for $Ti_{92}Nb_8$ alloys, the as-cast and water quenched samples exhibit shape memory effect. This is due to the reorientation of existing martensites. For $Ti_{74}Nb_{26}$ alloys, stress induced martensitic transformation was observed during compression. The transmission X-ray diffraction results show that the initial β phase transforms into martensitic α'' phase with deformation. Moreover, with increasing compressive strain, superelasticity becomes incomplete. Finally, the ternary $Ti_{73}Nb_{25}Sn_2$ alloy only shows linear elastic behavior prior to plastic deformation. The addition of Sn suppresses the transformation of β to α'', which in turn increases the stability of the β phase. The Young's moduli of alloys after different thermal treatments were determined by ultrasonic measurements. The results indicate that the equilibrium α phase exhibits the highest Young's modulus and Sn addition has little influence on the Young's moduli of the TiNb alloys.

Moreover, enhanced stability of superelasticity in $Ti_{74}Nb_{26}$ alloy was achieved by suitable thermomechanical treatment. The superelasticity hysteresis loop remains intact upon unloading even subjected to 400 MPa stress. The microstructure evolution during stress induced martensitic transformation was investigated by *in situ* synchrotron X-ray diffraction.

Chapter 4 Ti based biocompatible metallic glasses

4.1 Introduction

Metallic glasses (MGs) have attracted a lot of scientific and technological attention, due to their enhanced properties compared to their crystalline counterparts, including high mechanical strength [97, 99], large elastic limit [99, 173], high corrosion resistance [31] and wear resistance [82, 97]. Some are very promising candidates for implant alloys. Metallic glasses have about 0.5-2.0% lower density and they have no crystalline lattice or long-range order. They show about 6% lower bulk modulus, about 10% less Young modulus and about 30% less shear modulus than that of their crystalline counterparts [99]. From this point of view, they are good candidates for developing implant alloys of low Young's modulus.

So far, best glass forming ability has been found in Zr-, Fe-, Pd-, Mg-, Cu-, and Ni-based alloys. However, the high Young's moduli of Zr-, Fe-, Cu-based metallic glasses limits their potential applications as implant alloys. In addition, almost all of the above metallic glasses contain elements, such as Cu, Ni, V, Al, which can release toxic ions in human body environment. On the other hand, Ti possesses excellent biocompatibility and Ti based metallic glasses have relatively low Young's modulus compared to the above MGs. Therefore, Ti based MGs without toxic elements are good candidates for body implant alloys.

4.2 Composition design of Ti based metallic glasses

At present, Ti based alloys with good glass forming ability contain Ni and/or Cu. As can be seen in Table 1.8, there are mainly two families of Ti based MGs, Ti-Cu-Ni based and Ti-Cu based. By introducing minor elemental additions such as Be, Zr, Co, to the near eutectic compositions in Ti-Cu-Ni system, good glass formers in Ti-Cu-Ni based system were obtained. For Ni free Ti based MGs, the most successful one is Ti-Zr-Cu-Pd-Sn quinary system, whose critical thickness is 10 mm. However, both Ni and Cu can release metallic ions and cause toxic or hypersensitivity reactions and induce carcinogenesis [28, 29]. Therefore, Ni and Cu must be excluded in the newly designed MGs. This indicates the current Ti based MGs alloys cannot be used as a base for designing new biocompatible MGs.

Several criteria for developing MGs with high glass forming ability; including the near deep eutectic composition criterion [87], reduced glass transition temperature [94], large supercooled liquid region [97, 174], γ criterion [96] and Inoue's three empirical rules [97] have been suggested over the last 60 years. Among them, the deep eutectic criterion came up the most early and has been proven to be a very successful criterion of developing MGs.

Based on the binary phase diagrams and elements' biocompatibility, deep eutectic systems like Ti-Fe and Ti-Si can be considered as good starting systems for synthesizing new Ti based MGs. Louzguine et al. [175] investigated the glass formation of Ti-Fe binary system and found that no MGs can be synthesized in this system. The large solubility of Fe (up to 22 at.% at 1085^{o}C) in β-Ti, as shown in Fig.4.1, might be the reason why it is difficult to obtain MGs in Ti-Fe binary system. On the other hand, Polk [110] and Inoue [116] studied the Ti-Si binary system and found that Ti$_{85}$Si$_{15}$ and Ti$_{80}$Si$_{20}$ can be vitrified. Both of the compositions lie on the hyper eutectic side of the binary Ti-Si system. In addition, intermetallic Ti$_5$Si$_3$ phase of narrow composition range forms on the steeper (or the hyper-eutectic) side of the eutectic point.

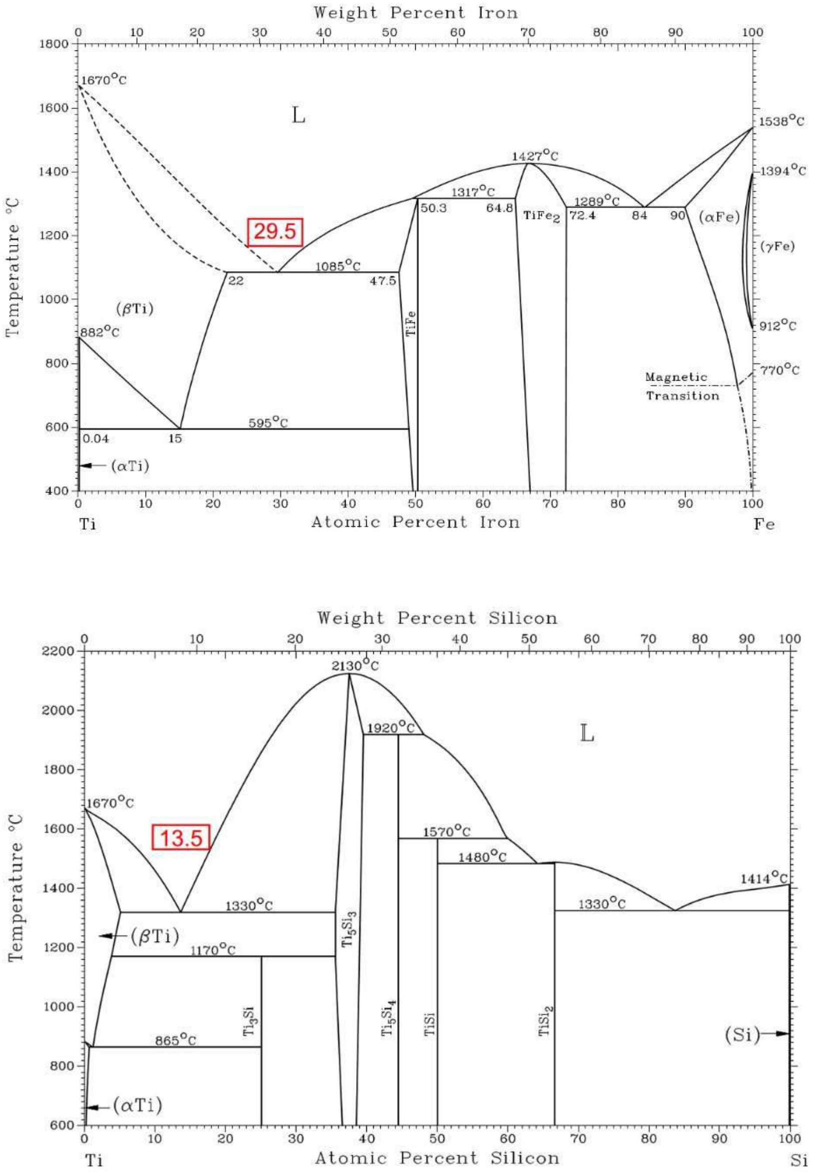

Fig.4.1 Ti-Fe and Ti-Si binary phase diagrams

Due to the marginal glass formability of Ti based binary systems, ternary systems were then considered. From the point of view of the elements' biocompatibility, as stated in chapter 1, only Fe, main group IV elements (Si, Ge and Sn), several of Ti's neighboring elements (Zr, Nb, Hf and Ta), as well as precious metals (Pd, Ag, Pt and Au) are suitable as candidate elemental additions. As for binary alloys, systems possessing deep eutectic point were selected.

Based on the data collected, Ti-Fe-Si ternary system was retained. The liquidus projection of Ti-Fe-Si system was determined by Weitzer [176] and is shown in Fig.4.2. There exists a ternary eutectic point on the Ti rich side. The ternary eutectic reaction (L-->TiFe + Ti$_5$Si$_3$ + β-Ti) occurs at

1034°C. Compared to the high melting temperature of Ti (1668°C) and binary eutectic reaction temperature of Ti-Si system (1330°C), this ternary eutectic point can be considered as a deep eutectic. Therefore, the glass formation around this ternary eutectic composition was then investigated and the detailed results are shown in the following section.

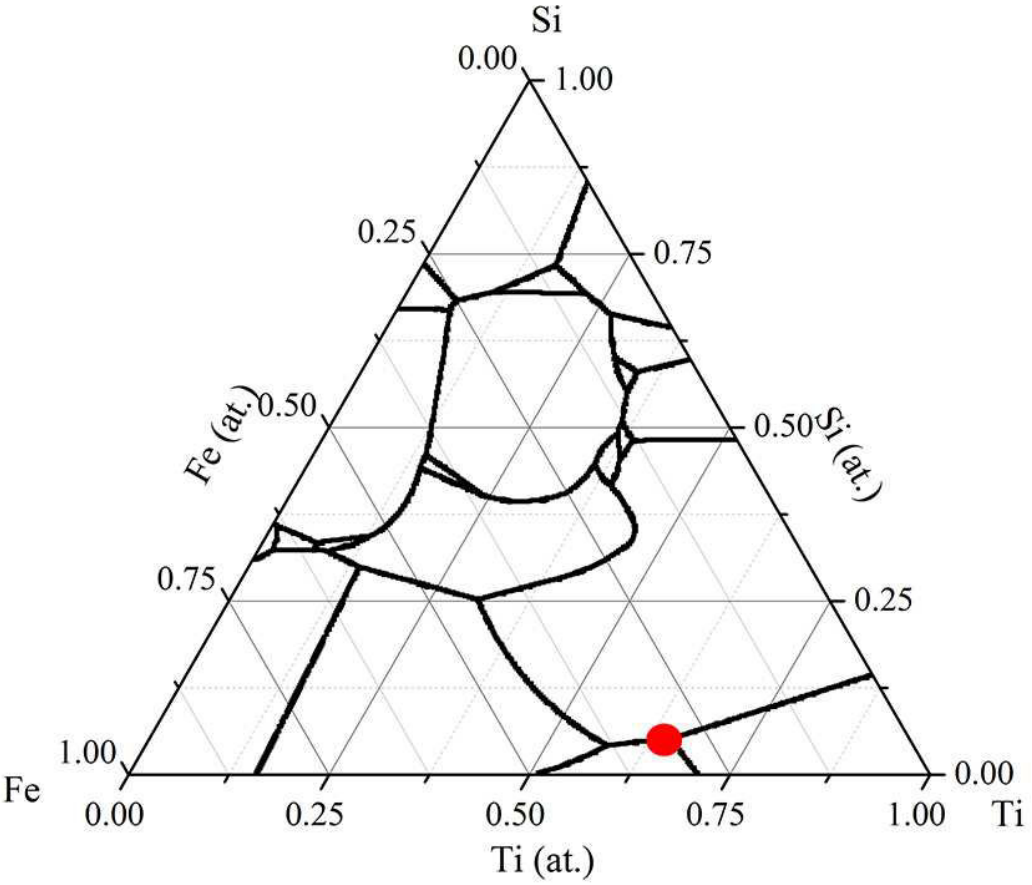

Fig.4.2 Liquidus projection of Ti-Fe-Si ternary system (digitalized from Fig.5 in [176]). Solid circle indicates the ternary eutectic point on Ti rich side.

4.3 Glass formation of Ti-Fe-Si based alloys

The glass formation in Ti-Fe-Si ternary system was investigated using the melt spinning technique. Melt spinning was carried out by rapid quenching of liquid alloys on a copper wheel rotating at a speed of 3500 rpm (46 m/s). In addition, lower wheel speeds of 2500 rpm (33 m/s) and 1500 rpm (20 m/s) were used for some selected cases. The results are shown in Fig.4.3. Ribbons of about 30 µm thickness were synthesized by melt spinning. The ternary eutectic composition ($Ti_{65}Fe_{30}Si_5$) cannot be vitrified. Instead, the melt spun ribbons show existence of icosahedral quasicrystal phase. In the range of compositions with melting temperatures below 1150°C, only $Ti_{65}Fe_{27.5}Si_{7.5}$ and $Ti_{67.5}Fe_{25}Si_{7.5}$ can be vitrified. The other compositions in this region form icosahedral phase on rapid quenching. Moreover, for one of the glassy compositions ($Ti_{67.5}Fe_{25}Si_{7.5}$), icosahedral phase was obtained when lower wheel speed (i.e. lower cooling rate) was used during melt spinning.

Based on the idea that compositions from the steeper side of the eutectic point are expected to be more easily amorphized, more compositions were then investigated in a region where liquid and

Ti_5Si_3 intermetallic coexist at 1150°C. According to Ti-Si binary phase diagram, as shown in Fig.4.1, the melting temperature of intermetallic Ti_5Si_3 is as high as 2130°C whereas the melting temperature of TiFe is only 1317°C.Therefore, the side where liquid and Ti_5Si_3 coexist can be expected to be the steeper side of ternary eutectic point. Moreover, as can be seen in the 1150°C isothermal section of ternary Ti-Fe-Si phase diagram, β-Ti solid solution of wide composition range forms in the region of low Si concentration. Glass formation is then expected to be more difficult in this region. Therefore, the high Si content region (10-15 at.%) was investigated. It can be seen in Fig.4.3 that all three compositions examined in this region and another composition reported previously by Polk [110] could be vitrified. Compositions with Si content higher than >15 at.% could not be investigated in the present work due to their high melting temperature (T_m > 1500°C). This limitation was imposed by the melt spinning technique, since quartz tube where the metals are melted becomes soft.

The XRD patterns shown in Fig.4.4 confirms the amorphous nature of melt spun ribbons of the compositions shown as solid circles in Fig.4.3. The diffuse peaks and the absence of sharp Bragg intensities indicate the amorphous structure of the ribbons.

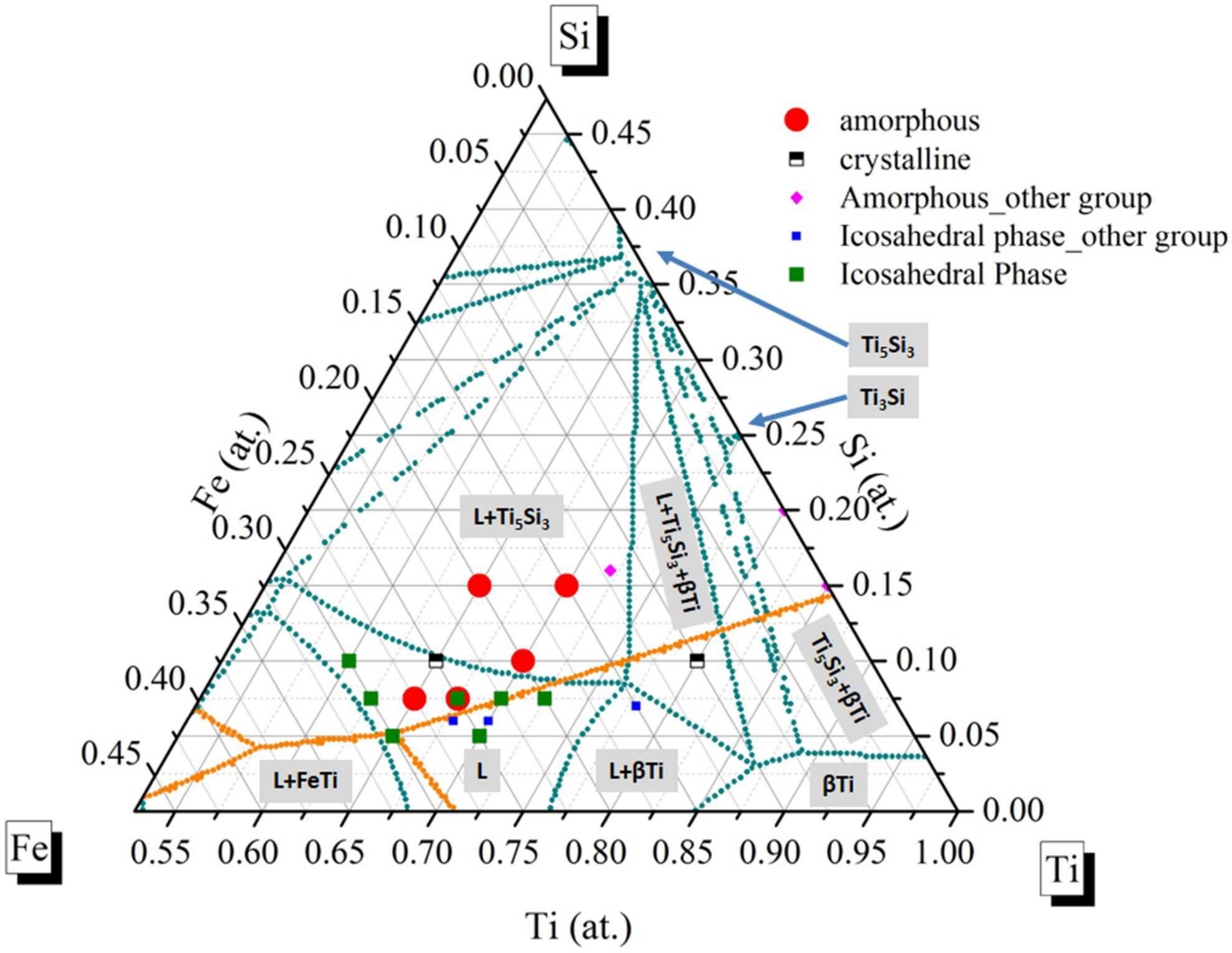

Fig.4.3 Glass forming ability of Ti-Fe-Si ternary system at Ti rich side. Liquidus projection and isothermal section at 1150°C of Ti-Fe-Si ternary system is delineated in solid line and dotted line, respectively.

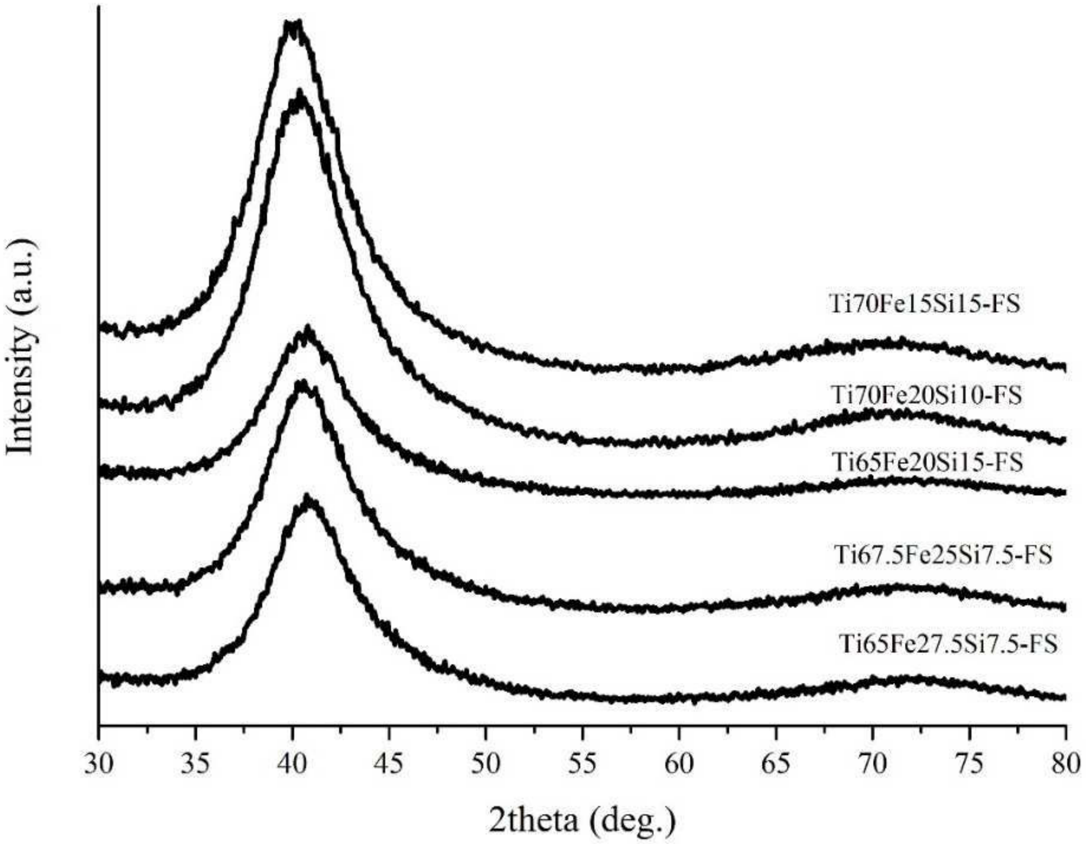

Fig.4.4 The conventional XRD patterns of glassy ternary alloys in Ti-Fe-Si system. FS indicates XRD patterns come from free side of melt spun ribbons.

On the other hand, the compositions (solid squares),which failed to vitrify during melt spinning, result in the formation of $Ti_{0.8}Fe_{0.2}$ (β-Ti solid solution), TiFe and Ti_5Si_3 crystalline phases and one icosahedral quasicrystalline phase. The composition of $Ti_{67.5}Fe_{25}Si_{7.5}$, which can be vitrified at the high rotating speed of 3500 rpm, shows crystallinity when cast at low rotating speed of 1500 rpm. The XRD patterns of the melt spun ribbons of these compositions are very similar and the pattern of $Ti_{67.5}Fe_{25}Si_{7.5}$ cast at rotation speed of 1500 rpm (hereafter named as TFS-1500) is shown in Fig.4.5 as representative. It can be seen that the formation of crystalline and quasicrystalline phases in as-cast ribbon leads to appearance of sharp Bragg intensities in the XRD pattern. This result indicates that the formation of the amorphous phase is in competition with the above crystalline phases during rapid quenching. Among the three simple crystalline phases shown in Fig.4.5, the $Ti_{0.8}Fe_{0.2}$ phase is of disordered BCC structure whereas TiFe is of ordered BCC structure with one element located at the body center and the other element occupying the eight vertices of cubic unit cell [36]. The intermetallic compound Ti_5Si_3 possesses a hexagonal close packed structure. The formation of these crystalline products is expected based on the ternary phase diagram, as shown in Fig.4.3. All the compositions which partially crystallize into the quasicrystalline phase upon solidification are located in the region where the liquidus temperature is below 1150^{o}C.

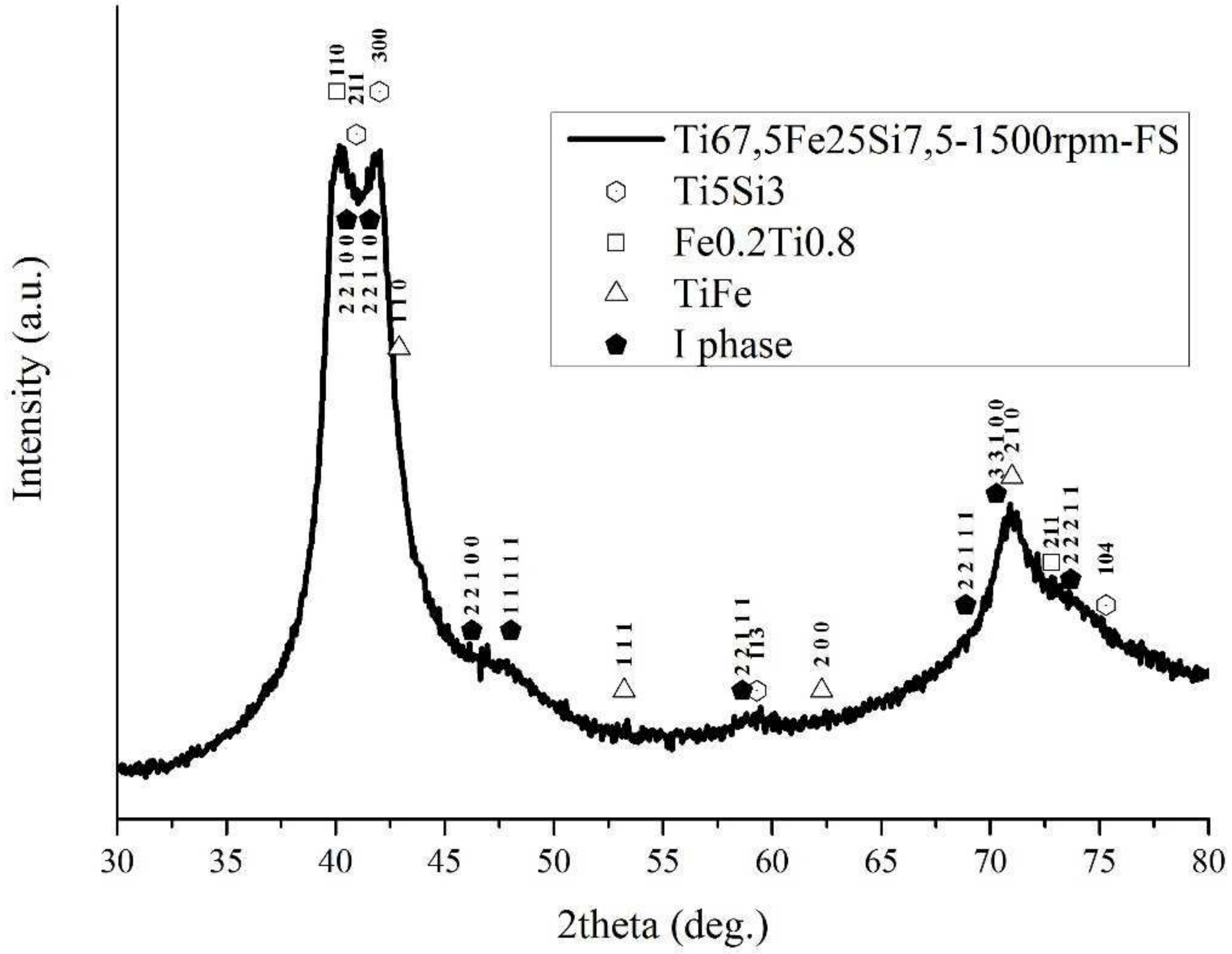

Fig.4.5 The composition of $Ti_{67.5}Fe_{25}Si_{7.5}$ leads to formation of crystalline phase of Ti_5Si_3, $Ti_{0.8}Fe_{0.2}$ and TiFe as well as one icosahedral quasicrystalline phase, when casted at low rotation speed (1500rpm) during melt spinning.

Transmission electron microscopy (TEM) was used to confirm the presence of icosahedral quasicrystalline phase in the as-cast TFS-1500 ribbons. The diffraction pattern obtained is shown in the inset of Fig.4.6, ring pattern indicates that the crystallites are of small size. The dark field image is then obtained from the region marked by red circle. It is found that the size of I-Phase and $Ti_{0.8}Fe_{0.2}$ crystalline precipitates are around 20 nm. Due to the small size of precipitates, the peaks in XRD patterns are much broadened and neither I-Phase nor simple crystalline phases produce sharp Bragg intensities. Due to the small size of crystallites, convergent beam electron diffraction (CBED) technique is then used to obtain the diffraction pattern.

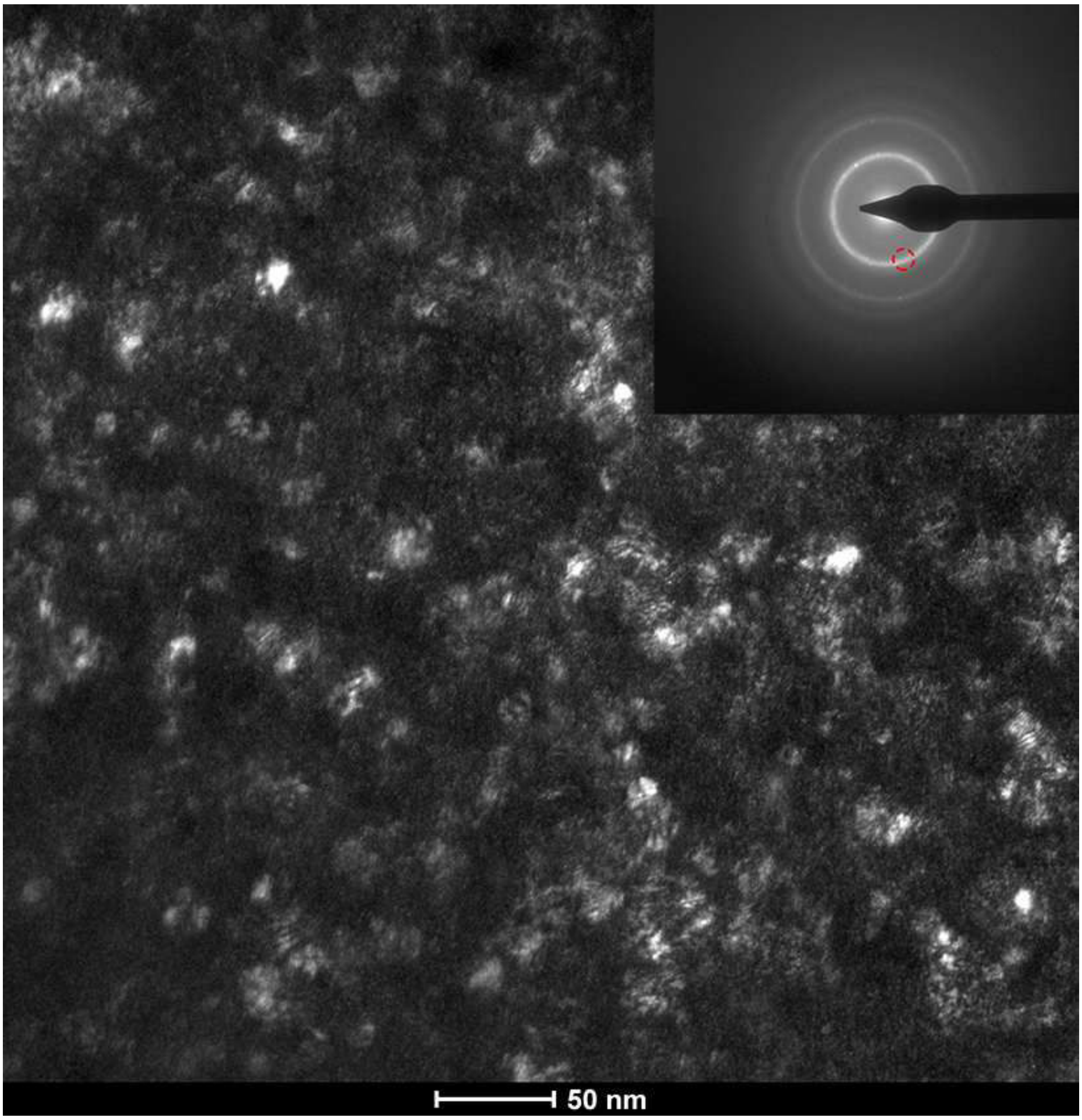

Fig.4.6 Dark field image shows precipitation of icosahedral quasicrystals and $Ti_{0.8}Fe_{0.2}$ crystalline phase. Zone axis is [111] $Ti_{0.8}Fe_{0.2}$. The inset shows the ring pattern from which the dark field image was obtained.

The CBED pattern of as-cast TFS-1500 is shown in Fig.4.7. It is found that although convergent beam is used, due to the small size of crystallites, there exist two phases (Icosahedral quasicrystal and $Ti_{0.8}Fe_{0.2}$) in the region where the CBED patterns were taken. The small solid circles indicate the diffraction pattern of $Ti_{0.8}Fe_{0.2}$ at [111] zone axis. Fig.4.7 also shows the three fold symmetry pattern corresponding to icosahedral quasicrystalline phase (I-Phase). The orientation relationship between $Ti_{0.8}Fe_{0.2}$ and I Phase is shown here as [111] $Ti_{0.8}Fe_{0.2}$ // three fold symmetry axis (I-Phase). The schematic presentation shows the indexation of the I-Phase using Elser's indexing method [177] and the size of solid circles indicates the intensity of diffraction spots based on Elser's theoretical calculation.

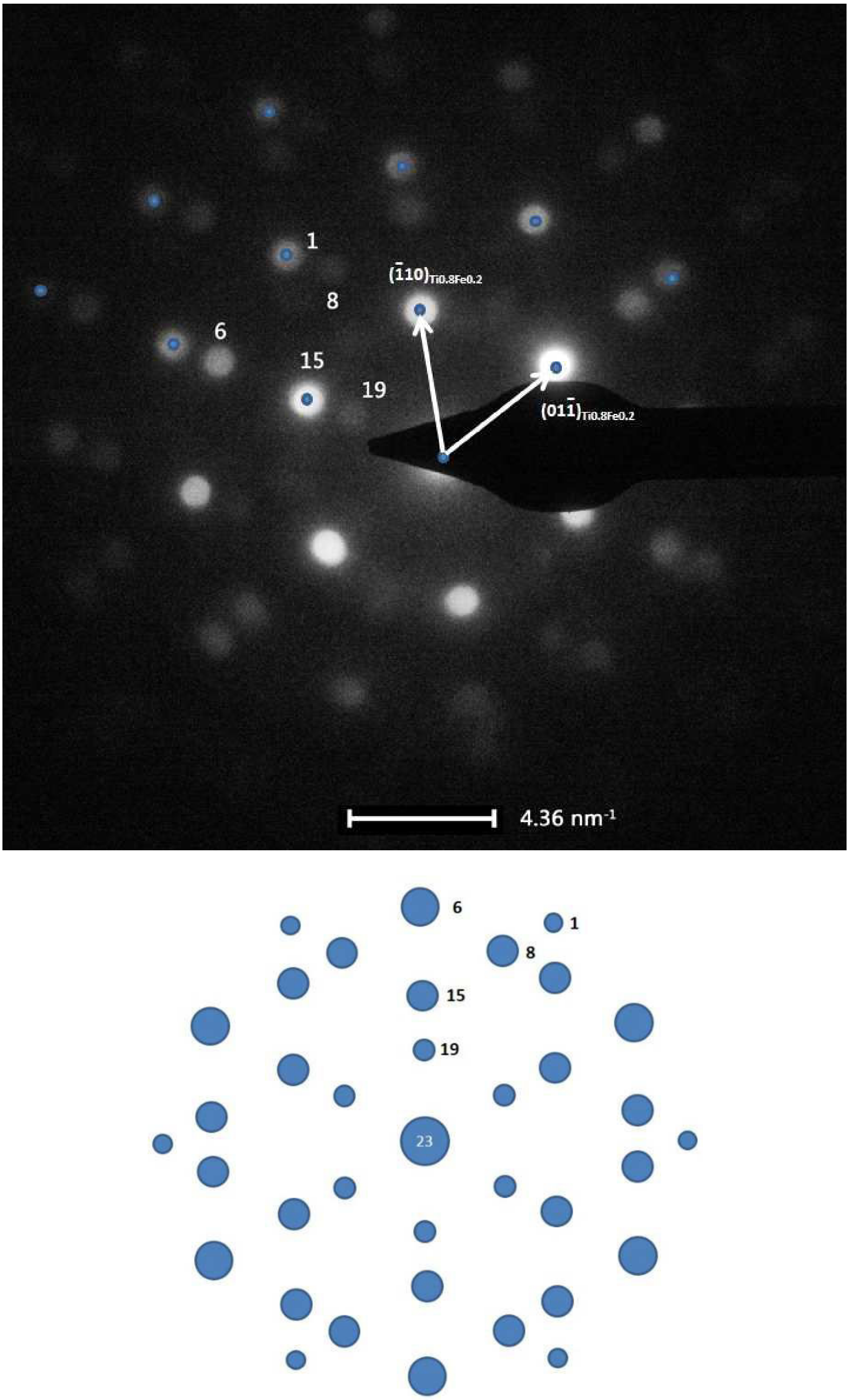

Fig.4.7 Convergent electron beam diffraction patterns pattern of as-cast TFS-1500, zone axis [111]$Ti_{0.8}Fe_{0.2}$ and schematic presentation of three fold symmetry pattern of icosahedral quasicrystal. The circle size in schematic presentation indicates the intensity of diffracted spots according to theoretical calculation [177]. The orientation relationship between $Ti_{0.8}Fe_{0.2}$ and icosahedral quasicrystal is [111] $Ti_{0.8}Fe_{0.2}$ // three fold symmetry axis (I-Phase).

The CBED patterns from different zone axis ([001] $Ti_{0.8}Fe_{0.2}$) of as-cast TFS-1500 is shown in Fig.4.8. The diffraction pattern also shows the presence of $Ti_{0.8}Fe_{0.2}$ crystalline phase and three fold symmetry of I-Phase. The orientation relationship between $Ti_{0.8}Fe_{0.2}$ and I Phase shown here is [001] $Ti_{0.8}Fe_{0.2}$ // two fold symmetric axis (I-Phase). The five fold symmetry pattern of I-Phase in as-cast TFS-1500 ribbons is shown in Fig.4.9. From the array of diffracted spots of five fold axis (spots labeled 6 and 15 in Fig.4.7) in two fold symmetry pattern, it can be found that the I-Phase in as-cast TFS-1500 ribbons is of primitive lattice in six dimensional hyperspace [177, 178]. The lattice constant of this primitive unit cell in six dimensional space is then calculated according to the peak positions obtained in both XRD and CBED patterns, as shown in Table 4.1. The quasilattice constant is a_q=0.4956 nm. This value is between those of Ti-TM-Si-O (TM=transition metal), Ti-Zr-Fe (0.46 - 0.48 nm) and Ti-Zr-Ni, Ti-Zr-Co (0.51 nm) [179]. It is found that although CBED is used, the small size of precipitates leads to intensities of some diffracted spots in CBED patterns being so low that one cannot distinguish them from the background noise, e.g. label No. 21 in Elser's theoretical diffraction pattern is too blurred to be seen in current CBED patterns, as shown in Fig.4.7. In addition, the interplanar spacing, d of (110)$Ti_{0.8}Fe_{0.2}$ (d=0.22486 nm) is very close to that of (221001) I-Phase (d=0.2219 nm). This leads to strong overlap of two kinds of diffracted spots in the CBED patterns. Therefore the intensity of label No. 15 of icosahedral quasicrystal is higher than that of label No. 6, as can be seen in Fig.4.7.

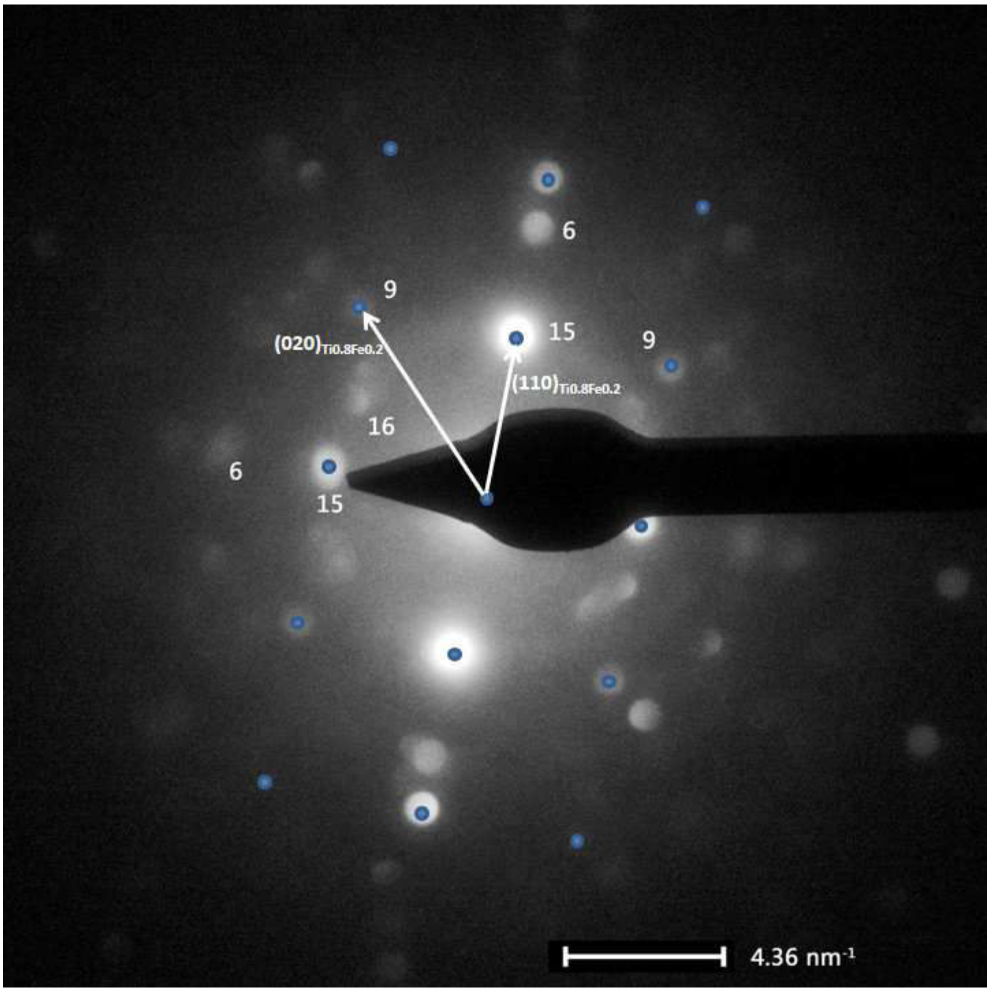

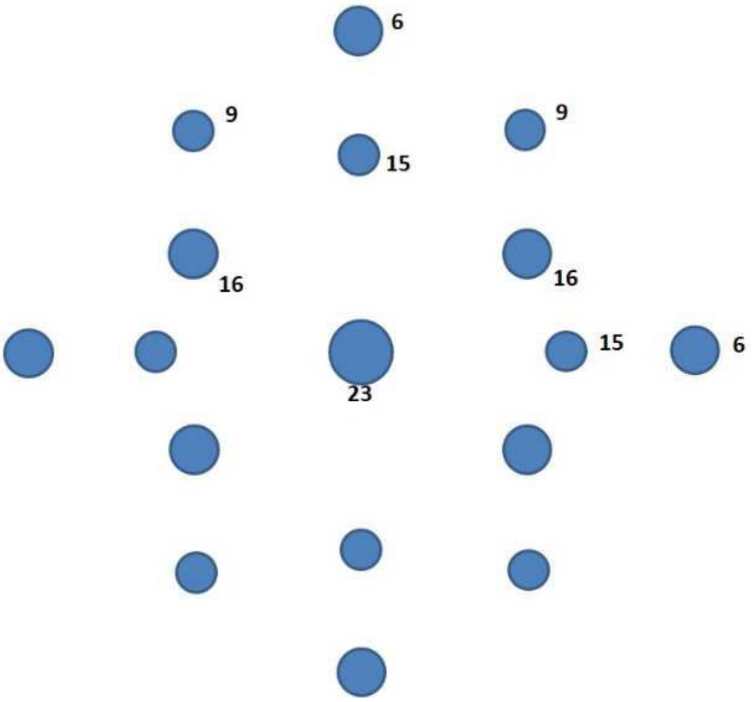

Fig.4.8 Convergent electron beam diffraction patterns of as-cast TFS-1500, zone axis [001]$Ti_{0.8}Fe_{0.2}$ and schematic presentation of two fold symmetry pattern of icosahedral quasicrystal. The solid circles in CBED pattern indicate $Ti_{0.8}Fe_{0.2}$ phase. The circle size in schematic presentation indicates the intensity of diffracted spots according to theoretical calculation [177]. The orientation relationship between $Ti_{0.8}Fe_{0.2}$ and icosahedral quasicrystal is [001] $Ti_{0.8}Fe_{0.2}$ // two fold symmetry axis (I-Phase).

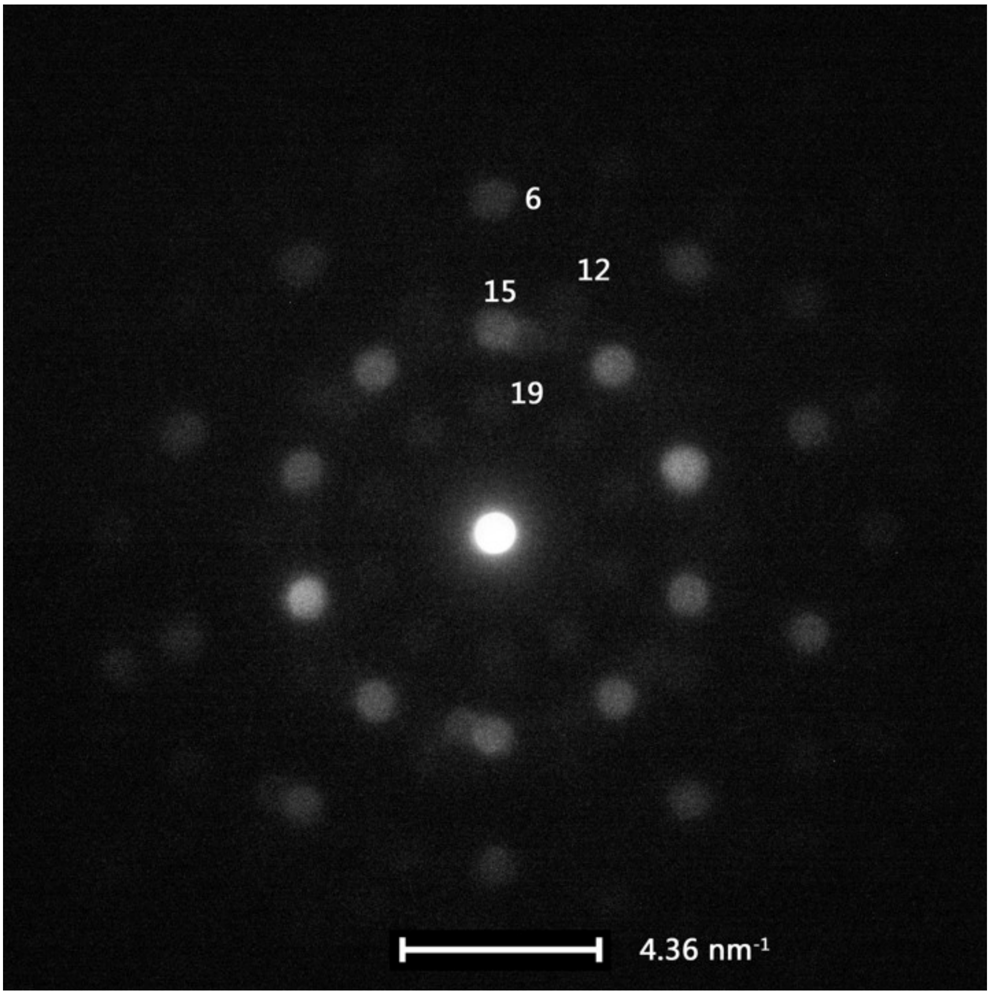

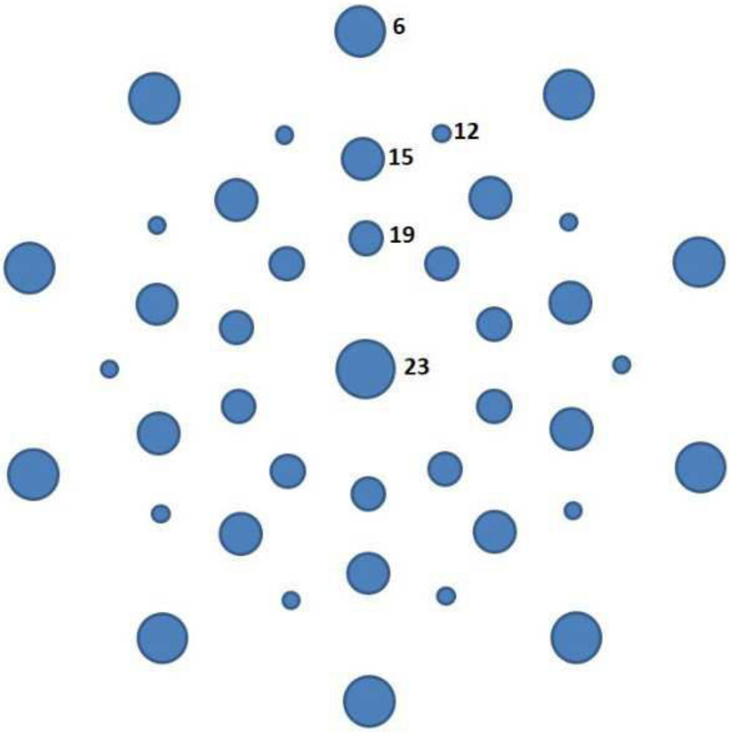

Fig.4.9 Convergent electron beam diffraction patterns of as-cast TFS-1500 five fold symmetry pattern of I-Phase and schematic presentation of five fold symmetry pattern of icosahedral quasicrystal. The circle size in schematic presentation indicates the intensity of diffracted spots according to theoretical calculation [177].

Table 4.1 Peak positions (d, 2ϑ and Q) of the icosahedral phase obtained in as-cast TFS-1500 ribbon. The indexing follows Elser's method [177].The quasilattice constant of I-Phase is a_q=0.4956 nm calculated from the peak indexing.

Index	Label	d (nm)	2theta (deg.)	Q (nm^{-1})
1 1 1 1 0 0	19	0.3601	24.70	17.45
2 1 1 1 1 1	16	0.0625	38.52	26.91
2 2 1 0 0 1	15	0.2219	40.63	28.32
3 1 1 1 1 1	12	0.1895	47.97	33.16
3 2 2 1 0 1	9	0.1111	56.91	38.86
3 2 2 1 1 1	8	0.1575	58.56	39.90
3 3 2 0 0 2	6	0.1376	68.08	45.66
4 2 2 2 1 1	1	0.1284	73.70	48.92

When one considers the arrangement of twelve atoms outside contacting another center atom, face center cubic (FCC), hexagonal close packed (HCP) and icosahedral cluster are the three possible arrangements. Although FCC and HCP structures prevail in crystalline materials, the icosahedral cluster (12 outside atoms + 1 center atom) possesses the lowest energy comparing to FCC and HCP [180], in terms of binding energy between atoms following Lennard-Jones interatomic potential. Therefore, icosahedral clusters are locally favored in the liquid. However, icosahedra alone cannot fill space. Then close packed structures like FCC and HCP become favoured.

Therefore, it can be expected that icosahedral clusters should prevail in the liquid and this has been proved in some metallic melts, like Ti-Ni-Zr[181], Al-Cu-Co, Al-Cu-Fe [182].

According to the classical nucleation theory and considering only homogeneous nucleation, the energy barrier between liquid and crystalline phase determines which phase will nucleate more readily when melts are cooled below liquidus temperature. This critical energy barrier ($\Delta G_{hom}*$) is shown in Equation 4.1[68].

$$\Delta G^{*}_{\mathrm{hom}} = \frac{16\pi\gamma^3}{3\Delta G_V^2}$$

Equation 4.1

where γ and ΔG_V is the interfacial energy and difference of Gibbs free energy between liquid and crystalline phase, respectively.

The interfacial energy (γ) is determining for the energy barrier for nucleation. For a high value of γ, larger undercooling (ΔT) is needed to overcome the energy barrier and initiate nucleation. Therefore, if assuming that icosahedral clusters prevail in melt, then for simple metals, such as FCC Ni, a large undercooling is expected to initiate homogeneous nucleation. It have been noted by Turnbull that a large undercooling as high as 319 K was achieved in supercooled Ni [183]. Moritz et al. studied the phase selection during solidification in Ti-Fe-Si-O melt using containerless electromagnetic levitation and synchrotron radiation [184-186]. It was observed that smaller undercooling is required to form approximant phases of icosahedral quasicrystals than that for simple crystalline phases, like BCC $Ti_{0.75}Fe_{0.25}$. He also calculated the normalized interfacial energy of different phases [182, 187] and found that the normalized interfacial energy gradually increases in the sequence of icosahedral quasicrystal, approximant phase and complicated crystalline phase, BCC crystalline phase, finally FCC and HCP simple crystalline phase. Table 4.2 lists the microstructure analysis of as-cast Ti-Fe-Si ternary alloys.

Table 4.2 Microstructure analysis of as-cast Ti-Fe-Si ternary alloys

composition	structure
$Ti_{65}Fe_{27.5}Si_{7.5}$	Amorphous
$Ti_{67.5}Fe_{25}Si_{7.5}$	
$Ti_{65}Fe_{20}Si_{15}$	
$Ti_{70}Fe_{20}Si_{10}$	
$Ti_{70}Fe_{15}Si_{15}$	
$Ti_{70}Fe_{25}Si_{5}$	Icosahedral quasicrystals + $Ti_{0.8}Fe_{0.2}$ + TiFe + Ti_5Si_3
$Ti_{60}Fe_{30}Si_{10}$	
$Ti_{65}Fe_{30}Si_{5}$	
$Ti_{70}Fe_{22.5}Si_{7.5}$	

$Ti_{72.5}Fe_{20}Si_{7.5}$		
$Ti_{62.5}Fe_{30}Si_{7.5}$		
$Ti_{67.5}Fe_{25}Si_{7.5}$-1500rpm		
$Ti_{65}Fe_{25}Si_{10}$	Crystalline	Ti_5Si_3 + $Ti_{0.8}Fe_{0.2}$
$Ti_{80}Fe_{10}Si_{10}$		$Ti_{0.8}Fe_{0.2}$

4.4 Effect of minor elemental addition on glass formation of Ti-Fe-Si system

After the investigation of Ti-Fe-Si ternary system, the effect the addition of a fourth element on the glass formation of this system was studied. As stated in the introduction to this chapter, the selection of a fourth element is limited by the biocompatibility of candidate elements. In this respect, the fourth element can be from the group IV elements (Ge, Sn), noble metals (Pd, Au, Pt, Ag) or Ti's neighboring elements (Zr, Nb, Hf, Ta).

The effect of Ge addition on glass forming ability of Ti-Fe-Si system was studied first. A near ternary eutectic composition ($Ti_{67.5}Fe_{25}Si_{7.5}$ metallic glass) was chosen as the base ternary alloy. It is shown in Fig.4.10 that with increasing amount of Ge substituting Si, the microstructure of as-cast Ti-Fe-Si-Ge quaternary alloys changes from amorphous to icosahedral quasicrystals and finally to Ti_5Ge_3 and "big cubic phase" Ti_2Fe.

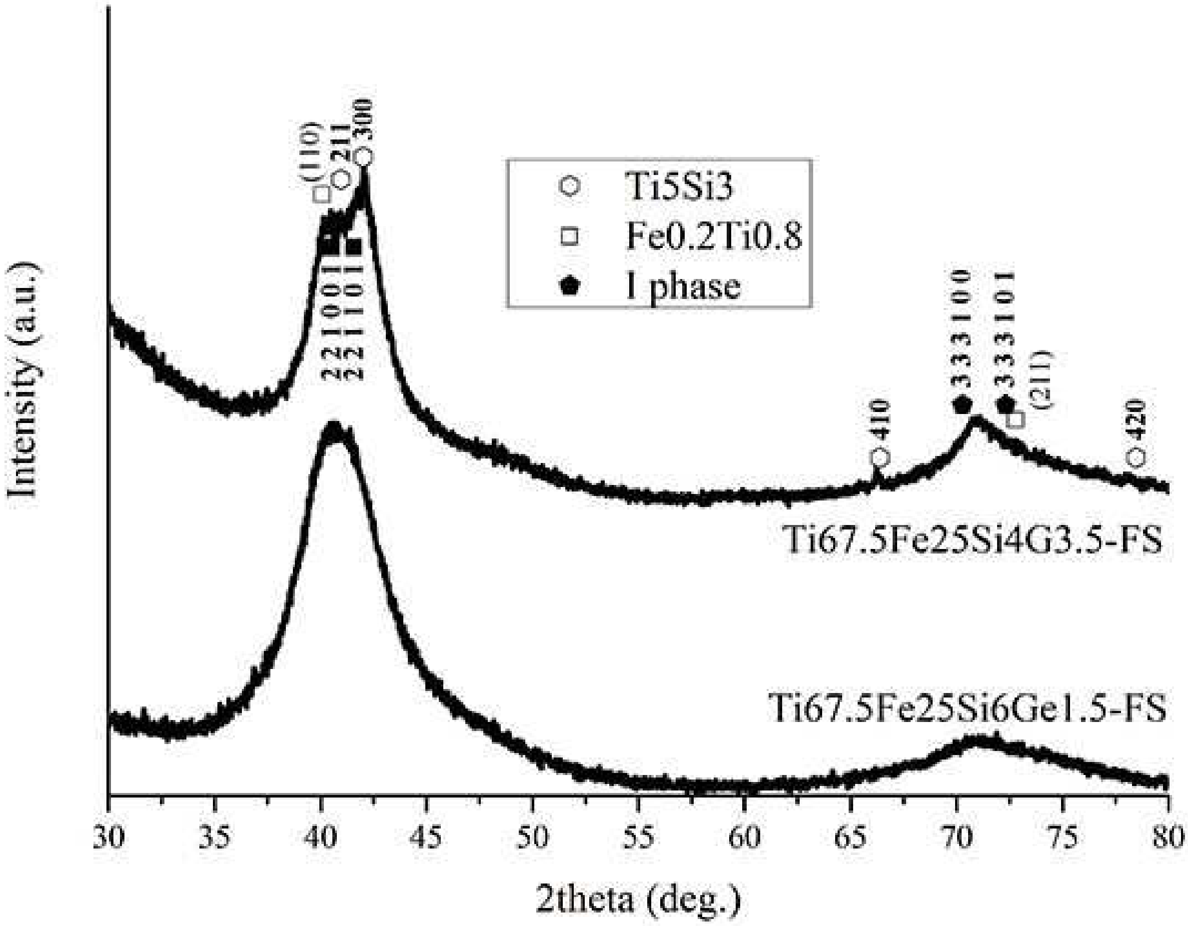

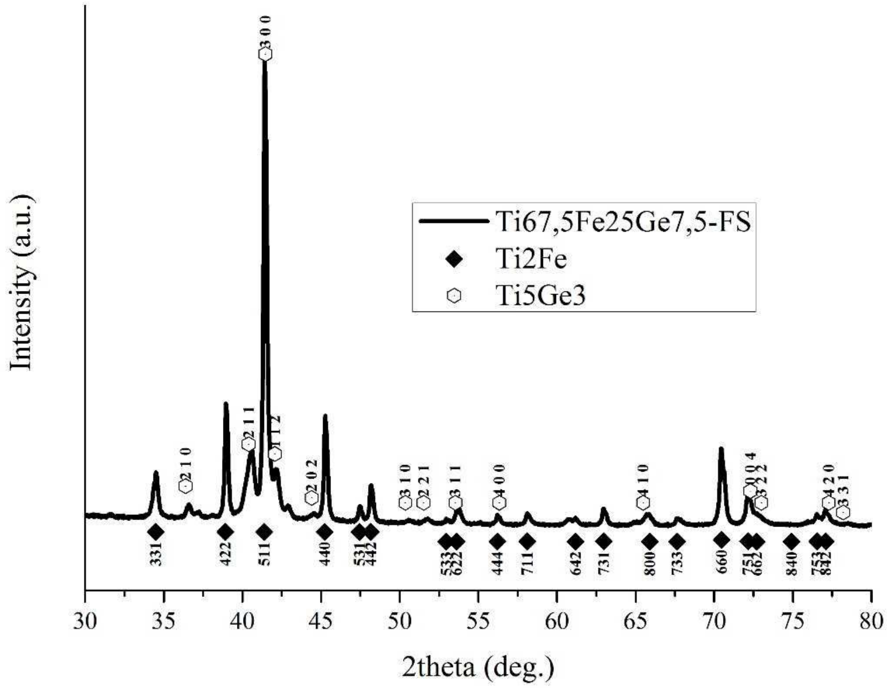

Fig.4.10 The XRD patterns of as-cast Ti-Fe-Si-Ge quaternary alloys.

The intermetallic Ti_5Ge_3 is of the same HCP structure as Ti_5Si_3 with Si substituted by Ge. The "big cubic phase" Ti_2Fe is of FCC type containing 96 atoms [188]. In Ti_2Fe unit cell, there exist three equivalent atom positions, Ti1, Ti2 and Fe1 [36]. As can be seen in Fig.4.11, the Ti2 and Fe1 positions both have distorted icosahedral environment around them. The atom arrangement around Ti1 position is a polyhedron with 21 faces, 18 triangle faces and 3 square faces. This is very close to the icosahedron which has 20 triangle faces.

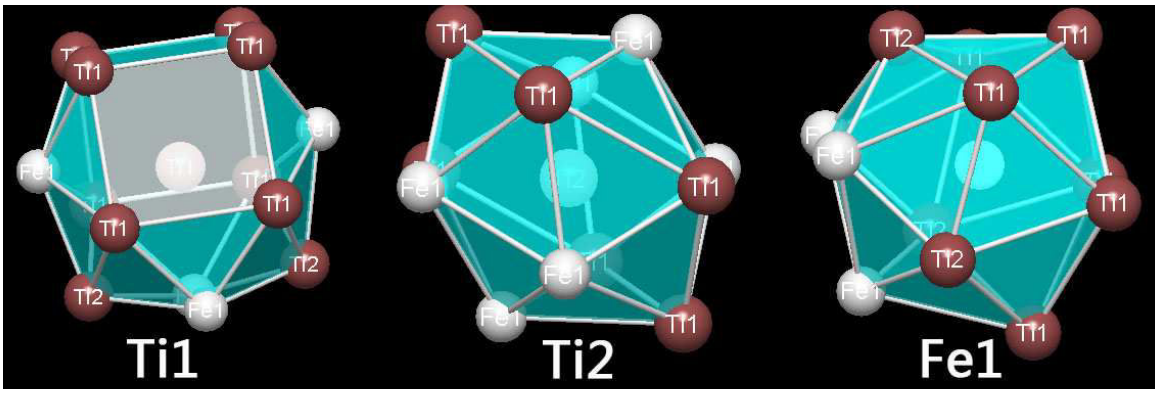

Fig.4.11 Three equivalent atom positions in FCC Ti_2Fe phase

The Effect of Pd addition substituting Fe on glass forming ability of Ti-Fe-Si ternary system was also investigated. The $Ti_{67.5}Fe_{25}Si_{7.5}$ glassy alloy was again selected as the base ternary alloy. It can be seen in Fig.4.12 that 2.5 at.% addition of Pd does not affect the glass formation of Ti-Fe-Si based alloys, while 5 at.% Pd leads to formation of three crystalline phases. 5 at.% Pd addition also increases liquidus temperature of Ti-Fe-Si based alloys. Table 4.3 lists the microstructure analysis of as-cast Ti-Fe-Si-(Ge or Pd) quaternary alloys. It can be summarized that both Ge and Pd additions lead to deviation from glass forming and quasicrystal forming region. Addition of Pd leads to larger deviation than Ge.

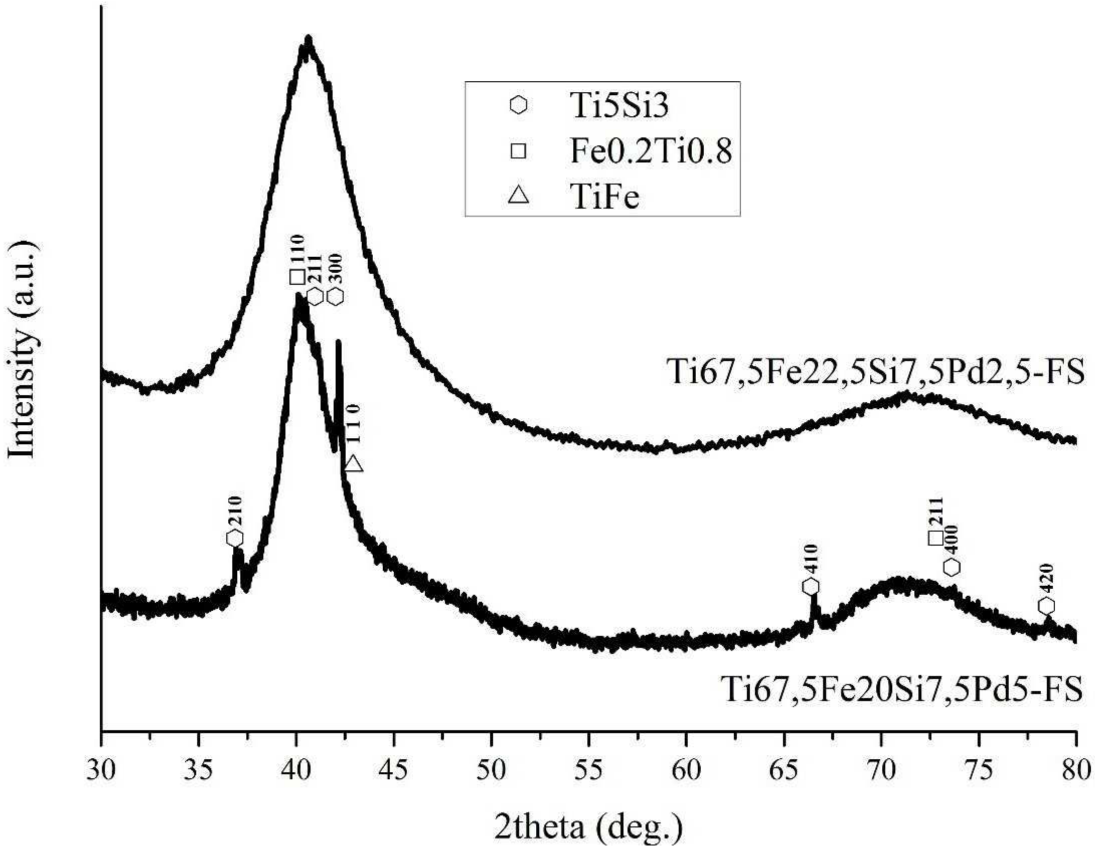

Fig.4.12 The XRD patterns of as-cast Ti-Fe-Si-Pd alloys.

The remaining suitable candidates as fourth elemental additions are Ti neighboring elements. Among Zr, Hf, Ta and Nb, Zr was finally selected due to its low melting temperature compared to the other three elements. Two starting glassy alloys were selected, $Ti_{67.5}Fe_{25}Si_{7.5}$.

Table 4.3 Microstructure analysis of as-cast Ti-Fe-Si-(Ge or Pd) quaternary alloys.

composition	structure	
$Ti_{67.5}Fe_{25}Si_6Ge_{1.5}$	Amorphous	
$Ti_{67.5}Fe_{25}Si_4Ge_{3.5}$	Crystalline	I + Ti_5Si_3 + $Ti_{0.8}Fe_{0.2}$
$Ti_{67.5}Fe_{25}Ge_{7.5}$		Ti_2Fe + Ti_5Ge_3
$Ti_{67.5}Fe_{22.5}Si_{7.5}Pd_{2.5}$	Amorphous	
$Ti_{67.5}Fe_{20}Si_{7.5}Pd_5$	Crystalline	$Ti_{0.8}Fe_{0.2}$ + FeTi + Ti_5Si_3

Table 4.4 lists the structure of Ti-Fe-Si-Zr quaternary alloys obtained by melt spinning. Glassy alloys of the composition of $Ti_{62.5}Zr_5Fe_{25}Si_{7.5}$ and $Ti_{65}Fe_{20}Si_{10}Zr_5$ were obtained, as can be seen in Fig.4.13. Alloys of the compositions based on $Ti_{67.5}Fe_{25}Si_{7.5}$ possess Zr_2Fe and $(Ti_3Zr_2)Si_3$ crystalline phases in as-cast ribbons, Fig.4.14. Zr_2Fe and $(Ti_3Zr_2)Si_3$ are of the same unit cell structures as Ti_2Fe and Ti_5Si_3, respectively. Zr addition leads to deviation from quasicrystal forming region, leading to the formation of Zr_2Fe precipitates instead of icosahedral quasicrystals, similar to the effect of Ge addition.

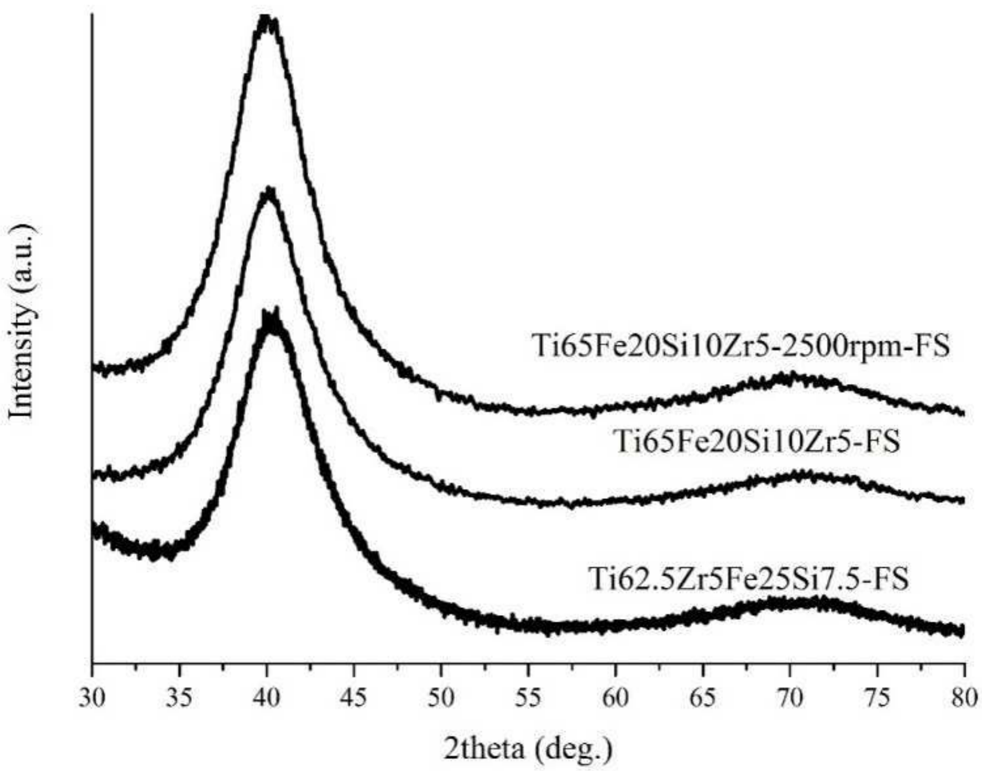

Fig.4.13 The XRD patterns of as-cast $Ti_{62.5}Zr_5Fe_{25}Si_{7.5}$ and $Ti_{65}Fe_{20}Si_{10}Zr_5$alloys showing its amorphous nature.

Table 4.4 Microstructure analysis of as-cast Ti-Fe-Si-Zr quaternary alloys.

composition (based on $Ti_{67.5}Fe_{25}Si_{7.5}$)		structure	
substituting Fe	$Ti_{67,5}Fe_{20}Si_{7,5}Zr_5$	Crystalline	$Zr_2Fe + (Ti_3Zr_2)Si_3$
	$Ti_{67,5}Fe_{15}Si_{7,5}Zr_{10}$		
	$Ti_{67,5}Fe_{10}Si_{7,5}Zr_{15}$		
substituting Ti	$Ti_{65}Zr_{2,5}Fe_{25}Si_{7,5}$	Crystalline	Ti_5Si_3
	$Ti_{62,5}Zr_5Fe_{25}Si_{7,5}$	Amorphous	
	$Ti_{57,5}Zr_{10}Fe_{25}Si_{7,5}$	Crystalline	$Zr_2Fe + (Ti_3Zr_2)Si_3$
composition (based on $Ti_{70}Fe_{20}Si_{10}$)		structure	
substituting Ti	$Ti_{65}Fe_{20}Si_{10}Zr_5$	Amorphous	
	$Ti_{65}Fe_{20}Si_{10}Zr_5$-2500rpm		
	$Ti_{65}Fe_{20}Si_{10}Zr_5$-1500rpm	Crystalline	$TiFe + Ti_2Fe + Ti_{0.8}Fe_{0.2}$
	$Ti_{60}Fe_{20}Si_{10}Zr_{10}$	Crystalline	Ti_5Si_3
	$Ti_{55}Fe_{20}Si_{10}Zr_{15}$		
	$Ti_{50}Fe_{20}Si_{10}Zr_{20}$	Amorphous	

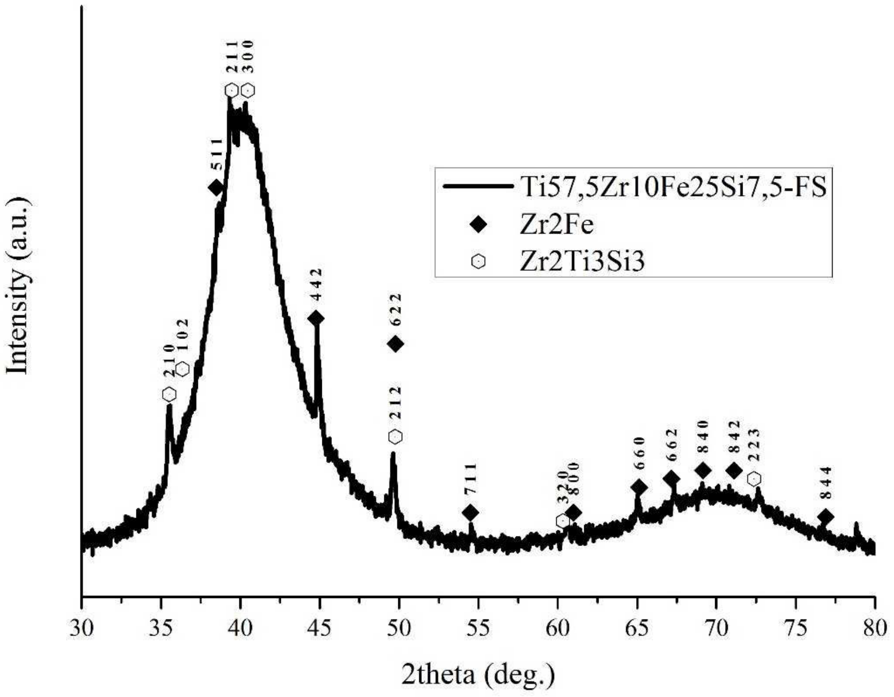

Fig.4.14 The XRD pattern of as-cast $Ti_{57.5}Zr_{10}Fe_{25}Si_{7.5}$ alloy showing precipitates of "big cubic phase" Zr_2Fe and $(Ti_3Zr_2)Si_3$

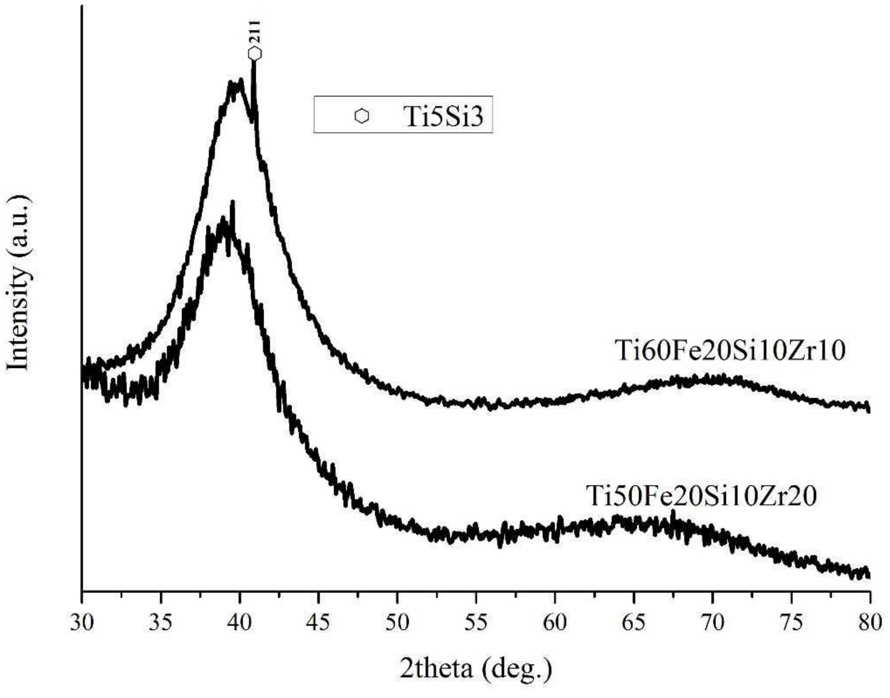

Fig.4.15 The XRD patterns of as-cast $Ti_{60}Fe_{20}Si_{10}Zr_{10}$ and $Ti_{50}Fe_{20}Si_{10}Zr_{20}$ alloys.

For compositions based on $Ti_{70}Fe_{20}Si_{10}$, alloys with small amount of Zr (up to 5 at.%) addition can be vitrified. Higher amount of Zr leads to high liquidus temperature, which in turn increases the difficulty of casting. As can be seen in Fig.4.15, the as-cast $Ti_{50}Fe_{20}Si_{10}Zr_{20}$ ribbons constitute mainly amorphous phase containing minor crystallinity. This crystallinity indicates that the cooling rate obtained by melt spinning at a wheel rotation speed of 3500 rpm was insufficient for complete amorphization. It is expected that these alloys can be vitrified with a higher rotation speed.

Finally, based on the above investigation of the effect of elemental addition on the glass formation of Ti-Fe-Si based alloys, it can be summarized that the compositional region near the ternary eutectic point ($Ti_{65}Fe_{30}Si_5$) is a quasicrystal forming region. Increasing the amount of a fourth element (Ge, Pd Zr) leads to gradual deviation from quasicrystal forming region. Consequently, with elevated fourth element additions, the microstructures of as-cast ribbons change in a sequence of first icosahedral quasicrystal, then complicated cubic phase (such as Ti_2Fe or Zr_2Fe possessing distorted icosahedral local atomic arrangements), and finally the simple crystalline phases (such as Ti_5Si_3, TiFe and $Ti_{0.8}Fe_{0.2}$).

For compositional regions located on the steeper side of ternary eutectic point, glass formation is favored. The high melting temperature of Ti_5Si_3 or $(Ti_3Zr_2)Si_3$ simple crystalline phases enhance the steepness of liquidus line. In the deep eutectic system, the liquid can be kept at lower temperature. When liquid is cooled below liquidus temperature, the increasing viscosity of liquid suppresses the nucleation and growth of crystalline phases. This in turn promotes the formation of glass. However, in the current Ti-Fe-Si(-Zr) system, the high liquidus temperature of the alloys from steeper side of eutectic point increases difficulty of obtaining as-cast ribbons through melt spinning.

4.5 Thermal stability of Ti-Fe-Si based metallic glasses

The thermal stability of as-cast $Ti_{67.5}Fe_{25}Si_{7.5}$ glassy alloy was investigated by DSC and DTA. As stated previously, this glassy alloy is of near ternary eutectic composition, i.e. within the quasicrystal forming region. It can be found in Fig.4.16 that no glass transition is observed at a heating rate of 40 K/min. Two exothermic peaks can be observed in the DSC curve of Fig.4.16 (a) during heating, which corresponds to two crystallization events. The enthalpy of the primary crystallization event (T_{x1}) is less than 1% of that of the main crystallization event (T_{x2}). The onset temperatures of the two crystallization processes, liquidus temperature (T_l) and solidus temperature (T_s) are indicated in Fig.4.16.

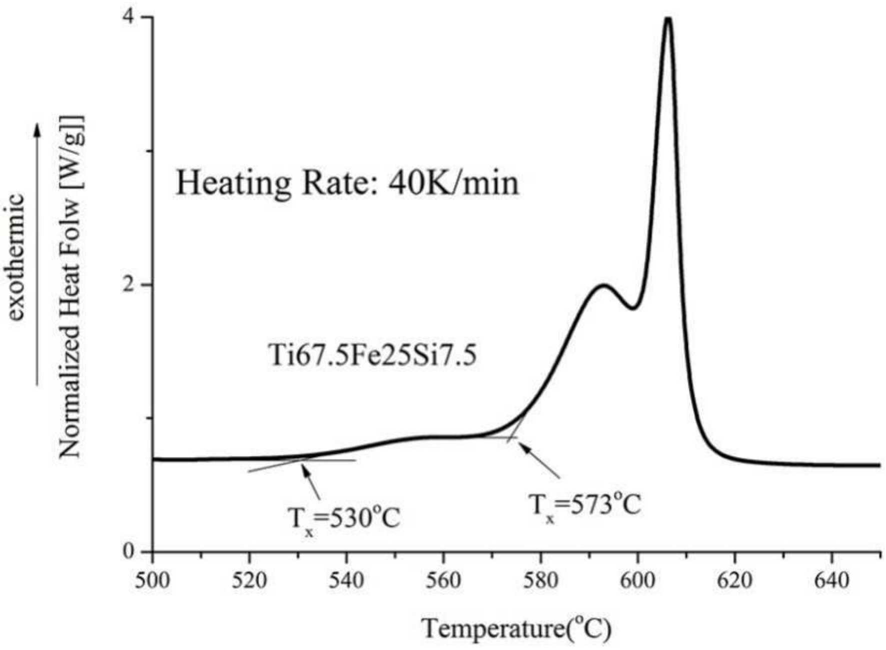

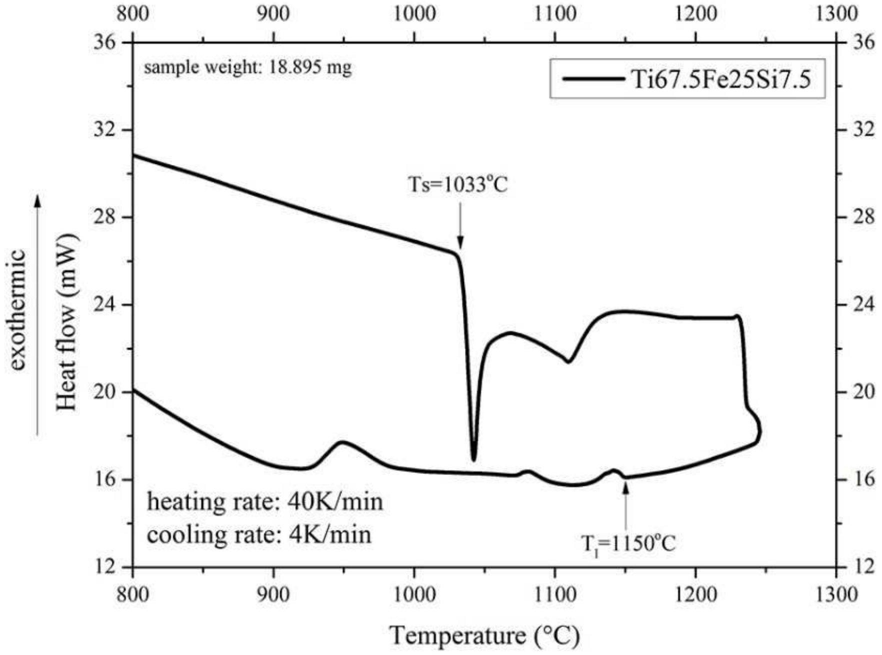

Fig.4.16 The DSC (a) and DTA (b) curves of as-cast $Ti_{67.5}Fe_{25}Si_{7.5}$ glassy alloy indicating crystallization and melting respectively.

In order to understand the crystallization process of the as-cast $Ti_{67.5}Fe_{25}Si_{7.5}$ glassy alloy, ribbons were heated up to designated temperature at a heating rate of 40 K/min in DSC and taken out. XRD was then used to investigate the structure of as annealed ribbons.

It can be seen in Fig.4.17 that the amorphous phase transforms to "big cubic phase" Ti_2Fe during primary crystallization. In secondary crystallization process, simple crystalline phases, such as $Ti_{0.8}Fe_{0.2}$, TiFe and Ti_5Si_3 form.

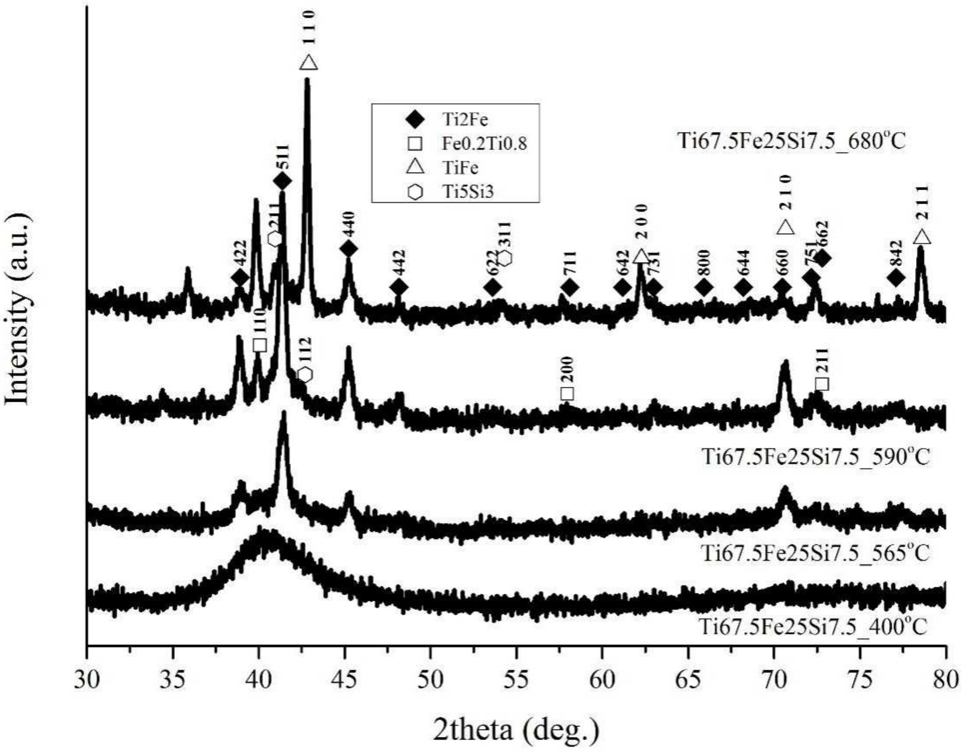

Fig.4.17 The XRD patterns of $Ti_{67.5}Fe_{25}Si_{7.5}$ glassy alloy heat treated at different temperatures.

The crystallization behavior of the as-cast $Ti_{70}Fe_{20}Si_{10}$ and $Ti_{62.5}Fe_{25}Si_{7.5}Zr_5$ glassy alloys were also studied. The former alloy is of composition located at the steeper side of the eutectic point, whereas the latter is based on a near eutectic composition. Similar to that of $Ti_{67.5}Fe_{25}Si_{7.5}$ glassy alloy, crystallization in $Ti_{70}Fe_{20}Si_{10}$ and $Ti_{62.5}Fe_{25}Si_{7.5}Zr_5$ glassy alloys occurs in two steps.

The small fraction of the primary crystallization products probably hinders the clear observation of sharp Bragg peaks in the XRD patterns of samples annealed at temperatures below the main crystallization event at T_{x2}, as shown in Fig.4.19 and Fig.4.20. Isothermal annealing at a temperature just above the onset temperature of primary crystallization indicates that Ti_2Fe phase precipitates during the primary crystallization reaction of $Ti_{62.5}Fe_{25}Si_{7.5}Zr_5$, as can be seen in Fig.4.20, similar to that of $Ti_{67.5}Fe_{25}Si_{7.5}$ alloy. It is believed that the same phase precipitates during the primary crystallization of $Ti_{70}Fe_{20}Si_{10}$. Isothermal annealing of this alloy at temperatures below T_{x2} triggers the main crystallization reaction, Fig.4.19.

After further heating at temperatures above the main crystallization reaction, the structure of the annealed alloys consists of Ti_2Fe and some simple crystalline phases (Ti_5Si_3, TiFe and $Ti_{0.8}Fe_{0.2}$). Nevertheless, the volume ratio of Ti_2Fe to simple crystalline phases is different in the above two alloys. Higher fraction of simple crystalline phases form after secondary crystallization in $Ti_{70}Fe_{20}Si_{10}$ than $Ti_{62.5}Fe_{25}Si_{7.5}Zr_5$ alloy.

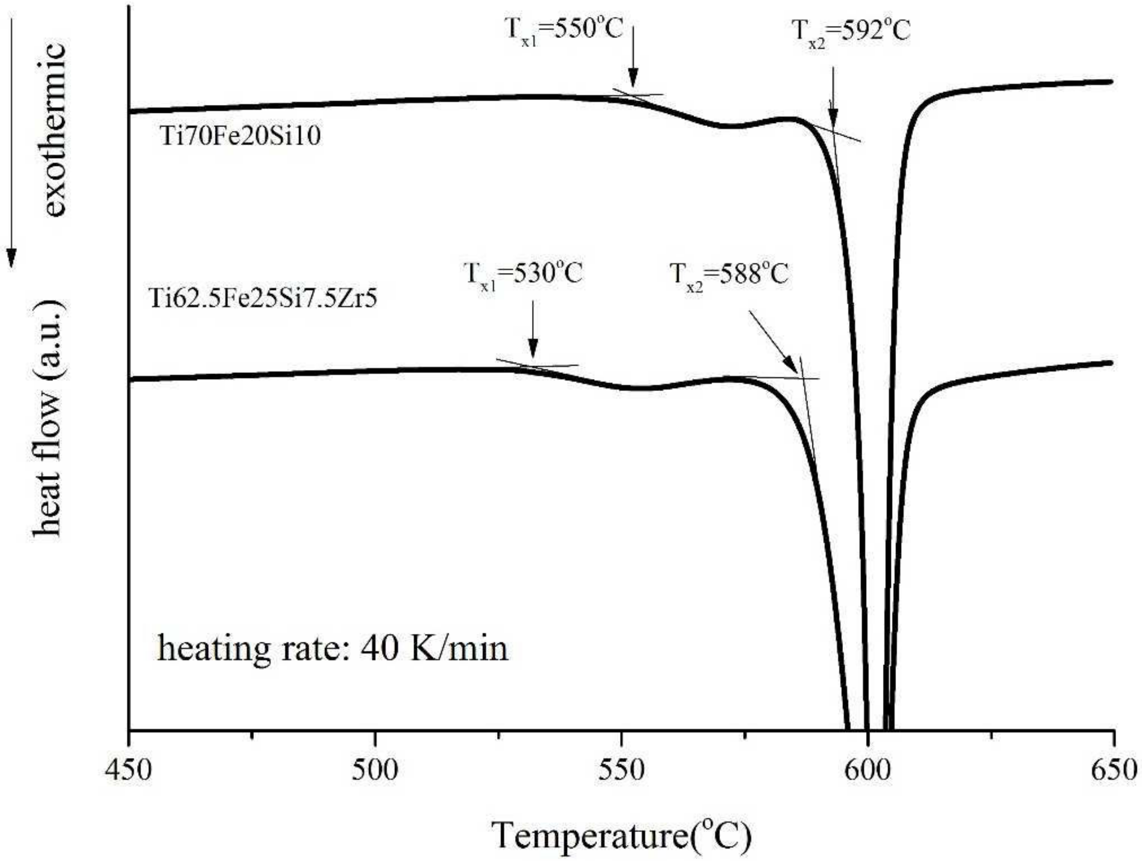

Fig.4.18 DSC curves of as-cast $Ti_{70}Fe_{20}Si_{10}$ and $Ti_{62.5}Fe_{25}Si_{7.5}Zr_5$ glassy alloys.

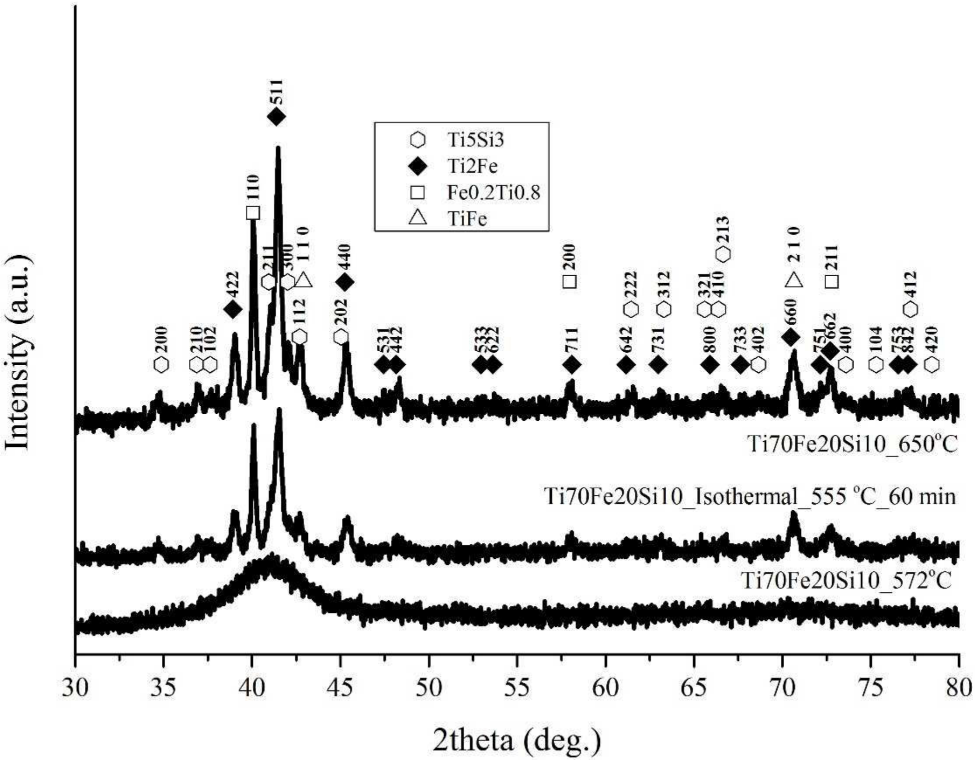

Fig.4.19 XRD patterns of $Ti_{70}Fe_{20}Si_{10}$ glassy alloy heat treated at different temperatures.

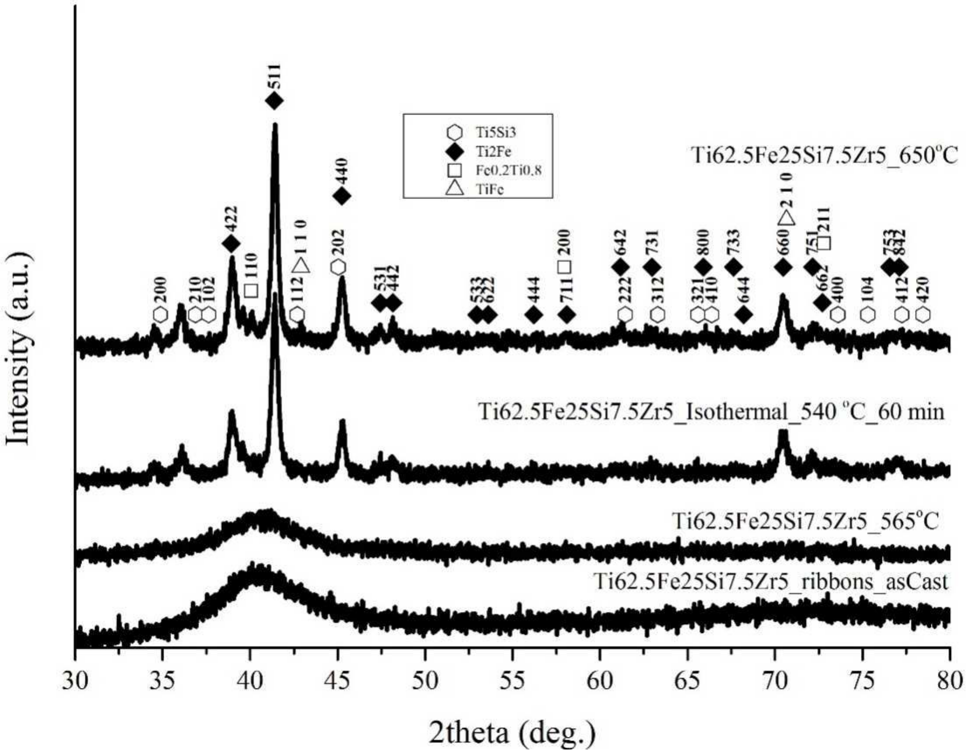

Fig.4.20 The XRD patterns of $Ti_{62.5}Fe_{25}Si_{7.5}Zr_5$ glassy alloy heat treated at different temperatures.

4.6 Corrosion resistance of Ti-Fe-Si based metallic glasses

The corrosion resistance of as-cast Ti-Fe-Si glassy alloys in simulated body fluid (Hanks solution) were investigated by potentiodynamic polarization. The most representative polarization curves are shown in Fig.4.21 and the corrosion data for all of the alloys studied are summarized in Table 4.5. It is found (Fig.4.21) that all the Ti-Fe-Si based glassy ribbons investigated exhibit wide passivation regions followed by pitting corrosion. They also possess higher corrosion potential (E_{cor}), lower corrosion current density (i_{cor}) and lower passivation current density (i_{pas}) in comparison with commercial purity Ti (cp Ti). In particular, the corrosion current density (i_{cor}) decreases by one order of magnitude on the average when compared with cp Ti.

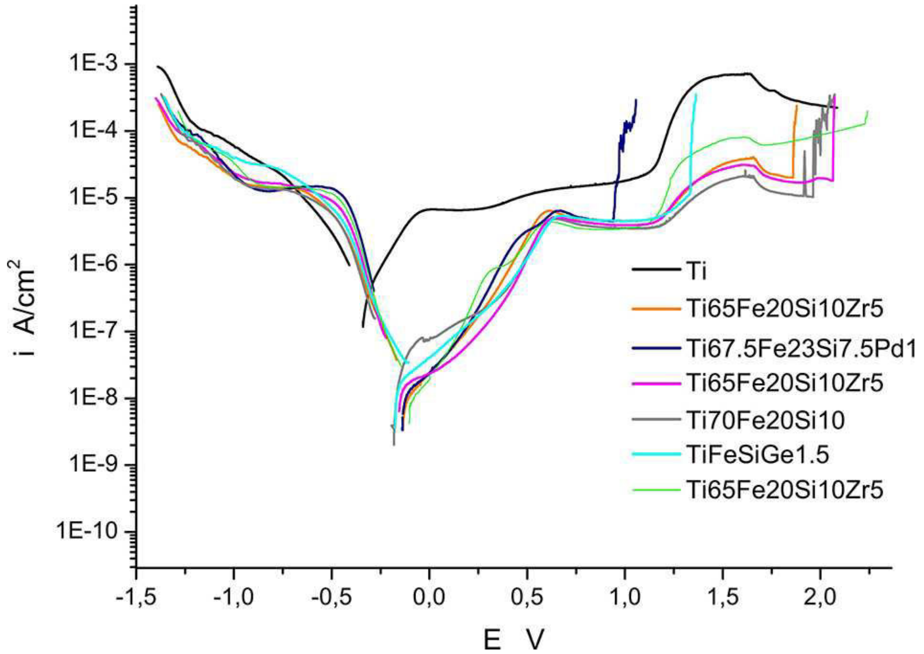

Fig.4.21 The potentiodynamic polarization curves of some Ti-Fe-Si based glassy alloys together with that of commercial purity Ti as reference.

Table 4.5 Corrosion properties of Ti-Fe-Si based alloys obtained from Fig.4.21.

Composition	Am. or Cryst	E_{cor} (V)	i_{cor} (A/cm2)	E_{pit} (V)
$Ti_{65}Fe_{27.5}Si_{7.5}$	Am	-0.183	3.907E-8	1.576
$Ti_{67.5}Fe_{25}Si_{7.5}$	Am	-0.175	4.497E-8	1.769
$Ti_{67.5}Fe_{25}Si_{7.5}$ (1500 rpm)	Cryst	-0.162	2.5E-8	1.779
$Ti_{65}Fe_{20}Si_{15}$	Am	-0.134	1.768E-8	1.971
$Ti_{70}Fe_{20}Si_{10}$	Am	-0.178	2.65E-8	1.959
$Ti_{70}Fe_{22.5}Si_{7.5}$	Am	-0.111	1.11E-8	2.02
$Ti_{67.5}Fe_{25}Si_{6}Ge_{1.5}$	Am	-0.166	1.405E-8	1.35
$Ti_{67.5}Fe_{24}Pd_{1}Si_{7.5}$	Am	-0.145	1.045E-8	0.943
$Ti_{67.5}Fe_{22.5}Pd_{2.5}Si_{7.5}$	Am	-0.159	1.1E-8	0.668
$Ti_{62.5}Zr_{5}Fe_{25}Si_{7.5}$	Am	-0.087	4.791E-9	1.515
$Ti_{65}Fe_{20}Si_{10}Zr_{5}$	Am	-0.156	1.23 E-8	2.067
$Ti_{65}Fe_{20}Si_{10}Zr_{5}$ (1500 rpm)	Cryst	-0.135	8.982E-9	>2.25
$Ti_{65}Fe_{20}Si_{10}Zr_{5}$ (2500 rpm)	Am	-0.143	7.419E-9	1.861
$Ti_{50}Fe_{20}Si_{10}Zr_{20}$	Am	-0.156	4.736E-9	1.173
Ti bulk (reference materials)	Cryst	-0.344	3.467E-7	>2.25

Am: amorphous, Cryst: crystal. E_{cor} = corrosion potential, i_{cor} = corrosion current, E_{pit} = pitting corrosion potential

It is found that there is no strong relationship between Ti concentration in glassy alloys and corrosion properties (E_{cor}, i_{cor}, i_{pas}) in these Ti-rich glasses. Therefore, the effect of compositions of glassy alloys on corrosion resistance is demonstrated by plotting corrosion data (i.e. E_{cor}, i_{cor} and E_{pit}) against Si/Fe ratio, as shown in Fig.4.22. There is no significant effect of composition variations within one amorphous system on corrosion properties. For instance all Ti-Fe-Si amorphous alloys possess approximately the same level of E_{cor}. On the other hand, there is difference between different glassy systems. It is also found that minor Zr additions exhibits positive effect on corrosion potential in Ti-Fe-Si system.

The origins of high corrosion resistance of metallic glasses is related to the high homogeneity of the alloys in comparison to their crystalline counterparts. The absence of grain boundaries and second phase precipitations significantly decreases galvanic effects associated with inhomogeneous distribution of alloying elements. Formation of predominantly amorphous oxide films with enhanced mechanical and corrosion resistance properties on the surface of metallic glasses reduces ionic transport, which is another mechanism contributing to improvement of corrosion resistance.

Different from the insensitivity of E_{cor} and i_{cor} to alloying composition, E_{pit} is highly sensitive to composition changes. As can be seen in Table 4.5 and Fig.4.22, $Ti_{70}Fe_{20}Si_{10}$ and $Ti_{65}Fe_{20}Si_{10}Zr_5$ show the highest pitting corrosion potential, ~ 2V. Additions of Pd, Ge and high amounts of Zr significantly decreased E_{pit}. In addition, the E_{pit} of all the alloys studied is lower than the potential of the human body (typically up to 0.4 V [189]). However, since pitting is one of the most common and dangerous corrosion mechanism in metallic implants [190], addition of Ge, Pd or high amount of Zr in Ti-Fe-Si system should be considered with care. Although from a theoretical point of view, metallic glasses are not subjected to pitting corrosion because of their perfect homogeneity, research presented to date show that in practice, pitting corrosion does occur [191, 192], most likely because of casting defects (oxides, nanocrystals, precipitation and so on).

Table 4.6 lists the information on Ti and Zr based metallic glasses proposed for biomedical application by other researchers. It can be seen that corrosion tests were frequently carried out in three different solutions, namely the Hank's solution, the Ringer's solution and the phosphate buffered saline (PBS). The results obtained in different body simulated solutions are comparable [193]. It can be concluded that Ti-Fe-Si and Ti-Fe-Si-Zr alloys studied in current thesis possess excellent corrosion properties, because they exhibit higher corrosion potential with wide passivation range compared to most of the alloys listed in Table 4.6. It can be also found in Table 4.6 that Ti based glassy alloys exhibit better corrosion resistance than Zr based glassy alloys.

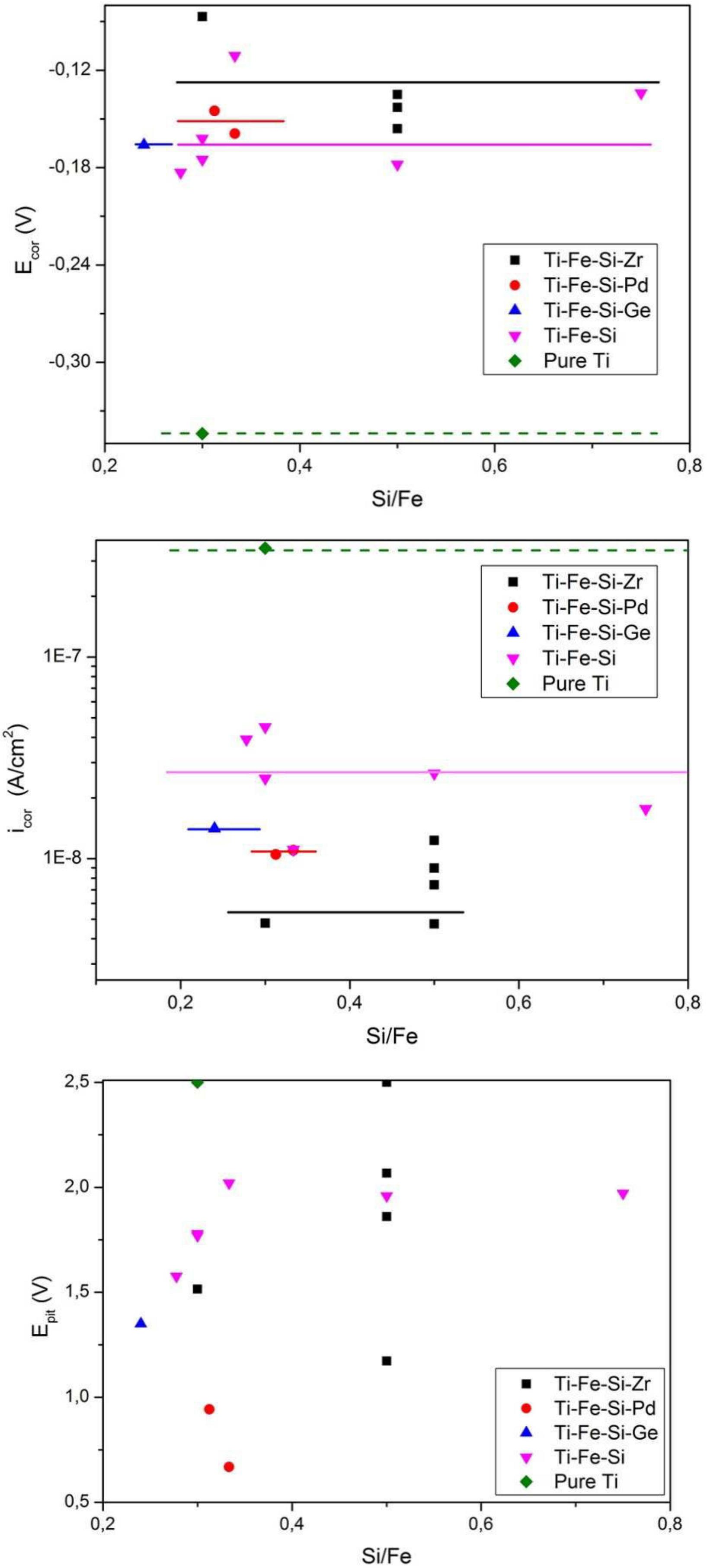

Fig.4.22 Diagrams showing the effect of alloy compositions on corrosion properties.

Table 4.6 Corrosion data of metallic glasses measured in biomedical solutions

Composition	Solution	E_{cor} (V)	i_{cor}(A/cm2)	I_{pas} (A/cm2)	E_{pit} (V)	reference
Ti75Zr10Si15	Ringer's	-0.274	2.8·10-8	2.7·10-7	>2**	Calin et al [194]
Ti60Zr10Nb10Si15		-0.295	1.5·10-8	1.8·10-7	>2**	
cp Ti (crystalline)		-0.286	2.6·10-8	3·10-6	>2**	
Ti40Zr10Cu38Pd12	Hank’s	-0.023	1.3·10-6	-	0.353	Fornell et al [195]
(Ti40Zr10Cu38Pd12)98Nb2		-0.041	5.93·10-6	-	0.282	
Ti40Zr10Cu38Pd12)97Nb3		0.007	3.77·10-6	-	0.412	
Ti40Zr10Cu38Pd12)96Nb4		0.019	3.17·10-7	-	0.270	
Ti60Zr10Ta15Si15	PBS	~-0.25 **	~5·10-8**	2·10-6	>1.5	Oak and Inoue [196]
Ti45 Zr15Pd35Si5	PBS	~0.05**	~1·10-7**	~3·10-6**	>2**	Oak and Inoue [134]
Ti45 Zr10Pd40Si5		~0.1**	~1·10-7**	~3·10-6**	>2**	
Ti45 Zr5 Pd45Si5		~0.15**	~1·10-7**	~3·10-6**	>2**	
Ti47.5Zr15Cu30Pd7.4Sn5 (ribbon)	PBS	~-0.05**	~7·10-8**	~4·10-7**	~0.38**	Qin et al [197]
Ti47.5Zr15Cu30Pd7.4Sn5 (ribbon)	Hank’s	~-0.01**	~8·10-8	~4·10-7	~0.42**	
Ti43.3Zr21.7Ni7.5Be27.5	PBS	-0.372±0.062	~7·10-8**	4·10-6 **	0.217±0.017	Morrison et al.[198]
Zr56Al16Co28	Hank’s	-0.635	-	-	0.459	A. Kawashima et al. [199]
Zr56Al16Co28	PBS	-0.580	-	-	-0.069	
Zr56Al16Co28	0.9%NaCl	-0.642	-	-	-0.062	
Zr60Cu22.5Fe7.5Al10	PBS	-0.37	2.01·10-7	-	-0.05	Monfared et al [200]
Zr60Cu20Fe10Al10		-0.39	2.64·10-7	-	0.07	
Zr60Ti6Cu19Fe5Al10		-0.42	2.34·10-7	-	0.28	
Zr65Pd17.5Fe10Al7.5	PBS	-0.179 ±69	2.51·10-7	-	0.187±0.037	Liu et al [201]
Zr65Pd12.5Ag5Fe10Al7.5		-0.171 ±0.39	0.71·10-7	-	0.335±0.116	

**calculated from the plots presented in their works.

4.7 *In situ* vitrification of Ti based metallic glasses

In the previous section, Ti-Fe-Si based metallic glasses were synthesized through melt spinning and their thermal properties as well as corrosion resistance were investigated. The properties of one material depend on its structure. If the structure of the material is resolved, then its properties can be easily analyzed and predicted. For glass former, the liquid transforms to glass during cooling from above liquidus temperature. The structure of the matter also experiences such a change during formation of metallic glass. Therefore, it is very important to understand the microstructural evolution of glass former during cooling process. The understanding can then be used as a guideline for synthesis of new metallic glass. $Ti_{40}Zr_{10}Cu_{34}Pd_{14}Sn_2$ possesses the highest glass forming ability among the known Ni-free Ti-based metallic glasses and its critical diameter for amorphization is 10 mm [202]. Therefore, it is an excellent candidate for vitrification during cooling in the levitation melting apparatus. A $Ti_{40}Zr_{10}Cu_{34}Pd_{14}Sn_2$ sphere of 2.4 mm diameter was heated up to melting (1200^{o}C) and cooled down to 300^{o}C. The temperature was recorded by a pyrometer during heating and cooling.

Fig.4.23 shows the cooling curve (temperature - time) of $Ti_{40}Zr_{10}Cu_{34}Pd_{14}Sn_2$ alloy during solidification process. It can be seen that the temperature decreases smoothly to the lower limit of pyrometer. No recalescence due to the release of latent heat was observed, implying that the $Ti_{40}Zr_{10}Cu_{34}Pd_{14}Sn_2$ alloy was successfully vitrified during cooling. An exponential fitting is then conducted to fit the recorded temperatures - time profile and cooling rate is calculated based on the fitting. It can be seen that the cooling rate varies from 160 ^{o}C/s at beginning of the cooling process to 30 ^{o}C/s at around 350^{o}C. Except the good glass forming ability of $Ti_{40}Zr_{10}Cu_{34}Pd_{14}Sn_2$, the use of a containerless solidification technique promotes the possibility of successful vitrification of the Ti based quinary alloys. Because it can diminishes the possibility of heterogeneous nucleation due to the contact with container walls.

X-ray diffraction patterns (diffracted intensity (I) - wave vector (Q)) of $Ti_{40}Zr_{10}Cu_{34}Pd_{14}Sn_2$ alloy obtained during cooling are shown in Fig.4.24. The absence of sharp Bragg peaks confirms the amorphous nature during cooling. It is interesting to notice that the second diffuse diffraction peak gradually splits into two subpeaks during cooling, indicating increasing ordering during formation of glass. The melting temperature (T_m) and glass transition temperature (T_g) temperatures reported by Zhu et al. [202] are also shown in Fig.4.24.

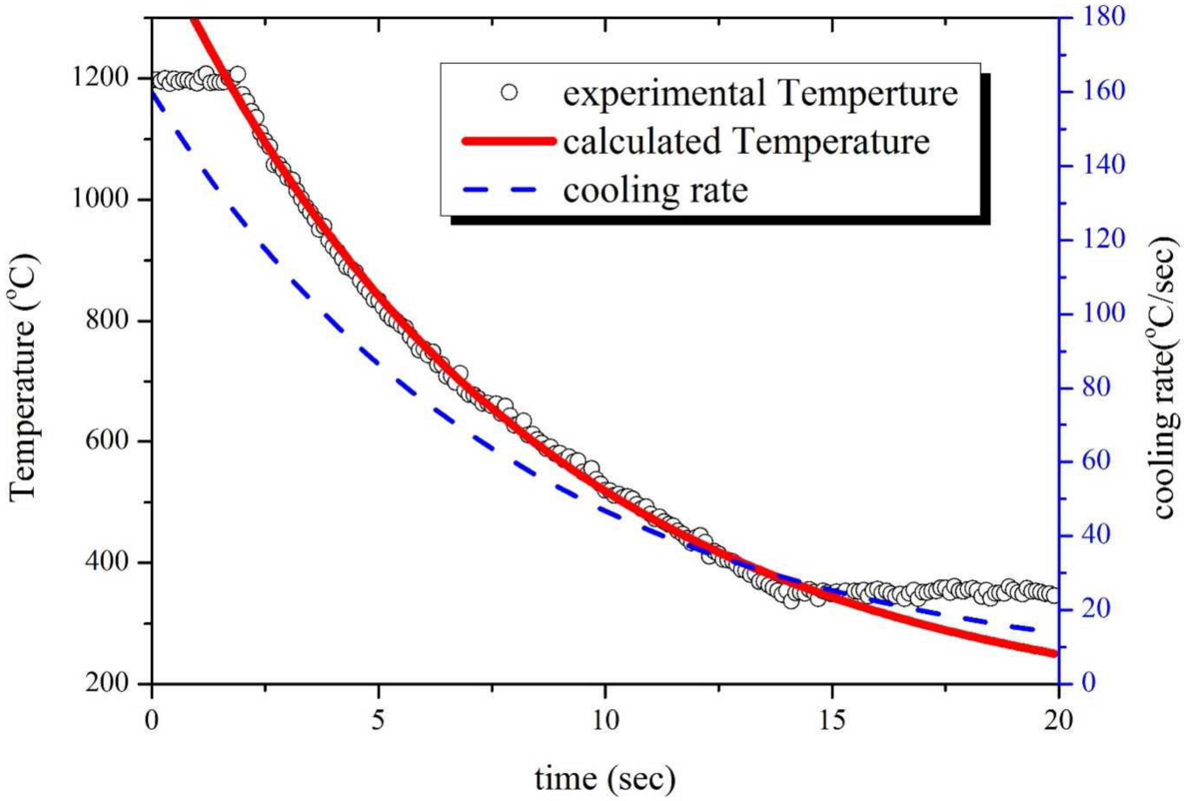

Fig.4.23 The calculated temperature (solid line) based on an exponential fitting of the experimental temperatures recorded by pyrometer (open circles). The cooling rate (dash line) is also calculated.

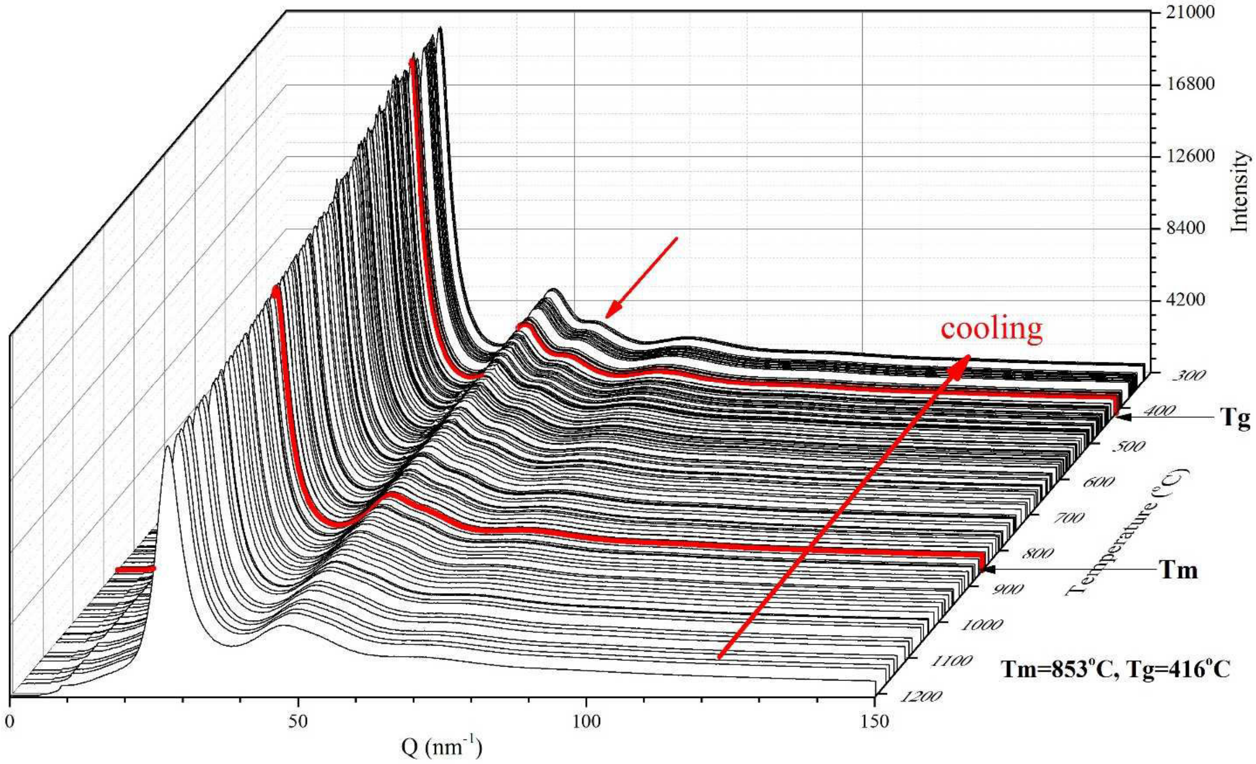

Fig.4.24 XRD spectra (intensity (I) - wave vector (Q) curves) obtained during continuous cooling of $Ti_{40}Zr_{10}Cu_{34}Pd_{14}Sn_2$ alloy. The characteristic temperatures are also indicated. (Tm, melting temperature and Tg, glass transition temperature [from [202]]. The arrow indicates the gradual splitting second peak.

Fig.4.25 shows the first diffuse peak of the XRD spectra at higher magnification. It can be seen that the position of the maximum of the first diffuse diffraction peak gradually shifts to high Q values during cooling. This result is in agreement with the decreasing interatomic distance during cooling. [203].

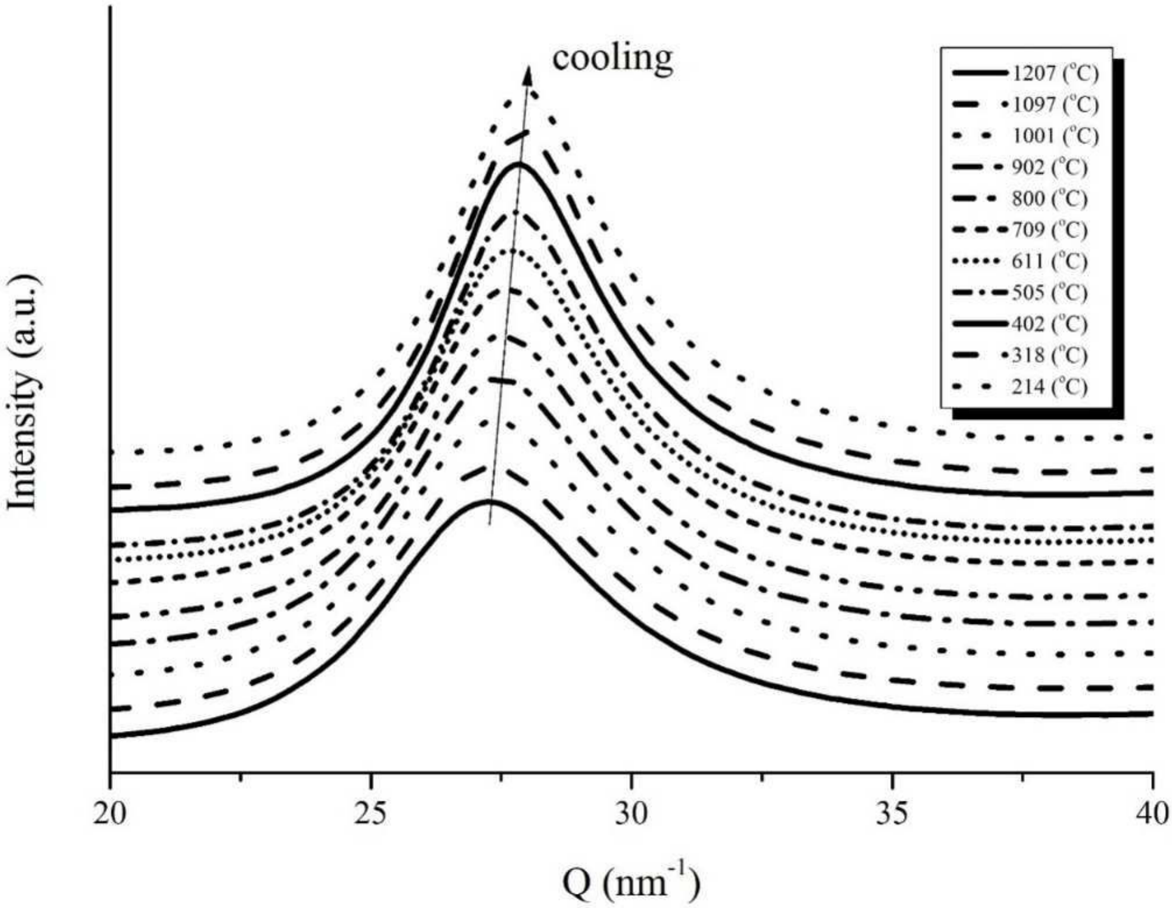

Fig.4.25 Variation of maxima of fist peak of intensity (I) - wave vector (Q) curves during cooling.

Yavari considered that if the variation of positions of maxima of first peak (Q_{max}) in I-Q curves is related to the mean atomic spacing [203], the third power of Q_{max} is inversely proportional to the mean atomic volume, as long as no structural change occurs. The temperature dependence of thermal expansion can then be calculated using Equation 4.2, where α_{th} is the volumetric thermal expansion coefficient, T_0 is the reference temperature and is selected arbitrarily as room temperature (298K).

$$\frac{V(T)}{V(T_0)} = \left[\frac{Q_{max}(T_0)}{Q_{max}(T)}\right]^3 = 1 + \alpha_{th} \times (T - T_0)$$

Equation 4.2

Fig.4.26 shows the temperature dependence of reduced position of first peak of I-Q curves ($(Q_{max}(T_0)/Q_{max}(T))^3$) during cooling. It can be found that a gradual slope change occurs between T_m and T_g, corresponding to the glass transition.

A linear fitting is performed to determine the volumetric thermal expansion coefficient, α_{th}. The α_{th} is 8.7×10^{-5} /K for the liquid state and 6×10^{-5} /K for glassy state.

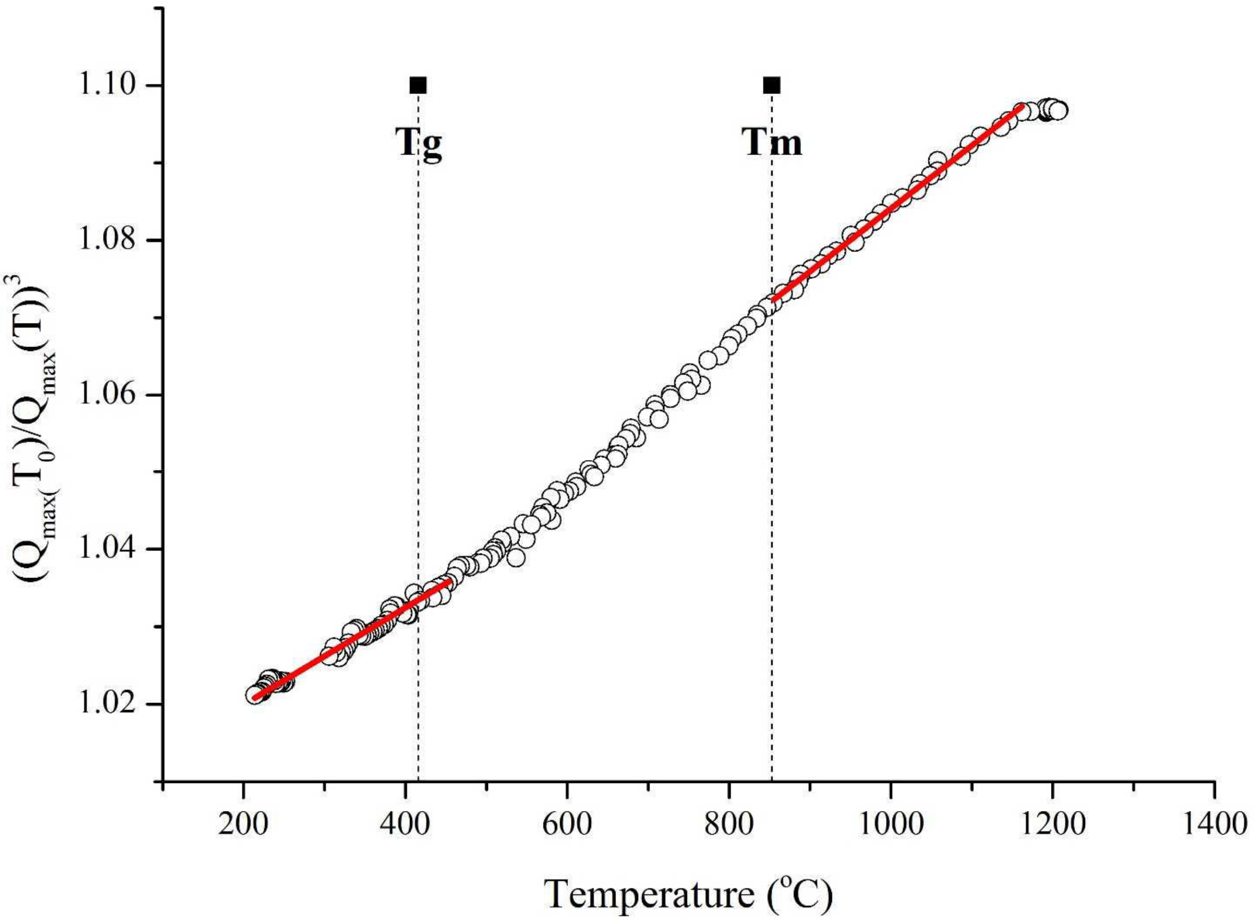

Fig.4.26 The variation of third power of reduced position of first peak of I-Q curves $[Q_{max}(T_0)/Q_{max}(T)]^3$ *during cooling. The slope of linear fitting curves indicates the thermal coefficient of* $Ti_{40}Zr_{10}Cu_{34}Pd_{14}Sn_2$ *alloy in supercooled liquid and glass state, respectively.*

The total structure factor, S(Q), is then obtained from I-Q curves using Equation 4.3

$$S(Q) = 1 + \frac{I(Q) - \sum_{i=1}^{n} c_i f_i^2}{(\sum_{i=1}^{n} c_i\, f_i)^2}$$

Equation 4.3

where I(Q) is the diffraction intensity, c_i is the atomic concentration and f_i is the X-ray atomic scattering factor of type i atoms [204, 205] and f_i depends on the atom chemical nature.

By using the Fourier transform of the structure factor, one can obtain the corresponding pair distribution function, G(r), as shown in Equation 4.4 [203, 206].

$$G(r) = 4\pi r^2[\rho(r) - \rho_0] = \frac{2}{\pi}\int_0^{\infty} Q[S(Q) - 1]\sin(rQ)\,dQ$$

Equation 4.4

where ρ(r) and ρ_0 is local and average atomic number density, respectively. G(r) is the reduced pair distribution function and it is related to the probability of finding another atom at a distance (r) from the atom at r = 0. The first peak of G(r) corresponds to the nearest neighbor shell. The second G(r) peak carries information on second nearest neighbor shell and therefore, reflects the atomic packing at medium range [206, 207]. The area below each peak of G(r) is correlated to the number of atoms in the corresponding coordination shell.

Metallic glasses exhibit short range order (SRO) and medium range order (MRO) but no long range order (LRO). Recent structural models are based on atomic cluster arrangements. For instance, Miracle proposed a face-center cubic packing of overlapping atom clusters connected by common shared atoms [208] and E. Ma et al. proposed an icosahedral packing of overlapping clusters [209]. The common feature of the above proposed structural models is that the atom clusters are connected by common shared atoms.

It has been reported that the splitting of second peak of G(r) is a characteristic difference between the metallic glass and its liquid state [206, 207, 210, 211]. The origin of the splitting is suggested to be related with the MRO [207, 211-213]. Pan et al. [207] studied the structural evolution of pure Fe and a glassy alloy $Cu_{50}Zr_{50}$ during solidification and found that the splitting of second peak of G(r) corresponds to the increase of vertex sharing and face sharing atoms.

The reduced pair distribution functions of $Ti_{40}Zr_{10}Cu_{34}Pd_{14}Sn_2$ at various temperatures during cooling are presented in Fig.4.27. Gradual structural changes occur during cooling from the liquid to the glassy structure as can be observed in the PDFs. Most characteristic is the shape change in the second PDF peak with a shoulder developing on the high r-side which gradually leads to a spitting of the peak at lower temperatures. The MRO in the liquid extends up to interatomic distances of about 15 nm or up to the sixth coordination shell, whereas in the glassy state, MRO extends up to 25 nm or up to the tenth coordination shell. It should be noted, however, there exist 15 different atomic pairs in this Ti-based quinary alloys. All of them contribute to the G(r), which in turn results in difficulty of analyzing the data.

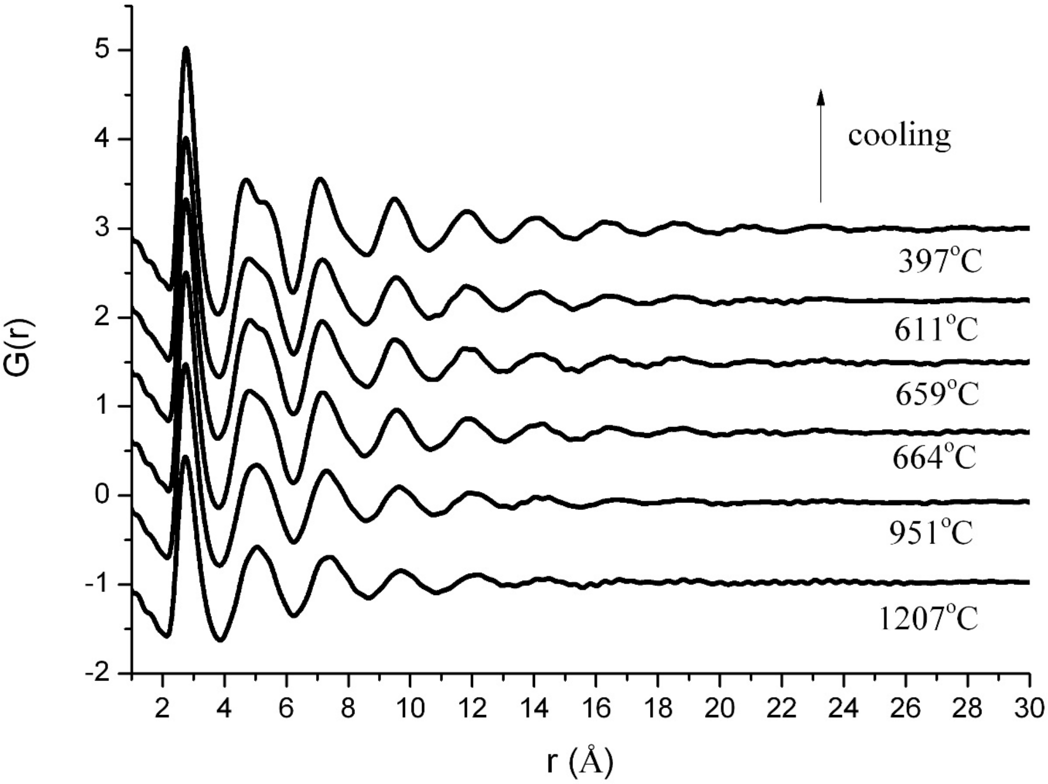

Fig.4.27 The reduced pair distribution function, G(r), of $Ti_{40}Zr_{10}Cu_{34}Pd_{14}Sn_2$ alloy at different temperatures during cooling

4.8 Conclusions

Ti based metallic glasses free of toxic elements were synthesized by rapid quenching. The glass formation of a wide range compositions based on the ternary Ti-Fe-Si system was investigated. It was found that the region near the ternary eutectic point ($Ti_{65}Fe_{30}Si_5$) is an icosahedral quasicrystal forming region, whereas the steeper side of this ternary eutectic point is the glass forming region. The icosahedral quasicrystal found in current Ti-Fe-Si system possess a quasi-lattice constant of 0.4956 nm.

Effect of minor elements addition on glass forming ability was also studied. It was found that with increasing content of Ge or Pd addition, the microstructure of as-cast ribbons changes from amorphous to icosahedral quasicrystal and finally to complicated cubic phase (Ti_2Fe) and simple crystalline phases. For Zr addition, when alloys are based on near eutectic compositions, similar tendency to that of Ge and Pd additions were found. On the other hand, when alloys are of high Si contents (10-15 at.%), i.e. a composition from steeper side of eutectic point, improved glass forming ability is obtained. However, as the Si content increases, the melting temperature of the alloys becomes higher, which in turn increases the difficulty of synthesizing glassy ribbons by the present melt spinning technique.

The thermal stability of the glassy Ti-Fe-Si based alloys was investigated by DSC. Upon annealing, the studied Ti-Fe-Si based alloys exhibit two stages of crystallization. The primary crystallization reaction corresponds to the partial transformation of amorphous phase to a complicated cubic phase Ti_2Fe. The secondary crystallization corresponds to formation of the simple crystalline phases which are predicted by the ternary phase diagram. The corrosion resistance of as-cast Ti-Fe-Si based glassy alloys in simulated body fluid (Hanks solution) was also investigated. It was found that the as-cast Ti-Fe-Si based glassy alloys possess better corrosion resistance than commercial purity Ti and most of the glassy alloys reported in the literature; Zr addition in Ti-Fe-Si based alloys improves the corrosion resistance. The $Ti_{65}Fe_{20}Si_{10}Zr_5$ glassy alloy possesses the highest corrosion potential and an extremely wide passivation region among the studied alloys.

In situ vitrification of a Ti based quinary metallic glass ($Ti_{40}Zr_{10}Cu_{34}Pd_{14}Sn_2$) was carried out using an aerodynamic levitation technique in a synchrotron beam. The alloy was successfully vitrified during cooling; the cooling rate was calculated to be 160 $^oC/s$ at beginning of cooling and exponentially decreases to 30 $^oC/s$ at around 350^oC. The volumetric thermal expansion coefficient was determined to be 8.7×10^{-5} /K for the liquid state and 6×10^{-5} /K for glassy state.

General Conclusions

There exist several major issues concerning the current orthopaedic implant alloys.

Firstly, the Young's moduli of currently used implant alloys are still much higher compared to those of human bones. Secondly, toxic or hypersensitive reactions occur due to ions released by constituent elements of implant alloys. Thirdly, relatively low wear or abrasive resistance of implant alloys makes them difficult to meet the needs of joint replacement.

Stainless steels, Co-Cr alloys and Ti-6Al-4V are the most used commercial alloys at the present time. The stainless steel alloys are the cheapest and easiest to fabricate.

It has been shown that Co, Cr and Ni ions released by implants can lead to carcinogenesis [28, 29]. These elements are mainly contained in the stainless steel and Co-Cr implant alloys. For Ti-based implant materials, V has been classified in the toxic group and the biocompatibility of Al is also not good due to tissue response of its capsule [12, 17, 30]. This leads to increasing concerns regarding utilization of Ti-6Al-4V implant alloys. Other elements like Mn, Cu, Mo, Zn, Ag are classified as low biocompatible or toxic [29, 31-34].

When compared to other metallic implant alloys, titanium and its alloys possess the Young's moduli closest to that of bone. This leads to the so called stress shielding effect and can result in bone regeneration [11]. The disadvantages of Ti based implant alloys are low shear strength, poor abrasion properties and high price compared to stainless steel.

Pure Ti and Ti-6Al-4V (commercial additions in weight percent) were initially designed as structural materials for aerospace. Later they were adopted in the medical use as implant materials. Addition of 6 wt.% Al and 4 wt.% V to pure Ti leads to much improved strength, comparable to cold worked stainless steel.

However, since it was found that V possesses toxicity [12], V-free Ti based implant alloys were then developed, such as Ti-6Al-7Nb [13] and Ti-5Al-2.5Fe [14], as well as Ti-15Zr and Ti-15Sn-based alloys [15]. All the above Ti based alloys are "HCP α + BCC β" type alloys. Although the Young's moduli of these α+β type alloys are much lower than those of stainless steels and Co-Cr alloys, they are still much higher than that of cortical bones, and this consequently leads to bone resorption.

It was later established that β-Ti possesses much lower Young's modulus than α-Ti. A series of β types was then been developed, such as Ti-13Nb-13Zr [16], Ti-15Mo [17], Ti-15Zr-4Nb-4Ta [18], Ti-35Nb-7Zr-5Ta [19] and others.

Besides α+β and β or near β type Ti-based implant alloys, researchers are also attempting to develop alloys exhibiting shape memory effect and superelasticity, such as Ti-Ni [20, 21], Ti-Nb-Ta [22] and Ti-Nb-Sn [23].

Please see chapter 1 for a thorough review of these issues.

TiNb has drawn great interest due to its good biocompatibility and excellent corrosion resistance. The Ti-Nb binary phase diagram shows a wide BCC β phase at high temperature and HCP α phase at low temperature. The β phase region becomes larger with increasing amount of Nb content as a β phase stabilizer.

The Young's modulus as a function of Nb content in the Ti-Nb binary system shows two minima around 15wt.% Nb and 40 wt.% Nb and therefore, the corresponding alloys $Ti_{92}Nb_8$ and $Ti_{74}Nb_{26}$ (at.%), were selected here for further studies. A new alloy with composition $Ti_{73}Nb_{25}Sn_2$ (at.%) was also synthesized in order to study the effect of Sn addition in Ti-Nb alloys since Sn has the ability to suppress the formation of the undesirable ω phase which has high elastic moduli [56].

The arc-melted ingots were injected into copper moulds. The as-cast samples were subsequently annealed at 1000°C for 5 hours followed by either slow furnace cooling to room temperature or fast quenching in ice water. The alloys were also cold rolled followed by heat treatment and then examined

Their microstructures were characterized by XRD, synchrotron radiation, SEM and optical microscope. Thermal properties and mechanical properties were investigated using DSC, compression, tension and ultrasonic measurements.

The compositions with higher Nb content, $Ti_{74}Nb_{26}$ and $Ti_{73}Nb_{25}Sn_2$, mainly consisted of β phase regardless of the preparation method.

For the lower Nb content alloy, $Ti_{92}Nb_8$, high cooling rate (copper mould casting and water quenching) favors the martensitic phase α'' and low cooling rate leads to precipitation of HCP α phase as predicted by the equilibrium phase diagram. The α'' martensitic phase is the transition phase between high temperature stable β phase and low temperature stable α phase.

The compressive behavior in three different states (as-cast, heat treated followed either by furnace cooling or water quenching) were investigated.

$Ti_{92}Nb_8$ samples of all three states exhibit non-linear behavior during loading-unloading cycles. Moreover, the residual strain was recovered to some extent when the sample was heated above the M_s temperature. The shape memory effect was observed for $Ti_{92}Nb_8$ samples and it results from the reorientation of existing martensites. However, due to the slower cooling rate, the non-linear elastic behavior is much less obvious in furnace cooled sample than in samples which were subjected to higher cooling rate. This results from the precipitation of equilibrium α phase

Full details about the microstructure and mechanical properties are given in chapter 3.

The non-linear elastic behavior is much stronger for the $Ti_{74}Nb_{26}$ alloy compared to the $Ti_{92}Nb_8$. This superelasticity originates from stress-induced martensitic transformation. The M_s of $Ti_{74}Nb_{26}$ is around 0°C. However, with the aid of stress during loading, this high temperature β phase can transform into martensitic α'' phase; while during unloading, the martensitic α'' phase becomes unstable and mostly transforms back to the β phase. The cyclic loading-unloading stress-strain curve of water quenched samples indicates that with increasing strain, the superelastic behavior becomes incomplete. This is due to the onset of permanent plastic deformation of TiNb alloy. In the $Ti_{74}Nb_{26}$ alloy, there exist two competitive deformation mechanisms, stress-induced martensitic transformation and permanent plastic deformation. The deformation with lower critical stress commences first and diminishes the extent of the other deformation. Low critical stresses in TiNb alloys impede the occurrence of superelasticity. Therefore any method that increases the critical stress for permanent plastic deformation (such as cold rolling) will enhance the stability of superelasticity.

Different from the non-linear behavior of stress-strain curve of the two binary alloys, the $Ti_{73}Nb_{25}Sn_2$ ternary alloy exhibits rather linear behavior during loading and unloading. There is also little difference among the three curves of as-cast and annealed samples, except that the yield stress of as-cast sample is slightly higher than those of the other two samples

Due to the existence of superelasticity, it is of little physical meaning to calculate the Young's modulus (E) from the stress-strain curves. Ultrasonic measurements were therefore conducted to measure E as reported in the Table below. It can be seen that the furnace cooled $Ti_{92}Nb_8$ possesses the highest E, resulting from the precipitation of equilibrium α phase. Comparing the Young's moduli of the ternary alloys and those of the binary, it is found that addition of Sn has little influence on Young's modulus. For alloys with higher Nb content, the samples subjected to water quenching exhibit the lowest E. Finally, the Young's moduli derived from stress-strain curves and measured by ultrasonic waves show similar values.

*Table 3.3 Young's moduli (E) obtained by ultrasonic measurements for $Ti_{92}Nb_8$, $Ti_{74}Nb_{26}$ and $Ti_{73}Nb_{25}Sn_2$ alloys in three different states (as-cast, heat treatment followed either by furnace cooling or water quenching). Some Young's moduli calculated from stress-strain curves are also listed as comparison (indicated by *).*

E (GPa)	$Ti_{92}Nb_8$	$Ti_{74}Nb_{26}$	$Ti_{73}Nb_{25}Sn_2$	
as-cast	71	81	77*	77
furnace cooling	93	77	76*	81
water quenching	72	60	69*	64

A processing strategy of work hardening was designed to increase the yield strength of $Ti_{74}Nb_{26}$ alloy. Work hardening was realized by cold rolling. Precipitation strengthening was achieved by annealing at intermediate temperatures.

Cyclic tensile tests were conducted to investigate the mechanical properties of thermomechanically treated $Ti_{74}Nb_{26}$ alloys. No residual strain is left upon unloading even subjected to 400 MPa. Compared to the incomplete loop of water quenched $Ti_{74}Nb_{26}$ alloy, the stability of superelasticity is greatly improved in the thermomechanically treated $Ti_{74}Nb_{26}$ alloys. As stated previously, this results from the enhanced critical stress of permanent plastic deformation. It can be concluded that on introducing high density of dislocations and suitable heat treatment, the stability of superelasticity is greatly improved in $Ti_{74}Nb_{26}$ alloys.

Thus, all three alloys show elastic moduli well below those of commercial titanium alloys. Superelasticity in Ti-Nb alloys is confirmed and can provide future application opportunity, such as dental fixation.

A different approach to reducing the moduli of Ti-based alloys is through the development of

Ti-based metallic glasses (MGs).

MGs show about 6% lower bulk modulus, about 10% less Young modulus and around30% less shear modulus than that of their crystalline counterparts [99]. From this point of view, they are good candidates for developing implant alloys of low Young's modulus.

So far, best glass forming ability has been found in Zr-, Fe-, Pd-, Mg-, Cu-, and Ni-based alloys. However, the high Young's moduli of Zr-, Fe-, Cu-based metallic glasses limits their potential applications as implant alloys. In addition, almost all of the above metallic glasses contain elements, such as Cu, Ni, V, Al, which can release toxic ions in human body fluid environment.

On the other hand, Ti metallic glasses have relatively low Young's modulus compared to the above MGs.

So far, Ti based alloys with good glass forming ability contain Ni and/or Cu. There are mainly two families of Ti based MGs, Ti-Cu-Ni based and Ti-Cu based. By introducing minor elemental additions, such as Be, Zr, Co to the near eutectic compositions in Ti-Cu-Ni system, the glass forming ability of Ti-Cu-Ni based MGs can increase. For Ni free Ti based MGs, the most successful is Ti-Zr-Cu-Pd-Sn quinary system, whose glass forming ability is up to 10 mm thickness. However, because of toxic or hypersensitivity reactions and resulting possible carcinogenesis [28, 29], Ni and Cu must be excluded in the newly designed MGs. From the point of view of the elements' biocompatibility, as stated in chapter 1, only Fe, main group IV elements (Si, Ge and Sn), several of Ti's neighboring elements (Zr, Nb, Hf and Ta), as well as precious metals (Pd, Ag, Pt and Au) are suitable as candidate elemental additions.

Based on the binary phase diagrams and elements' biocompatibility, deep eutectic systems like Ti-Fe and Ti-Si can be considered as good starting systems for synthesizing new Ti based MGs. Louzguine et al [175] investigated the glass formation of Ti-Fe binary system and found that no MGs can be synthesized in this system. The large solubility of Fe (up to 22 at.% at 1085°C) in β-Ti might be the reason why it is difficult to obtain MGs in Ti-Fe binary system.

Based on the data collected, Ti-Fe-Si ternary system was retained for development of glassy alloys free of toxic elements.

It was found that the region near the ternary eutectic point ($Ti_{65}Fe_{30}Si_5$) is an icosahedral quasicrystal forming region, whereas the steeper side of this ternary eutectic point is a glass forming region.

Effect of minor elements addition on glass forming ability was also studied. It was found that with increasing content of Ge or Pd addition, the microstructure of as-cast ribbons changes from amorphous to icosahedral quasicrystal and finally to complicated cubic phase (Ti_2Fe) and simple crystalline phases. For Zr addition, similar tendency upon alloys is found.

On the other hand, when alloys of high Si contents, i.e. a composition from steeper side of eutectic point, exhibit better glass forming ability. However, as the Si content increases, the melting temperature of the alloys become higher and increases the difficulty in synthesizing glassy ribbons by the present melt spinning techniques.

The corrosion resistance of as-cast Ti-Fe-Si based glassy alloys in simulated body fluid (Hanks solution) was investigated. It was found that the as-cast Ti-Fe-Si based glassy alloys possess better corrosion resistance than commercial purity Ti and most of the glassy alloys reported in the literature.

The $Ti_{65}Fe_{20}Si_{10}Zr_5$ glassy alloy possesses the highest corrosion potential and an extremely wide passivation region among the studied alloys.

This work was funded by the EC ITN Network “BioTiNet” grant No. 264635.

References

[1] B.D. Ratner, S.J. Bryant, Annual Review of Biomedical Engineering, 6 (2004) 41-75.
[2] B.M. Holzapfel, J.C. Reichert, et al., Advanced Drug Delivery Reviews, 65 (2013) 581-603.
[3] L.L. Hench, Biomaterials, 19 (1998) 1419-1423.
[4] J.M. Anderson, A. Rodriguez, et al., Seminars in Immunology, 20 (2008) 86-100.
[5] marketsandmarkets.com, 2013.
[6] J. Black, Biomaterials for internal fixation, Philadelphia, 1980.
[7] M.J. Yaszemski, Biomaterials in orthopedics, New York, 2004.
[8] C.D. Newton, N.D. M., Textbook of small animal orthopaedics, Lippincott, Philadelphia, 1985.
[9] M. Kamitakahara, C. Ohtsuki, et al., Journal of Biomaterials Applications, 23 (2008) 197-212.
[10] J. Tinschert, G. Natt, et al., Journal of Biomedical Materials Research Part B: Applied Biomaterials, 80B (2007) 317-321.
[11] D.R. Sumner, J.O. Galante, Clin. Orthop. Rel. Res., (1992) 202-212.
[12] European Conference on Biomaterials - Evaluation of biomaterials, J. Wiley, Chichester, New York, 1980.
[13] M. Semlitsch, Clinical Materials, 2 (1987) 1-13.
[14] K.H. Browy, K.H. Kramer, in: G. Lutjering, et al. (Eds.) Titanium science and technology, Deutsche Geshellshaft fur Metallkunde E.V. , 1985, pp. 1381-1386.
[15] Y. Okazaki, Y. Ito, et al., Journal of the Japan Institute of Metals, 59 (1995) 108-115.
[16] J.A. Davidson, A.K. Mishra, et al., Bio-medical materials and engineering, 4 (1994) 231-243.
[17] Y. Okazaki, Y. Ito, et al., Materials Science and Engineering: A, 213 (1996) 138-147.
[18] Y. Okazaki, Current Opinion in Solid State & Materials Science, 5 (2001) 45-53.
[19] T. Ahmed, M. Long, et al., in: P.A. Blenkinsop, et al. (Eds.) Titanium '95, UK: Institute of Metals, London, 1996, pp. 1760-1767.
[20] A. Wichelhaus, L. Brauchli, et al., American Journal of Orthodontics and Dentofacial Orthopedics, 137 (2010) 671-678.
[21] A. Bansiddhi, T.D. Sargeant, et al., Acta Biomater., 4 (2008) 773-782.
[22] E. Bertrand, T. Gloriant, et al., Journal of the Mechanical Behavior of Biomedical Materials, 3 (2010) 559-564.
[23] T. Ozaki, H. Matsumoto, et al., Materials Transactions JIM, 45 (2004) 2776-2779.
[24] M. Kutz, Biomedical engineering and design handbook, McGraw-Hill, New York, 2009.
[25] D.T. Reilly, A.H. Burstein, Journal of Biomechanics, 8 (1975) 393-405.
[26] R. Huiskes, H. Weinans, et al., Clin. Orthop. Rel. Res., (1992) 124-134.
[27] D.R. Sumner, T.M. Turner, et al., Journal of Biomechanics, 31 (1998) 909-917.
[28] K.L. Wapner, Clin. Orthop. Rel. Res., (1991) 12-20.
[29] D.B. McGregor, R.A. Baan, et al., European Journal of Cancer, 36 (2000) 307-313.
[30] E. Eisenbarth, D. Velten, et al., Biomaterials, 25 (2004) 5705-5713.
[31] M. Calin, A. Gebert, et al., Materials Science and Engineering: C, 33 (2013) 875-883.
[32] G. Sjögren, G. Sletten, et al., The Journal of Prosthetic Dentistry, 84 (2000) 229-236.

[33] J.C. Hornez, A. Lefèvre, et al., Biomolecular Engineering, 19 (2002) 103-117.
[34] W.M. Elshahawy, I. Watanabe, et al., Dent Mater, 25 (2009) 1551-1555.
[35] R. Boyer, G. Welsch, et al., Materials properties handbook titanium alloys, ASM International, Materials Park, OH, 1994.
[36] P. Villars, K. Cenzual, Pearson's Crystal Data: Crystal Structure Database for Inorganic Compounds (on CD-ROM), Release 2010/11, ASM International®, Materials Park, Ohio, USA.
[37] F.B. Cuff, N.J. Grant, et al., Trans. Am. Inst. Min. Metall. Pet. Eng. , 194 (1952) 848-853.
[38] W.G. Burgers, Physica, 1 (1934) 561-586.
[39] C. Leyens, M. Peters, Titanium and Titanium Alloys Fundamentals and Applications, WILEY-VCH, 2003.
[40] D.L. Moffat, U.R. Kattner, Metall Trans A, 19 (1988) 2389-2397.
[41] J.M. Silcock, Acta Metall Mater, 6 (1958) 481-493.
[42] S.L. Sass, Acta Metall Mater, 17 (1969) 813-820.
[43] S.L. Sass, Journal of Applied Crystallography, 4 (1971) 252-254.
[44] A.T. Balcerzak, S.L. Sass, Metall. Trans. B, 3 (1972) 1601-1605.
[45] D.L. Moffat, D.C. Larbalestier, Metall Trans A, 19 (1988) 1687-1694.
[46] D.L. Moffat, D.C. Larbalestier, Metall Trans A, 19 (1988) 1677-1686.
[47] S.K. Sikka, Y.K. Vohra, et al., Progress in Materials Science, 27 (1982) 245-310.
[48] B.S. Hickman, Journal of Materials Science, 4 (1969) 554-563.
[49] D. De Fontaine, Acta Metall Mater, 18 (1970) 275-279.
[50] D. De Fontaine, N.E. Paton, et al., Acta Metall Mater, 19 (1971) 1153-1162.
[51] D. De Fontaine, R. Kikuchi, Acta Metall Mater, 22 (1974) 1139-1146.
[52] T. Ahmed, H.J. Rack, Journal of Materials Science, 31 (1996) 4267-4276.
[53] H.Y. Kim, Y. Ikehara, et al., Acta Materialia, 54 (2006) 2419-2429.
[54] H. Matsumoto, S. Watanabe, et al., Materials Transactions JIM, 46 (2005) 1070-1078.
[55] Y.L. Zhou, M. Niinomi, et al., Materials Science and Engineering a-Structural Materials Properties Microstructure and Processing, 371 (2004) 283-290.
[56] J.C. Williams, B.S. Hickman, et al., Metallurgical and Materials Transactions A, 2 (1971) 477-484.
[57] Y.L. Zhou, M. Niinomi, et al., Materials Transactions JIM, 45 (2004) 1549-1554.
[58] C.R. Wong, R.L. Fleischer, Journal of Materials Research, 9 (1994) 1441-1448.
[59] S.G. Fedotov, T.V. Chelidze, et al., Fizika Metallov 62 (1986) 328-332.
[60] K.A. Bywater, J.W. Christian, Philosophical Magazine, 25 (1972) 1275-1289.
[61] S. Hanada, T. Ozaki, et al., Thermec'2003, 426-4 (2003) 3103-3108.
[62] Y.L. Hao, S.J. Li, et al., Materials Science and Engineering A, 441 (2006) 112-118.
[63] A.R. Yavari, K. Ota, et al., Acta Materialia, 56 (2008) 1830-1839.
[64] A.R. Yavari, Y. Li, et al., Journal of Materials Research, 24 (2009) 1513-1521.
[65] Y. Li, K. Georgarakis, et al., Journal of Alloys and Compounds, 477 (2009) 346-349.
[66] K. Otsuka, Shape memory materials, Cambridge Univ. Press, Cambridge, 1999.
[67] H. Warlimont, L. Delaey, et al., Journal of Materials Science, 9 (1974) 1545-1555.
[68] D.A. Porter, K.E. Easterling, Phase transformations in metals and alloys, Van Nostrand Reinhold, New York, 1981.
[69] K. Otsuka, R. X, Progress in Materials Science, 50 (2005) 511-678.

[70] R.V. Krishnan, L. Delaey, et al., Journal of Materials Science, 9 (1974) 1536-1544.
[71] L. Delaey, R.V. Krishnan, et al., Journal of Materials Science, 9 (1974) 1521-1535.
[72] T. Zhou, M. Aindow, et al., Scripta Materialia, 50 (2004) 343-348.
[73] L.C. Zhang, T. Zhou, et al., Applied Physics Letters, 87 (2005).
[74] L.C. Zhang, T. Zhou, et al., Journal of Materials Science, 40 (2005) 2833-2836.
[75] H.Y. Kim, H. Satoru, et al., Materials Transactions JIM, 45 (2004) 2443-2448.
[76] H.Y. Kim, J.I. Kim, et al., Materials Science and Engineering A, 438 (2006) 839-843.
[77] E. Takahashi, T. Sakurai, et al., Materials Transactions JIM, 43 (2002) 2978-2983.
[78] H. Matsumoto, S. Watanabe, et al., Journal of Alloys and Compounds, 439 (2007) 146-155.
[79] Y.L. Hao, S.J. Li, et al., Acta Biomater., 3 (2007) 277-286.
[80] K.F. Kelton, A.L. Greer, Nucleation in condensed matter applications in materials and biology, Pergamon, Amsterdam, 2010.
[81] M.K. Miller, P.K. Liaw, Bulk metallic glasses an overview, Springer, New York, 2008.
[82] C. Suryanarayana, A. Inoue, Bulk metallic glasses, CRC Press, Boca Raton, FL, 2011.
[83] F. Faupel, W. Frank, et al., Reviews of Modern Physics, 75 (2003) 237-280.
[84] C.A. Angell, Science, 267 (1995) 1924-1935.
[85] R. Busch, Y.J. Kim, et al., J Appl Phys, 77 (1995) 4039-4043.
[86] C.A. Angell, J Phys Chem Solids, 49 (1988) 863-871.
[87] W. Klement, R.H. Willens, et al., Nature, 187 (1960) 869-870.
[88] H.S. Chen, D. Turnbull, Acta Metall Mater, 17 (1969) 1021-1031.
[89] A. Inoue, T. Zhang, et al., Materials Transactions JIM, 31 (1990) 425-428.
[90] A. Inoue, T. Zhang, et al., Materials Transactions JIM, 31 (1990) 177-183.
[91] A. Inoue, H. Yamaguchi, et al., Materials Transactions JIM, 31 (1990) 104-109.
[92] A. Peker, W.L. Johnson, Applied Physics Letters, 63 (1993) 2342-2344.
[93] A. Inoue, N. Nishiyama, et al., Materials Transactions JIM, 38 (1997) 179-183.
[94] D. Turnbull, M.H. Cohen, J Chem Phys, 29 (1958) 1049-1054.
[95] D. Turnbull, Contemporary Physics, 10 (1969) 473-488.
[96] Z.P. Lu, C.T. Liu, Acta Materialia, 50 (2002) 3501-3512.
[97] A. Inoue, Acta Materialia, 48 (2000) 279-306.
[98] W.H. Wang, Progress in Materials Science, 57 (2012) 487-656.
[99] C.A. Schuh, T.C. Hufnagel, et al., Acta Materialia, 55 (2007) 4067-4109.
[100] A. Inoue, A. Takeuchi, Acta Materialia, 59 (2011) 2243-2267.
[101] D.C. Hofmann, Journal of Materials, 2013 (2013) 8.
[102] T. Zhang, A. Inoue, et al., Materials Science and Engineering: A, 181–182 (1994) 1423-1426.
[103] A. Inoue, T. Masumoto, et al., J. Phys. Colloques, 41 (1980) C8-758-C758-761.
[104] A. Inoue, A. Hoshi, et al., Scripta Metallurgica, 14 (1980) 1077-1082.
[105] A. Inoue, H. Kimura, et al., in: H. Kimura, O. Izumi (Eds.) 4th International Conference on Titanium, Metallurgical Society of AIME, Kyoto, 1980, pp. 1137-1145.
[106] A. Inoue, N. Nishiyama, et al., Materials Letters, 19 (1994) 131-135.
[107] G. He, J. Eckert, et al., Metall Mater Trans A, 35A (2004) 3605-3612.
[108] G. He, J. Eckert, et al., Acta Materialia, 52 (2004) 3035-3046.
[109] G. He, J. Eckert, et al., J Appl Phys, 95 (2004) 1816-1821.

[110] D.E. Polk, A. Calka, et al., Acta Metall Mater, 26 (1978) 1097-1103.
[111] K. Amiya, N. Nishiyama, et al., Materials Science and Engineering A, 179 (1994) 692-696.
[112] T. Zhang, A. Inoue, Materials Transactions JIM, 39 (1998) 1001-1006.
[113] G. He, J. Eckert, et al., Acta Materialia, 51 (2003) 1621-1631.
[114] Y.C. Kim, W.T. Kim, et al., Materials Science and Engineering A, 375 (2004) 127-135.
[115] T. Zhang, A. Inoue, Materials Transactions JIM, 40 (1999) 301-306.
[116] A. Inoue, H.S. Chen, et al., Journal of Non-Crystalline Solids, 68 (1984) 63-73.
[117] Y.C. Kim, W.T. Kim, et al., Materials Transactions JIM, 43 (2002) 1243-1246.
[118] C.L. Ma, S. Ishihara, et al., Materials Transactions JIM, 45 (2004) 1802-1806.
[119] J.M. Park, H.J. Chang, et al., Scripta Materialia, 53 (2005) 1-6.
[120] M.X. Xia, C.L. Ma, et al., Materials Science and Engineering A, 390 (2005) 372-375.
[121] K.B. Kim, B.C. Ko, et al., Materials Science and Engineering A, 366 (2004) 421-425.
[122] K. Fujita, T. Hashimoto, et al., Journal of the Japan Institute of Metals, 70 (2006) 816-823.
[123] J.J. Oak, A. Inoue, Materials Science and Engineering A, 449 (2007) 220-224.
[124] B.C. Lu, Y.L. Wang, et al., Journal of Alloys and Compounds, 475 (2009) 157-164.
[125] J.J. Oak, H. Kimura, et al., Advanced Materials and Processing, 26-28 (2007) 785-788.
[126] Z.Y. Suo, K.Q. Qiu, et al., Materials Science and Engineering A, 527 (2010) 2486-2491.
[127] J.J. Oak, D. Louzguine, et al., Materials Science and Engineering C, 29 (2009) 322-327.
[128] E.H. Yin, M. Zhang, et al., Journal of Alloys and Compounds, 504 (2010) S10-S13.
[129] S.L. Zhu, X.M. Wang, et al., Materials Transactions JIM, 48 (2007) 2445-2448.
[130] L. Zhao, Z.Q. Zhang, et al., Int J Mod Phys B, 24 (2010) 2326-2331.
[131] S.L. Zhu, X.M. Wang, et al., Intermetallics, 16 (2008) 1031-1035.
[132] X.F. Zhang, H.X. Li, et al., Nano-Scale and Amourphous Materials, 688 (2011) 400-406.
[133] L. Bai, C.X. Cui, et al., Journal of Non-Crystalline Solids, 354 (2008) 3935-3938.
[134] J.J. Oak, A. Inoue, Journal of Non-Crystalline Solids, 354 (2008) 1828-1832.
[135] M.X. Xia, H.X. Zheng, et al., Acta Metallurgica Sinica, 41 (2005) 199-202.
[136] M.X. Xia, H.X. Zheng, et al., Journal of Non-Crystalline Solids, 351 (2005) 3747-3751.
[137] M.X. Xia, H.X. Zheng, et al., Rare Metal Mat Eng, 34 (2005) 1235-1238.
[138] F.X. Qin, X.M. Wang, et al., Intermetallics, 16 (2008) 1026-1030.
[139] E.H. Yin, S.J. Pang, et al., Journal of Alloys and Compounds, 546 (2013) 7-13.
[140] I. Seki, H. Kimura, et al., Materials Transactions JIM, 49 (2008) 498-501.
[141] W.J. Boettinger, DTA and heat-flux DSC measurements of alloy melting and freezing, U.S. Dept. of Commerce, Technology Administration, National Institute of Standards and Technology, [Gaithersburg, Md.], 2006.
[142] M.B. Reynolds, The Determination of the Elastic Constants of Metals by the Ultrasonic Pulse Technique, Knolls Atomic Power Laboratory, 1952.

[143] P. Goodhew, J. Humphreys, Electron microscopy and analysis, Taylor & Francis, London, 2001.
[144] L. Hennet, I. Pozdnyakova, et al., Rev Sci Instrum, 77 (2006).
[145] C. Landron, L. Hennet, et al., Rev Sci Instrum, 71 (2000) 1745-1751.
[146] M. Long, H.J. Rack, Biomaterials, 19 (1998) 1621-1639.
[147] J.L. Murray, Phase diagrams of binary titanium alloys, ASM International, 1987.
[148] E.W. Collings, The Physical Metallury of Titanium Alloys (Asm Series in Metal Processing, Vol 3), Asm Intl, 1984.
[149] D. Kuroda, M. Niinomi, et al., Materials Science and Engineering a-Structural Materials Properties Microstructure and Processing, 243 (1998) 244-249.
[150] W.Y. Kim, H.S. Kim, et al., Scripta Materialia, 54 (2006) 887-891.
[151] H. Matsumoto, S. Watanabe, et al., Metall Mater Trans A, 37A (2006) 3239-3249.
[152] B. European Conference on, Evaluation of biomaterials / edited by George D. Winter, Jean L. Leray, Klaas de Groot, J. Wiley, Chichester ; New York :, 1980.
[153] C.M. Chan, S. Trigwell, et al., Surf Interface Anal, 15 (1990) 349-354.
[154] Y. Shugo, Materials Science Forum, 56-58 (1990) 631-636.
[155] E. Cerreta, G.T. Gray, et al., J Appl Phys, 100 (2006) -.
[156] S. Uehara, H. Sasano, et al., Journal of the Japan Society of Powder and Powder Metallurgy, 33 (1986) 73-77.
[157] J. Otubo, O.D. Rigo, et al., Materials Science and Engineering: A, 481–482 (2008) 639-642.
[158] K. Bhattacharya, Microstructure of martensite : why it forms and how it gives rise to the shape-memory effect, Oxford University Press, Oxford, 2003.
[159] D.S. Lieberman, M.S. Wechsler, et al., J Appl Phys, 26 (1955) 473-484.
[160] J.L. Murray, Phase diagram of binary titanium alloys, ASM (1987).
[161] M. Rappaz, C.A. Gandin, Acta Metallurgica and Materialia, 41 (1993) 345-360.
[162] C.Y. Wang, C. Beckermann, Metall Trans A, 24 (1993) 2787-2802.
[163] C.Y. Wang, C. Beckermann, Metall Mater Trans A, 25 (1994) 1081-1093.
[164] C.A. Gandin, M. Rappaz, Acta Metallurgica Et Materialia, 42 (1994) 2233-2246.
[165] W. Kurz, C. Bezençon, et al., Science and Technology of Advanced Materials, 2 (2001) 185.
[166] M.A. Martorano, C. Beckermann, et al., Metall Mater Trans A, 34A (2003) 1657-1674.
[167] G. Welsch, R. Boyer, et al., Materials Properties Handbook: Titanium Alloys, Asm International, 1994.
[168] C.M. Lee, C.P. Ju, et al., J Oral Rehabil, 29 (2002) 314-322.
[169] D. Hull, D.J. Bacon, Introduction to Dislocations, Elsevier Science, 2011.
[170] C.S. Barrett, Structure of metals, McGraw-Hill, 1943.
[171] R.W. Davidge, Mechanical behaviour of ceramics, Cambridge University Press, Cambridge, 1980.
[172] J. Huang, H. Xing, et al., Scripta Materialia, 66 (2012) 682-685.
[173] W.H. Wang, Journal of Non-Crystalline Solids, 351 (2005) 1481-1485.
[174] C. Suryanarayana, I. Seki, et al., Journal of Non-Crystalline Solids, 355 (2009) 355-360.
[175] D.V. Louzguine-Luzgin, L.V. Louzguina-Luzgina, et al., Materials for Space Applications, 851 (2005) 227-232

581.
[176] F. Weitzer, J.C. Schuster, et al., Intermetallics, 16 (2008) 273-282.
[177] V. Elser, Physical Review B, 32 (1985) 4892-4898.
[178] J.Q. Guo, E. Abe, et al., Physical Review B, 62 (2000) R14605-R14608.
[179] K.F. Kelton, MRS Online Proceedings Library, 553 (1998) 471-482.
[180] F.C. Frank, Proceedings of the Royal Society of London. Series A. Mathematical and Physical Sciences, 215 (1952) 43-46.
[181] K.F. Kelton, G.W. Lee, et al., Physical Review Letters, 90 (2003).
[182] D. Holland-Moritz, D.M. Herlach, et al., Physical Review Letters, 71 (1993) 1196-1199.
[183] D. Turnbull, R.E. Cech, J Appl Phys, 21 (1950) 804-810.
[184] D. Holland-Moritz, O. Heinen, et al., Materials Science and Engineering A, 413 (2005) 403-407.
[185] O. Heinen, D. Holland-Moritz, et al., J Cryst Growth, 286 (2006) 146-151.
[186] O. Heinen, D. Holland-Moritz, et al., Materials Science and Engineering A, 449 (2007) 662-665.
[187] D. Holland-Moritz, Materials Science and Engineering: A, 304–306 (2001) 108-113.
[188] G.A. Yurko, J.W. Barton, et al., Acta Crystallographica, 12 (1959) 909-911.
[189] W.Kajzer, A. Krauze, et al., Journal of Achievements in Materials and Manufacturing Engineering, 31 (2008) 247-253.
[190] R.A. Gittens, R. Olivares-Navarrete, et al., Journal of Dental Research, 90 (2011) 1389-1397.
[191] F. Qin, M. Yoshimura, et al., Materials Transactions, 48 (2007) 1855-1858.
[192] F. Qin, X. Wang, et al., Materials Transactions, 47 (2006) 1934-1937.
[193] L. C.-h., M. Z.-q., Transactions of Nonferrous Metals Society of China, 11 (2001) 579-582.
[194] M. Calin, A. Gebert, et al., Materials Science and Engineering C, 33 (2013) 875-883.
[195] J. Fornell, E. Pellicer, et al., Materials Science and Engineering A, 559 (2013) 159-164.
[196] J.J. Oak, A. Inoue, Materials Science and Engineering A, 448-451 (2007) 220-224.
[197] F. Qin, X. Wang, et al., Materials Transactions, 48 (2007) 167-170.
[198] M.L. Morrison, R.A. Buchanan, et al., Journal of Non-Crystalline Solids, 353 (2007) 2115-2124.
[199] A. Kawashima, T. Wada, et al., Materials Science and Engineering A, 542 (2012) 140-146.
[200] A. Monfared, S. Faghihi, et al., International Journal of Electrochemical Science, 8 (2013) 7744-7752.
[201] Z. Liu, K.C. Chan, et al., Materials Transactions, 52 (2011) 61-67.
[202] S.L. Zhu, X.M. Wang, et al., Materials Science and Engineering: A, 459 (2007) 233-237.
[203] A.R. Yavari, A. Le Moulec, et al., Acta Materialia, 53 (2005) 1611-1619.
[204] C. Kittel, Introduction to Solid State Physics (8 ED.) John Wiley & Sons, 2004.
[205] J. Bednarcik, S. Michalik, et al., J Phys-Condens Mat, 23 (2011) 254204.
[206] Y. Waseda, The structure of non-crystalline materials : liquids and amorphous

solids, McGraw-Hill International Book Co., New York; London, 1980.
[207] S.P. Pan, J.Y. Qin, et al., Phys Rev B, 84 (2011) 092201.
[208] D.B. Miracle, Nat Mater, 3 (2004) 697-702.
[209] H.W. Sheng, W.K. Luo, et al., Nature, 439 (2006) 419-425.
[210] T. Ichikawa, physica status solidi (a), 29 (1975) 293-302.
[211] B.W. van de Waal, J Non-Cryst Solids, 189 (1995) 118-128.
[212] V.P. Voloshin, Y.I. Naberukhin, J Struct Chem, 38 (1997) 62-70.
[213] K. Zhang, H. Li, et al., Applied Physics Letters, 102 (2013) 071907.

Abstract

The Ti-based biocompatible human body implants of low Young's modulus and without toxic elements are developed in two regime of materials, crystalline Ti-Nb(-Sn) based alloys and amorphous Ti-Fe-Si based alloys.

A series of Ti-Nb(-Sn) alloys were synthesized by copper mould suction casting and subjected to different heat treatments (furnace cooling or water quenching). The microstructure, thermal and mechanical properties of the as-cast and heat treated samples were investigated. It is shown that the addition of Sn increases the stability of the β phase. The Young's moduli of these alloys were also measured by ultrasonic measurements. Water-quenched $Ti_{74}Nb_{26}$ alloy was found to exhibit the lowest Young's modulus. Sn addition has little impact on the Young's moduli of the TiNb alloys.

The Ti-Fe-Si based amorphous alloys were synthesized by melt spinning. The glass forming ability, thermal properties and corrosion properties of Ti-Fe-Si based alloys were investigated. The glassy compositions were designed according to the deep eutectic rule. It was found that the region near ternary eutectic point ($Ti_{65}Fe_{30}Si_5$) is an icosahedral quasicrystal forming region, whereas the steeper side (Si rich side) of this ternary eutectic point is the glass forming region. Effect of minor elemental addition (Ge, Pd, Zr) on glass forming ability of the Ti-Fe-Si based alloys was also studied. The *in situ* observation of amorphization of $Ti_{40}Zr_{10}Cu_{34}Pd_{14}Sn_2$ glassy alloy in synchrotron beam was conducted. The alloy was successfully vitrified in an aerodynamic levitation apparatus.

Keywords: Ti based alloys, biocompatibility, metallic implants, rapid solidification, mechanical properties, glass formation, quasicrystal

Résumé

Les implants de corps humain biocompatibles à base de Ti de faible module de Young et sans éléments toxiques sont développés dans deux régimes de matériaux, les alliages cristallins à base de Ti-Nb(-Sn) et les alliages amorphes à base de Ti -Fe -Si.

Une série d'alliages à base de Ti-Nb(-Sn) a été synthétisée par solidification rapide et soumis à différents traitements thermiques (refroidissement du four ou trempe à l'eau). La microstructure, les propriétés thermiques et mécaniques des échantillons traités telles que la coulée et la chaleur ont été étudiées. On montre que l'addition de Sn augmente la stabilité de la phase β. Les modules de Young de ces alliages ont été également mesurés avec des mesures par ultrasons. Les alliages $Ti_{74}Nb_{26}$ trempés à l'eau avaient le plus faible module de Young. L'addition de Sn a peu d'impact sur le module de Young des alliages Ti-Nb.

Les alliages amorphes à base de Ti- Fe-Si ont été synthétisés par trempe rapide. La capacité de formation des verres, les propriétés thermiques et les propriétés de corrosion des alliages à base de Ti- Fe-Si ont été étudiées. La composition vitreuse a été conçue en fonction de la règle de l'eutectique profond. On a constaté que la région la plus proche du point eutectique ternaire ($Ti_{65}Fe_{30}Si_5$) est une région quasi-cristalline icosaédrique, tandis que le côté plus raide (Si côté riche) de ce point eutectique ternaire est la région de formation de verre. L'effet de L'addition élémentaire mineur (Ge, Pd, Zr) sur la capacité de formation de verre des alliages à base de Ti- Fe-Si a été également étudié. L'observation *in situ* d'amorphization des alliages vitreux $Ti_{40}Zr_{10}Cu_{34}Pd_{14}Sn_2$ en faisceau synchrotron a été effectuée. L'alliage a été vitrifié avec succès dans un appareil à sustentation aérodynamique.

Mots clef : Les alliages à base de Titane, biocompatibilité, implants métalliques, solidification rapide, propriétés mécaniques, formation du verre, quasicristal